PATIENT SPECIFIC AIDED SURGERY APPROACH OF DEVIATED NASAL SEPTUM USING COMPUTATIONAL FLUID DYNAMICS

KHAISANG HEMTIWAKORN

A THESIS SUBMITTED IN PARTIAL FULFILLMENT
OF THE REQUIREMENT FOR THE DEGREE OF
DOCTOR OF ENGINEERING IN ELECTRICAL ENGINEERING
FACULTY OF ENGINEERING
KING MONGKUT'S INSTITUTE OF TECHNOLOGY LADKRABANG
2014

KMITL-2014-EN-D-018-190

PATIENT SPECIFIC AIDED SURGERY APPROACH OF DEVIATED NASAL SEPTUM USING COMPUTATIONAL FLUID DYNAMICS

KHAISANG HEMTIWAKORN

A THESIS SUBMITTED IN PARTIAL FULFILLMENT

OF THE REQUIREMENT FOR THE DEGREE OF

DOCTOR OF ENGINEERING IN ELECTRICAL ENGINEERING

FACULTY OF ENGINEERING

KING MONGKUT'S INSTITUTE OF TECHNOLOGY LADKRABANG

2014

KMITL-2014-EN-D-018-190

หัวข้อวิทยานิพนธ์	วิธีการช่วยผ่าตัดแบบจำเพาะเจาะจงในผู้ป่วยที่มีภาวะผนังกั้นช่องจมูกคดโดยใช้พลศาสตร์ของไหลเชิงคำนวณ
นักศึกษา	นางสาว ไขแสง เหมทิวากร
รหัสนักศึกษา	51600153
ปริญญา	วิศวกรรมศาสตรดุษฎีบัณฑิต
สาขาวิชา	วิศวกรรมไฟฟ้า
พ.ศ.	2557
อาจารย์ที่ปรึกษาวิทยานิพนธ์	รศ.ดร.ชูชาติ ปิณฑวิรุจน์
อาจารย์ที่ปรึกษาวิทยานิพนธ์ร่วม	ผศ.ดร.สุพันธุ์ ตั้งจิตกุศลมั่น

บทคัดย่อ

ในการผ่าตัดโพรงจมูกเพื่อรักษาผู้ป่วยที่มีภาวะผนังกั้นช่องจมูกคดนั้น ศัลยแพทย์จะทำการรักษาโดยประเมินจากแบบประเมินการอุดตันในโพรงจมูกด้วยตนเองของผู้ป่วย เช่น NOSE score และข้อมูลที่ได้จากเครื่องวัด Rhinomanometry เป็นต้น อย่างไรก็ดี วิธีการประเมินดังกล่าวไม่สามารถระบุตำแหน่งที่เกิดภาวะผนังกั้นช่องจมูกคดได้อย่างชัดเจน อีกทั้งยังไม่สามารถประเมินความผิดปกติของลมหายใจภายในโพรงจมูกอันเนื่องมาจากภาวะผนังกั้นช่องจมูกคดได้อีกด้วย งานวิจัยนี้จึงได้นำเสนอวิธีการช่วยผ่าตัดแบบจำเพาะเจาะจงในผู้ป่วยที่มีภาวะผนังกั้นช่องจมูกคดโดยใช้พลศาสตร์ของไหลเชิงคำนวณร่วมกับเอกซเรย์คอมพิวเตอร์ (CFD-CT aided surgery approach) ซึ่งประกอบไปด้วย 3 ขั้นตอนหลัก ได้แก่ กระบวนการก่อนวางแผนการผ่าตัด, กระบวนการวางแผนการผ่าตัด, และกระบวนการประเมินผลหลังการผ่าตัด เป็นต้น นอกจากนั้น แม่แบบโพรงจมูกของคนปกติจำนวน 5 ราย ยังถูกสร้างขึ้นเพื่อเป็นต้นแบบเปรียบเทียบกับข้อมูลของผู้ป่วยแต่ละรายที่เข้ารับการรักษาอีกด้วย

ผู้วิจัยได้ทำการวิเคราะห์ความเป็นไปได้ที่จะใช้วิธีการช่วยผ่าตัดที่ได้นำเสนอนี้เป็นเครื่องมือช่วยแพทย์ในการวางแผนการรักษาและผ่าตัด โดยทำการวิเคราะห์ในผู้ป่วยที่มีภาวะผนังกั้นช่องจมูกคดรายที่ 1 ซึ่งเป็นผู้ป่วยที่ได้รับการผ่าตัดรักษาตามแบบวิธีปกติ (แพทย์ทำการผ่าตัดโดยไม่ได้ใช้วิธีการช่วยผ่าตัดที่นำเสนอในงานวิจัยนี้) ผลการศึกษาเชิงเปรียบเทียบก่อนและหลังการผ่าตัดพบว่าถึงแม้ผู้ป่วยรายที่ 1 จะพึงพอใจในผลการรักษา โดยประเมินจากค่า NOSE score ที่ลดลงหลังจากได้รับการผ่าตัดก็ตาม แต่ผลการลดลงของค่าความต้านทานลมภายในโพรงจมูกของผู้ป่วยรายที่ 1 ที่วัดด้วยเครื่อง Rhinomanometer นั้น ไม่เป็นที่พึงพอใจสำหรับแพทย์ผู้ทำการรักษา นอกจากนั้น

ข้อมูลพลศาสตร์ของไหลเชิงคำนวณของลมในโพรงจมูกภายหลังการผ่าตัดนั้น ยังคงมีความผันผวนเมื่อเทียบกับคนปกติ ผู้วิจัยจึงตั้งสมมุติฐานว่าความผันผวนที่เกิดขึ้น อาจเกิดจากศัลยแพทย์ทำการผ่าตัดเนื้อเยื่อในโพรงจมูกออกในปริมาณมากเกินไป จนส่งผลให้ความเร็วลมภายในโพรงจมูกลดลงอย่างมากเมื่อเทียบกับค่ามาตรฐานในโพรงจมูกของคนปกติ ด้วยเหตุนี้ แพทย์จึงทำการวางแผนการผ่าตัดอีกครั้ง โดยใช้วิธีการช่วยผ่าตัดที่นำเสนอในงานวิจัยนี้ พบว่า วิธีช่วยผ่าตัดดังกล่าวมีความเป็นไปได้สูงที่จะสามารถวางแผนและจำลองการผ่าตัดที่เหมาะสมสำหรับผู้ป่วยรายนี้ได้ และยังสามารถทำนายผลการผ่าตัดล่วงหน้า ทั้งในเชิงโครงสร้างของโพรงจมูกและพลศาสตร์ของไหลเชิงคำนวณของลมหายใจได้อีกด้วย

ด้วยเหตุนี้ จึงได้มีการประยุกต์ใช้วิธีการช่วยผ่าตัดดังกล่าว ในการรักษาผู้ป่วยผนังกั้นช่องจมูกคดรายที่ 2 โดยข้อมูลที่ได้จากการวิเคราะห์ ได้แก่ ข้อมูลเชิงโครงสร้างของโพรงจมูก, ข้อมูลพลศาสตร์ของไหลเชิงคำนวณของลมหายใจ, NOSE score และ Rhinomanometric data ของผู้ป่วยก่อนผ่าตัด และหลังจากได้รับการผ่าตัด (โดยแพทย์ได้ใช้วิธีการช่วยผ่าตัดที่นำเสนอ และทำการผ่าตัดตามวิธีการรักษาที่เหมาะสมที่สุดสำหรับผู้ป่วยรายที่ 2) ได้ถูกนำมาเปรียบเทียบกัน รวมทั้งเปรียบเทียบกับข้อมูลแม่แบบโพรงจมูกของคนปกติอีกด้วย ทั้งนี้ เพื่อประเมินผลสำเร็จของการผ่าตัดของผู้ป่วยรายที่ 2 นั่นเอง ผลการศึกษาพบว่า วิธีช่วยวางแผนการผ่าตัดที่นำเสนอนี้ สามารถช่วยแพทย์ในการระบุตำแหน่งที่เกิดภาวะผนังกั้นช่องจมูกคดได้อย่างชัดเจน และสามารถช่วยแพทย์วิเคราะห์ปริมาณเนื้อเยื่อโพรงจมูกที่ต้องผ่าตัดออกได้อย่างเหมาะสม นอกจากนั้นยังสามารถช่วยแพทย์ตัดสินใจเลือกวิธีการผ่าตัดที่เหมาะสมที่สุดกับผู้ป่วยรายที่ 2 ได้อีกด้วย โดยผลการรักษาเป็นที่พึงพอใจและเป็นที่ยอมรับทั้งในผู้ป่วยรายที่ 2 และศัลยแพทย์ที่ทำการรักษาอีกด้วย

จากผลการศึกษาดังกล่าวในข้างต้น แสดงให้เห็นว่าวิธีการช่วยผ่าตัดแบบจำเพาะเจาะจงโดยใช้พลศาสตร์ของไหลเชิงคำนวณนี้เหมาะสมที่จะนำมาใช้เป็นเครื่องมือช่วยวางแผนการผ่าตัดผู้ป่วยที่มีภาวะผนังกั้นช่องจมูกคด โดยที่ผลประเมินหลังการผ่าตัดมีความแตกต่างจากผลที่ทำการทำนายไว้ในขั้นตอนการวางแผนการผ่าตัดเพียงเล็กน้อย

Thesis Title	Patient Specific Aided Surgery Approach of Deviated Nasal Septum using Computational Fluid Dynamics
Student	Ms. Khaisang Hemtiwakorn
Student I.D	51600153
Degree	Doctoral of Engineering
Program	Electrical Engineering
Year	2014
Thesis Advisor	Assoc. Prof. Dr. Chuchart Pintavirooj
Thesis Co-Advisor	Asst. Prof. Dr. Supan Tungjitkusolmun

ABSTRACT

In treating a patient with deviated nasal septum (DNS), a surgeon draws up a surgical plan based on the patient's rhinomanometry outcomes and self-assessment of nose conditions, e.g. the nasal obstruction septoplasty effectiveness (NOSE) score. However, the procedure fails to localize the DNS and determine the nose's aerodynamic effects. This research proposes a DNS aided surgery approach using the computational fluid dynamics (CFD) and the computed tomography (CT) techniques consisting of three main processes: pre-operative, pre-surgical planning, and post-operative processes. The healthy baseline refers to a benchmark consisting of five subjects without DNS and nasal airway obstructions. To assess the possibility of using the CFD-CT aided surgery approach as a pre-surgical planning tool in the DNS operation, comparative tests were carried out with DNS patient #1, who received a conventional nasal surgery without the proposed pre-surgical planning. Although DNS patient #1's surgical outcome was relatively satisfying to the patient, evaluating from the reduction of the NOSE score, the conventional surgical method could induce an excessive excision of nasal airway, resulting in a water loss in nasal mucosa and a large airflow velocity reduction. In addition, the post-operative nasal resistance measured by a rhinomanometer was not acceptable to the surgeon. Virtual surgery

using the CFD-CT approach performed after surgery could suggest suitable patient-specific components of nasal operation with predictable results. Subsequently, implementation of the proposed CFD-CT approach in aid of the DNS surgery was performed in DNS patient #2. The benefits of the CFD-CT aided surgery approach is determined based on the pre- and post-operative's outcomes (i.e. nasal geometric data and nasal airflow patterns), NOSE scores, and rhinomanometric data of DNS patient #2, which were compared against those of the healthy baseline benchmark. The CFD-CT approach could assist the surgeon to localize the DNS and determine the defective nasal tissues to remove. The post-actual-operative outcomes were clinically acceptable to the surgeon and DNS patient #2. It is evident that the CFD-CT aided surgery approach is suitable for and applicable to surgery of DNS patients with small variability from the pre-surgical planning stage.

ACKNOWLEDGMENTS

I would like to express my deepest appreciation to my thesis advisor *Assoc. Prof. Dr. Chuchart Pintavirooj* and my thesis co-advisor *Asst. Prof. Dr. Supan Tungjitkusolmun* for all valuable advice, personal attention, and continuous encouragement throughput my doctoral program at KMITL. It was great experience learning with both of them. I am also deeply grateful to my thesis committee members for their involvement and the time they spared to review this thesis.

My sincere gratitude also goes to *Assoc. Prof. Dr. Manas Sangworasil* who has supported me in so many ways, i.e. giving me suggestion, encouraging me to improve engineering skill, and supporting me enormously for going to Japan in ASIA SIMULATION CONFERENCE 2009. My appreciation is extended to all KMITL's staffs, lecturers, professors, and BIOSIS laboratory members for suggestion and supporting me during whole years of study.

Special thanks also go to *Assoc. Prof. Visan Mahasithtiwat M.D.*, Department of Otolaryngology, Faculty of Medicine, Srinakarinwirot University (SWU), for providing DNS patient's CT data and financial support throughout this research work; and *Prof. Jiraporn Laothamatas M.D.*, Director of Advance Diagnostic Imaging Center (AIMC), Ramathibodi Hospital, Mahidol University, for giving me healthy CT data used as the basis for comparison of this research study; and also offering me opportunity to do other research works with professional researchers.

Finally, this research work is dedicated to my parent, my sisters, and my brother for their truly love, encouragement, and supports. My deep appreciation also goes to *Mr. Chousak Jantaco*, who held me up over the years of Ph.D study. I definitely cannot finish my work without his supports.

Khaisang Hemtiwakorn, 2014

TABLE OF CONTENTS

Page

LIST OF TABLES

LIST OF FIGURES

Figure Page

LIST OF ABBREVIATIONS

CFD	Computational Fluid Dynamics
CSA	Cross-Sectional Area
CT	Computed Tomography
DNS	Deviated Nasal Septum
ENT	Ear-Nose-Throat
MCA	Minimal Cross Sectional Area
MRI	Magnetic Resonance Imaging
NAO	Nasal Airflow Simulation
NOSE	Nasal Obstruction Septoplasty Effectiveness
Post-op	Post-Operative
Pre-op	Pre-Operative
ΔP	Pressure Drop
Q	Volumetric Flow
R_N	Nasal Resistance
SD	Standard Deviation
SIMPLE	Semi-Implicit Method for Pressure-Linked Equation (SIMPLE)

Chapter 1
Introduction

1.1 Deviated Nasal Septum (DNS)

Nasal airway obstruction (NAO) is common in ear-nose-throat (ENT) patients with sino-nasal diseases and contributes to poor quality of life of the sufferers [1]. The septal cartilage symmetrically divides nasal cavity into two sides. However, deformation of the septal cartilage from the midline to either side of the nose is possible and thereby induces NAO. The deformation is thus named deviated nasal septum (DNS).

DNS patients account for a large proportion of ENT patients with NAO [2, 3]. DNS could be found in patients of all ages from neonates [4-7], children [8, 9], to mature adults [2, 3, 10]; and DNS in children and adults would worsen with increasing age [2, 8-10]. In addition, DNS was more common in male adults than female adults [3, 10]; however, the ratio was similar in children of both genders [8]. Moreover, history of nasal trauma was reported to be statistically correlated in adult patients with DNS [10]. In addition, DNS could severely affect olfactory perception [11] and thus induce sinusitis, epistaxis, snoring, upper airway infection, and various middle ear infections [9].

1.2 Current Diagnostic Approaches of DNS

Surgeons have many approaches at their disposal to diagnose DNS patients. According to [12], an assessment using the nasal obstruction septoplasty effectiveness (NOSE) scoring technique could fail to reveal irregular airflow patterns and to localize septal deformity in the nasal passage. The NOSE scoring technique is a clinical symptoms scoring system that evaluates the degrees of: (i) nasal congestion, (ii) nasal blockage, (iii) breathing difficulty, (iv) sleep disorder, and (v) insufficient air through the nose during exertion.

Rhinomanometry evaluates the nasal functioning by simultaneously measuring nasal resistance (R_N, in Pa/mL/s) and air flow rate (Q, in mL/s) [13]. R_N is used to determine the pressure-flow relationship in each side of the nose. Compared with a patient without NAO, inside the obstructed side of the nose, R_N of an NAO patient is higher while Q is lower. Rhinomanometry nonetheless failed to identify the exact location of NAO in a patient [14]. Meanwhile, acoustic rhinometry is an anatomical assessment whereby sound waves are transmitted into nasal cavity and then echoing sound waves are registered and used to plot the cross-sectional areas (CSA) inside the nose as a function of distance from the nostrils [15]. Although the acoustic rhinometry technique is pragmatic and non-invasive, it is most suited to rendering the CSA of the anterior end of the nose as the technique yields good results when the distance from nostrils does not exceed 5 cm [16]. CSA beyond the narrow or virtually collapsed areas in nasal cavity tended to be inaccurate [17].

Several advanced medical imaging modalities, including the computed tomography (CT) and magnetic resonance imaging (MRI) technologies, were adopted to diagnose anatomical deformities in the nasal cavity [18, 19]. The technologies produce high resolution images of nasal airway and thereby enable localization of DNS. However, similar to the rhinomanometry technique, the CT and MRI fail to show the airflow characteristics, e.g. velocity and pressure. To overcome this limitation, the CFD technique should be employed together with either CT or MRI.

1.3 Combined CFD with CT Techniques to Create an Aided Surgery Approach of DNS: New Opportunities and Challenges

In [20-24], the CFD-CT technique was used to generate images of the anatomy and physiology of nasal cavity of normal noses. [25-27] studied the effects that DNS had on the nasal airflow patterns prior to surgery using the CFD-CT technique. [28, 29] examined the post-operative nasal airflow patterns using the same technique. [30-32] studied the post-operative outcomes of applying CFD-CT to various surgical procedures. Previous studies by [33, 34] used the CFD-CT technique as a pre-surgical tool in surgery of nasal cavity. However, no study on the use of

CFD-CT as a pre-surgical tool in DNS patients exists. To our knowledge, this study is the first that has proposed the comprehensive aided surgery system for treatment of DNS patients.

1.4 Thesis Research Objectives

In the current study, we propose the integrated CFD-CT aided surgery approach as a patient-specific surgical planning tool in DNS noses. The approach is designed for a non-invasive procedure where surgeons map out DNS surgical plans on reconstructed airways relying on the data from the pre-operative DNS noses to achieve optimal post-virtual-operative outcomes, i.e. nasal geometric data (i.e. septal deviation angle and cross-sectional area) and nasal airflow patterns (i.e. velocity magnitude, pressure drop and, nasal resistance (R_N). Post-actual-operative outcomes are compared with the pre-operative conditions (both nasal geometric data and nasal airflow patterns) to determine the success of the DNS surgery and to assess the efficacy of the CFD-CT aided surgery approach. In addition, the healthy baseline consists of five subjects without DNS and nasal airway obstructions and is used as a benchmark against which the comparisons are made.

1.5 Scope of the Thesis

Steady-state inspiratory laminar airflows will be focused in all nose models of this study. Fixed wall will be assumed in entire models. Thus, the effects of nasal cycle will not be involved in this research study.

1.6 Organization of the Thesis

The dissertation is organized into six chapters.

Chapter 2: describes the conservation laws of fluid motion and boundary conditions, pre-processing process, and post-processing process.

Chapter 3 reviews all topics regarding the proposed CFD-CT aided surgery approach, i.e. nasal anatomy and physiology of the healthy nose and nasal cavity;

causes, symptoms, and incidences of DNS; effects of DNS on nasal patency and nasal airflow; CFD simulation in healthy and DNS noses: the application for a surgical aiding tool. The present research study is described in the end of the chapter.

Chapter 4 presents the design of the proposed CFD-CT aided surgery approach; 6-steps of the CFD simulation method; establishing the healthy baseline; and assessing the possibility of using the CFD-CT aided surgery approach.

Chapter 5 presents the implementation of the CFD-CT aided surgery approach in the DNS patient and post-operative results.

Chapter 6 draws discussion and conclusion; and gives suggestions for future works.

Chapter 2

Fundamentals and Practical Guidelines of Computational Fluid Dynamics (CFD)

2.1 Introduction of Computational Fluid Dynamics (CFD) [35]

2.1.1 What is CFD ?

Computational fluid dynamics (CFD) has definitely developed into an advanced industrial applications and academia research. In the beginning this popular field of study, CFD was primarily limited to high-technology engineering areas of aeronautics and astronautics, but now it is a widely adopted methodology for solving complex problems in many modern engineering fields. CFD, derived from different disciplines of fluid mechanics and heat transfer, is also finding its way into other important uncharted areas especially in process, chemical, civil, and environment engineering.

CFD is the analysis of systems involving fluid flow, heat transfer and associated phenomena such as chemical reactions by means of computer-based simulation. The technique is very powerful and spans a wide range of industrial and non-industrial application areas. In retrospect, it has certainly become a new branch integrating not only the disciplines of fluid mechanics with mathematics but also with computer science as illustrated in Fig. 2.1.

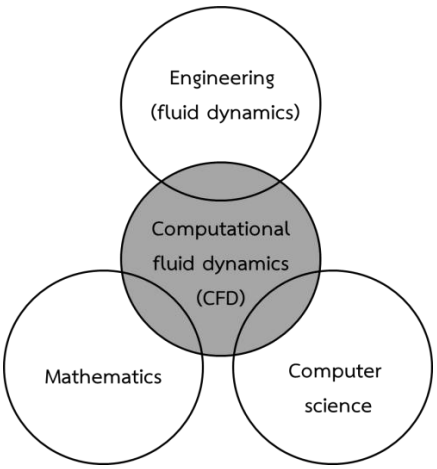

Fig. 2.1 The different disciplines contained within computational fluid dynamics

Fluid mechanics is essentially the study of fluids either in motion (fluid in dynamic mode) or at rest (fluid in stationary mode). CFD is particularly dedicated to the former, fluids that are in motion, and how the fluid flow behavior influences processes that may include heat transfer and possibly chemical reactions in combusting flows. Additionally, the physical characteristics of the fluid motion can usually be described through fundamental ***mathematical equations***, usually in partial differential form, which govern a process of interest and are often called governing equations in CFD.

In order to solve these mathematical equations, they are converted by computer scientists using high level computer programming languages into computer programs or software packages. The **computational part** simply means the study of the fluid flow through numerical simulations, which involves employing computer programs or software packages performed on high-speed digital computer to attain the numerical solutions.

CFD has also become one of the three basic methods or approaches that can be employed to solve problems in fluid dynamics and heat transfer. As demonstrated in Fig. 2.2, each approach is strongly interlinked and does not lie in isolation.

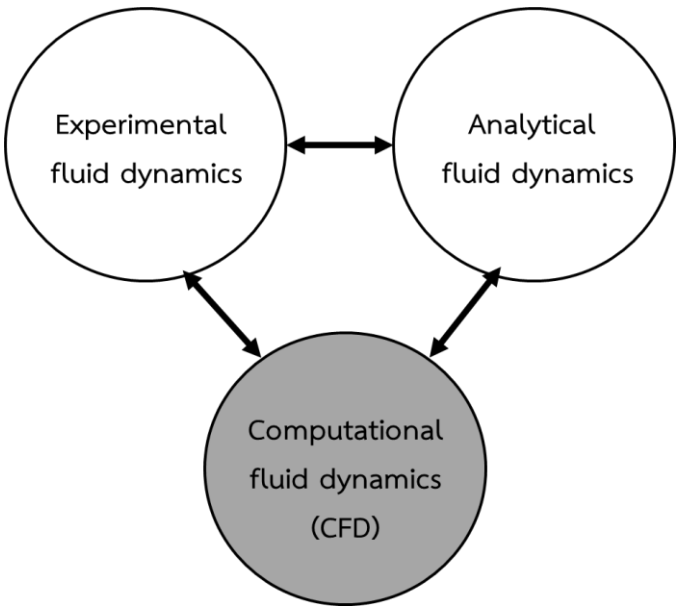

Fig. 2.2 Three approaches to solve problems in fluid dynamics and heat transfer.

Traditionally, both ***experimental and analytical methods*** have been used to study the various aspects of fluid dynamics and to assist engineers in the design of equipment and industrial processes involving fluid flow and heat transfer. With the advent of digital computers, the ***computational (numerical) aspect*** has emerged as another viable approach. Although the analytical method is still practiced by many and experiments will continue to be significantly performed, the trend is clearly toward greater reliance on the computational approach for industrial designs, particularly when the fluid flows are very complex.

CFD has indeed become a powerful tool to be employed either for pure or applied research or industrial applications. Computational simulations and analyses are increasingly performed in many fluid engineering applications that include airplanes (aerospace engineering), motor vehicles (automotive engineering), breathing and blood flow (biomedical engineering), fluid flowing through pumps and pipes (chemical engineering), rivers pollutants (civil and environmental engineering), turbines and furnaces (power engineering), and swimming and golf sports engineering. Through CFD, one can gain an increased knowledge of how system components are expected to perform, so as to make the required improvements for design and optimization studies.

2.1.2 Advantages of CFD

There are many advantages in considering computational fluid dynamics. Firstly, the theoretical development of the computational sciences focuses on the construction and solution of the governing equations and the study of various approximations to these equations. CFD presents the perfect opportunity to study specific terms in the governing equations in a more detailed fashion. New paths of theoretical development are realized, which could not have been possible without the introduction of this branch of computational approach.

Secondly, CFD complements experimental and analytical approaches by providing an alternative cost-effective means of simulating real fluid flows. Particularly, CFD substantially reduces lead times and costs in designs and

production compared to experimental-based approach and offers the ability to solve a range of complicated flow problems where the analytical approach is lacking. These advantages are realized through the increasing performance power in computer hardware and its declining costs.

Thirdly, CFD has the capacity of simulating flow conditions that are not reproducible in experimental tests found in geophysical and biological fluid dynamics, such as nuclear accident scenarios that are too huge or too remote to be simulated experimentally (e.g., Indonesian Tsunami 2004).

Finally, CFD can provide rather detailed, visualized, and comprehensive information when compared to analytical and experimental fluid dynamics.

The utilization of such an approach is usually very effective in the early stages of development for fluid-system designs. It may also prove to be significantly cheaper in contrast to the ever increasing spiraling cost of performing experiments. With technological improvements and competition requiring a higher degree of optimal designs and as new high technological applications demand precise prediction of flow behaviors, experimental development may eventually be too costly to initiate. CFD presents an alternative option. Nevertheless, the favorable appraisal of CFD thus far does not suggest that it will soon replace experimental testing as a means to gather information for design purposes. Instead it is considered a viable alternative.

2.1.3 Applications of CFD in Biomedical Science and Engineering

Medical researchers are nowadays relying on simulation tools to assist in predicting the behavior of circulatory blood flow inside the human body. Computational simulations can provide invaluable information that is extremely difficult to be obtained experimentally; they also many variations of fluid dynamics problems to be parametrically studied.

Figure 2.3 illustrates just one of the many sample applications of CFD in the biomedical area where the blood flow through an abnormal artery has been predicted. With the breadth of physical models and advances in areas of

fluid-structure interaction, particle tracking, turbulence modeling and better meshing facilities, rigorous CFD analysis is increasingly performed to study the fluid phenomena inside the human vascular system.

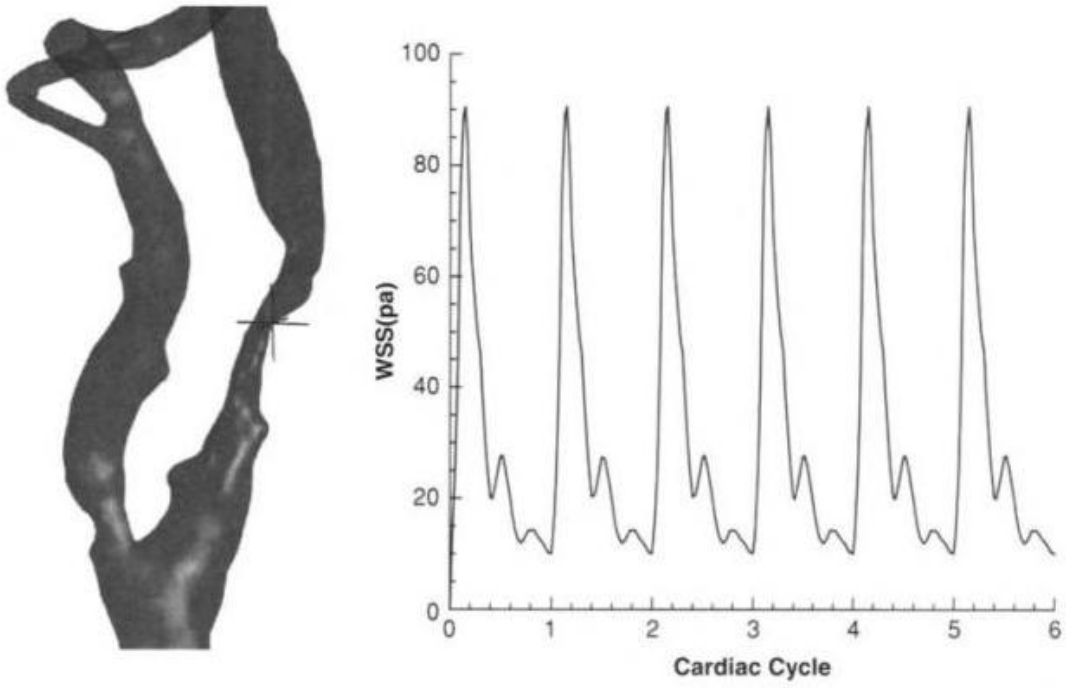

Fig. 2.3 CFD prediction of time-dependent wall shear stress (WSS) fluctuation at the narrowest point.

Medical simulations of circulatory functions offer many benefits. They can lower the chances of postoperative complications, assist in developing better surgical procedures, and deliver a good understanding of biological processes, as well as more efficient and less destructive medical equipment such as blood pumps. For example, CFD is being increasing employed via virtual prototyping to recommend the best design for surgical reconstructions, such as carotid endarterectomy (a sample computational mesh is shown in Fig 2.4), and to better understand the blood flow through an aneurysm in the abdominal artery.

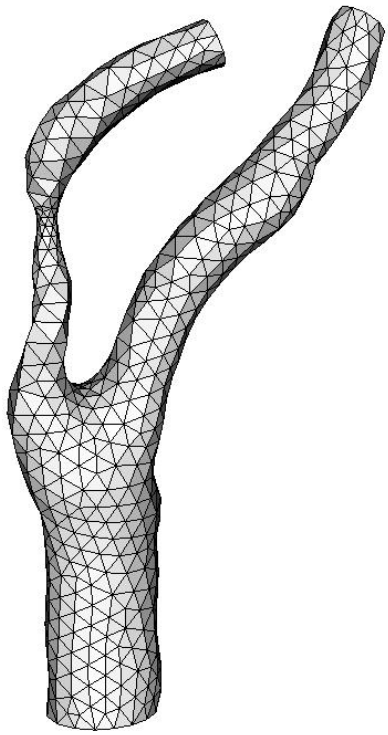

Fig. 2.4 Example of carotid artery bifurcation computational meshes.

2.2 Conservation laws of fluid motion and boundary conditions [36]

2.2.1 Governing equations of fluids flow

The governing equations of fluid flow represent mathematical statements of the conservation laws of physics.

1. The mass of a fluid is conserved.

2. The rate of change of momentum equals the sum of the forces on a fluid particle (Newton's second law).

3. The rate of change of energy is equal to the sum of the rate of heat addition to and the rate of work done on a fluid particle (first law of thermodynamics).

The fluid will be regarded as a continuum. For the analysis of fluid flows at macroscopic length scales (say 1 μm and larger) the molecular structure of matter and molecular motions may be ignored. We describe the behavior of the fluid in terms of macroscopic properties, such as velocity, pressure, density and temperature, and their space and time derivatives. These may be thought of as averages over suitably large numbers of molecules. A fluid particle or point in a fluid is then the

smallest possible element of fluid whose macroscopic properties are not influenced by individual molecules.

We consider such a small element of fluid with sides δx, δy, and δz (Fig. 2.5)

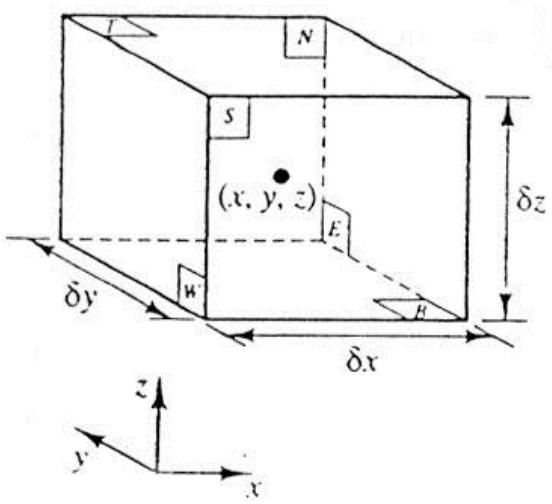

Fig. 2.5 Fluid element for conservation laws

The six faces are labeled N, S, E, W, T, B which stands for North, South, East, West, Top and Bottom. The positive directions along the co-ordinate axes are also given. The center of the element is located at position (x, y, z). A systematic account of changes in the mass, momentum and energy of the fluid element due to fluid flow across its boundaries and, where appropriate, due to the action of source inside the element, leads to the fluid flow equations. All fluid properties are functions of space and time so we would strictly need to write ρ(x, y, z, t), p(x, y, z, t), T(x, y, z, t) and **u**(x, y, z, t) for the density, pressure, temperature and the velocity vector respectively.

2.2.1.1 Mass conservation in three dimensions

The first step in the derivative of the mass conservation equation is to write down a mass balance for the fluid element.

Rate of increase of mass in fluid element = Net rate of flow of mass into fluid element

The rate of increase of mass in the fluid element is

$$\frac{\partial}{\partial t}\left(\rho \delta x \delta y \delta z\right) = \frac{\partial \rho}{\partial t}\delta x \delta y \delta z \tag{2.1}$$

Next we need to account for the mass flow rate across a face of the element which is given by the product of density, area and the velocity component normal to the face.

From Fig. 2.6 it can be seen that the net rate of flow of mass into the element across its boundaries is given by

$$\begin{aligned}
&\left(\rho u - \frac{\partial(\rho u)}{\partial x}\tfrac{1}{2}\delta x\right)\delta y \delta z - \left(\rho u + \frac{\partial(\rho u)}{\partial x}\tfrac{1}{2}\delta x\right)\delta y \delta z \\
&+\left(\rho v - \frac{\partial(\rho v)}{\partial y}\tfrac{1}{2}\delta y\right)\delta x \delta z - \left(\rho v + \frac{\partial(\rho v)}{\partial y}\tfrac{1}{2}\delta y\right)\delta x \delta z \\
&+\left(\rho w - \frac{\partial(\rho w)}{\partial z}\tfrac{1}{2}\delta z\right)\delta x \delta y - \left(\rho w + \frac{\partial(\rho w)}{\partial z}\tfrac{1}{2}\delta z\right)\delta x \delta y
\end{aligned} \tag{2.2}$$

Flows which are directed into the element produce an increase of mass in the element and get a positive sign and those flows that are leaving the element are given a negative sign.

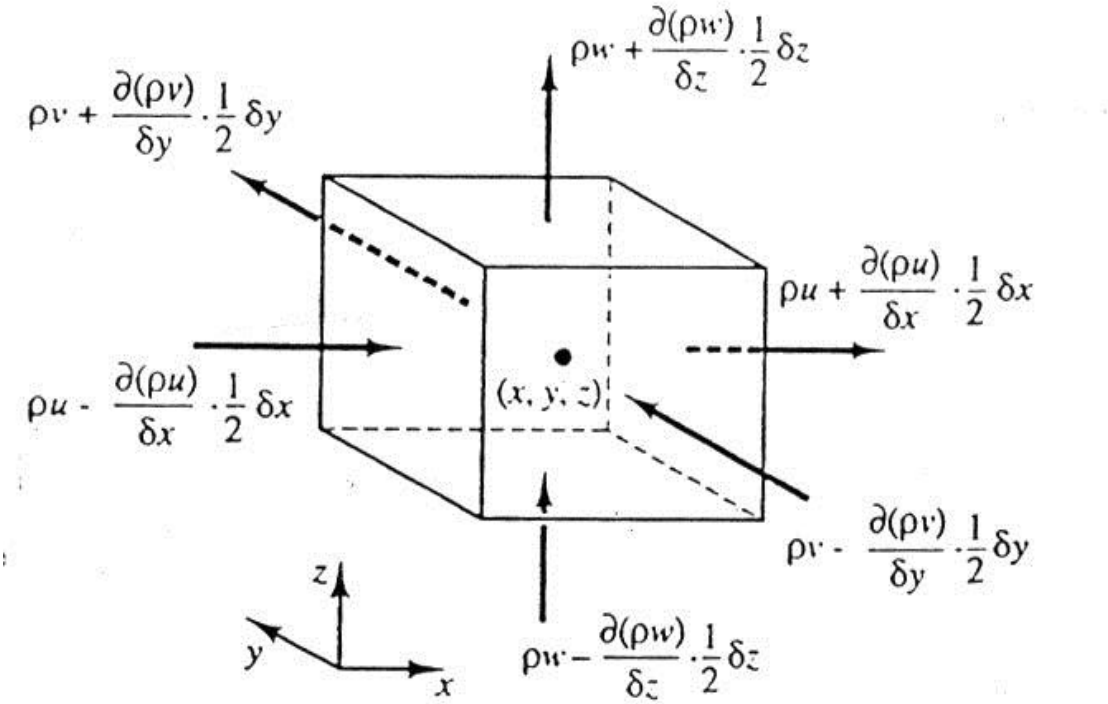

Fig. 2.6 Mass flows in and out of fluid element.

The rate of increase of mass inside the element (2.1) is now equated to the net rate of flow of mass into the element across its faces (2.2). All terms of the resulting mass balance are arranged on the left hand side of the equals sign and the expression is divided by the element volume $\delta x \delta y \delta z$.

This yields

$$\frac{\partial \rho}{\partial t} + \frac{\partial (\rho u)}{\partial x} + \frac{\partial (\rho v)}{\partial y} + \frac{\partial (\rho w)}{\partial z} = 0 \tag{2.3}$$

or in more compact vector notation

$$\boxed{\frac{\partial \rho}{\partial t} + div(\rho \mathbf{u}) = 0} \tag{2.4}$$

Equation (2.4) is the **unsteady, three-dimensional mass conservation or continuity equation** at a point in a **compressible fluid**. The first term on the left hand side is the rate of change in time of the density (mass per unit volume). The second term describes the net flow of mass out of the element across its boundaries and is called the convective term.

For an **incompressible fluid** (i.e. a liquid) the density is constant and equation (2.4) becomes

$$div(\rho \mathbf{u}) = 0 \tag{2.5}$$

or in longhand notation

$$\frac{\partial u}{\partial x} + \frac{\partial v}{\partial y} + \frac{\partial w}{\partial z} = 0 \tag{2.6}$$

2.2.1.2 Momentum equation in three dimensions

Newton's second law states that the rate of change of momentum of a fluid particle equals the sum of the forces on the particle.

Rate of increase of momentum of fluid particle = Sum of forces on fluid particle

The **rates of increase of x-, y- and z- momentum** per unit volume of a fluid particle are given by

$$\partial \frac{Du}{Dt} \qquad \partial \frac{Dv}{Dt} \qquad \partial \frac{Dw}{Dt} \tag{2.7}$$

We distinguish two types of **forces** on fluid particles:

Surface forces - pressure forces

- viscous forces

Body forces - gravity force

- centrifugal force

- Coriolis force

- electromagnetic force

It is common practice to highlight the contributions due to the surface forces as separate terms in the momentum equation and to include the effects of body forces as source terms.

The state of stress of a fluid element is defined in terms of the pressure and the nine viscous stress components shown in Fig. 2.7. The pressure, a normal stress, is denoted by p. Viscous stresses are denoted by $\boldsymbol{\tau}$. The usual suffix notation $\boldsymbol{\tau_{ij}}$ is applied to indicate the direction of the viscous stresses. The suffices i and j in $\boldsymbol{\tau_{ij}}$ indicate that the stress component acts in the j-direction on a surface normal to the i-direction.

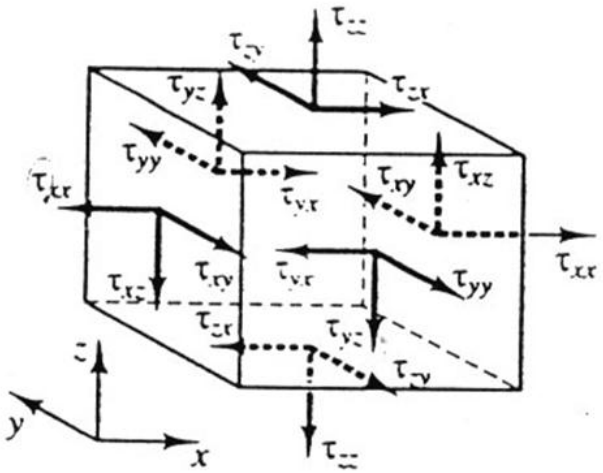

Fig. 2.7 Stress components on three faces of fluid element

First we consider the x-components of the forces due to pressure p and stress components τ_{xx}, τ_{yx} and τ_{zx} shown in Fig. 2.8. The magnitude of a force resulting from a surface stress is the product of stress and area. Forces aligned with the direction of a co-ordinate axis get a positive sign and those in the opposite direction a negative sign. The net force in the x-direction is the sum of the force components acting in that direction on the fluid element.

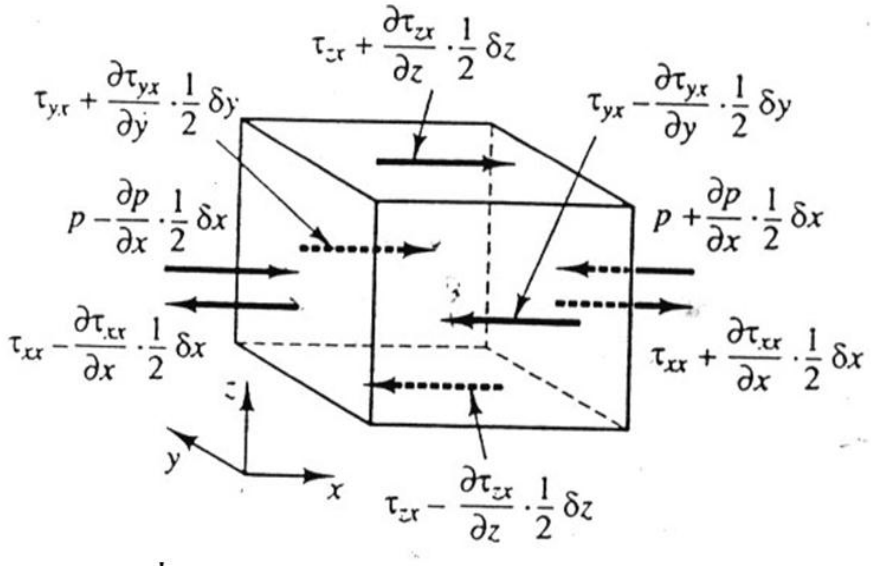

Fig. 2.8 Stress components in the x-direction

On the pair of faces (E,W) we have

$$\left[\left(p-\frac{\partial p}{\partial x}\frac{1}{2}\delta x\right)-\left(\tau_{xx}-\frac{\partial \tau_{xx}}{\partial x}\frac{1}{2}\delta x\right)\right]\delta y\delta z+\left[-\left(p+\frac{\partial p}{\partial x}\frac{1}{2}\delta x\right)+\left(\tau_{xx}+\frac{\partial \tau_{xx}}{\partial x}\frac{1}{2}\delta x\right)\right]\delta y\delta z$$
$$=\left(-\frac{\partial p}{\partial x}+\frac{\partial \tau_{xx}}{\partial x}\right)\delta x\delta y\delta z \qquad (2.8a)$$

The net forces in the x-direction on the pair of faces (N, S) is

$$-\left(\tau_{yx}-\frac{\partial \tau_{yx}}{\partial y}\frac{1}{2}\delta y\right)\delta x\delta z+\left(\tau_{yx}+\frac{\partial \tau_{yx}}{\partial y}\frac{1}{2}\delta y\right)\delta x\delta z=\frac{\partial \tau_{yx}}{\partial y}\delta x\delta y\delta z \qquad (2.8b)$$

Finally the net force in the x-direction on faces T and B is given by

$$-\left(\tau_{zx}-\frac{\partial \tau_{zx}}{\partial z}\frac{1}{2}\delta z\right)\delta x\delta y+\left(\tau_{zx}+\frac{\partial \tau_{zx}}{\partial z}\frac{1}{2}\delta z\right)\delta x\delta y=\frac{\partial \tau_{zx}}{\partial z}\delta x\delta y\delta z \qquad (2.8c)$$

The total force per unit volume on the fluid due to these surface stresses is equal to the sum of (2.8a), (2.8b) and (2.8c) divided by the volume $\delta x\delta y\delta z$:

$$\frac{\partial(-p+\tau_{xx})}{\partial x}+\frac{\partial \tau_{yx}}{\partial y}+\frac{\partial \tau_{zx}}{\partial z} \tag{2.9}$$

Without forces in further detail their overall effect can be included by defining a source S_{Mx} of x-momentum per unit volume per unit time.

The **x-component of the momentum equation** is found by setting the rate of change of x-momentum of the fluid particle (2.7) equal to the total force in the x-direction on the element due to surface stresses (2.9) plus the rate of increase of x-momentum due to sources:

$$\boxed{\rho\frac{Du}{Dt}=\partial\frac{(\rho u)}{\partial t}+div(\rho u\mathbf{u})=\frac{\partial(-p+\tau_{xx})}{\partial x}+\frac{\partial \tau_{yx}}{\partial y}+\frac{\partial \tau_{zx}}{\partial z}+S_{Mx}} \tag{2.10a}$$

It is not too difficult to verify that the **y-component of the momentum equation** is given by

$$\boxed{\rho\frac{Dv}{Dt}=\partial\frac{(\rho v)}{\partial t}+div(\rho u\mathbf{u})=\frac{\partial \tau_{xy}}{\partial x}+\frac{\partial(-p+\tau_{yy})}{\partial y}+\frac{\partial \tau_{zy}}{\partial z}+S_{My}} \tag{2.10b}$$

and the **z-component of the momentum equation** by

$$\boxed{\rho\frac{Dw}{Dt}=\partial\frac{(\rho w)}{\partial t}+div(\rho w\mathbf{u})=\frac{\partial \tau_{xz}}{\partial x}+\frac{\partial \tau_{yz}}{\partial y}+\frac{\partial(-p+\tau_{zz})}{\partial z}+S_{Mz}} \tag{2.10c}$$

The sign associated with the pressure is opposite to that associated with the normal viscous stress, because the usual sign convention takes a tensile stress to be the positive normal stress so that the pressure, which is by defining a compressive normal stress, has a minus sign.

The effects of surface stresses are accounted for explicitly; thee source terms S_{Mx}, S_{My} and S_{Mz} in (2.10 a-c) included contributions due to body forces only. For example, the body force due to gravity would be modeled by $S_{Mx}=0$, $S_{My}=0$ and $S_{Mz}=\rho g$.

2.2.1.3 Energy equation in three dimensions

The energy equation is derived from the **first law of thermodynamics** which states that the rate of change of energy of a fluid particle is

equal to the rate of heat addition to the fluid particle plus the arte of work done on the particle.

Rate of increase of energy of fluid particle
= Net rate of heat added to fluid particle + Net rate of work done on fluid particle

As before we will be deriving an equation for the **rate of increase of energy** of a fluid particle per unit volume which is given by

$$\partial\frac{(\rho E)}{\partial t}+div(\rho E\mathbf{u})=\rho\frac{DE}{Dt} \tag{2.11}$$

Work done by surface forces

The **rate of work done** on the fluid particle in the element by a **surface force** is equal to the product of the force and velocity component in the direction of the force. For example, the forces given by (2.8a-c) all act in the x-direction. The work done by these forces is given by

$$\begin{aligned}\left[\left(pu-\frac{\partial(pu)}{\partial x}\frac{1}{2}\delta x\right)-\left(\tau_{xx}u-\frac{\partial(\tau_{xx}u)}{\partial x}\frac{1}{2}\delta x\right)\right.&\\ \left.-\left(pu+\frac{\partial(pu)}{\partial x}\frac{1}{2}\delta x\right)+(\tau_{xx}u+\frac{\partial(\tau_{xx}u)}{\partial x}\frac{1}{2}\delta x)\right]\delta y\delta z&\\ +\left[-\left(\tau_{yx}u-\frac{\partial(\tau_{yx}u)}{\partial y}\frac{1}{2}\delta y\right)+\left(\tau_{yx}u+\frac{\partial(\tau_{yx}u)}{\partial y}\frac{1}{2}\delta y\right)\right]\delta x\delta z&\\ +\left[-\left(\tau_{yx}u-\frac{\partial(\tau_{zx}u)}{\partial z}\frac{1}{2}\delta z\right)+\left(\tau_{zx}u+\frac{\partial(\tau_{zx}u)}{\partial z}\frac{1}{2}\delta z\right)\right]\delta x\delta y&\end{aligned}$$

The net rate of work done by these surface forces acting in the x-direction is given by

$$\left[\frac{\partial\left[u\left(-p+\tau_{xx}\right)\right]}{\partial x}+\frac{\partial\left(u\tau_{yx}\right)}{\partial y}+\frac{\partial\left(u\tau_{zx}\right)}{\partial z}\right]\delta x\delta y\delta z \tag{2.12a}$$

Surface stress components in the y- and z-direction also do work on the fluid particle. A repetition of the above process gives the additional rates of work done on the fluid particle due to the work done by these surface forces:

$$\left[\frac{\partial(v\tau_{xy})}{\partial x}+\frac{\partial[v(-p+\tau_{yy})]}{\partial y}+\frac{\partial(v\tau_{zy})}{\partial z}\right]\delta x\delta y\delta z \qquad (2.12b)$$

$$\left[\frac{\partial(w\tau_{xz})}{\partial x}+\frac{\partial(w\tau_{yz})}{\partial y}+\frac{\partial[w(-p+\tau_{zz})]}{\partial z}\right]\delta x\delta y\delta z \qquad (2.12c)$$

The total rate of work done per unit volume on the fluid particle by all the surface forces is given by the sum of (2.12a-c) divided by the volume $\delta x\delta y\delta$. The terms containing pressure can be collected together and written more compactly in vector form:

$$-\frac{\partial(up)}{\partial x}-\frac{\partial(vp)}{\partial y}-\frac{\partial(wp)}{\partial z}=-div(p\mathbf{u})$$

This yields the following **total rate of work done on the fluid particle by surface stresses**:

$$[-div(p\mathbf{u})]+\left[\frac{\partial(u\tau_{xx})}{\partial x}+\frac{\partial(u\tau_{yx})}{\partial y}+\frac{\partial(u\tau_{zx})}{\partial z}+\frac{\partial(v\tau_{xy})}{\partial x}+\frac{\partial(v\tau_{yy})}{\partial y}\right.$$
$$\left.+\frac{\partial(v\tau_{zy})}{\partial z}+\frac{\partial(w\tau_{xz})}{\partial x}+\frac{\partial(w\tau_{yz})}{\delta y}+\frac{\partial(w\tau_{zz})}{\partial z}\right] \qquad (2.13)$$

Energy flux due to heat conduction

The heat flux vector **q** has three components qx, qy and qz (Fig. 2.9).

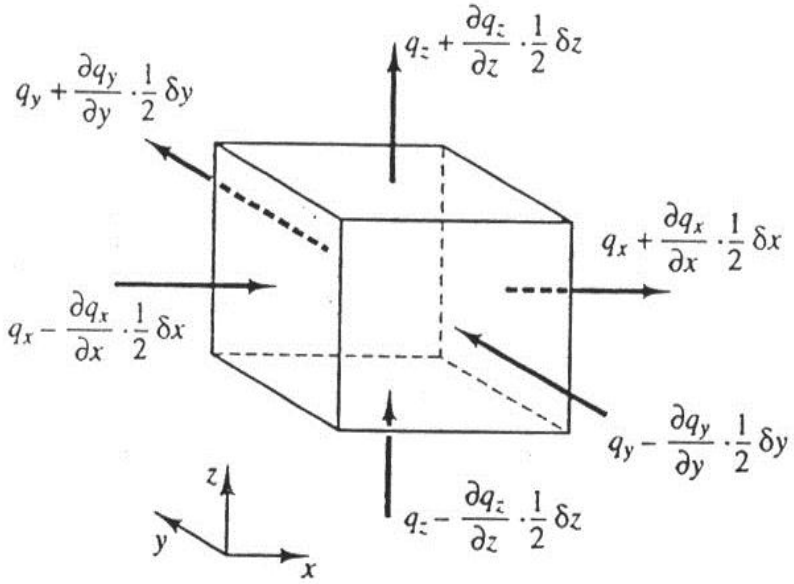

Fig. 2.9 Components of the heat flux vector

The **net rate of heat transfer to the fluid particle** sue to heat flow in the x-direction is given by the difference between the rate of heat input across face W and the rate of heat loss across face E:

$$\left[\left(q_x - \frac{\partial q_x}{\partial x}\frac{1}{2}\delta x\right) - \left(q_x + \frac{\partial q_x}{\partial x}\frac{1}{2}\delta x\right)\right]\delta y\delta z = -\frac{\partial q_x}{\partial x}\delta x\delta y\delta z \qquad (2.14a)$$

Similarly, the net rates of heat transfer to the fluid due to heat flows in the y- and z-direction are

$$-\frac{\partial q_y}{\partial y}\delta x\delta y\delta z \qquad \text{and} \qquad -\frac{\partial q_z}{\partial z}\delta x\delta y\delta z \qquad (2.14b\text{-}c)$$

The total rate of heat added to the fluid particle per unit volume due to heat flow across its boundaries is the sum of (3.14a-c) divided by the volume $\delta x\delta y\delta z$

$$-\frac{\partial q_x}{\partial x} - \frac{\partial q_y}{\partial x} - \frac{\partial q_z}{\partial x} = -div\ \boldsymbol{q} \qquad (2.15)$$

Fourier's law of heat conduction relates the heat flux to the local temperature gradient. So

$$q_x = -k\frac{\partial T}{\partial x} \qquad q_y = -k\frac{\partial T}{\partial y} \qquad q_z = -k\frac{\partial T}{\partial z}$$

This can be written in vector form as follows:

$$\boldsymbol{q} = -k\ grad\ T \qquad (2.16)$$

Combining (3.15) and (3.16) yields the final form of the **rate of heat addition to the fluid particle due to heat conduction** across element boundaries:

$$-div\ \boldsymbol{q} = div(k\ grad\ T) \qquad (2.17)$$

Energy equation

Thus far we have not defined the specific energy *E* of a fluid. Often the energy of a fluid is defined as the sum of internal (thermal) energy *i*, kinetic energy $\frac{1}{2}(u^2 + v^2 + w^2)$ and gravitational potential energy. This definition takes the view that the fluid element is storing gravitational potential energy. It is also possible to regard the gravitational force as a body force which does work on the fluid element as it moves through the gravity field.

Here we shall take the latter view and include the effects of potential energy changes as a source term. As before we define a source of energy S_E

per unit volume per unite time. Conservation of energy of the fluid particle is ensured by equation the rate of change of energy of the fluid particle (2.11) to the sum of the net rate of work done on the fluid particle (2.13) and the net rate of heat addition to the fluid (2.17) and the rate of increase of energy due to sources. The energy equation is

$$\rho\frac{DE}{Dt}=\left[-div(p\mathbf{u})\right]+\left[\frac{\partial(u\tau_{xx})}{\partial x}+\frac{\partial(u\tau_{yx})}{\partial y}+\frac{\partial(u\tau_{zx})}{\partial z}+\frac{\partial(v\tau_{xy})}{\partial x}+\frac{\partial(v\tau_{yy})}{\partial y}+\frac{\partial(v\tau_{zy})}{\partial z}+\frac{\partial(w\tau_{xz})}{\partial x}+\frac{\partial(w\tau_{yz})}{\delta y}+\frac{\partial(w\tau_{zz})}{\partial z}\right]-div(k\ grad\ T)+S_E \tag{2.18}$$

2.2.2 Equation of state

The motion of a fluid in three dimensions is described by a system of five partial differential equations: mass conservation (2.4), x-, y- and z-momentum equations (2.10a-c) and energy equation (2.18). Among the unknowns are four thermodynamic variables: ρ, p, i and T. In this brief discussion we point out the linkage between these four variables. Relationships between the thermodynamic variables can be obtained through the assumption of **thermodynamic equilibrium**. The fluid velocities may be large, but they are usually small enough that, even though the properties of a fluid particle change rapidly from place to place, the fluid can thermodynamically adjust itself to new conditions so quickly that the changes are effectively instantaneous. Thus the fluid always remains in thermodynamic equilibrium. The only exceptions are certain flows with strong shockwaves, but even some of those are often well enough approximately by equilibrium assumptions.

We can describe the state of a substance in thermodynamic equilibrium by means of just two state variables. **Equations of state** relate the other variables to the two state variables. If we use ρ and T as state variables we have state equations for pressure *p and specific internal energy i*:

$$p=p(\rho,T) \quad \text{and} \quad i=i(\rho,T) \tag{2.19}$$

For a perfect gas the following, well-known, equations of state are useful:

$$p = \rho RT \quad \text{and} \quad i = C_v T \tag{2.20}$$

The assumption of thermodynamic equilibrium eliminates all but the two thermodynamic state variables. In the of **compressible fluids** the equations of state provide the linkage between the energy equation on the one hand and mass conservation and momentum equations on the other. This linkage arises through the possibility of density variations as a result of pressure and temperature variations in the flow field.

Liquids and gasses flowing at low speeds behave as **incompressible fluids**. Without density variations there is no linkage between the energy equation and the mass conservation and momentum equations. The flow field can often be solved by considering mass conservation and momentum equations only. The energy equation only needs to be solved alongside the others if the problem involves heat transfer.

2.2.3 Navier-Stokes equations for a Newtonian fluid

The governing equations contain as further unknowns the viscous stress components τ_{ij}. The most useful forms of the conservation equations for fluid flows are obtained by introducing a suitable model for the viscous stresses τ_{ij}. In many fluid flows the viscous stresses can be expressed as functions of the local deformation rate (or strain rate). In three-dimensional flows the local rate of deformation is composed of the linear deformation rate and the volumetric deformation rate.

All gases and many liquids are isotropic. Liquids which contain significant quantities of polymer molecules may exhibit anisotropic or directional viscous stress properties as a result of the alignment of the chain-like polymer molecules with the flow. Such fluids are beyond the scope of this introductory course and we shall continue the development by assuming that the fluids are isotropic.

The rate of linear deformation of a fluid element has nine components in three dimensions, six of which are independent in isotropic fluids (Schlichting, 1979). They are denoted by the symbol e_{ij}. The suffix system is identical to that for stress components (see section 2.4). There are three linear elongating deformation components:

$$e_{xx} = \frac{\partial u}{\partial x} \qquad e_{yy} = \frac{\partial v}{\partial y} \qquad e_{zz} \frac{\partial w}{\partial z} \tag{2.21a}$$

There are also six shearing linear deformation components:

$$e_{xy} = e_{yx} = \tfrac{1}{2}\left(\frac{\partial u}{\partial y} + \frac{\partial v}{\partial x}\right) \qquad e_{xz} = e_{zx} = \tfrac{1}{2}\left(\frac{\partial u}{\partial z} + \frac{\partial w}{\partial x}\right)$$

$$e_{yz} = e_{zy} = \tfrac{1}{2}\left(\frac{\partial v}{\partial z} + \frac{\partial w}{\partial y}\right) \tag{2.21b}$$

The volumetric deformation is given by

$$\frac{\partial u}{\partial x} + \frac{\partial v}{\partial y} + \frac{\partial w}{\partial z} = div\,\mathbf{u} \tag{2.21c}$$

In a Newtonian fluid the viscous stresses are proportional to the rates of deformation. The three-dimensional form of Newton's law of viscosity for compressible flows involves two constants of proportionality: the (first) dynamic viscosity, μ, to relate stresses to linear deformations, and the second viscosity, λ, to relate stresses to the volumetric deformation. The nine viscous stress components, of which six are independent, are

$$\tau_{xx} = 2\mu\frac{\partial u}{\partial x} + \lambda\, div\,\mathbf{u} \quad \tau_{yy} = 2\mu\frac{\partial v}{\partial y} + \lambda\, div\,\mathbf{u} \quad \tau_{zz} = 2\mu\frac{\partial w}{\partial z} + \lambda\, div\,\mathbf{u}$$

$$\tau_{xy} = \tau_{yx} = \mu\left(\frac{\partial u}{\partial x} + \frac{\partial v}{\partial x}\right) \qquad \tau_{xz} = \tau_{zx} = \mu\left(\frac{\partial u}{\partial z} + \frac{\partial w}{\partial x}\right)$$

$$\tau_{yz} = \tau_{zy} = \mu\left(\frac{\partial v}{\partial z} + \frac{\partial w}{\partial y}\right) \tag{2.22}$$

Not much is known about the second viscosity λ, because its effect is small in practice. For gases a good working approximation can be obtained by taking the value $\lambda = -\frac{2}{3}\mu$ (Schlichting, 1979). Liquids are incompressible so the mass conservation equation is *div* $\mathbf{u}$ *= 0* and the viscous stresses are just twice the local rate of linear deformation times the dynamic viscosity.

Substitution of the above shear stresses (2.22) into (2.10a-c) yields the so-called Navier-Stokes equations named after the two 19th century scientists who derived them independently:

$$\rho\frac{Du}{Dt}=-\frac{\partial p}{\partial x}+\frac{\partial}{\partial x}\left[2\mu\frac{\partial u}{\partial x}+\lambda\,div\,\mathbf{u}\right]+\frac{\partial}{\partial y}\left[\mu\left(\frac{\partial u}{\partial y}+\frac{\partial v}{\partial x}\right)\right]+\frac{\partial}{\partial z}\left[\mu\left(\frac{\partial u}{\partial z}+\frac{\partial w}{\partial x}\right)\right]+S_{Mx} \tag{2.23a}$$

$$\rho\frac{Dv}{Dt}=-\frac{\partial p}{\partial y}+\frac{\partial}{\partial x}\left[\mu\left(\frac{\partial u}{\partial y}+\frac{\partial v}{\partial x}\right)\right]+\frac{\partial}{\partial y}\left[2\mu\frac{\partial v}{\partial y}+\lambda\,div\,\mathbf{u}\right]+\frac{\partial}{\partial z}\left[\mu\left(\frac{\partial v}{\partial z}+\frac{\partial w}{\partial y}\right)\right]+S_{My} \tag{2.23b}$$

$$\rho\frac{Dw}{Dt}=-\frac{\partial p}{\partial z}+\frac{\partial}{\partial x}\left[\mu\left(\frac{\partial u}{\partial z}+\frac{\partial w}{\partial x}\right)\right]+\frac{\partial}{\partial y}\left[\mu\frac{\partial v}{\partial z}+\frac{\partial w}{\partial y}\right]+\frac{\partial}{\partial z}\left[2\mu\frac{\partial w}{\partial z}+\lambda\,div\,\mathbf{u}\right]+S_{Mz} \tag{2.23c}$$

Often it is useful to re-arrange the viscous stress terms as follows:

$$\begin{aligned}\frac{\partial}{\partial x}\left[2\mu\frac{\partial u}{\partial x}+\lambda\,div\,\mathrm{u}\right]+\frac{\partial}{\partial y}\left[\mu\left(\frac{\partial u}{\partial y}+\frac{\partial v}{\partial x}\right)\right]+\frac{\partial}{\partial z}\left[\mu\left(\frac{\partial u}{\partial z}+\frac{\partial w}{\partial x}\right)\right]&\\ =\frac{\partial}{\partial x}\left(\mu\frac{\partial u}{\partial x}\right)+\frac{\partial}{\partial y}\left(\mu\frac{\partial u}{\partial y}\right)+\frac{\partial}{\partial z}\left(\mu\frac{\partial u}{\partial z}\right)&\\ +\left[\frac{\partial}{\partial x}\left(\mu\frac{\partial u}{\partial x}\right)+\frac{\partial}{\partial y}\left(\mu\frac{\partial v}{\partial x}\right)+\frac{\partial}{\partial z}\left(\mu\frac{\partial w}{\partial x}\right)\right]&\\ +\frac{\partial}{\partial x}\left(\lambda\,div\,\mathbf{u}\right)=div\left(\mu\,grad\,u\right)+S_{Mx}&\end{aligned}$$

The viscous stresses in the y- and z-component equations can be re-cast in a similar manner. We clearly intend to simplify the momentum equations by 'hiding' the two smaller contributions to the viscous stress terms in the momentum source. Defining a new source by

$$S_M=S_M+s_M \tag{2.24}$$

the **Navier-Stokes equations** can be written in the most useful form for the development of the finite volume method:

$$\rho\frac{Du}{Dt} = -\frac{\partial p}{\partial x} + div(\mu\, grad\, \mathbf{u}) + S_{Mx} \tag{2.25a}$$

$$\rho\frac{Dv}{Dt} = -\frac{\partial p}{\partial y} + div(\mu\, grad\, \mathbf{u}) + S_{My} \tag{2.25b}$$

$$\rho\frac{Dw}{Dt} = -\frac{\partial p}{\partial z} + div(\mu\, grad\, \mathbf{u}) + S_{Mz} \tag{2.25c}$$

2.2.4 Conservative form of the governing equations of fluid flow

To summarize the findings thus far we quote in Table 2.1 the conservative or divergence form of the system of equations which governs the time-dependent three-dimensional fluid flow and heat transfer of a compressible Newtonian fluid.

Table 2.1 Governing equations of the flow of a compressible Newtonian fluid

Mass	$\frac{\partial \rho}{\partial t} + div(\rho\vec{\mathrm{u}}) = 0$	(2.4)
x-momentum	$\frac{\partial(\rho \mathrm{u})}{\partial \mathrm{t}} + div(\rho u\vec{\mathrm{u}}) = -\frac{\partial p}{\partial x} + div(\mu\, grad\, u) + S_{Mx}$	(2.26)
y-momentum	$\frac{\partial(\rho v)}{\partial \mathrm{t}} + div(\rho v\vec{\mathrm{u}}) = -\frac{\partial p}{\partial y} + div(\mu\, grad\, v) + S_{My}$	(2.27)
z-momentum	$\frac{\partial(\rho \mathrm{w})}{\partial \mathrm{t}} + div(\rho w\vec{\mathrm{u}}) = -\frac{\partial p}{\partial z} + div(\mu\, grad\, w) + S_{Mz}$	(2.28)
Internal energy	$\frac{\partial(\rho i)}{\partial \mathrm{t}} + div(\rho i\vec{\mathrm{u}}) = -p\, div\,\vec{\mathrm{u}} + div(k\, grad\, T) + \Phi + S_i$	(2.29)
Equation of state	$p = p(\rho, T) and\ i = i(\rho, T)$	(2.19)
	e.g. perfect gas	
	$p = \rho RT\ and\ i = C_v T$	(2.20)

2.3 Problem Setup: Pre-Process [35]

2.3.1 Creation of geometry- Step 1

The first step in any CFD analyses is the definition and creation of geometry of the flow region (i.e., the *computational domain*) for the CFD calculations. Figure. 2.10 presents a simple geometry of fluid flowing between two stationary parallel plates. The fluid flow is bounded within a domain of rigid walls as represented by the horizontal external walls of the two stationary parallel plates. It is important that the CFD user should always acknowledge the real physical flow representation of the problem that is to be solved as demonstrated by the respective physical domains in Fig. 2.10.

One important aspect that the CFD user should always note in the creation of the geometry for CFD calculations is to allow the flow dynamics to be sufficiently developed across the length L of these computational domains. In Fig. 2.10, the flow is required to be fully developed as it exits the domain.

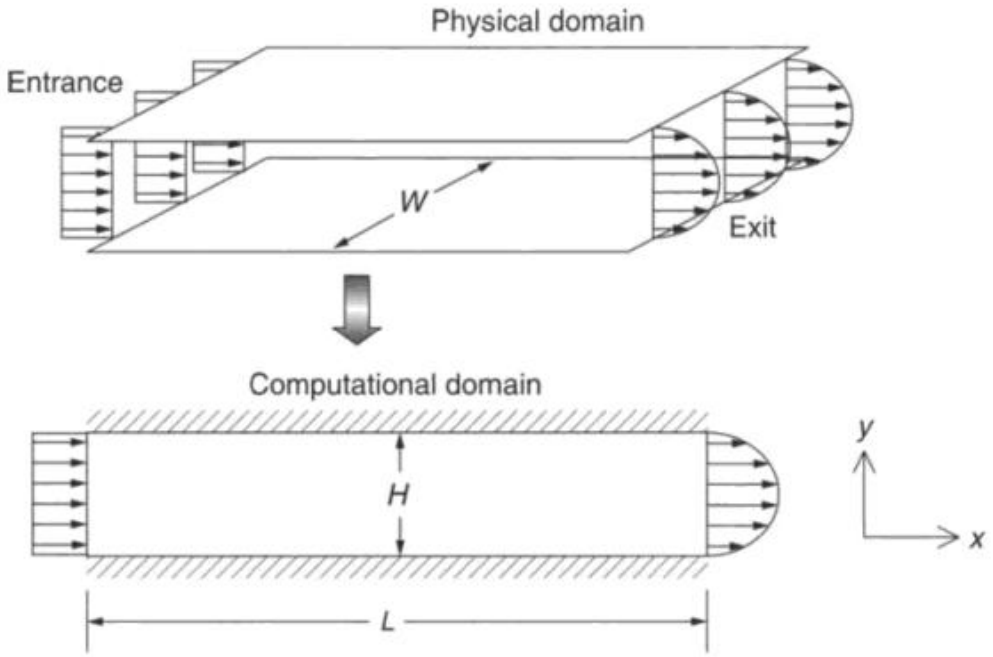

Fig. 2.10 Fluid flowing between two stationary parallel plates.

2.3.2 Mesh generation- Step 2

The second step—mesh generation—constitutes one of the most important steps during the pre-process stage after the definition of the domain geometry. CFD requires the subdivision of the domain into a number of smaller, nonoverlapping subdomains in order to solve the flow physics within the domain geometry that has been created; this results in the generation of a *mesh* (or grid) or *cells* (elements or control volumes) overlaying the whole domain geometry. The essential fluid flows that are described in each of these cells are usually solved numerically so that the discrete values of the flow properties such as the velocity, pressure, temperature, and other transport parameters of interest are determined. This yields the CFD solution to the flow problem that is being solved.

The accuracy of a CFD solution is governed by the number of cells in the mesh within the computational domain. In general, the provision of a large number of cells leads to the attainment of an accurate solution. However, the accuracy of a solution is strongly dependent on the imposed limitations dominated by the computational costs and calculation turnover times. The CFD user should be well aware that is still up to the skills of the user to design a mesh that is a suitable compromise between the desired accuracy and solution cost.

For relatively simple geometries such as the created geometry domain shown in Fig. 2.10, an overlay mesh of structured cells that generally comprises a regular distribution of rectangular cells can be readily realized. Figure 2.11 shows a mesh 20 (L) x 20 (H) cells resulting in a total number of 400 cells. For more complex geometries, the meshing by triangular cells allows the flexibility of mesh generation for geometries having complicated shape boundaries. Figure 2.12 illustrates a typical distribution of triangular cells within the computational domain for fluid passing over two cylinders in an open surrounding with a mesh totaling 16,637 cells mapping the whole flow domain.

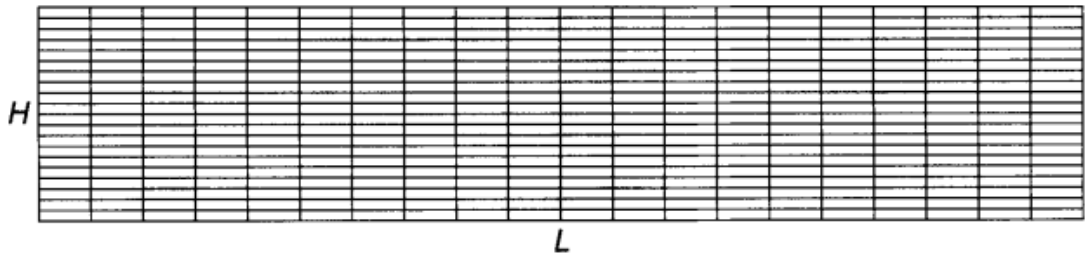

Fig. 2.11 Structured meshing for fluid flowing between two stationary parallel plates.

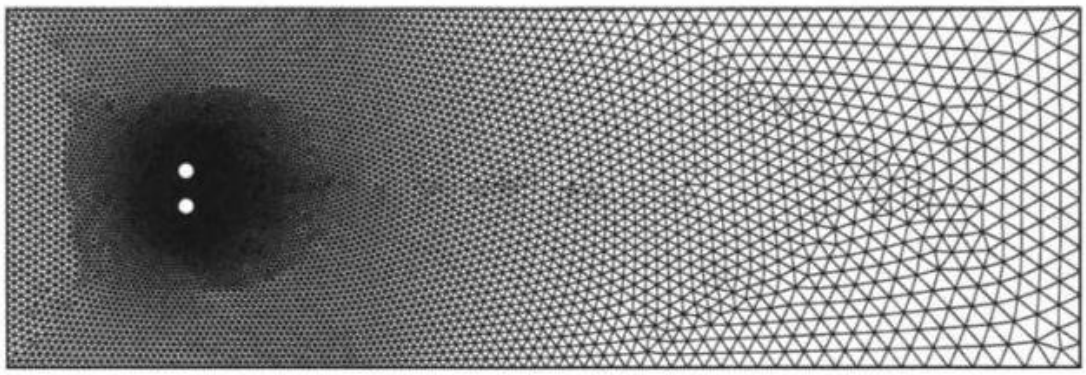

Fig. 2.12 Unstructured meshing for fluid passing over two cylinders in an open surrounding.

2.3.3 Selection of physics and fluid properties- Step 3

For clarity and ease of reference, a flowchart highlighting the various flow physics that may be encountered within the framework of CFD and heat transfer processes is presented in Fig. 2.13. Under the main banner of Computational Fluid Dynamics & Heat Transfer, a CFD user declares initially whether simulations to the fluid flow system are to be attained for transient/unsteady or steady solutions. He/she subsequently defines which class of fluids that the flows may belong: inviscid or viscous. Inviscid fluid flows are generally compressible and the consideration of fluid compressibility in the flow physics can usually be handled through the Panel Method. Viscous fluid flows can, however, exist in their laminar or turbulent state. Under these two flow conditions, prior knowledge of whether the fluids are compressible or in compressible is required. The classification of internal and external flows for viscous fluids allows the user to appropriately treat these types of flow problems.

Also, the transport of heat may contribute significantly to the fluid flow process, which comprises three heat transfer modes: conduction, convection, and radiation. For convection, the domain mode of heat transfer will more likely be driven by the convective fluid flow rather than by other modes of conduction and radiation. Nevertheless, there are circumstances where radiation and convection can co-exist and dominate the heat transfer especially in the expansion of fires.

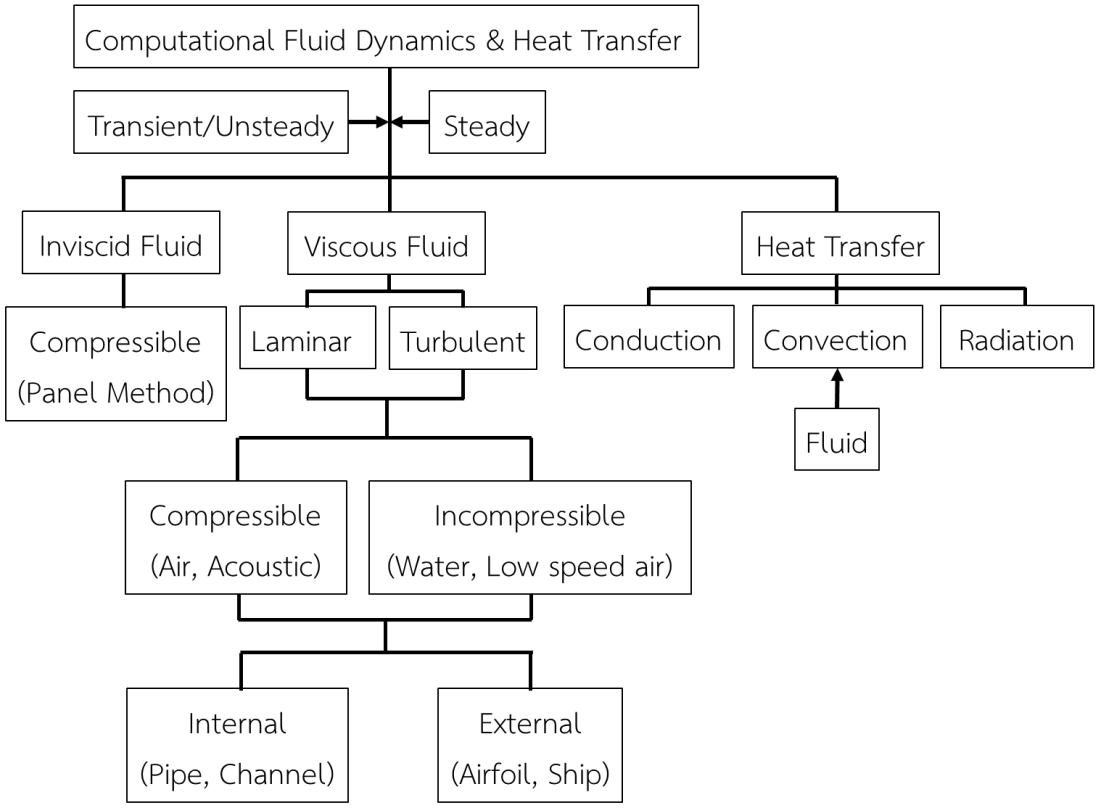

Fig. 2.13 A flowchart encapsulating the various flow physics in CFD.

2.3.4 Specification of boundary conditions- Step 4

The complex nature of many fluid flow behaviors has important implications in which boundary conditions are prescribed for the flow problem. A CFD user needs to define appropriate conditions that are available for impending simulations. Evidently, where there exist inflow and outflow boundaries within the flow domain, suitable fluid flow boundary conditions are required to accommodate the fluid behavior entering and leaving the flow domain. The flow domain may also be

bounded by open boundaries. Although the intricacies of open boundary conditions are still subject to much theoretical debate, this boundary condition remains the simplest and cheapest form to prescribe when compared with other theoretically more satisfying selections in CFD. Appropriate boundary conditions are also required to be assigned for external stationary solid wall boundaries that bound the flow geometry and the surrounding walls of possible internal obstacles within the flow domain.

In section 2.3.3, the considerations of a viscous fluid, laminar, incompressible, and isothermal are assumed for the purpose of illustration in Fig. 2.10 and require the prescription of only the fluid velocity on all the bounding walls of the computational domain. By definition, the velocities are zero for the external stationary solid walls bounding the flow domain in Fig. 2.10 (see Fig. 2.14).

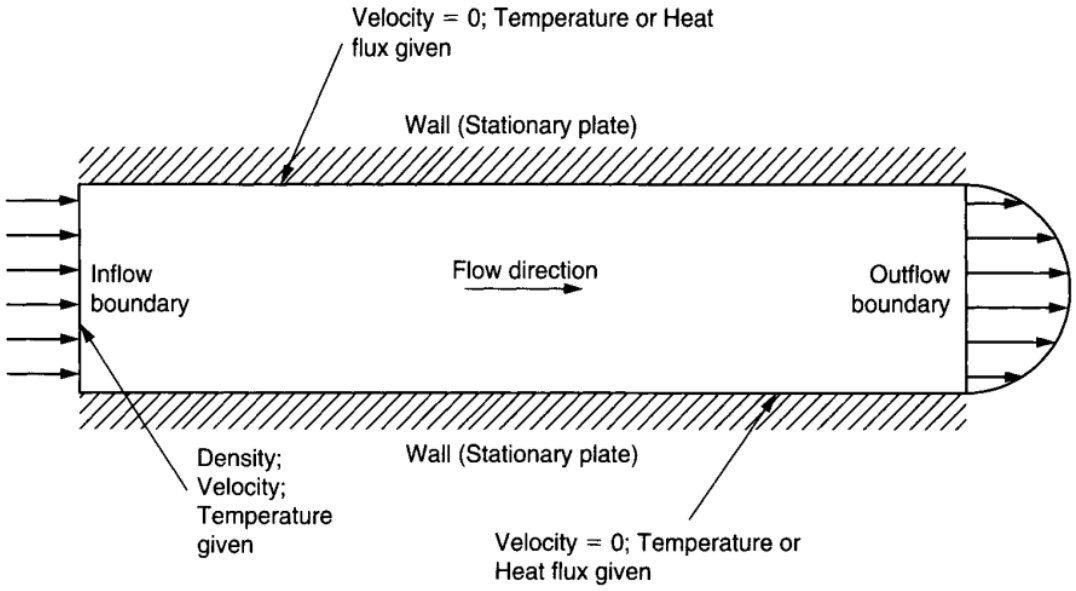

Fig. 2.14 Boundary conditions for an internal flow problem between two stationary parallel plates.

For the inflow boundary conditions, the user is required to ascertain the inlet fluid velocity in order to stipulate the fluid entering into the flow domains. At the outflow boundaries indicating the fluid departure, only one outlet condition, typically a specified relative pressure, is imposed. A far-field flow boundary condition can be

imposed for the open boundaries that either applies the inflow or outflow boundary conditions. Care should always be exercised in handling these open boundaries, where they have to be defined far enough away from the region of interest within the solution domain in order to obtain physically meaningful results.

2.3.5 Numerical solution—CFD Solver-Step 5

In-house or a commercial CFD code commands the core understanding of the underlying numerical aspects inside the CFD solver. This section focuses on the treatment of the solver element. A CFD solver can usually be described and envisaged by the solution procedure presented in Fig. 2.15. The prerequisite processes in the solution procedure that have implications on the computational solutions are *initialization, solution control, monitoring solution, CFD calculation, and checking for convergence*. A CFD user whether applying in-house or commercial codes needs to gain the necessary insights and knowledge pertaining to the workings of these prerequisite processes in order to skillfully utilize the many solver features and better navigate the underlying “black box” operations that reside in many of these codes.

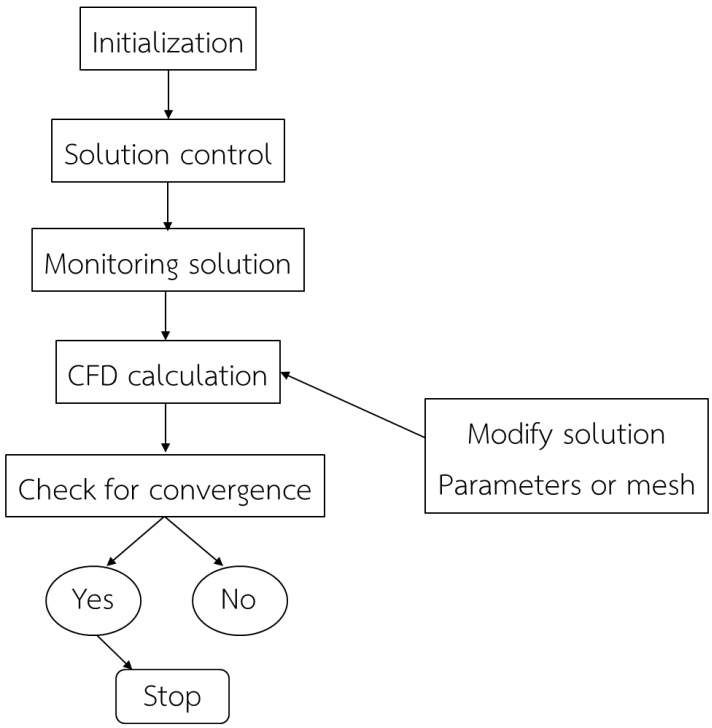

Fig. 2.15 An overview of the solution procedure.

2.4 Result report and visualization—Post-process [35]

CFD has a reputation of generating vivid graphic images and, while some of them are promotional and are usually displayed in stunning and superb colorful outputs, the ability to present the computational results effectively is an invaluable design tool. In this section, we concentrate on some essential computer graphic techniques frequently encountered in the presentation of CFD data. The majority of ways that the CFD results are emphasized graphically can be classified under different categories. Each of these categories, to be discussed below, assists the CFD user to better analyze and visualize the many relevant physical characteristics within the fluid flow problem.

2.4.1 X-Y plots

These plots are mainly two-dimensional graphs that represent the variation of one dependent transport variable against another independent variable. They can usually be drawn by hand or more conveniently by many plotting packages. Such X-Y plots are the most precise and quantitative way to present the numerical data. Often, laboratory data is gathered by straight-line traverses. These graphs are therefore a popular way of directly comparing the numerical data with the experimental measured values. Also, logarithmic scales allow the identification of important flow effects occurring especially in the vicinity of solid boundaries. These graphs are widely used for presenting line profiles of velocity and for plots of surface quantities such as pressure and skin-friction coefficient. They are usually meant to be very easily identifiable; the reader can readily read the results without resorting to any mental or arithmetic interpolation.

An X-Y plot of a laminar velocity profile at the fully developed region for an internal flow problem between two stationary parallel plates (Fig. 2.10) is shown in Fig. 2.16. The significance of a parabolic profile characterizes the flow physics typically experienced for a fluid flowing within a parallel-plate channel. Another possible way of visualizing the development of the fluid flow is through the use of successive two-dimensional graphic profiles as shown in Fig. 2.17. The flow distribution gradually

changes from a uniform profile specified at the entrance boundary (left) to a parabolic profile as it travels downstream toward the channel exit boundary (right).

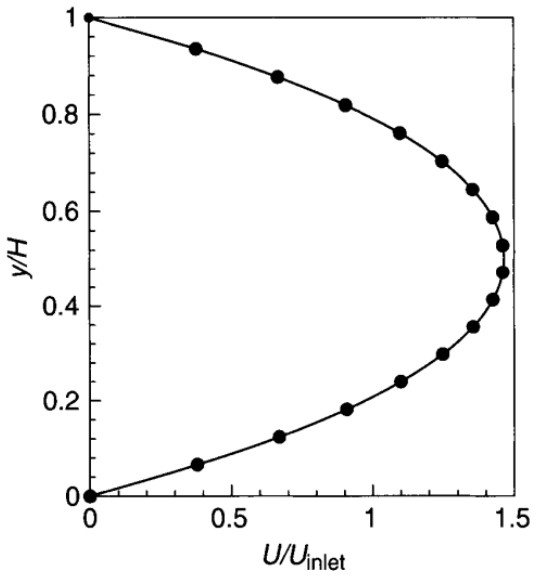

Fig. 2.16 X-Y plot of a parabolic laminar velocity profile at the fully developed region.

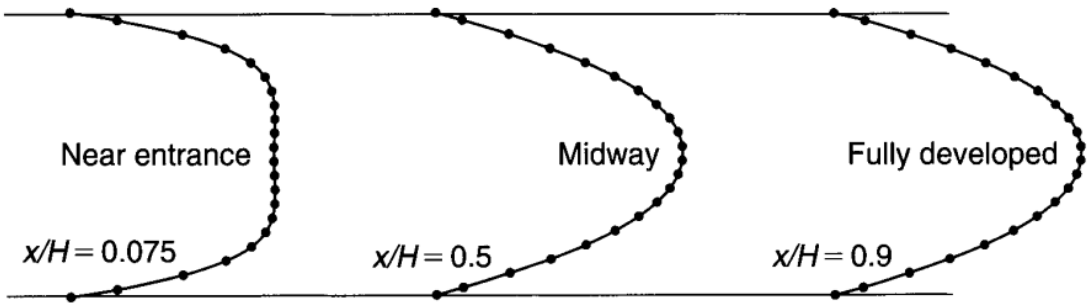

Fig. 2.17 Successive two-dimensional velocity profiles of a developing flow.

2.4.2 Vector plots

A vector plot provides the means whereby a vector quantity is displayed at discrete points (usually velocity, with arrows) whose orientation indicates direction and whose size indicates magnitude. It generally presents a perspective view of the flow field in two dimensions. In a three-dimensional flow field, different slices of two-dimensional planes containing the vector quantities can be generated in different orientations to better scrutinize the global flow phenomena. If the mesh densities are

considerably high, the CFD user can either interpolate or reduce the numbers of output locations to prevent the clustering of these arrows “obliterating” the graphical plot.

Figure 2.18 illustrates a typical velocity vector plot representing the fluid flowing along the parallel-plate channel. This plot gives an alternative view of the developing flow previously envisaged in Fig. 2.17. The different arrow intensities in the plot depict the composite association of the velocity vectors with another dependent transport variable. For this particular flow case, we have arbitrarily chosen the distribution of dynamic pressure within the flow domain that impels the fluid flow. The different intensities indicate the distribution of pressures that are effective inside the fluid flow process. Nevertheless, the CFD user can also freely select other transport variables that better emphasize significant physical aspects of the flow phenomena. For example, where heat transfer may be important, the velocity vectors can be coupled with the temperature distribution to illustrate the transport of hot fluid within the flow domain.

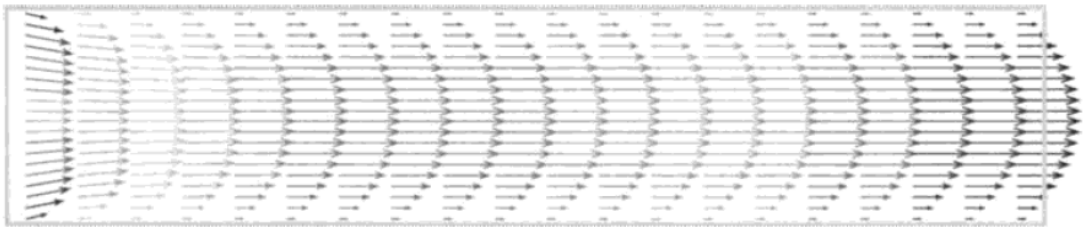

Fig. 2.18 Velocity vectors showing the flow-development along the parallel-plate channel.

2.4.3 Control plots

Contour plotting presents another useful and effective graphic technique that is frequently utilized in viewing CFD results. It is not surprising to imagine the proliferation of contour plots ever since the advent of the computer. In CFD, contour plots are one of the most commonly found graphic representations of data. A contour line (also known as *isoline*) can be described as a line indicative of some property that is constant in space. The equivalent representation in three-dimensions is as

isosurface. In contrast to X-Y plots, contour plots like vector plots provide a global description of the fluid flow encapsulated in one view. Generally, contours are plotted such that the difference between the numerical value of the dependent transport variable from one contour line to an adjacent contour line is held constant. The use of contour plots is usually not targeted for precision evaluation of the numerical values between contour lines. Although some mental and/or numerical interpolation can be performed between the contour lines in space, it is at the very least an imprecise process. The actual numerical values represented by the isolines of these plots are sometimes less important than their overall disposition. In practice, the contours are usually linearity scaled. However, to better understand the hidden details in some small regions within the flow field, the reader may be required to intrepidly employ other types of scaling choices to reveal these isolated flow behaviors. For the contour plots, where the intervals are the same, clustering of these lines indicates rapid changes in the flow quantities. Such plots are particularly useful, especially in locating propagating shocks and discontinuities.

Figures 2.19 and 2.20 are examples of *flooded* contour plots of flow-development along the parallel-plate channel. A constant flow-field property of any transport variable is denoted by the constant intensity of the color shading. In these two plots, the so-called “gray-scaled” color map is employed to illustrate the distributions of the dimensionless resultant velocity normalized with respect to the inlet velocity and the dynamic pressure within the flow domain. The changing flooded contours near the entrance (left boundary) in Fig. 2.19 further confirms the development of the fluid flow as previously observed by the successive velocity profiles in the X-Y plot in Fig. 2.17 and velocity vector plot in Fig. 2.18. In contrast, no appreciable change of the velocity is observed near the exit (right boundary). The successive reduction of the pressure as indicated by the contour plot in Fig. 2.20 demonstrates the pressure gradient driving the fluid flow from the source composed at the left boundary towards the sink located at the right boundary of the parallel-plate channel. At this point, we would like to draw the reader’s attention of

the color map represented by the pressure contour plot that is associated with the array of colors represented by the velocity vectors in Fig. 2.18.

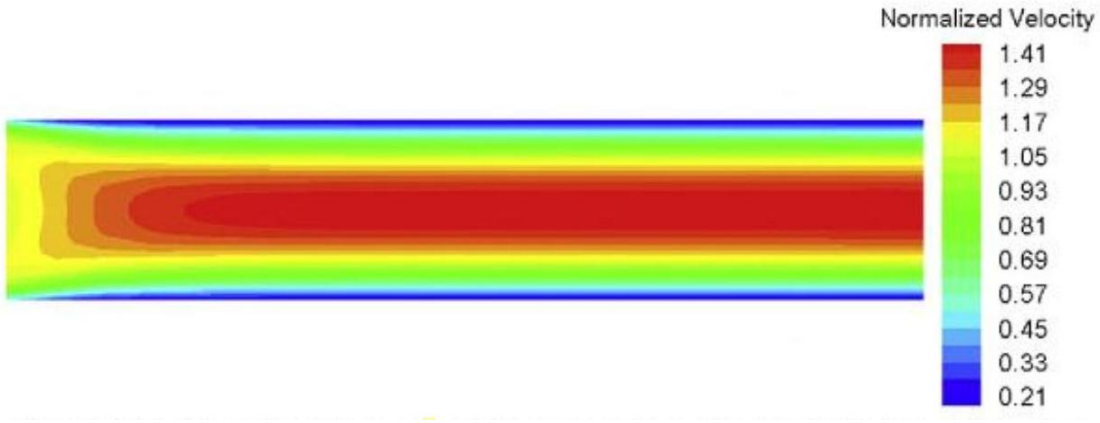

Fig. 2.19 Flooded contours for the distribution of flow between two stationary parallel plates normalized velocity

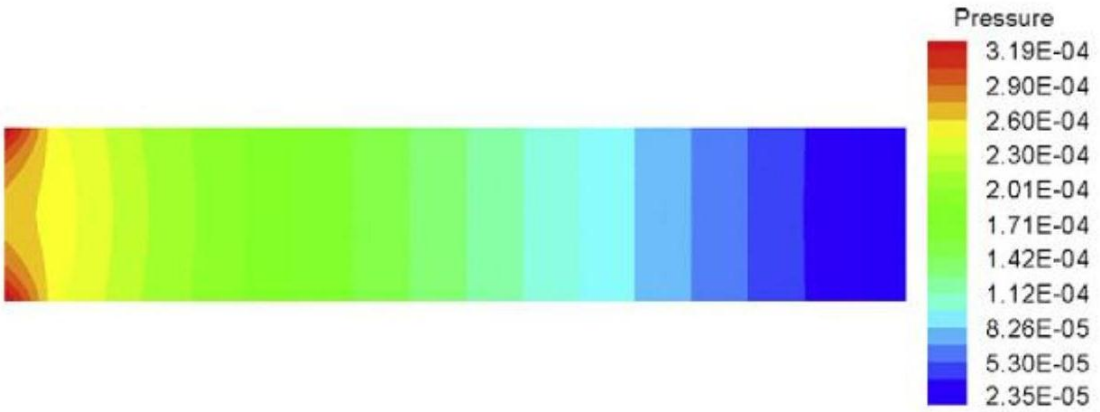

Fig. 2.20 Flooded contours for the distribution of flow between two stationary parallel plates dynamic pressure

2.4.4 Other plots

The application of *streamlines* in the pre-processing CFD stage, as in all aspects of fluid dynamics, is another exceptional tool for examining the nature of a flow either in two or three dimensions. By definition, streamlines are parallel to the mean velocity vector, where they trace the flow pattern using *massless* particles. For an example, they can generally be obtained by integrating the spatial three velocity components expressed in a three-dimensional Cartesian frame: $dx/dt = u$, $dy/dt = v$,

and *dz/dt = w*. For edification purpose, the reader may well benefit at this point of time to be accustomed to other existing terminologies synonymous to streamlines that are widely used in many graphic software packages. They are *stream traces, streak lines*, or *path lines*.

In more complex flow problems such as multiphase flows that involve the transport of solid particles, the *particle tracks* associated with the discrete particles of certain diameter and mass being injected inside the parent fluid fall in this same category. Here, important information on the particle residence time, particle velocity magnitude, and other properties can be duly extracted. An example of a streamline plot illustrated in Fig. 2.21 defines the basic flow topology of localized recirculation zones behind the two cylinders as previously identified in Fig. 2.12. This tool can often reveal important features that could be obscured in some isolated flow regimes, which is clearly demonstrated by a more definitive representation of the observed wake-developing vortices through the streamline plot.

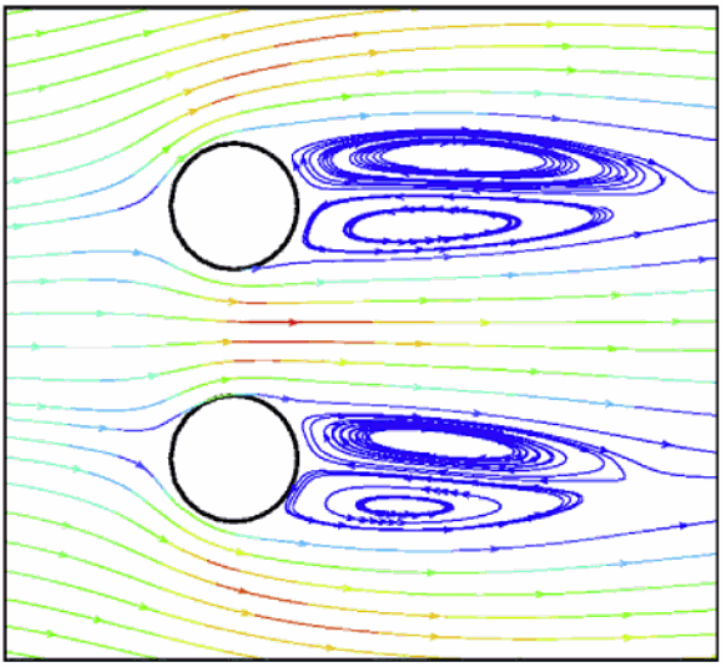

Fig. 2.21 Streamline plot emphasizing the definitive localized wake-recirculation zones behind the two cylinders

Chapter 3
Literature Review

Prior to design and utilize the CFD-CT aided surgery approach, there are essential topics that fundamentally reviewed and presented in Chapter 3.

Topic 3.1 describes the nasal anatomy and physiology of healthy noses. In addition, nasal patency and nasal airflow's characteristics and their measurements are presented. Lastly, paranasal CT images of the healthy humans are illustrated.

Topic 3.2 describes the causes, symptoms, and incidence of deviated nasal septum (DNS) and its effects on the nasal patency and airflow. Then, paranasal CT images of the DNS patients are illustrated. Moreover, the present surgical operations and post-treatment evaluation of the DNS noses are explained in this topic.

In topic 3.3, previous CFD studies in both healthy and DNS noses are reviewed. In addition, existing research studies, which applied the CFD simulation on the surgical nasal operation, are discussed. Finally, the inspiration for creation of the CFD-CT aided surgery approach as a pre-surgical DNS aiding tool is introduced.

3.1 Healthy Nose and Nasal Cavity [37]

An essential part in human respiratory system, nasal cavity serves three main physiological functions [1]. First, with three turbinates, i.e. inferior turbinate, middle turbinate, and superior turbinate, covered with mucosa, nasal cavity adjusts the temperature and humidity of inhaled air whereby the air is warmed to the body temperature with full water saturation prior to entering the upper and lower respiratory tracts. Second, it provides senses of smell using the olfactory receptors located on the roof of the nasal cavity above the upper turbinate. Last, it filters out dust, bacteria and other pollutants.

In this research work, the terms proposed by Proctor [38] were used to identify the regions inside nasal cavity. A human nose is divided medially by a nasal cartilage into two sides or cavities, i.e., left and right (Fig. 3.1). Once entering the nasal

cavity, air passes through the nostril, vestibule, nasal valve (i.e., the narrowest area in the nasal cavity), main nasal passage which comprises the inferior, middle and superior turbinates, and the nasopharynx (i.e., the last component of a nasal cavity) before travelling to the lower respiratory tract (Fig. 3.1).

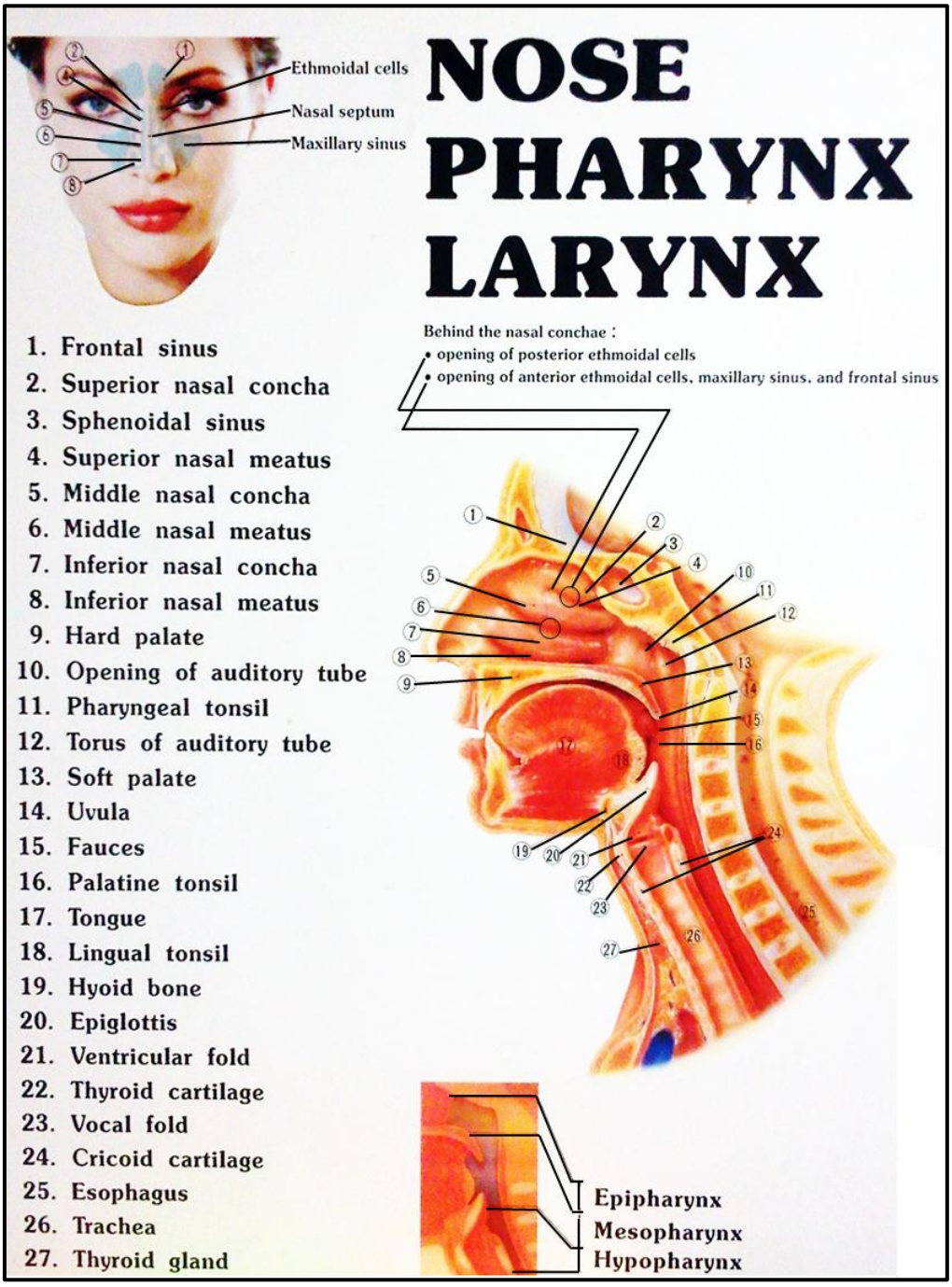

Fig. 3.1 Human upper airway consists of nose, pharynx, and larynx

Details of basic anatomy and physiology of the human nose will be described as follows.

3.1.1 Basic Anatomy of Nose

The supporting structure of the nose consists of bone, cartilage, and connective tissue. Figure 3.2 shows the most important nasal skeleton. The shape, position, and properties of the bone and cartilage of the nose considerably influence the face aesthetic and the function of the nasal cavity.

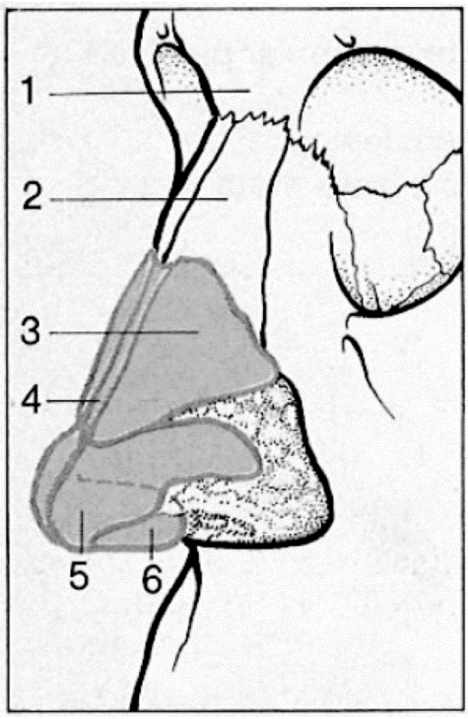

Fig. 3.2 Nasal skeleton: 1, glabella; 2, nasal bone; 3, lateral nasal cartilage; 4, upper edge of the cartilaginous nasal septum; 5, greater alar cartilage; 6, medial crus of (5) [37].

The nasal cavity is divided by the nasal septum into two halves which are usually unequal in size. Each side may be divided into the nasal vestibule and the nasal cavity proper (Fig. 3.3).

The nasal vestibule is covered by epidermis containing hairs (vibrissae) and sebaceous glands. The medial wall of the nasal vestibule encloses the supporting structure of the anterior part of the cartiginous septum and the connective tissue septum, i.e., the columella. The roof of the vestibule is formed by the

horseshoe-shaped lower lateral or alar cartilage whose medial crus extends into the columella and whose lateral crus supports the external wall of the vestibule (see Fig. 3.1 and Fig. 3.3). The alar cartilage thus determines the shape of the nasal tip and the nasal apertures. Correction of this area is thus often an important part of rhinoplasty.

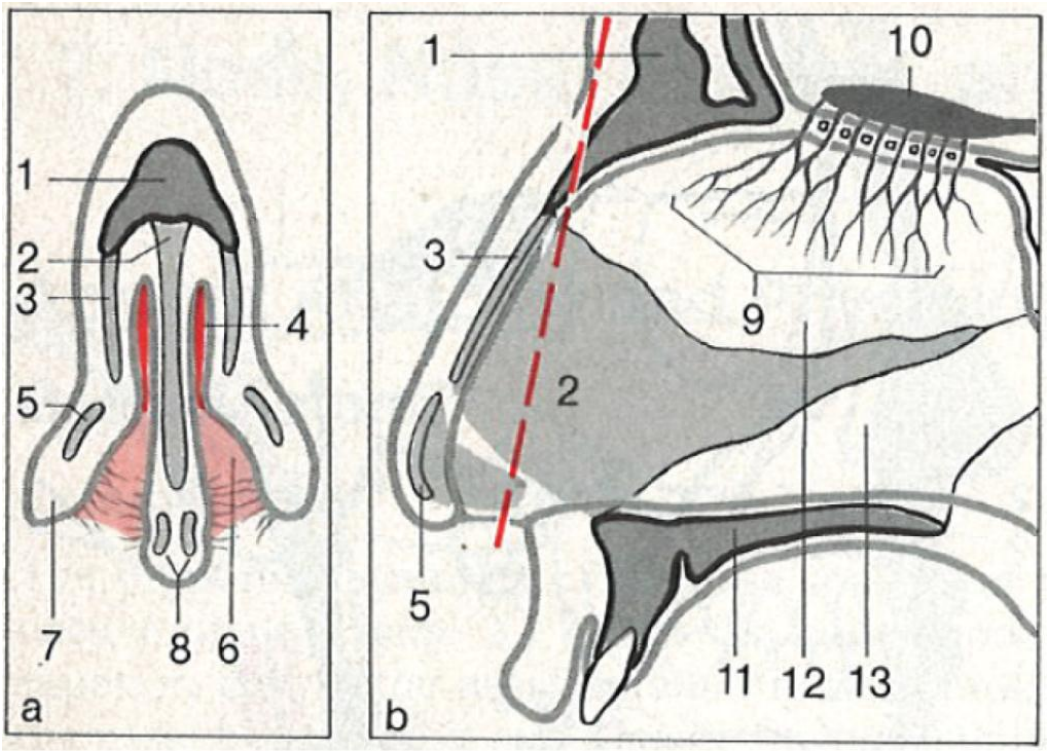

Fig. 3.3 (a) Section through the anterior nose showing the vestibule and the nasal valve. The nasal valve lies at the junction of the pink and red areas.

(b) Medial nasal wall: 1, Bony nasal bridge; 2, nasal septum;

3, lateral nasal cartilage; 4, nasal cavity;

5, alar cartilage; 6, nasal vestibule;

7, nasal ala; 8, nasal columella with medial crus of the cartilaginous ala;

9, filaments of the olfactory nerve; 10, olfactory bulb;

11, palatine bone; 12, perpendicular plate of the ethmoid;

13, vomer.

The dashed line shows the plane of section of (a) [37].

A very important structure from the physiologic point of view is the internal nasal valve. This lies at the junction of the vestibule and the nasal cavity. It is formed by a prominence of the anterior edge of the upper lateral or triangular cartilage on the lateral wall of the nose (Fig. 3.3 (a)).

The internal nasal valve is normally the narrowest point of the entire cross section of the nasal cavity, and thus has an important influence on nasal respiration. The nasal cavity extends from the internal nasal valve to the choana. The structure of the floor and roof of the nose, of the medial wall, and of the nasal septum can be seen in Fig. 3.3.

The outline of the lateral wall of the nasal cavity is more complex than that of the medial wall. It contains several structures that are important in the function of the nose and nasal cavity (Fig. 3.4), i.e. three turbinates; ostia of the nasal sinuses with the exception of that for the sphenoid sinus; and opening of the nasolacrimal duct.

The superior, middle, and inferior meatus lie inferior to the three turbinates, and the nasal sinuses and the nasolacrimal duct open into them. Thus, they are of diagnostic and therapeutic significance.

The inferior meatus, lying between the floor of the nose and the insertion of the lower turbinate, does not contain a sinus ostium, but does have the opening of the nasolacrimal duct lying about 3 cm posterior to the external nasal opening.

The middle meatus, between the inferior and middle turbinate, is of clinical importance because the nasofrontal duct, the anterior ethmoid cells, and the maxillary antrum open into it.

The superior meatus, between the middle and superior turbinate, contains the opening for the posterior ethmoid cells. The sphenoid ostium lies on the anterior wall of the sphenoid sinus at the level of the superior meatus. Moreover, the nasal cavity is lined by two different types of epithelium: respiratory and olfactory (Fig. 3.5).

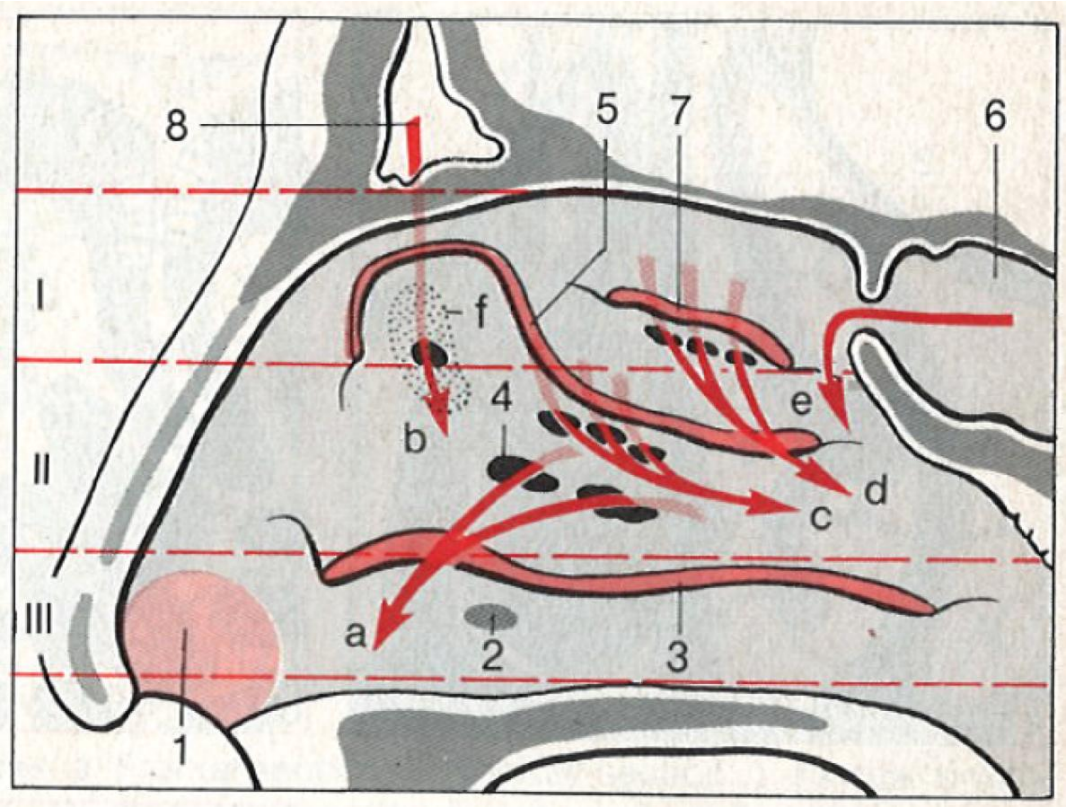

Fig. 3.4 Lateral nasal wall. I, superior meatus; II, middle meatus; III, inferior meatus.

1, Nasal vestibule; 2, opening of the nasolacrimal duct;

3, origin of the inferior turbinate; 4, maxillary ostium;

5, insertion of the middle turbinate; 6, sphenoid sinus;

7, insertion of the superior turbinate;

8, frontal sinus: a, drainage of the antral cavity;

b, drainage of the frontal sinus through the nasofrontal duct;

c, drainage of the anterior ethmoid cells;

d, drainage of the posterior ethmoid cells;

e, drainage of the sphenoid sinus;

f, area of infundibulum (black dotted area) [37].

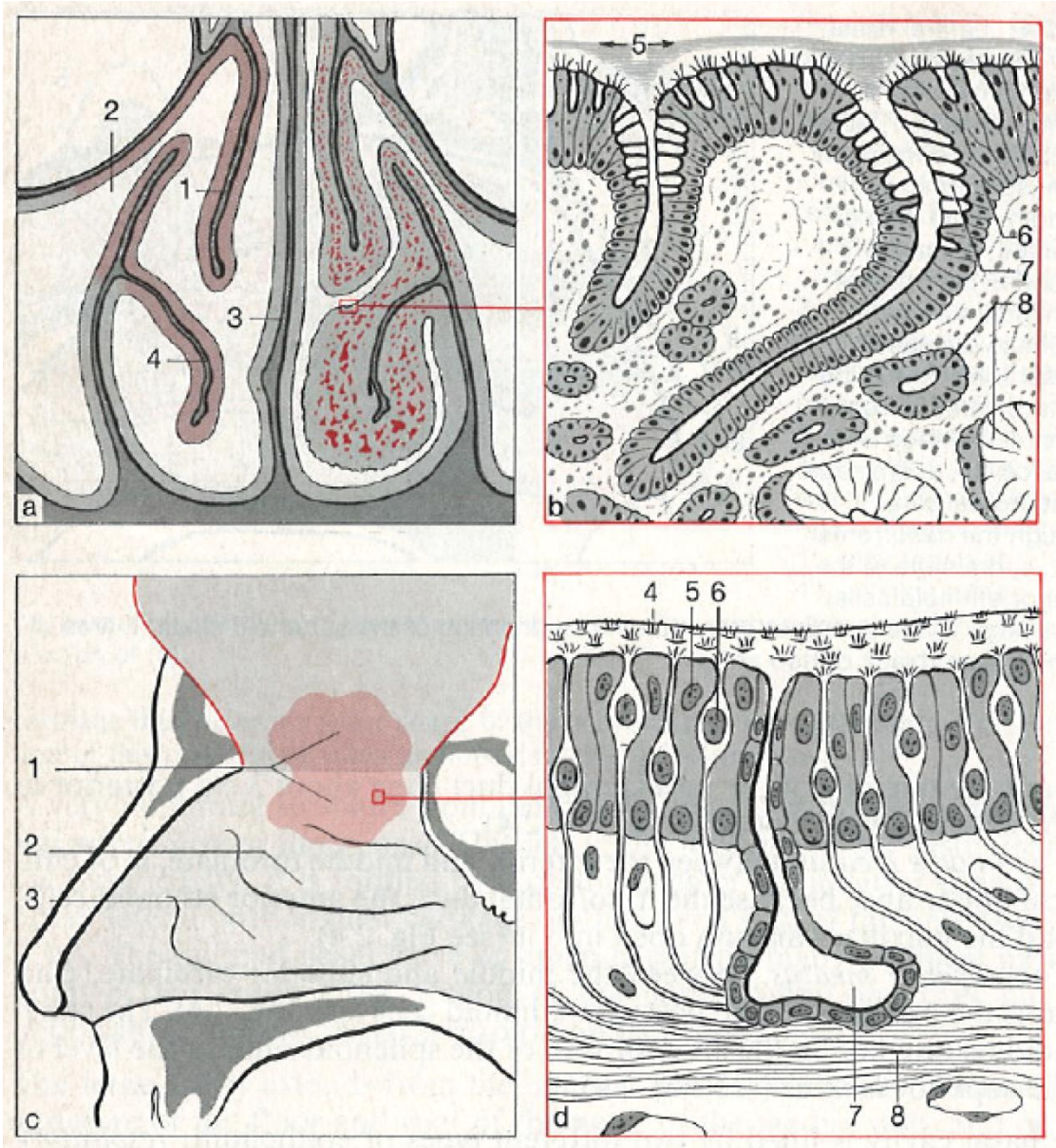

Fig. 3.5 (a) Frontal section through the nasal cavity. On the left the nasal mucosa is constricted, and on the right the nasal mucosa is normal.

(b) Respiratory mucosa. 1, Middle turbinate; 2, antrum with ostium; 3, nasal septum; 4, inferior turbinate; 5, layer of mucus; 6, respiratory epithelium with cilia; 7, goblet cells; 8, mucosal glands.

(c). Sagittal section through the nose with the septum turned upward.

(d) olfactory mucosa. 1, Olfactory region; 2, middle turbinate; 3, inferior turbinate; 4, olfactory zone with cilia; 5, supporting cell; 6, olfactory cell; 7, Bowman's gland; 8, olfactory fibers [37].

3.1.2 Basic Physiology of the Nose

The nose is both a *sense* organ and a *respiratory organ*. In addition, the nose performs an important function for the entire body by providing *both physical and immunologic protection from the environment.* Finally, it is also important in the formation of speech sounds.

3.1.2.1 The Nose as an Olfactory Organ

The human sense of smell is poorly developed compared to most mammals and insects. Despite that, it is still very sensitive in the human and is almost indispensable for the individual. For example, taste is only partially a function of the taste buds since these can only recognize the qualities of sweet, sour, salty, and bitter. All other sensory impressions caused by food such as aroma and bouquet are mediated by olfaction. This gustatory olfaction is due to the fact that the olfactory substances of food or drink pass through the olfactory cleft during expiration while eating or drinking.

The olfactory area of the nose is relatively small (Figs. 3.5 (c) and 3.6). It contains the olfactory cells, i.e., the bipolar nerve cells, which are to be regarded as the sensory cells and first-order neurons. They are collected into about 20 fibers in the olfactory nerves which run to the primary olfactory center of the olfactory bulb (Figs. 3.3 (b) and 3.7).

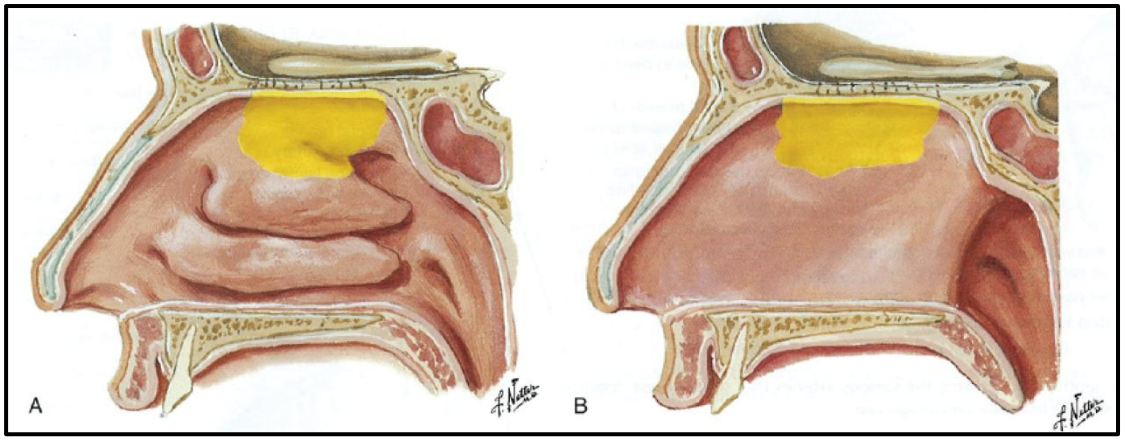

Fig. 3.6 Sagittal views of the lateral nasal wall (A) and the nasal septum (B) showing the olfactory mucosa (yellow areas). (Figure from www.netterimages.com)

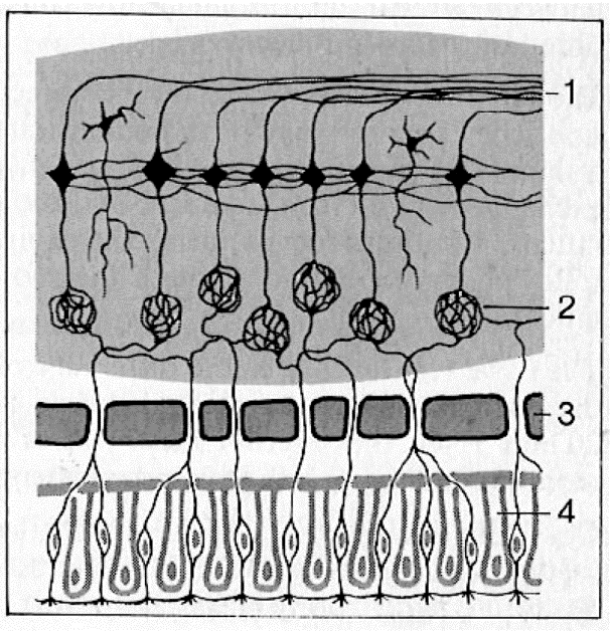

Fig. 3.7 Olfactory organ.
1, Olfactory fibers in the olfactory bulb; 2, olfactory glomeruli;
3, cribriform plate; 4, olfactory epithelium [37].

3.1.2.2 The Nose as a Respiratory Organ

In the human, the only physiologic respiratory pathway is via the nose. Mouth breathing is unphysiologic and is only brought into play in an emergency to supplement nasal respiration.

During normal nasal respiration, the inspired air is *warmed, moistened, and purified* during its passage through the nose. The *warming* of the inspired air through the nose is very effective, and the constancy of the temperature in the lower airways is remarkably stable. The nasal mucosa humidifies and warms the air. The temperature in the nasopharynx during normal (exclusively nasal) respiration is constant at 31 ° to 34 °C independent of the external temperature. The heat output of the nose increases as the external temperature falls so that the lower airways and the lungs can function at the correct physiologic temperature.

The *optimal relative humidity* of room air for subjective well-being and function of the nasal mucosa lies between 50% and 60%. The water vapor saturation of the inspired air in the nasopharynx lies between 80% and 85%, and in the lower airway is fairly constant between 95% and 100%, independent of the

relative humidity of the environmental air. The water vapor secreted by the entire respiratory tract per 1,000 liters of air can reach 30 g. Most of this is supplied by the nose. On the other hand, the mucosal blanket renders the nasal mucosa watertight and prevents release of too much water into the air, which would cause drying of the mucosa.

The *cleaning function* of the nose includes: first, cleaning of the inspired air from foreign bodies, bacteria, dust, etc., and second, cleaning of the nose itself. About 85% of particles larger than 4.5 μm are filtered out by the nose, but only about 5% of particles less than 1 μm in size are removed. Foreign bodies entering the nose come into contact with the moist mucosal surface and the mucosal blanket, which continually carries away the foreign bodies.

The physiology of the airstream through the normal nose in inspiration and expiration may be summarized as follows:

1) The average ventilation through a normal nose in physiologic breathing is 6 L/min and 50 to 70 L/min in maximal ventilation.

2) The internal nasal valve is the narrowest point in the normal nose. It thus acts like a nozzle, and the speed of the airstream is very high at this point.

3) The nasal cavity between the valve and the head of the turbinates acts as a diffusor, i.e. it slows the air current and increases turbulence. The central part of the nasal cavity with its turbinates and meatus is the most important part for nasal respiration. The column of air consists of a laminar stream and a turbulent stream. The proportion between laminar and turbulent flows considerably influences the function and condition of the nasal mucosa.

4) The airstream passes in the reverse direction through the nasal cavities on expiration. The expiratory airstream demonstrates considerably less turbulence in the central part of the nose, and thus offers less opportunity for heat and metabolic exchange between the airstream and the nasal wall than on inspiration. The nasal mucosa can thus recover during the expiratory phase.

Inspiration through the nose followed by expiration through the mouth leads rapidly to drying of the nasal mucosa.

5) The nasal resistance, i.e., the difference of pressure between the nostrils and the nasopharynx, is normally between 8 and 20 mm H_2O. If the values exceed 20 mm H_2O, the internal nasal valves expand during breathing. Supplemental mouth breathing begins at values greater than 40 mm H_2O.

6) Complete exclusion of the nose from breathing leads in the long term to deep-seated mucosal changes. Mechanical obstruction within the nose, e.g., due to septal deviation, hypertrophy of the turbinates, cicatricial stenosis, etc., can lead to mouth breathing and its damaging consequences and can also cause mucosal disease of the nose and nasal sinuses.

3.1.3 Nasal Patency and Nasal Airflow in Healthy Nose

Doctors have many techniques in their disposal to assess the human nose including subjective measurement (patient self-assessment), e.g. NOSE scoring, and objective measurement. The NOSE technique is a clinical symptoms scoring system that evaluates the degrees of: (i) nasal congestion, (ii) nasal blockage, (iii) breathing difficulty, (iv) sleep disorder, and (v) insufficient air through the nose during exertion (Appendix A). Unfortunately, NOSE score cannot reveal nasal patency and calculate exact nasal airflow in the nose. *To overcome this limitation, objective assessments, e.g. acoustic rhinometry, rhinomanometry, and other advanced techniques, were employed to evaluate the human noses.*

3.1.3.1 Nasal Patency [37]

Nasal patency is thus a measure of *how open the nose is*, and it is not equivalent to airflow or resistance to airflow. If the word patency is used in a correct way it should only comprise *cross-sectional areas* of a nasal cavity or the *volume* of a part or the whole of a cavity.

According to such a definition, methods to measure nasal patency are acoustic rhinometry, computed tomography (CT), and magnetic resonance imaging (MRI), etc. Many authors, however, include methods for recording nasal

airflow with or without simultaneous pressure recording among nasal patency methods, e.g. rhinomanometry and nasal peak flow [39].

A rough qualitative test of nasal patency can be achieved by holding a polished metal plate in front of the nose during inspiration and expiration. The surface area of the resulting fogging gives an approximation of the patency of the two sides of the nose [40].

Acoustic rhinometry: most equipment uses an acoustic pulse from a spark source for the measurements. The pulse wave is transmitted along the respiratory tract, mainly in the nose, and is then reflected back, determined by changes in the cross-sectional area of the nasal cavity. The reflected sound passed via a microphone to a computer, where it is processed and then presented as an area-distance graph. The acoustic waves can also be produced from a sound generator, which has the advantage that the sound is well defined as to amplitude, frequency and number of waves [41] (Fig. 3.8). Figure 3.9 illustrates the acoustic rhinometry profile measured from the healthy nose. Minimal cross-sectional area (cm^2) is measured and focused. In healthy nose, the minimal cross-sectional area (MCA) is located at about 2 cm from the tip of nostrils, i.e. nasal valve region.

The nasal patency can be influenced by many different factors, including temperature and humidity of the surrounding air, the position of the body, bodily activity, changes of body temperature, the influence of cold on different parts of the body, e.g., the feet, hyperventilation, and psychological stimuli. The state of the pulmonary function, of the heart, and of the circulation, endocrinologic disorders such as pregnancy, hyper- or hypofunction of the thyroid gland, and some local, oral, or parenteral drugs, e.g., rauwolfia and ephedrine, may have considerable influence on the patency of the nose.

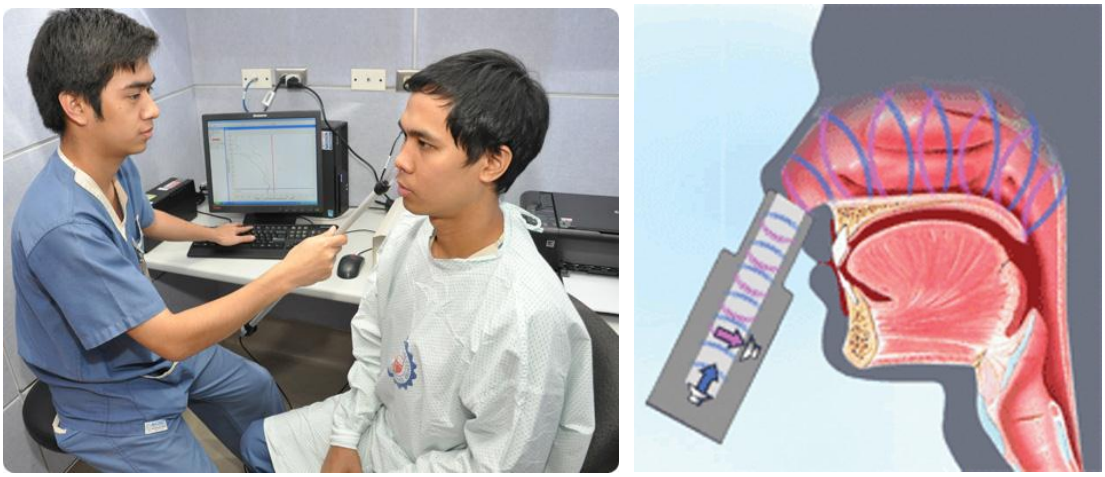

(a) (b)

Fig. 3.8 Acoustic rhinometry examination is presented in (a) and principle of acoustic rhinometry is illustrated in (b) showing the transmitting of pulse wave and receiving the reflected wave to measure the cross-sectional area inside the nose. (Source of figures: (a) www.stlukesmedicalcenter.com.ph, (b) www.glidewelldental.com)

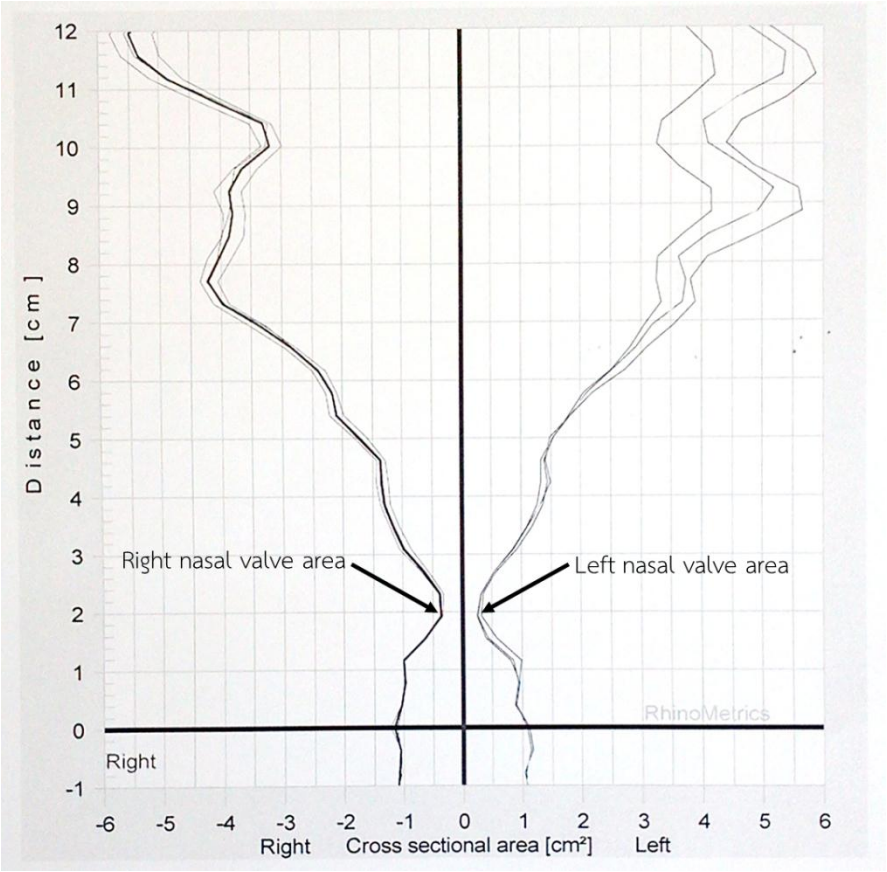

Fig. 3.9 Example of acoustic rhinometry data from one of healthy noses. Arrows depict the narrowest areas of nasal cavity, i.e. nasal valve regions.

3.1.3.2 Nasal Airflow and Resistance to Airflow

Nasal volume flow and nasal resistance to flow are achieved by rhinomanometry. In practice, the following directly measureable parameters of the respiratory flow are available.

1. The nasal differential pressure (ΔP), i.e., the difference between the pressure at the nostrils and the nasopharynx.

2. The volume flow (Q), which is the volume of air passing through the nose in unit time

3. The nasal resistance (R_N)

$$(R_N) = \Delta P/Q \quad (3.1)$$

Usually, measurements are carried out during spontaneous respiration (Fig. 3.10 (a)). The volume of air passing through the nose during active nasal respiration is recorded at the same time as the pressure differential across the nose. The results may be recorded either by a pair of curves (Fig. 3.10 (b)) or as an xy function (Fig. 3.10 (c)) and provide information about unilateral or bilateral nasal patency. Figure 3.11 show the example of rhinomanometry data from the healthy nose.

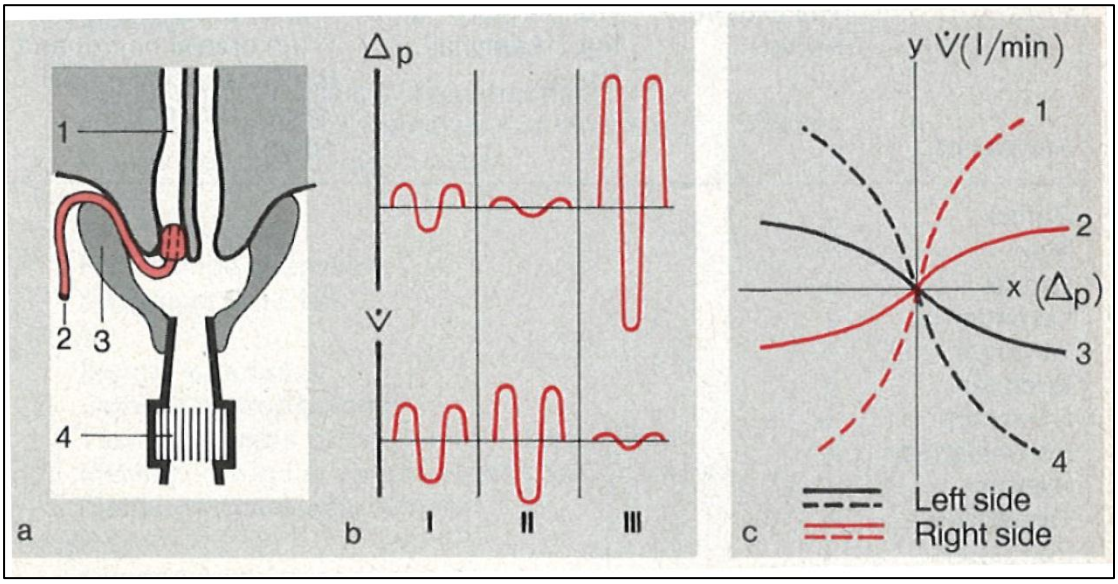

Fig. 3.10 Rhinomanometry. a. Principle of unilateral measurement. 1, Right nasal cavity; 2, pressure tubing with olive; 3, face mask; 4, flow resistance (Fleisch). b. Recording of two simultaneous curves. I, normal; II, above-average nasal patency; III, reduced nasal patency. c. xy plot: inspiration is shown on the right of the y axis and expiration is on the left. Inspiration is recorded right and above, and expiration left and below. 1, Respiratory resistance curve, right side, with good nasal breathing; 2, respiratory resistance curve, right side, with poor nasal breathing; 3, respiratory resistance with poor nasal respiration on the left; 4, respiratory resistance curve with good with good nasal respiration on the left [37].

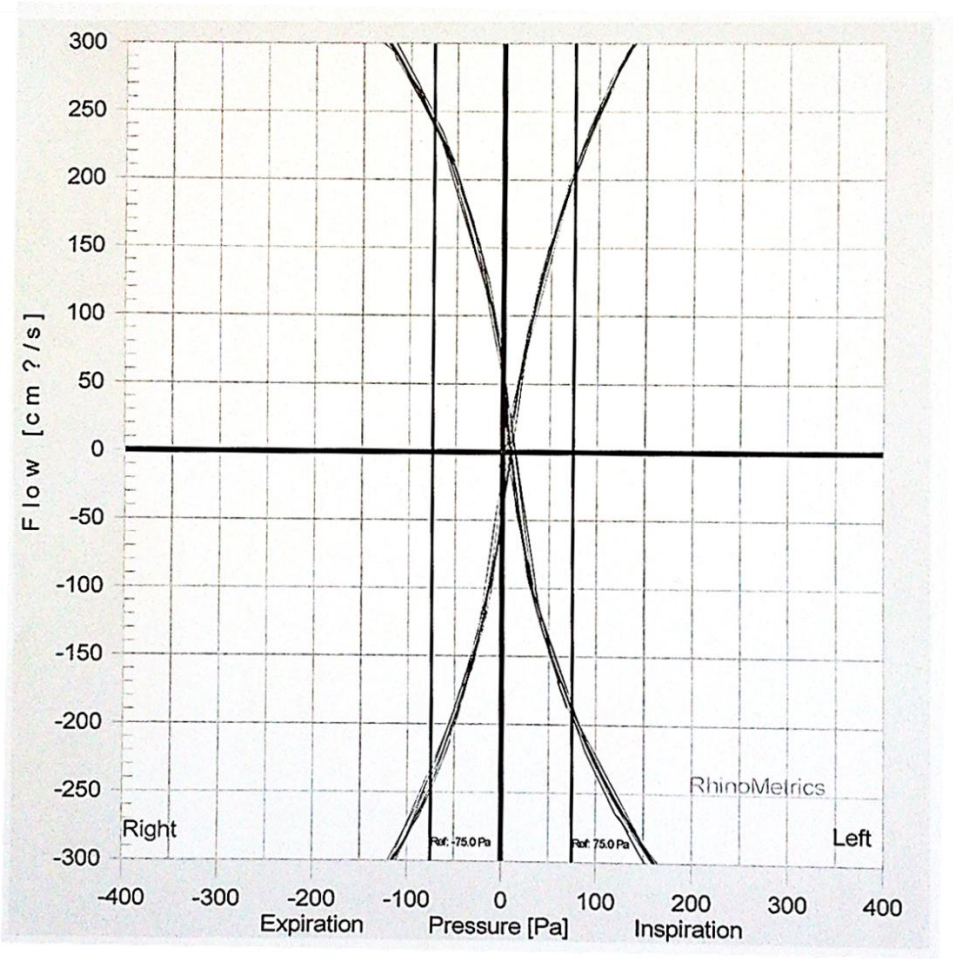

Fig. 3.11 Example of rhinomanometry data from one of healthy noses.

3.1.4 CT Imaging of Nose and Surrounding Organs [42]

Computed tomography (CT) scanner is the advanced medical imaging technology which reveals organs inside the human body in cross-sections. This topic illustrates CT axial (Fig. 3.12) and coronal (Fig. 3.13) cross-sections of paranasal sinuses and nasal cavity.

Figures 3.12 and 3.13 present the axial and coronal cross-sectional CT images of paranasal sinuses and nasal cavity. Three color scales in each cross-section, i.e. white, black, and gray, represent air, bone, and soft tissue areas, respectively. For example, oral cavity, nasal cavity, and paranasal sinuses are presented in black. Skull bones, orbit bones, facial bones, nasal bones (external nose, nasal septum, and nasal turbinates), and teeth can be seen as white. Soft tissues, e.g. brain, nasal mucosa, eye balls, nerves, tongue, etc., are shown in gray.

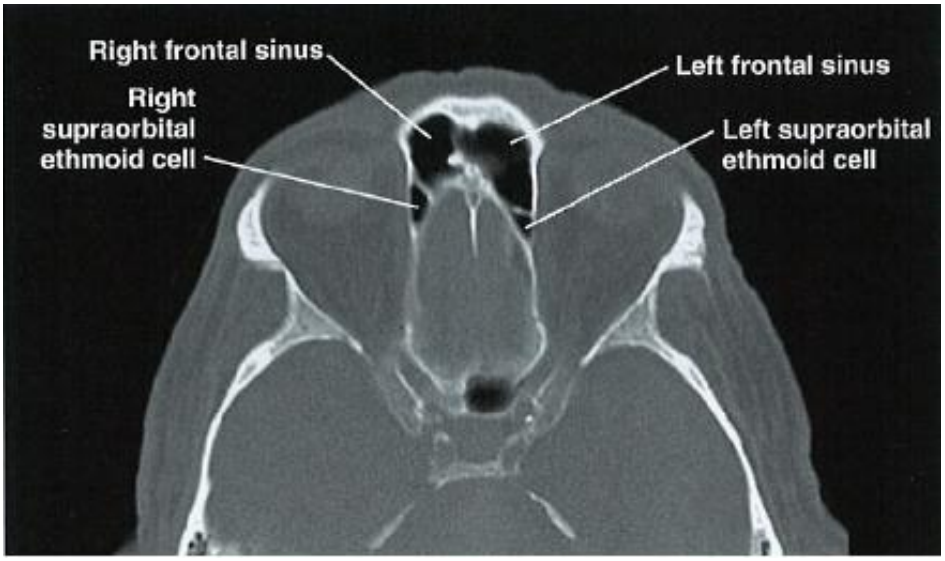
Right frontal sinus
Left frontal sinus
Right supraorbital ethmoid cell
Left supraorbital ethmoid cell

(a)

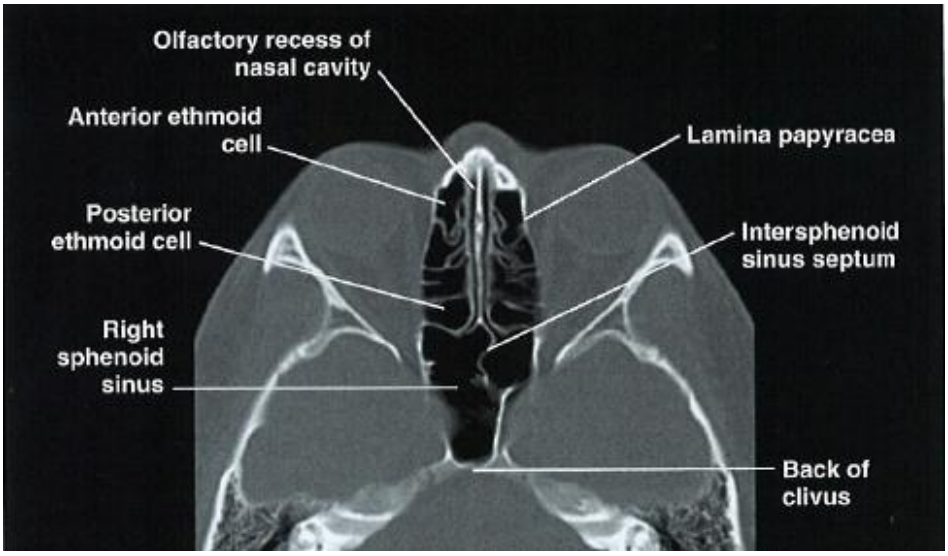
Olfactory recess of nasal cavity
Anterior ethmoid cell
Lamina papyracea
Posterior ethmoid cell
Intersphenoid sinus septum
Right sphenoid sinus
Back of clivus

(b)

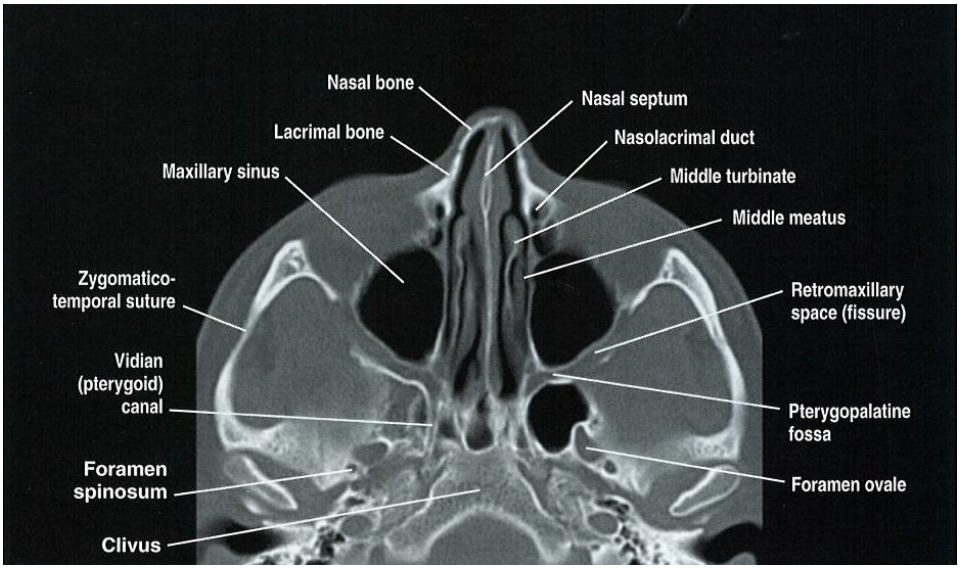
Nasal bone
Nasal septum
Lacrimal bone
Nasolacrimal duct
Maxillary sinus
Middle turbinate
Middle meatus
Zygomatico-temporal suture
Retromaxillary space (fissure)
Vidian (pterygoid) canal
Pterygopalatine fossa
Foramen spinosum
Foramen ovale
Clivus

(c)

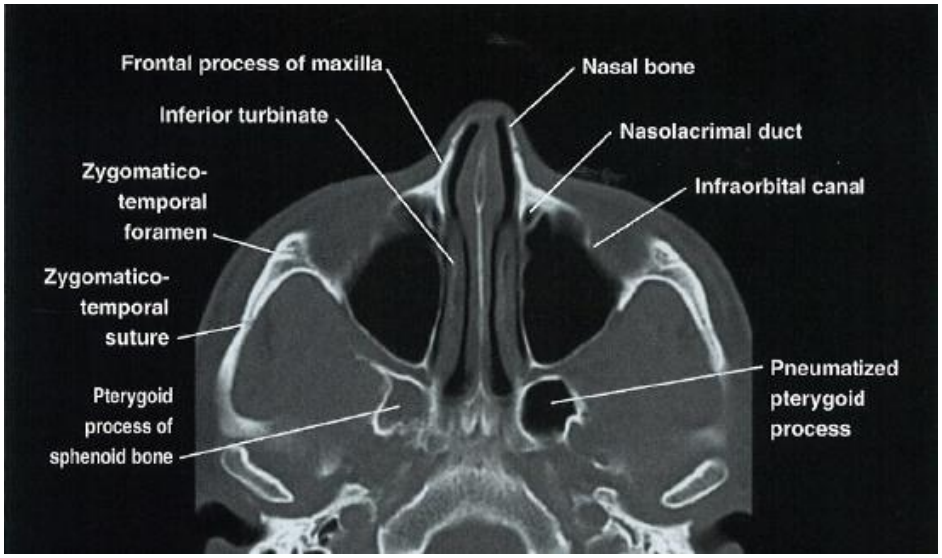

(d)

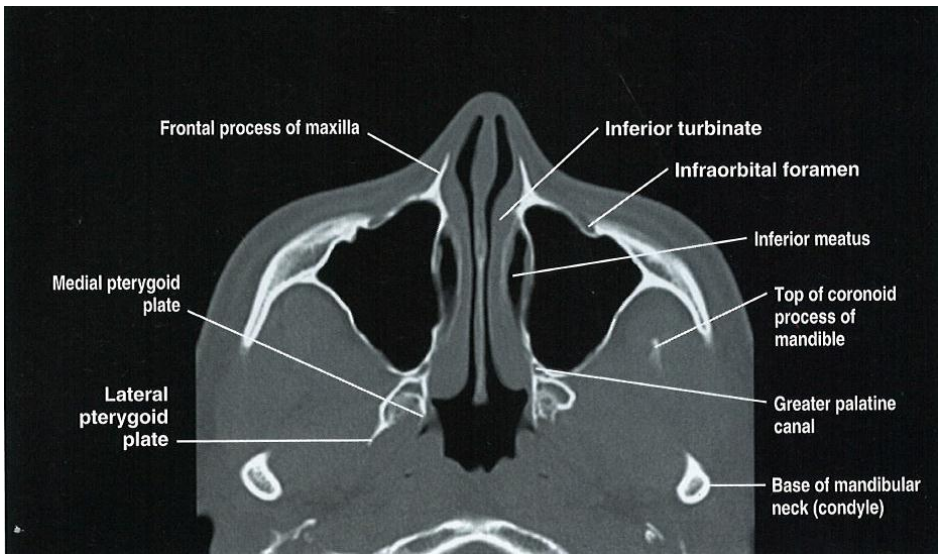

(e)

Fig. 3.12 CT axial cross-sections illustrate the anatomy of the nasal cavity, paranasal sinuses (frontal, ethmoid, sphenoid, and maxillary sinuses), skull and facial bones, and surrounding tissues. [42].

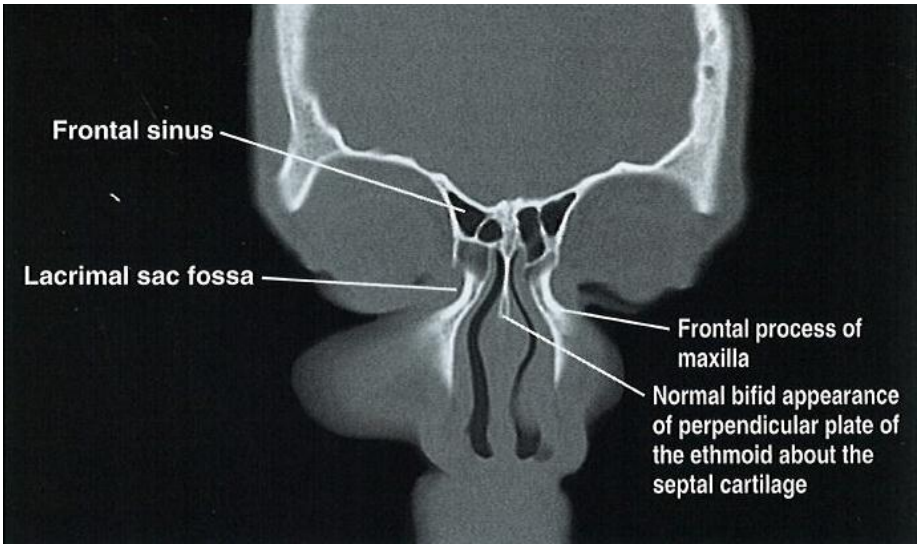
Frontal sinus
Lacrimal sac fossa
Frontal process of maxilla
Normal bifid appearance of perpendicular plate of the ethmoid about the septal cartilage

(a)

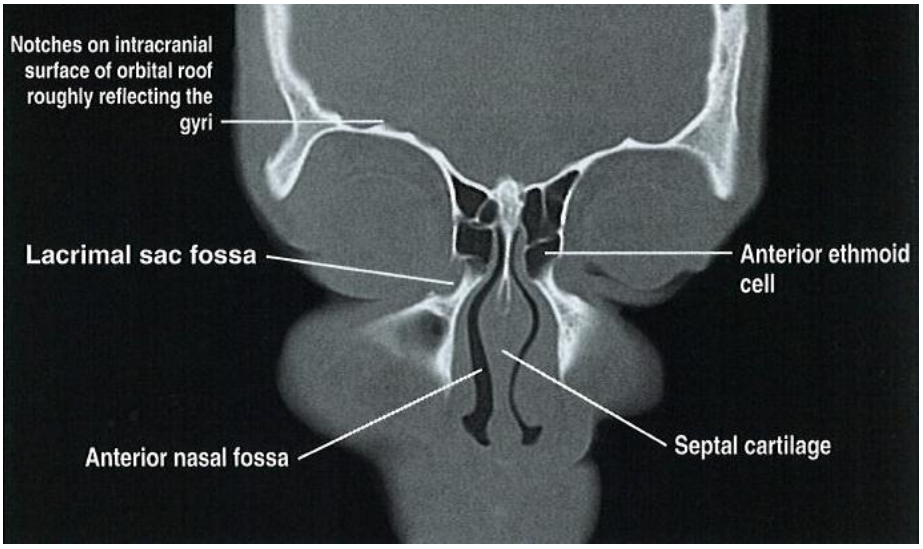
Notches on intracranial surface of orbital roof roughly reflecting the gyri
Lacrimal sac fossa
Anterior ethmoid cell
Anterior nasal fossa
Septal cartilage

(b)

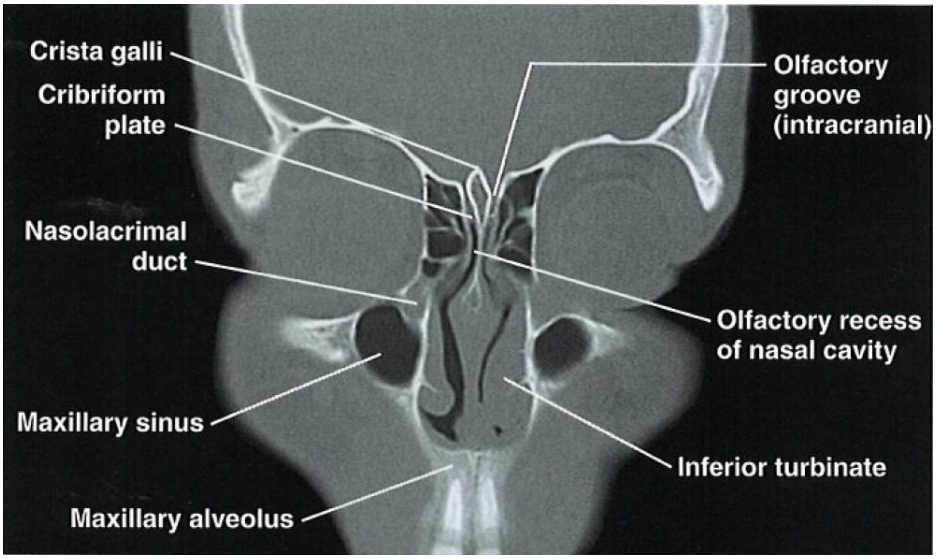
Crista galli
Cribriform plate
Olfactory groove (intracranial)
Nasolacrimal duct
Olfactory recess of nasal cavity
Maxillary sinus
Inferior turbinate
Maxillary alveolus

(c)

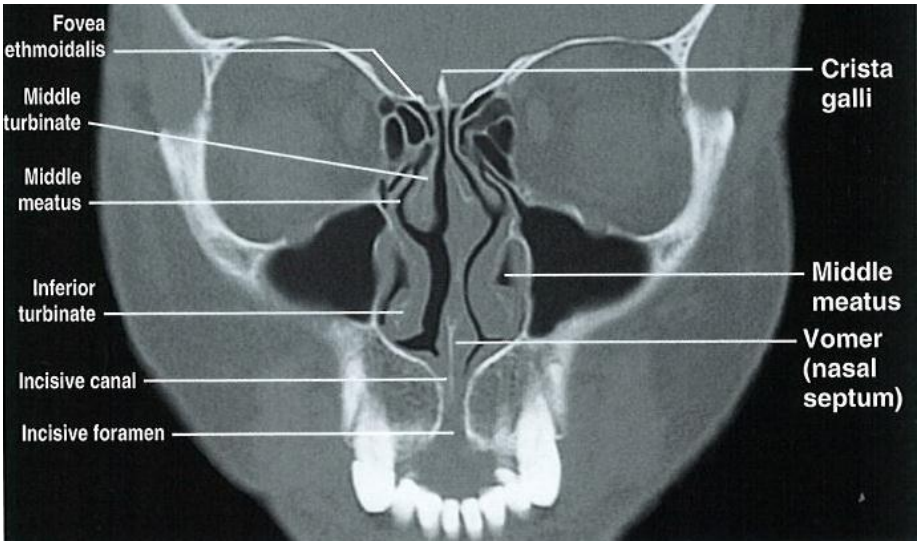
Fovea ethmoidalis
Middle turbinate
Middle meatus
Inferior turbinate
Incisive canal
Incisive foramen
Crista galli
Middle meatus
Vomer (nasal septum)

(d)

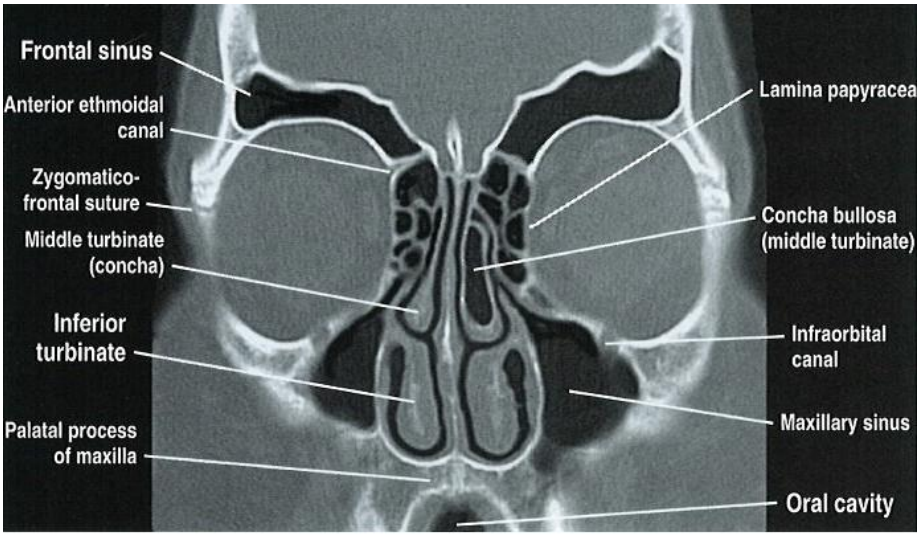
Frontal sinus
Anterior ethmoidal canal
Zygomatico-frontal suture
Middle turbinate (concha)
Inferior turbinate
Palatal process of maxilla
Lamina papyracea
Concha bullosa (middle turbinate)
Infraorbital canal
Maxillary sinus
Oral cavity

(e)

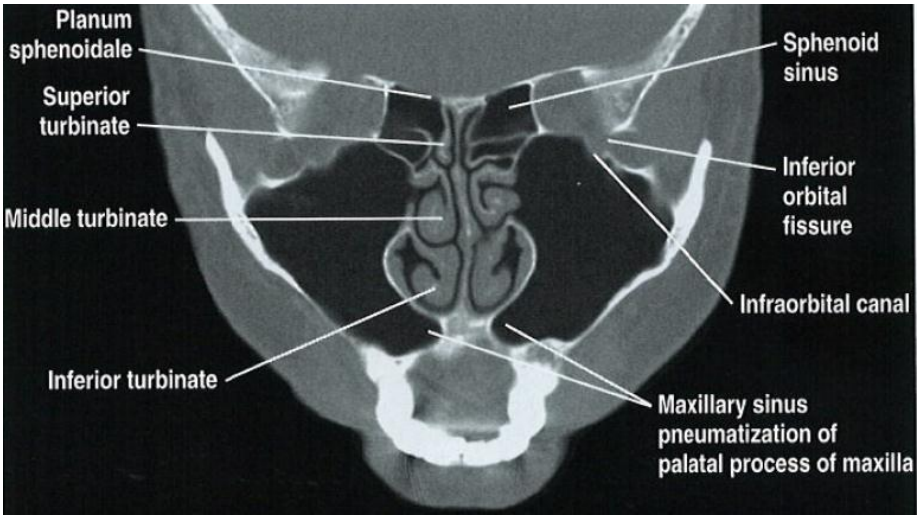
Planum sphenoidale
Superior turbinate
Middle turbinate
Inferior turbinate
Sphenoid sinus
Inferior orbital fissure
Infraorbital canal
Maxillary sinus pneumatization of palatal process of maxilla

(f)

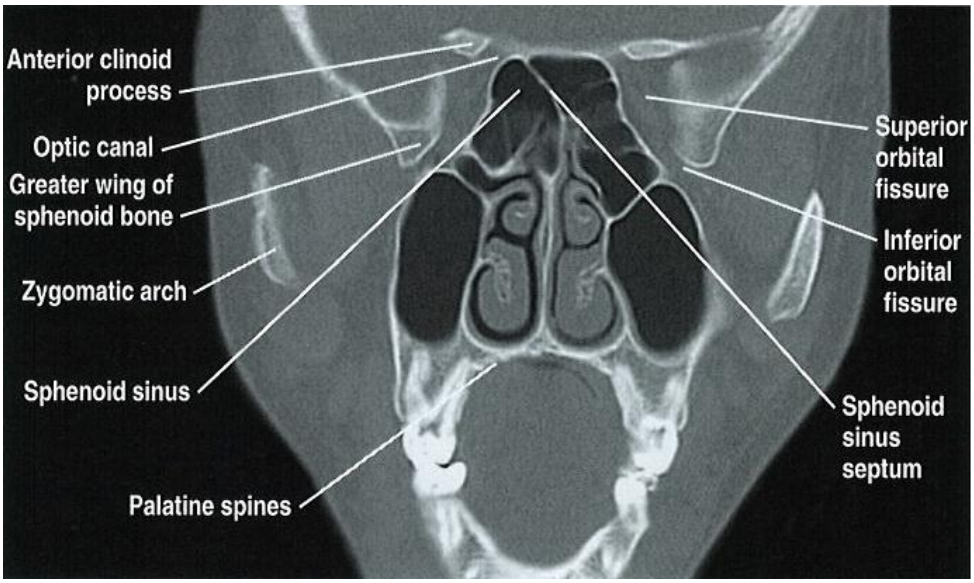

(g)

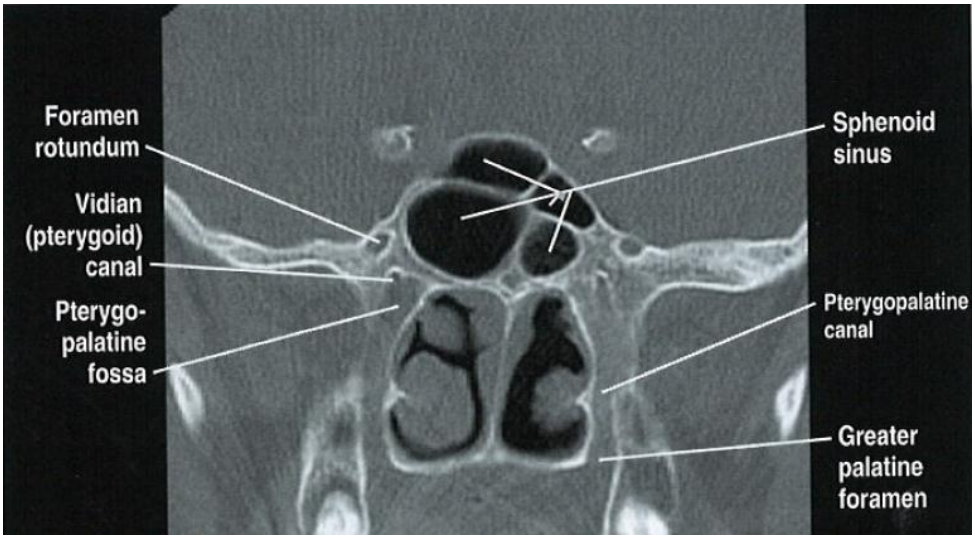

(h)

Fig. 3.13 CT coronal cross-sections illustrate the anatomy of the nasal cavity, paranasal sinuses (frontal, ethmoid, sphenoid, and maxillary sinuses), skull and facial bones, and surrounding tissues. [42].

3.2 Deviated Nasal Septum (DNS)

3.2.1 Causes, Symptoms, and Incidences of DNS

Few people have a perfectly straight and perpendicular nasal septum. The nasal septum usually shows slight bends and spurs. Provided that these do not hinder nasal perspiration, they are not to be regarded as abnormal. This may first be *developmental* due to unequal growth of the cartilage and bone of the nasal septum; second, it may be *traumatic* due to facial fracture, fracture of the nose or septum, or possibly due to injury at birth. The parts of the septum are then either too large for the given skeletal space, or are dislocated and heal in an incorrect position. In these cases deviations, spurs, and crests are caused which reduce the patency of the nasal cavity.

DNS symptoms include nasal obstruction, which is often unilateral and may be intermittent, hyposmia or anosmia, and headaches which can vary depending on the condition of the nasal cavity. A displacement of the ventral edge of the septum and obstruction of the nasal cavity on the other side is especially likely after *trauma*. This combination of factors can lead to complete bilateral obstruction of the nasal cavity. There are four types of septal deflection [43] (Fig. 3.14) as follows:

1. Isolated caudal deflection (Fig. 3.14-1)
2. C-shaped deformity (Fig. 3.14-2)
3. S-shaped deformity (Fig. 3.14-3 and Fig. 3.15)
4. Generalized deviation (Fig. 3.14-4)

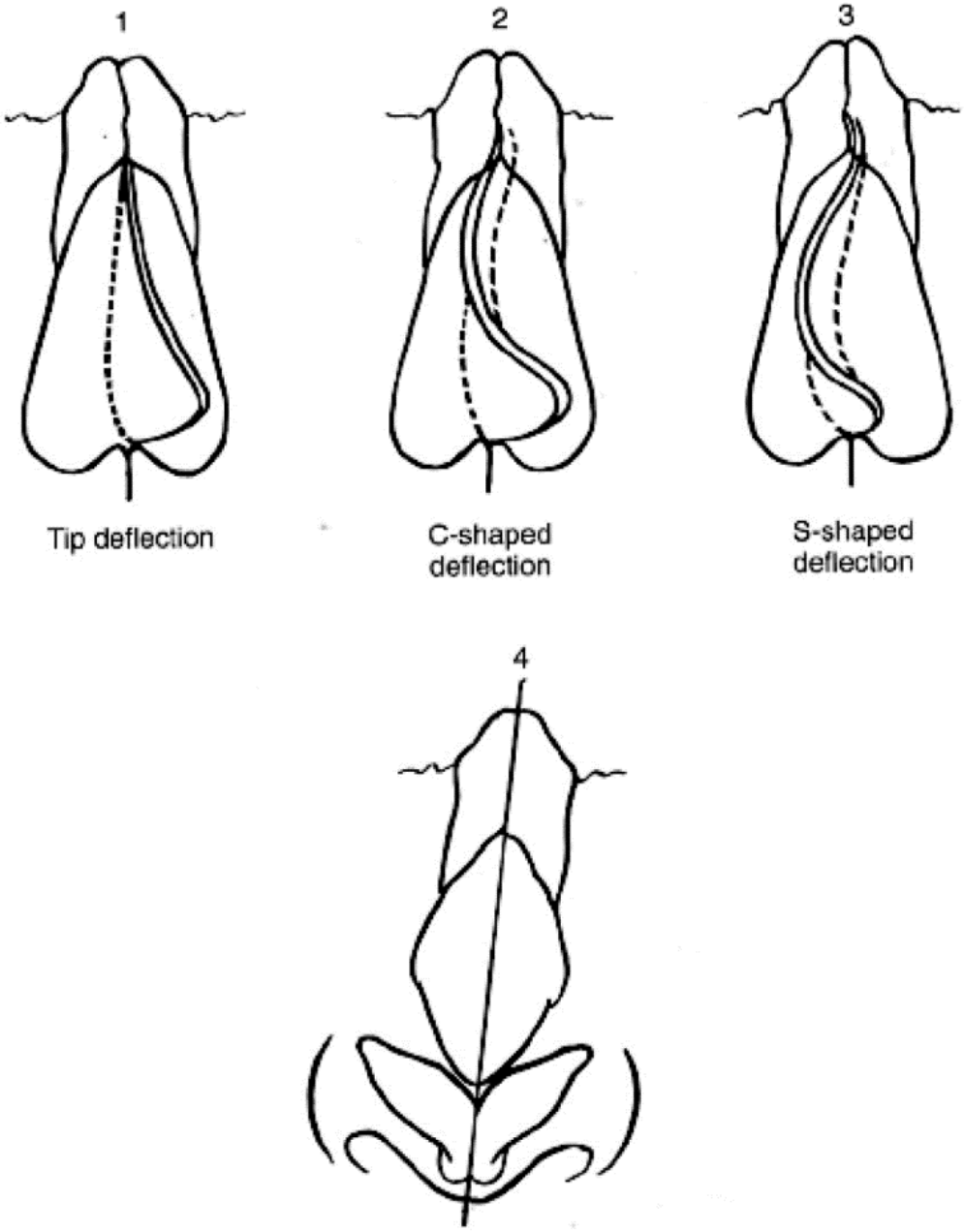

Fig 3.14 Septal deflection. 1, Tip deflection; 2, C-shaped deflection; 3, S-shaped deflection; 4, generalized deviation [37].

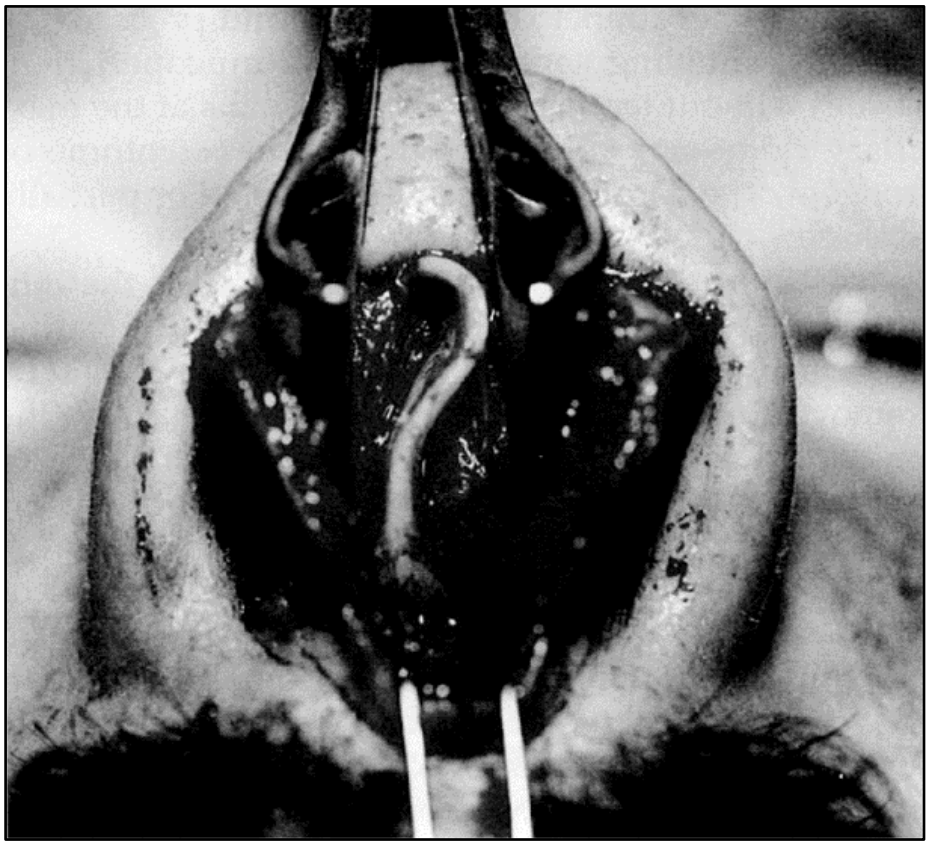

Fig 3.15 S-shaped septal deflection [37].

3.2.2 Effects of DNS on Nasal Patency and Nasal Airflow

When the nasal septum deviated toward one side, the increased space of the contralateral nasal cavity is filled with the inferior turbinate (IT) [44]. This is a counterbalanced mechanism characterized by compensatory hypertrophy of the IT, which protects the more patent nasal side from the drying and crusting effects of excess airflows [45]. However, DNS toward to one side leading to nasal airway obstruction on that side.

Figure 3.16 illustrates an example of a cross-sectional area of the DNS patient's nose, which was measured by an acoustic rhinomanometer. It can be seen that the minimal cross-sectional area (MCA) of the DNS nose is not found at the nasal valve region, while MCA is observed in the nasal valve of the healthy noses. MCA is observed at 5 cm from the nostril (see arrow), i.e. the nasal turbinates areas, of the right cavity. The narrowest cross-sectional area on the left side is also found at the same distance. Therefore, surgeons can use the acoustic rhinomanometry data to confirm the side of defected nose, estimated narrowest area, and its location in DNS patients.

Figure 3.17 illustrates an example of a nasal airflow volume of the DNS patient, which was measured by a rhinomanometer at the fixed pressure drop (Δp) of 75 Pa. The figure shows that the inspiratory and expiratory airflow volumes (Q) dramatically decreased due to the nasal obstruction on the left side of nose. Thus, a nasal resistance ($R'_N = \Delta p/Q$) was increased on the left side of nose, while the nasal resistance on the right side was not affected.

However, both acoustic rhinometry and rhinomanometry techniques are unable to measure the exact location of the DNS. Although the acoustic rhinometry technique is pragmatic and non-invasive, it is most suited to rendering the CSA of the anterior end of the nose as the technique yields good results when the distance from nostrils does not exceed 5 cm [16]. Nasal cross-sectional area beyond the narrow or virtually collapsed areas in nasal cavity tended to be inaccurate [17].

Limitations of rhinomanometry and acoustic rhinometry include:

(1) Irreproducibility of measurements made on the same patient on different days.

(2) Poor correlation between these objective measures of airflow and the patient's subjective assessment of nasal patency, and

(3) Dependence of accurate measurements on the experience level of the technician [46-52].

Therefore, advanced medical imaging modalities such as CT or MRI are attempting to fulfill an improvement of diagnostic techniques of DNS.

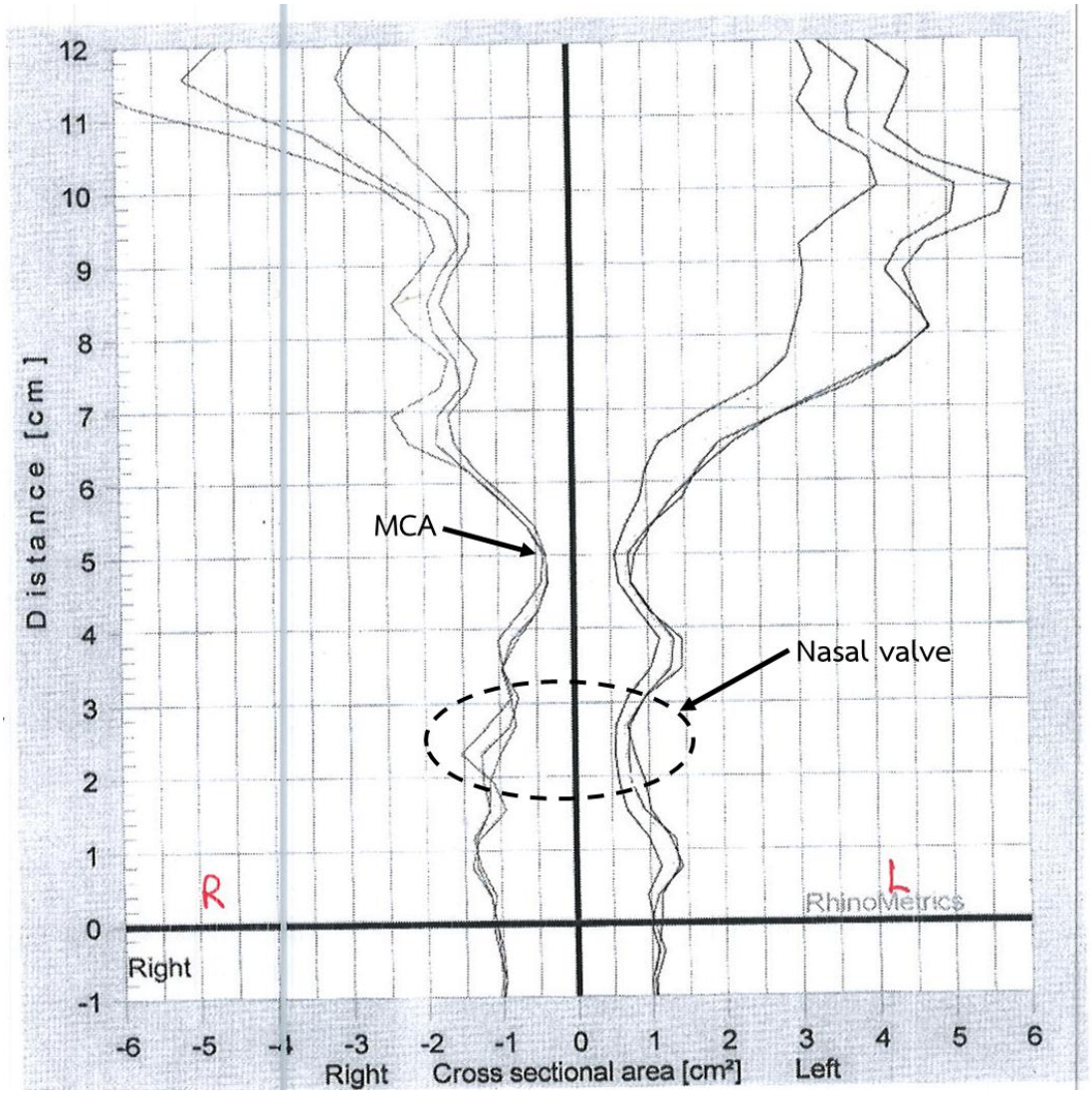

Fig. 3.16 Example of an acoustic rhinometry data from a patient with DNS toward the right side. Nasal obstructions are found on the right side and some part of the left side (about 5 cm from the tip of nostrils) of the nose.

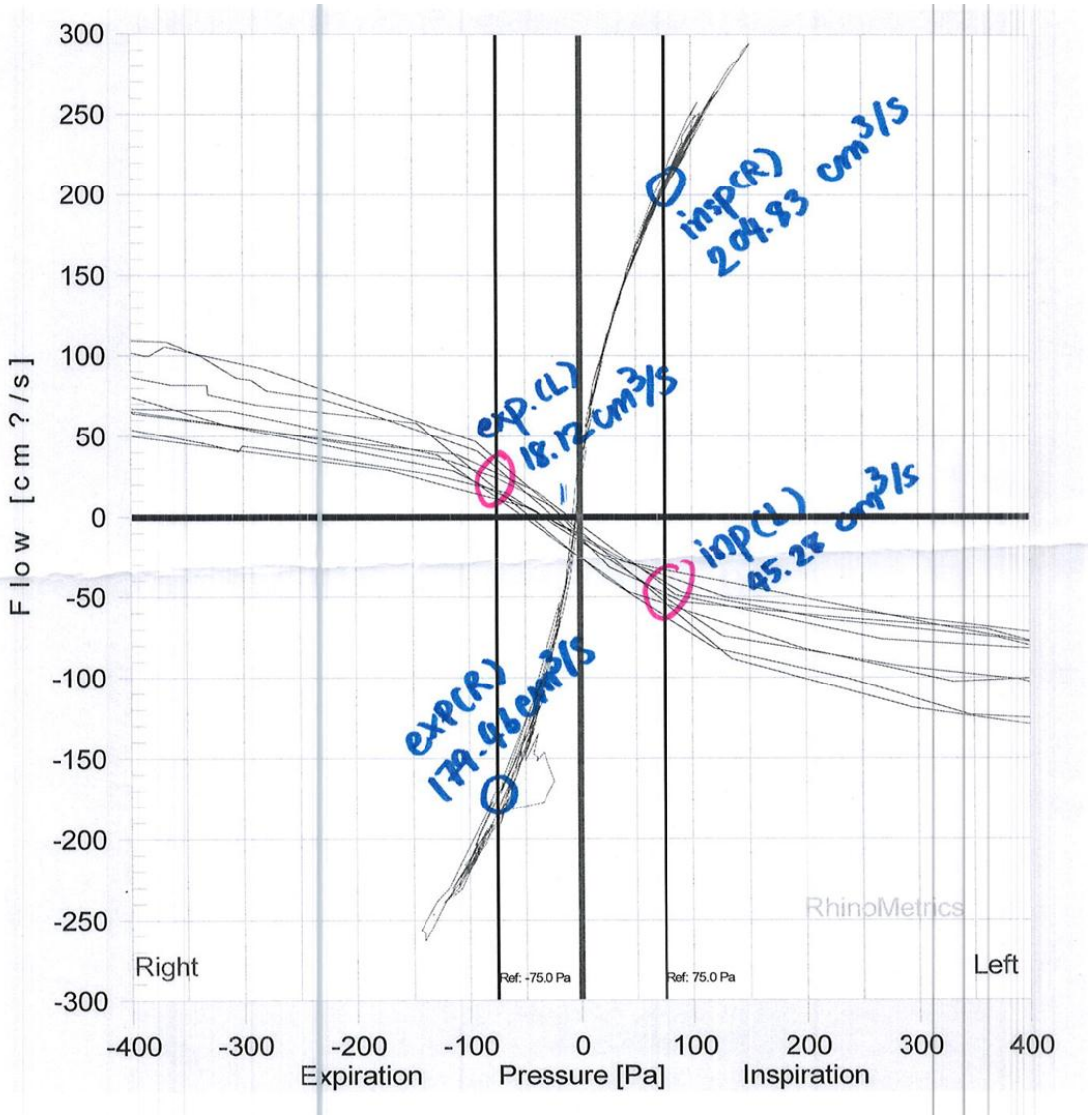

Fig. 3.17 Example of a rhinomanometry data from the patient with DNS toward the left side. Nasal obstruction is found on the left side of the nose. The nasal flow volume is dramatically decreased on the left side, while the normal nasal airflow are shown on the right side.

3.2.3 CT Imaging of the Nose with DNS

Figures. 3.18 and 3.19 present the axial and coronal CT images, which were compared between normal (Figs. 3.18 (a) and 3.19 (a)) and DNS (Figs. 3.18 (b) and 3.19 (b)) noses. The comparison shows that the nasal septum of the healthy nose is straight along the nasal cavity, while the nasal septum is deviated toward one side of the DNS nose. Direction of nasal septal deviation was determined by the convexity of the septal curvature. Figures 3.18 (b) and 3.19 (b) present the leftwards DNS, which lead to a nasal airway obstruction (NAO) due to the virtually collapse of the septum (see circles).

In addition, Bahar K. et al. [53] and Alireza M. et al. [54] presented the way to measure the degree of DNS using CT images. Figures 3.21 (a) and (b) present the Bahar K.'s and Alireza M.'s method, respectively. In this thesis, we used the Alireza M.'s method for measuring the deviation angle of DNS. It can be seen that CT images can reveal the exact locations of DNS and sites of NAO. Moreover, it can be used to assess severity of the DNS.

Parul G. [55] presented the comparison of CT with endoscopic images at the corresponding positions among normal and DNS noses (see Fig. 3.20). Moreover, Ertap et. al. [56] evaluated the turbinate hypertrophy using CT in DNS patients and reported that CT is a useful tool for the diagnosis of turbinate hypertrophy. When making a decision about the type of surgery, the mucosal and bony dimensions measured on CT scans should be considered [56].

However, it can be mention that CT scanner can measure only the nasal patency of the nose [37]. Measurements of nasal airflow inside the nasal cavity of both healthy and DNS noses are not possible in CT scanner. *Therefore, computational fluid dynamics (CFD) is combined to CT for development the integrated technique, which will aid surgeons to reveal both nasal patency and nasal airflow for diagnosis and surgical planning the DNS.*

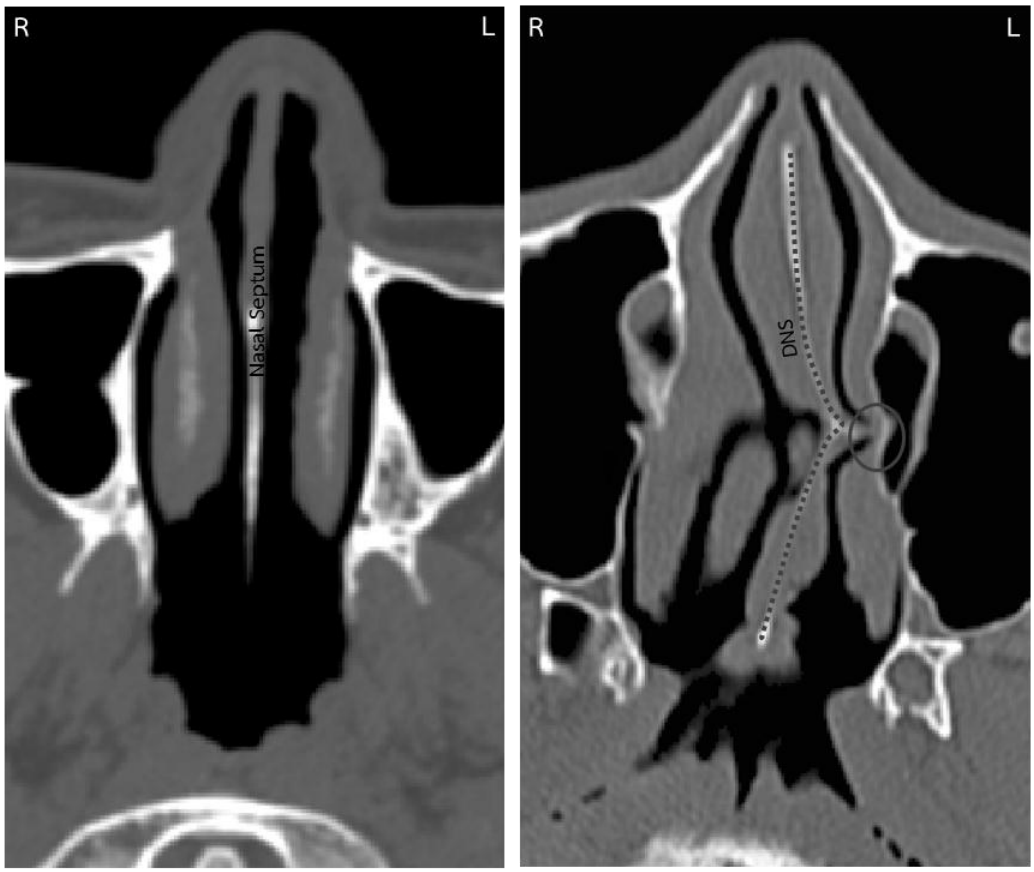

Fig. 3.18 Axial CT images compared between healthy nasal cavity (a) and leftward DNS (b). Straight nasal septum is presented in healthy nose. Deviated nasal septum (dotted line) is virtually collapsed (circle) shown in DNS nose.

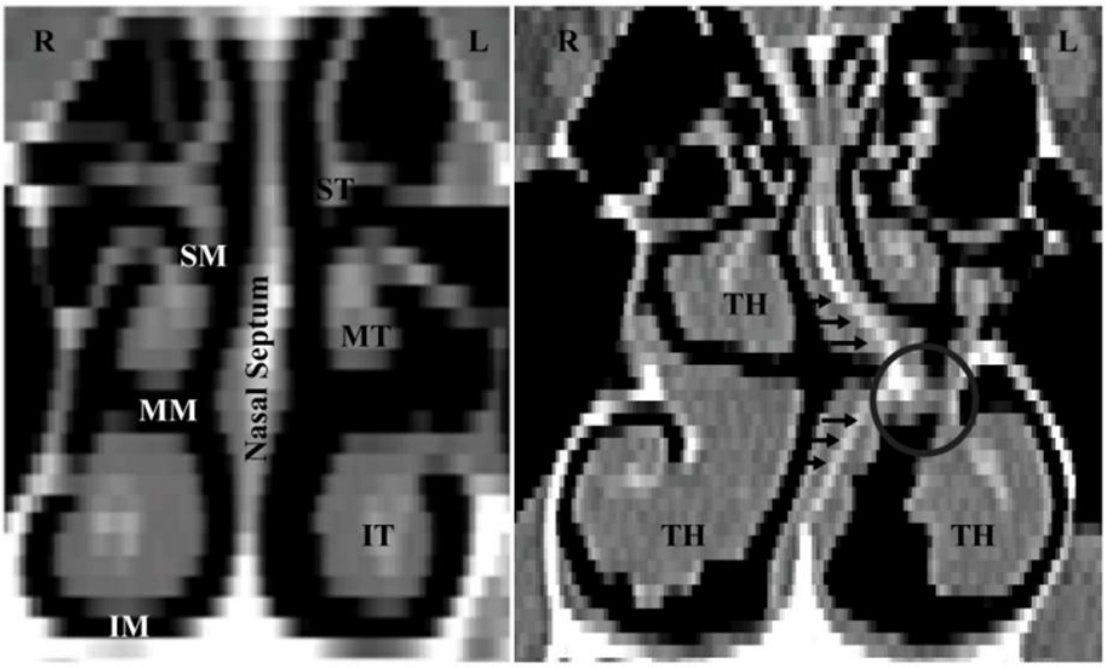

Fig. 3.19 Coronal CT images compared between healthy nasal cavity (a) and leftward DNS (b), where IT is the inferior turbinate, MT the middle turbinate, ST the superior turbinate, IM the inferior meatus, MM the middle meatus, and SM the superior meatus. Compensatory turbinate hypertrophies (TH) are frequently observed in DNS noses.

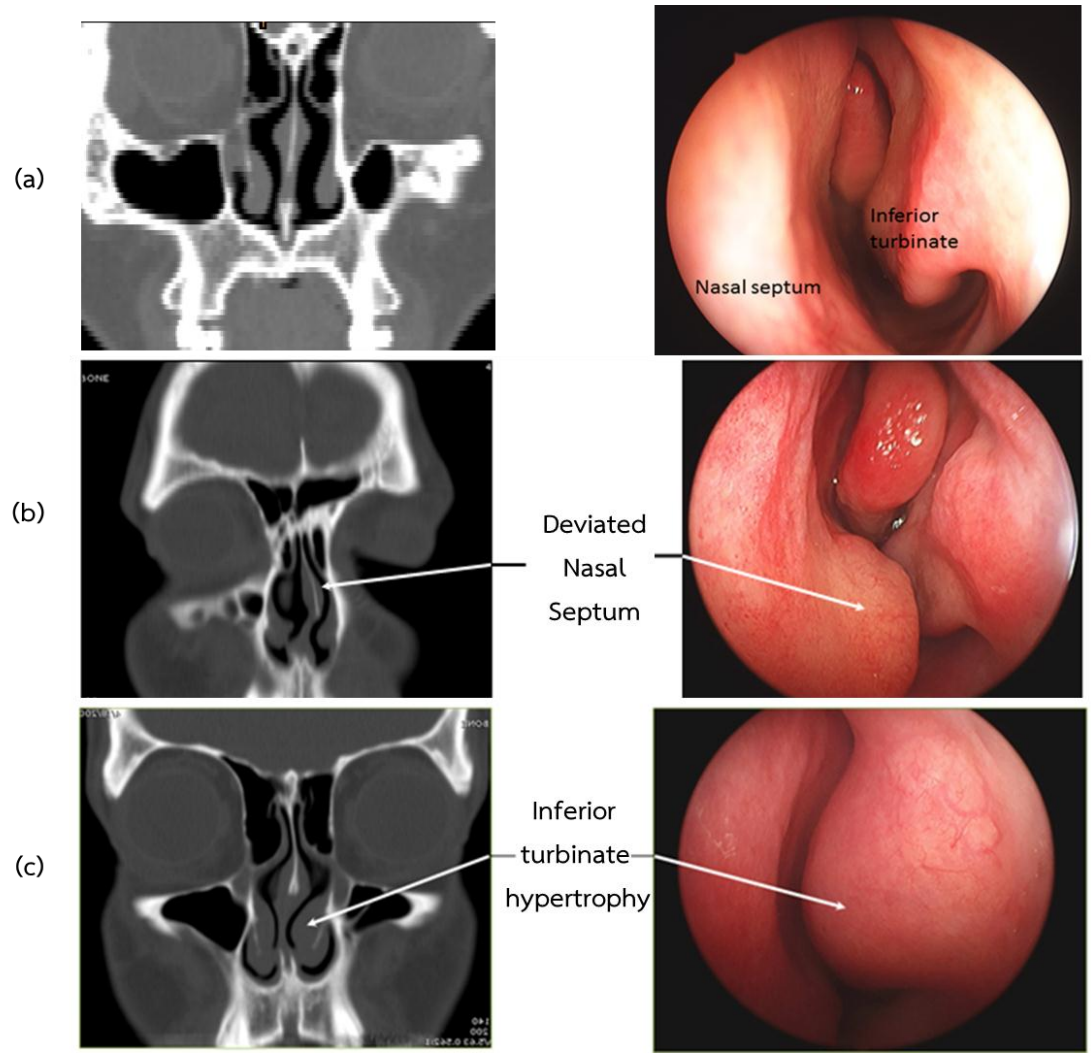

Fig. 3.20 Comparison of CT and endoscopic images at the corresponding positions. (a) Normal nasal septum. (b) presents leftward DNS. (c) presents rightward DNS with inferior turbinate hypertrophy. [55] (figure was modified from http://care.american-rhinologic.org/septoplasty_turbinates)

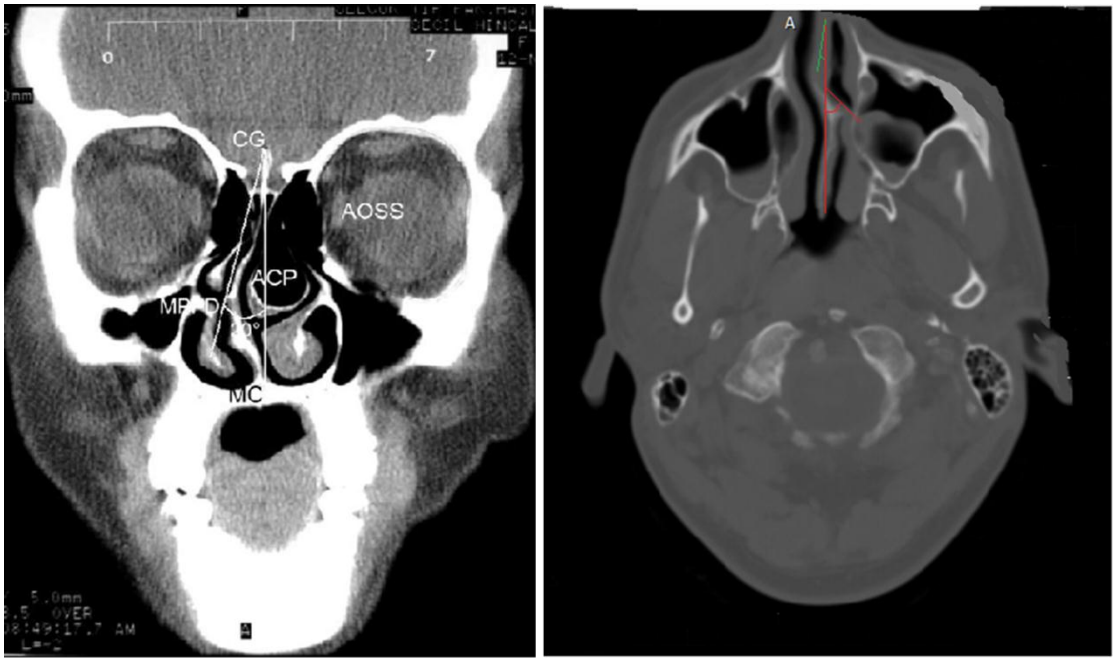

(a) (b)

Fig. 3.21 (a) presents Bahar K ‘s method measuring the deviation angle in coronal CT images: CG, crista galli; AOSS, area of orbit on the same site; ACP, area of concha pneumatization; MPPD, most prominent point of the deviation; MC, maxillary crest. Calculation of deviation angle according to the angle between CG and MPPD. (b) presents Alireza M ‘s method measuring the deviation angle of the center line in axial CT images: 0<normal<5; 5<mild<10; 10<moderate<20; and severe>20 (figure was modified from Bahar K. and Alireza M. [53, 54])

3.2.4 Surgical Operation and Post-Treatment Evaluation of DNS

Surgery to correct a deviated septum is called a septoplasty. Septoplasty is most commonly performed to help relieve nasal obstruction. The surgical technique is done in the operating room under anesthesia.

During a septoplasty, surgeon will attempt to straighten the cartilage and bone that have led to the septum being deviated. During the procedure, the lining (the mucosa) is first raised off the cartilage and bone. The cartilage and bone can then be reshaped. Sometimes, portions of the cartilage and bone need to be removed. The lining is then laid back down. Because the septal cartilage has 'memory', i.e. it has an intrinsic tendency to assume its initial shape, the septal cartilage can sometimes bend after the surgery.

Figures 3.22 (a) and (b) shows the principles of septoplasty. It is possible to remove all parts of the septum and to reimplant them if necessary after shifting and remodeling. However, the function of the nasal cavity can often only be restored satisfactorily by simultaneous correction of the external nasal pyramid.

Figure 3.22 (c) present the second method called Killian's submucous resection of the septum. After creating a mucosal tunnel, all deviated cartilaginous and bony parts of the nasal septum may be removed, straightened, and reimplanted if necessary. Complications of septoplasty and Killian's method above include septal perforations. If too much cartilage is resected, the cartilaginous part of the nose may fall in, causing an anterior or inferior saddle, or duckbill nose (Fig. 3.23 (d)). In both cases reconstructive procedures are available and indicated.

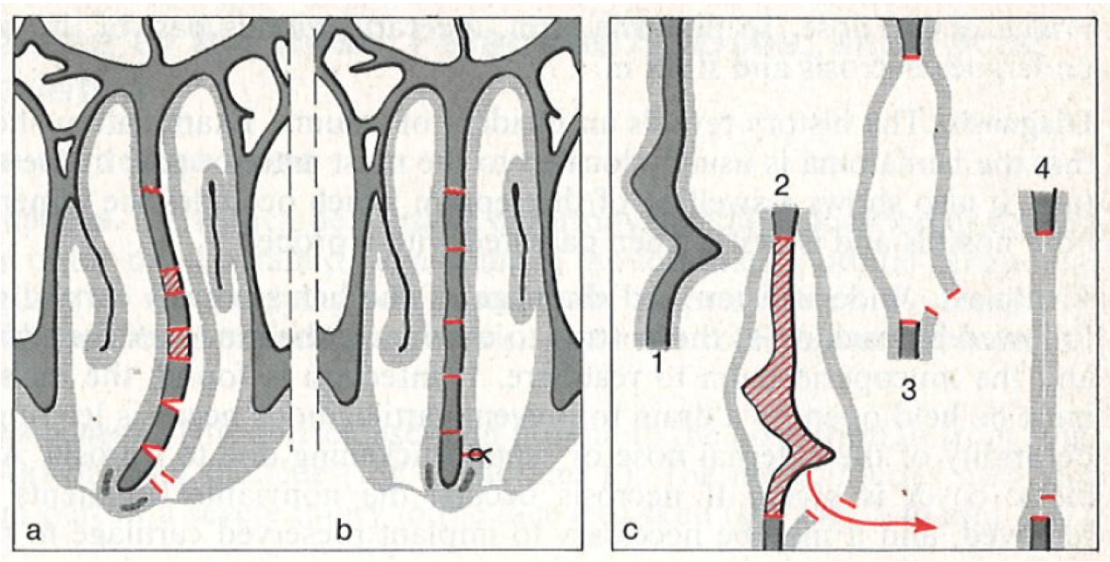

Fig. 3.22 Operations on the nasal septum. (a) Septal deviation with incisions and segmental resection. (b) Final condition. (c) Submucosal septal resection by Killian's method: 1, septum with spurs; 2, submucosal dissection of the cartilaginous bony septum and partial removal; 3, mucosal pocket after septal resection; 4, final condition with mucosal layers replaced [57].

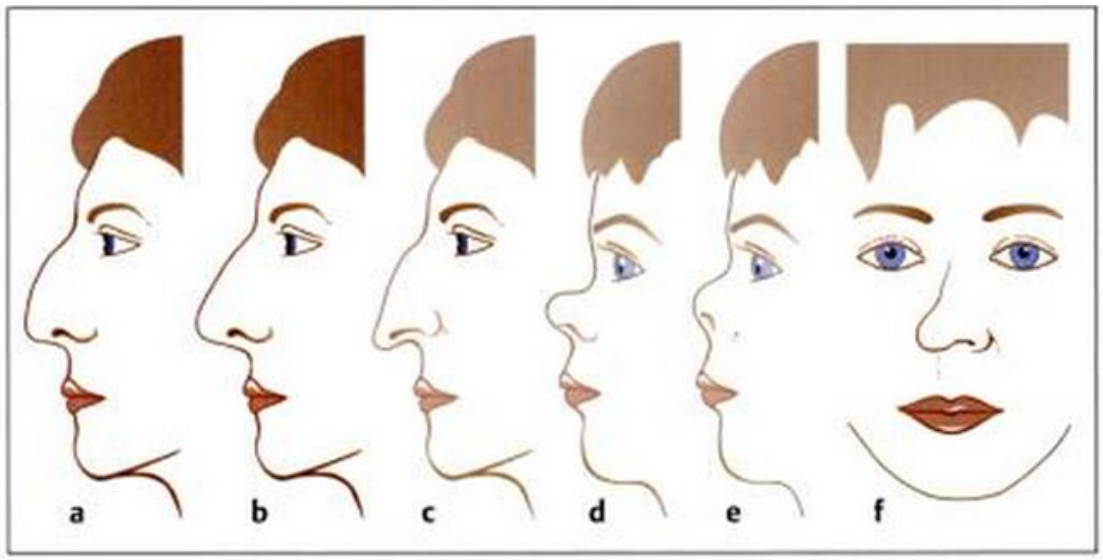

Fig. 3.23 Different nasal types. (a) Hump nose. (b) Overprojecting nose, functional tension nose. (c) Drooping nasal tip. (d) Saddle nose. (e) Short nose. (f) Deviated nose [58].

In many instances, turbinate surgery is performed in conjunction with septoplasty. There are many ways to shrink the size of the turbinates. Surgery is typically called turbinate reduction or turbinate resection. It is important that the turbinate not be removed completely because its removal can result in a very dry and crusty nose. In the absence of a turbinate, the air that is breathed may not be to adequately humidified and warmed. Occasionally, turbinate tissue will re-grow after turbinate surgery and the procedure may need to be repeated. This is preferable to the situation of totally removing the turbinate.

Inferior turbinate reduction (ITR) surgery is often performed for chronic nasal obstruction attributed to refractory turbinate enlargement. Numerous techniques for ITR have been reported [59, 60], and most studies indicate a significant rate of clinical success in improving nasal patency. The amount of tissue reduction needed to achieve positive results is uncertain. Some investigators [61-64] have reported that partial turbinectomy methods are effective, whereas others [65, 66] have advocated total turbinectomy. Partial turbinectomy itself can take a variety of forms, and various surgical techniques may be used. In most ITR studies, the available outcome data consist of subjective measures of satisfaction with the nasal airway. Although these studies provide important information, the physiologic interpretation of such subjective measures is limited. Therefore, it is desirable to quantify the effects of ITR on nasal airflow and pressure-flow relationships.

The objective evidence to support the efficacy of septoplasty is controversial [46, 48, 67-69]. However, studies with a more prolonged follow-up have suggested a gradual deterioration in patient satisfaction [48, 70]. Jessen and collaborators [70] found that only 26% of their patients were symptom free 9 years postoperatively. Ho and colleagues [48] observed that the percentage of patients with >50% reduction in the subjective feeling of obstruction decreased from 73% to 60% to 41% and then to 27% at 3 months, 6 months, 1 year, and 2.5 years postoperatively. It has been suggested that the higher success rates of short-term studies may be a placebo effect [48, 67, 68].

Recently, Singh and colleagues [46] conducted a systematic review and meta-analysis of the literature on septoplasty. Despite the abundant literature on this topic, these authors found only three articles that fulfilled certain credibility criteria, which included the use of at least one objective method (rhinomanometry or acoustic rhinometry) to evaluate the surgical outcome. Their analysis suggested that septoplasty reduces nasal resistance in most patients. However, these authors were startled by the small number of articles that met their eligibility criteria and concluded that more standardized, long-term studies are needed to sustain a definitive, objective argument in flavor of septal surgery [46].

Traditionally, the decision to perform septoplasty usually relies on clinical observations alone [68]. Selection for surgery is challenging in many patients because there are no agreed criteria by which to decide how much septum should be deviated before surgery is indicated [46, 67]. Rhinomanometry and acoustic rhinometry have been tested as possible objective methods to evaluate nasal airflow and select patients for surgery, but conflicting results have been reported.

Although some authors found a significant correlation between objective and subjective measures of airflow [49, 71-76], others found poor correlation and concluded that rhinomanometry and acoustic rhinometry are not useful to select patients for surgery [47, 48, 69, 77-79]. In their critical review of the literature, Robin and Eccles [67] concluded that little progress in understanding the involvement of septal deviations in nasal disease will be made until a better objective method is developed to qualify the degree of septal deviation and its impact in nasal physiology.

3.3 CFD Simulation in Healthy and DNS Noses

As compared to rhinomanometry and acoustic rhinometry, which provide quantitative information only of nasal resistance and cross sectional areas, CFD enables additional measurements of airflow passing through the nasal cavity that help visualize the physiologic impact of alterations in intranasal structures. In several

past decades, following topics show that CFD has been utilized to evaluate the nasal airflow in both healthy and DNS noses.

3.3.1 CFD Studies in Healthy Noses

Prior to the CFD studies, nasal airflow patterns in human noses have been experimentally studied by a number of researchers. The nasal anatomy characterized by rigid cast models has been used to experimentally study the airflow patterns.

Hahn et al. (1993) [80] used a hot-film anemometer probe to measure the velocity distributions on five cross-sections of a 20× enlarged human nasal cavity model. In these experiments a steady non-oscillatory flow was applied and the flow was considered laminar up to a flow rate of 24 L/min.

Kelly et al. (2000) [81] investigated 2D velocity fields in parallel planes to the flow direction, throughout a nasal cavity model using particle image velocimetry (PIV). It was reported that approximately half of the inspired airflow passed through the middle and inferior portions of the nasal airway, while a small fraction of the flow passed through the olfactory region locating in the superior part of nose.

Churchill et al. (2004) [82] studied airflow patterns using water and dye flowing through anatomically accurate acrylic models of 10 different human nasal cavities. It was observed that the nasal morphological features, e.g. the inferior orientation of the nostrils, the relative size of the nasal valve, and the height of the nasal, did not show statistically significant correlations among the 10 models. However, one parameter, i.e. the projection of the turbinate bones into the nasal cavity, was shown to laminate the flow.

Recent developments in medical imaging (MRI and CT scanning) coupled with computational fluid dynamics (CFD) have opened new possibilities for physically realistic numerical simulations of the human nasal airflow. Keyhani K. et al. (1995) [83] have constructed an anatomically correct finite element method (FEM) of a healthy human nasal cavity, and have unilaterally computed velocity profiles for quiet resting breathing flow rates (125 mL/s or Re= 610 at naris) through the healthy nose. The numerical results have been validated by comparison with detailed

experimentally measured velocity profiles in the large scale model constructed by Hahn et al. (1993) [80]. The steady-state Navier-Stokes and continuity equations were solved numerically to determine the laminar airflow patterns in the nasal cavity. It was found that the highest inspiratory air speed occurred along the nasal floor (below the inferior turbinate) of the main nasal passages.

This is consistent with the numerical simulation of Elad et al. (1993) [84]. In the anterior end of the main nasal passages, the peak is about 4 m/s and is close to the septum side of the airway. As flow moves toward the posterior end of the nasal cavity, the peak remains along the nasal floor, but shift from the septum side towards the lateral side, and the values decreases to about 2.5 m/s in the posterior region. A second lower peak of about 2 m/s occurred in the middle of the airway (between inferior and middle turbinates and septum). Nearly 30% of the inspired volumetric flow passed below the inferior turbinate and about 10% passed through the olfactory airway. During expiration, the peaks in velocity were smaller than inspiration, and the flow was more uniform in the turbinate region. The numerical results showed good agreement with the experimental measurements at different locations in the airways, and confirmed that at resting breathing flow rates, airflow through the nasal cavity is laminar.

Zhao K. et al. (2004) [85] have developed a method to quickly (<few days) convert nasal CT scans from an individual patient into an anatomically accurate 3D numerical nasal model that can be used to predict airflow and odorant transport, which may ultimately determine olfactory sensitivity, using FVM-CFD techniques. Results suggest that anatomical changes in the olfactory region and the nasal valve region will strongly affect airflow patterns and odorant transport through the olfactory region, with subsequent effects on olfactory function. The ability to model odorant transport through individualized models of the nasal passages holds promise for relating anatomical deviations to generalized or selective disturbances in olfactory perception and may provide important guidance for treatments for nasal-sinus disease, occupational rhinitis and surgical interventions that seek to optimize airflow and improve deficient olfactory function.

In the same year, Press D. et al. (2004) [86] investigated cooling of the expiratory air for heat recovery within the human nose applying numerical simulation. The results showed that heating if inspired air not only depends on inspiration but also on expiration. Cooling the warm expiratory air may be regarded as an important factor for heat recovery. The results also demonstrate the close relation between heat exchange and airflow patterns during the period of expiration.

Naftali S. et al. (2005) [87] studied the air conditioning capacity of the human nose. Unsteady simulations in 3D models have been developed to study transport patterns in the human nose and its overall air-conditioning capacity. The results suggested that the healthy nose can efficiently provide about 90% of the heat and the water fluxes required to condition the ambient inspired air to near alveolar conditions in a variety of environmental conditions and independent of variations in internal structural components.

Croce C. et al. (2006) [88] measured pressure-flow relationships measured in human plastinated specimen of both nasal cavities and maxillary sinuses were compared to those obtained by numerical airflow simulation in a numerical 3D reconstruction issued from CT scans of the plastinated specimen. The good agreement between measured and numerically computed total pressure drops observed up to a flow rate of 250 mL/s is an important step to validate the ability of CFD software to describe flow in a physiologically realistic binasal model. The major total pressure drop was localized in the nasal valve region. Airflow was found to be predominant in the inferior median part of nasal cavities.

Wen J. et al. (2008) [24] used CFD methods to present flow patterns between the left and right nasal cavities and compared the results with experimental and numerical data that are available in literature. Laminar steady flow rates of 7.5 L/min and 15 L/min were adopted in the CFD simulation. The computational model based on CT scans of an Asian male volunteer exhibited a narrower nasal valve region, wider turbinates and a shorter length in comparison with other models. Despite this a general trend was observed for the cross-sectional area profile of the airway along the axial distance. Nasal resistance was found to contribute up to half

of the total airway resistance within the first 2–3 cm of the airway. The formation of vortices was found primarily in the upper olfactory region and just posterior to the nasal valve where the geometry begins to expand. The majority of the flow in this region remained close to the septum walls and only a small proportion reached the olfactory region and the outer meatus extensions that were created by the turbinate protrusions. Low flow in the olfactory region is a defense mechanism that prevents particles whose trajectories are heavily dependent on flow patterns from being deposited onto the sensitive olfactory nerve fibers, while vapors are allowed to diffuse for olfaction. However, the low flows in the meatus regions bring into the question the efficiency of the turbinate protrusions condition the inspired air.

In the same year, Segal R.A. et al. (2008) [22] investigated effects of differences in nasal anatomy on airflow distribution by comparison of four individuals at rest. The results showed that the majority of flow passed through the middle and ventral regions of the nasal passages; however, the amount and location of swirling flow differed among individuals. Cross-sectional flow allocation analysis also indicated inter-individual differences.

3.3.2 Trends and Possibilities of Using CFD in the Nasal Surgery

- Wexler D et al. (2005) [32] used the CFD simulation to evaluate the aerodynamic effects of inferior turbinate reduction (ITR). Computer-simulated left ITR was used for assessment the effects of post-op ITR. There are many methods of turbinate reduction, and this study examined only 1 relatively conservative reduction pattern. The results showed that conservative ITR produced marked changes in nasal pressure, airspeed, and relative airflow distribution throughout the nasal passages. Simulated ITR resulted in a broad reduction of pressure along the nasal airway, including the regions distant from the inferior turbinate vicinity.

In contrast, relative airflow changes were regional: airflow was minimally affected in the valve region, increased in the lower portion of the middle and posterior nose, and decreased dorsally. This study suggested that use of CFD methods should help clarify the aerodynamic significance of specific surgical

interventions and refine surgical approaches to the nasal airway. Moreover, a series of comparative simulations should enable determination of optimal anatomic configurations and serve as a guide for planning nasal airway surgery.

- Kimbell JS et al. (2012) [89] developed methods for comparing nasal resistance computed by CFD models with patient-reported symptoms of NAO using early data from a 4-year prospective study. The results showed that Nasal Obstruction Symptom Evaluation (NOSE) and visual analog scale (VAS) scores improved after surgery, bilateral CFD-NR decreased, and unilateral CFD-NR decreased on the affected side. In addition, NOSE and VAS scores tracked with unilateral CFD-NR on the affected side. The results suggested a possible correlation between unilateral NR and patient-reported symptoms and imply that analysis of unilateral obstruction should be focus on the affected side. A formal investigation of unilateral CFD-NR and patient-reported symptoms in a series of NAO patients is needed to determine if these variables are correlated.

- Rhee JS et al. (2012) [31] demonstrate the effect of individual components of functional nasal airway surgery in a patient with multifactorial obstruction and discuss the potential benefit of CFD-aided virtual surgery. A 53 year old female underwent septoplasty, turbinate reduction, and nasal valve repair. Pre- and post-operative digital nasal models were created from CT images and nasal resistance was calculated using CFD techniques. The digital models were then manipulated to isolate the effects of the components of the surgery, creating a nasal valve repair alone model and a septoplasty-turbinate reduction alone model.

They found that most of the reduction in nasal resistance was accomplished with performance of septoplasty and inferior turbinate reduction. The contribution from nasal valve repair was less in comparison but not insignificant. They implied that CFD-aided virtual surgery may be useful as part of pre-operative planning in patients with multifactorial anatomic nasal airway obstruction.

- Na Y et al. (2012) [30] established a procedure to create anatomically correct physical and numerical post-surgery models using CFD. The benefits and drawbacks of inferior turbinectomy should be considered by analysis of the results

reported in this article. Airflow inside one normal and three bilateral post-surgery models was investigated both experimentally and numerically to simulate inferior turbinectomy. The left cavities of all three models are normal and right cavity is modified by (1) excision of the head of the inferior turbinate, (2) resection of the lower fifth of the inferior turbinate, and (3) resection of almost the entire inferior turbinate. The turbinectomy obviously altered the main stream direction. The flow rate in the upper airway near the olfactory slit decreased in model (1) and (3). This may weaken the olfactory function of the nose.

Fluid and thermal properties that are believed to be related with physiology and prognosis are dependent on turbinate resection volume, position, and manner. Widening of the inferior airway does not always result in decreased flow resistance or wall heat transfer. The gains and losses of inferior turbinectomy were considered by analysis of the post-surgery model results. Nasal resistance was increased in model (1) due to sudden airway expansion. Nasal resistance increased and the wall heat transfer decreased in model (3) due to sudden airway expansion and excessive reduction of the mucosal wall surface area. Local shear stress and pressure gradient levels were increased in model (1) and (3).

- Kimbell JS et al. (2013) [33] presented study were to expand the results from Rhee JS et al. (2012) [31] ‘s research work to a larger cohort of NAO patients and compute airflow, wall shear stress, and heat flux in addition to CFD-NR pre- and post-surgery. In order to improve the success rate of NAO surgery using CFD, biophysical variables need to be identified that can be markers for symptoms of NAO so that these variables can eventually help guide virtual surgeries. The results provided a quantitative evaluation of these requirements indicating that CFD-derived Airflow-OS (OS=most obstructed nasal side), Heat Flux-OS, Airflow Partition-OS, and CFDNR Ratio-OS have the most potential to help guide future virtual surgery planning.

Correlations of CFD variables with symptoms were stronger for symptoms reported using the NOSE survey than for those measured by the VAS scale. Moreover, because the nasopharynx is dynamic and often showed different widths in

pre- and post-surgery scans, we compared pre- and post-surgery simulations in which the pressure drop from the nostrils to the non-dynamic posterior end of the nasal septum was the same, rather than equating overall pressure drops from nostrils to the model's outlet. As further analysis is undertaken to better understand the predictive capability of CFD methods, it is not too hard to imagine a day when a tool will be at hand to aid surgeons in designing specific surgical techniques or interventions that will maximize successful outcomes.

3.3.3 Aerodynamic Effects of DNS on the Nasal Airflow

- Chen XB et al. (2009) [25] analyzed severe DNS effects on nasal airflow pattern compared with that of a normal nose using CFD simulation tools. For the healthy case, airflow is almost uniform for the left and right sides. The main airflow occurs in the middle of the airway (between the inferior and middle turbinates around the septum), with the peak velocity in this area. The pressure decreased smoothly along the airway from the nostril to the nasopharyngeal region. For the DNS case, the air flow pattern shows major differences as compared with that of a healthy one. There is obviously less air going through the deviated side especially for inspiration. The main airflow is found passing through the floor (left side) and superior part (right side) of the nasal cavity. A greater pressure gradient or abrupt pressure jump is found posterior to the side of the deviation (more in right side than the left). The increase of total negative pressure is more drastic in the deviated nose (40.66 Pa) than the healthy nose (29.12 Pa). Thus, the nasal resistance of the DNS nose is almost twice that of the healthy one and it is larger during inspiration than expiration. This study suggested that the use of CFD techniques will help in qualitative and quantitative investigations of the changes or pathological impact of septal deviation on airflow patterns, wall shear stress distributions, and pressure loss inside the nasal cavities, which may benefit physiological and medical treatments in the future.

- Garcia GJM et al. (2010) [26] investigate how nasal resistance is affected by the location of a septal deviation using CFD. Moreover, they tried to validate

computational modeling as a tool to estimate nasal resistance. This study illustrated how computational modeling and virtual manipulation of the nasal geometry are useful to investigate nasal pathology. A 3D model of the left nasal passage of a 37-year-old woman was used as an original model. Septal deviations were created in nine different locations. The result revealed that the posterior nasal cavity can accommodate significant septal deviations without a substantial increase in airway resistance. In contrast, a deviation in the nasal valve region more than doubled nasal resistance. Thus, patients with anterior septal deviations benefit the most from septoplasty. This suggests, in agreement with the literature, that other cause of nasal obstruction should be carefully considered in patients with posterior septal deviations because such deviations may not affect nasal resistance. The results provide evidence that CFD predicted nasal resistance is in good agreement with past clinical observations. In the future, computational modeling may be used as a tool to select patients that benefit the most from septoplasty, plan patient specific surgeries, and optimize surgical outcome.

- Liu T et al. (2012) [27] investigated the airflow patterns and air velocity in fifteen different septal deviation models during inspiration, using CFD method. In models of septal deviation, the airflow patterns and airflow velocity are asymmetrical. Similar to the results of Leong et al. [90] which reported that the main inspiratory airflow is channeled away from the middle part of the common meatus toward the inferior meatus in septal deviation models, with less airflow through the middle of the airway, and results in less airflow in the olfactory area. In addition, the airflow patterns varied in the convex and concave sides in different septal deviation models. Caudal septal deviation models had the maximum peak velocity, while the minimal peak velocity was found in the media deviation models. In addition, the peak velocity was not always located in the convex side, but was sometimes in the concave side. According to Yu et al. [91], with a certain pressure drop, more airflow would pass through the wider side of the nasal cavity as the airflow resistance is lower. However, the concave side was not always the wider side, in some models, hypertrophy of the inferior turbinate made the concave side even narrower than the

convex side. This has some conflict with other studies [25, 83], where the peak velocity was always located in the convex side.

3.3.4 CFD based Surgical Aiding Tool Studied in DNS Patients

Surgical correlation of septal deviations has been one of the most common procedures in otolaryngology, but, the objective evidence to support the efficacy of surgery is controversial. Although septoplasty and turbinectomy were two of the most commonly performed surgical procedures for relieving NAO [92], the long-term outcomes of such treatments are still not satisfactory [48, 76]. Without any standard criteria, the decision to perform septoplasty was usually based on clinical observations alone [46, 68]. The main reason behind this was the lack of knowledge on the correlation between patient-reported symptoms and objective findings, including fluid mechanical properties [93].

Many authors applied CFD methods to help surgeons evaluated pre- and post-operations in patients with nasal septal perforation [94], sinus surgery [95, 96], and atrophic rhinitis [97], etc. For nasal surgery in DNS, there are limited works using CFD as diagnostic and pre-surgical tools.

- Ozlugedik S et al. (2008) [29] investigated the effects of septal deviation and concha bullosa on nasal airflow; and the aerodynamic changes induced by septoplasty and partial lateral turbinectomy in the nasal cavity, using CFD. A 3D model of a nasal cavity was generated using paranasal sinus computed tomography images of a cadaver with concha bullosa and septal deviation. In the preoperative model, the air flow mostly pass through a narrow area close to the base of the nasal cavity. The reduction in intranasal pressure occurred particularly in the right nasal passage in a very short segment anteriorly where deviation was present, whereas postoperatively the nasal valve region and the reduction were more gradual. Following septoplasty and partial lateral turbinectomy, total nasal resistance is reduced significantly.

The total nasal resistance in the preoperative model was 0.41 Pa/mL/second and decreased to 0.14 Pa/mL/second following septoplasty and

partial lateral turbinectomy. These results confirm that the most significant structure providing resistance in the nose is the nasal valve region [88]. Septal deviations in nasal valve region lead to greater increments in nasal resistance, and surgery of deviations in the anterior nasal segment has greater clinical success rates [68]. They reported that the most significant advantages of using CFD analysis in evaluation of nasal pathologies are the ability of assessing local aerodynamics at any point inside the nasal cavity and the chance of investigating the aerodynamic effects of planned surgical interventions via performing virtual operations on models and might increase the success rate of the surgical treatment.

In conclusion, CFD simulations promise to make great contributions to understand the airflow characteristics of healthy and pathologic noses. Before surgery, planning for any specific intervention using CFD techniques on the nasal cavity model of the patient may help foreseeing the aerodynamic effects of the operation and might increase the success rate of the surgical treatment.

- Moghadas H et al. (2011) [28] had evaluated the details of the airflow in the nasal passages pre- and post-septoplasty using CFD. Three-dimensional nose model obtained by CT scan images of an adult male subject were used to construct a smooth airway passage for the pre and post-operative cases. Before septoplasty, the amount of air passing through the right nasal cavity was much smaller than that after the operation. The right post-operative passage had roughly the same volumetric airflow rate as the normal left cavity. Also for a given pressure drop, the nasal airflow in the abnormal right cavity before septoplasty was about 40-50% less than that in the normal left passage.

After septoplasty, however, the differences reduced to less than 6%. Moreover, the velocity magnitude was highest in the nasal valve and the main airway regions where the deviated resides. However, after the septoplasty, the peak velocity occurred in the nasal valve region, which was similar to normal nasal cavities. Similarly, for the same pressure drop, the air speed was smaller in the preoperative right nasal cavity because of lower volume flow rate.

The present study further shows that CFD could provide a tool for predicting the airflow patterns in nasal passages which specific surgical interventions would produce. Such a tool is expected to help to refine surgical approaches for correcting nasal airway abnormalities and blockages. It is expected that CFD could help the medical professional to select and optimize the surgical interventions for specific patients.

- Rhee JS et al. (2011) [34] evaluated whether virtual surgery (VS) performed on 3D nasal airway models can predict post-surgical, biophysical parameters obtained by CFD. The ability of CFD modeling to predict actual surgical outcomes using a virtual nasal surgery computational model was evaluated. Pre- and post-surgery CT scans of a patient undergoing septoplasty and right inferior turbinate reduction (ITR) were used to generate 3D models of the nasal airway. Pre-surgery model was digitally altered to generate 3 VS models: right ITR, septoplasty only, septoplasty with right ITR. The results showed that post-surgery CFD analysis and all VS models predicted similar reductions in overall nasal resistance, as well as more balanced airflow distribution between sides, primarily in the middle region, when compared with the pre-surgery state.

In contrast, virtual ITR alone produced little change in either nasal resistance or regional airflow allocation. They presented an innovative approach for assessing functional outcomes of nasal surgery using CFD technique. They suggested that virtual nasal surgery has the potential to be a predictive tool that will enable surgeons to perform personalized nasal surgery using computer simulation techniques. Further investigation involving correlation of patient reported measures with CFD outcome measures in multiple individuals is underway.

- Kim SK et al. (2014) [98] aimed to find the correlation between fluid dynamic parameters and the geometry of nasal cavity with DNS using numerical simulation. They investigated the airflow characteristics in human nasal airways constructed from CT images of 6 different adults with DNS (3 symptomatic and 3 asymptomatic patients after clinical diagnosis). They tried to correlate the flow characteristics (nasal resistance, flow rate allocation, velocity, pressure, wall shear

stress) with patient-reported symptoms of DNS to nasal airway obstruction (NAO). They found that the symptoms of NAO seem to be related more to the nasal resistance from the naris to the end of the septum than to the total nasal resistance from naris to nasopharynx. This study suggested that factors correlated with NAO by CFD can be used as elements in patient-specific objective diagnostic tools for NAO in the presence of DNS. Therefore, CFD simulation for a patient-specific model can be useful tool for diagnosis.

3.4 Present Research Study

CFD is a novel technique which can reveal both anatomy and physiological functions of the human noses. Outcomes of CFD also strongly correlated with the symptom measures, e.g. NOSE and VAS. Moreover, using CFD for predicting the outcomes of various treatment approaches was widely observed. However, there was still limited research works investigated in DNS patients.

As our knowledge, this research work is the first study that utilized CFD with CT imaging techniques for aiding surgeons in a pre-surgical planning of DNS patients. We propose the CFD-CT aided surgery approach for treating DNS and increasing the successful outcomes. Correlation of computed CFD variables such as air speed, pressure drop, and nasal resistance with the data acquired from standard objective measurements, i.e. rhinomanometry, and patient's symptom score, i.e. NOSE, will be evaluated in this research study.

Chapter 4

Research Methodology

4.1 Design of the CFD-CT aided surgery approach

The proposed CFD-CT aided surgery approach was created for a patient-specific surgical planning tool. Figure 4.1 present the design process of the CFD-CT approach consisting of three main parts: pre-operative process, pre-surgical planning process, and post-operative process.

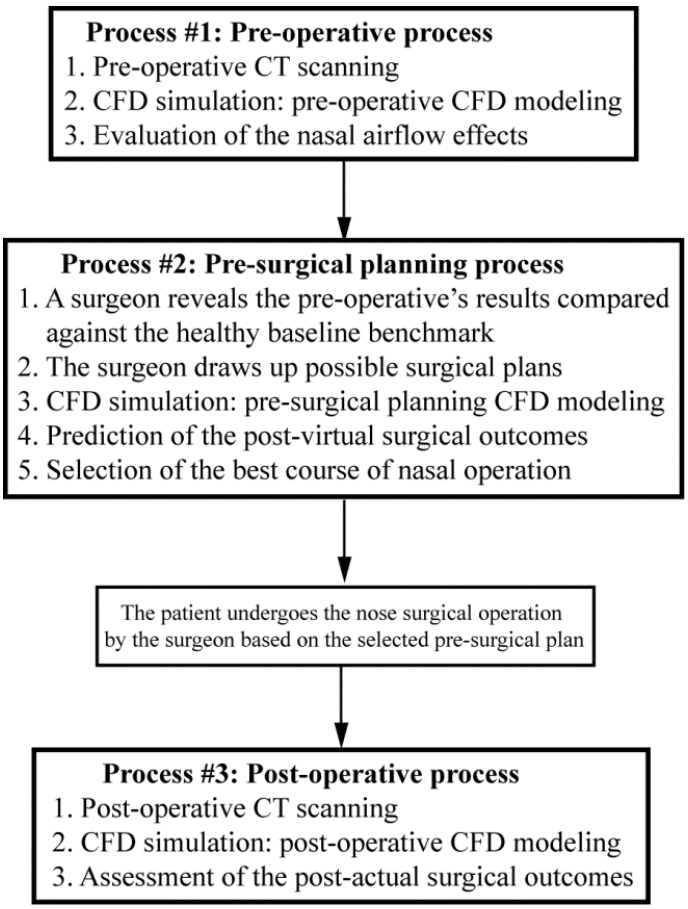

Fig. 4.1 The three-process CFD-CT aided surgery approach.

First, the pre-operative process aims to investigate the effects of septal deviation on nasal airflow. Second, the pre-surgical planning process purposes to demonstrate the effect of individual components of nasal airway surgery designed by

a surgeon; and to predict the post-virtual-surgical outcomes. The best course of surgical operation will be selected to perform in an actual nasal surgical procedure. Finally, the post-operative process aims at investigating the aerodynamic changes induced by the nasal operation, then actual-post-operative outcomes were assessed.

Each process individually determined both nasal geometric data (i.e. septal deviation angle and cross-sectional area) and nasal airflow patterns (i.e. velocity magnitude, pressure drop, and R_N) using the CFD simulation method.

4.2 CFD simulation method

A six-step CFD simulation method (Fig. 4.2) is described as follows:

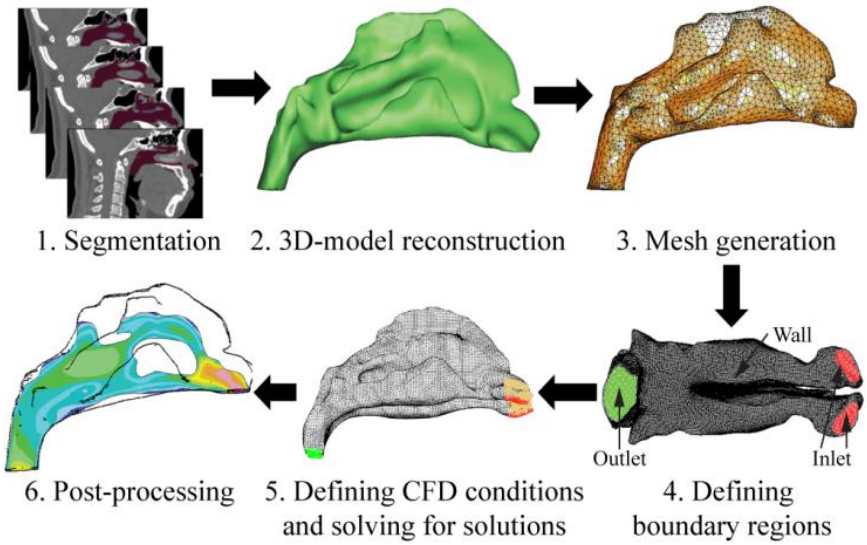

Fig. 4.2 The six-step CFD method.

4.2.1 Image Segmentation

Two-dimensional CT images containing nasal cavity, oral cavity, paranasal sinuses and skull bones are imported to the Mimics medical imaging program (Mimics, Materialise version 13.1, Ann Arbor, MI). The area of skull bones on the images is filtered out by setting the lower and upper thresholds at -1024 and -210 Hounsfield unit to retain the air regions of nasal cavity, oral cavity and paranasal sinuses. Then, the areas of paranasal sinuses and oral cavity are manually removed with the Mimics software's manual editing tools to keep only the nasal cavity for the next step (Fig. 4.3).

(a) Import CT data into the MIMIC software program. The program shows three windows of the CT cross-sections, i.e. coronal, sagittal, and axial views. CT cross-sections comprise of airways (i.e. PNS, nasal cavity, pharynx, oral cavity, surrounding air), bones, and soft tissues.

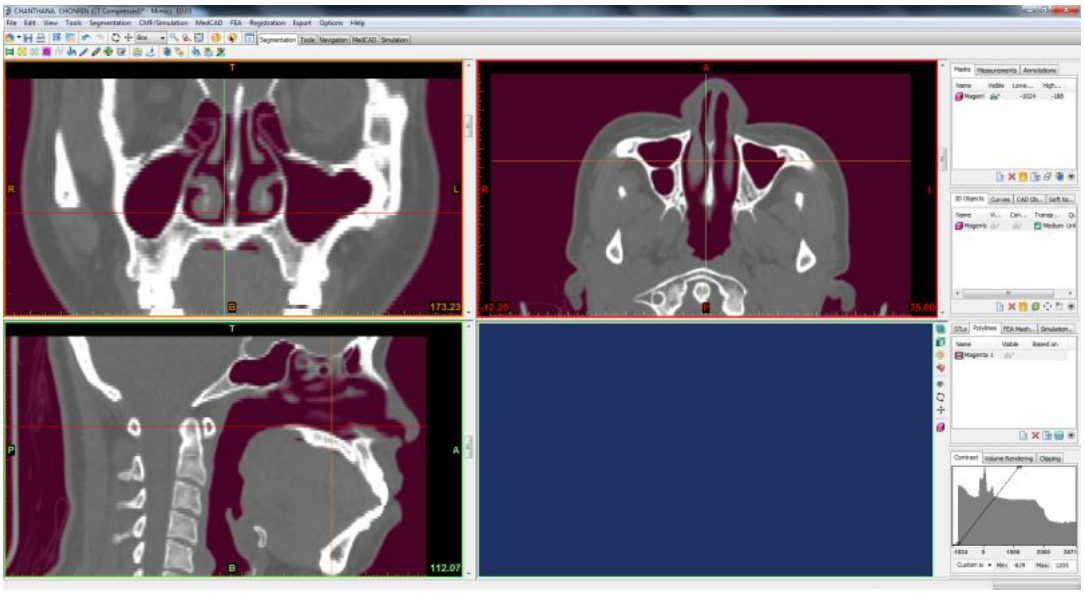

(b) Set up a thresholding intensity of air (−1024 to −210) to automatically separate the airway out from the bones and soft tissues. The purple areas depict the air.

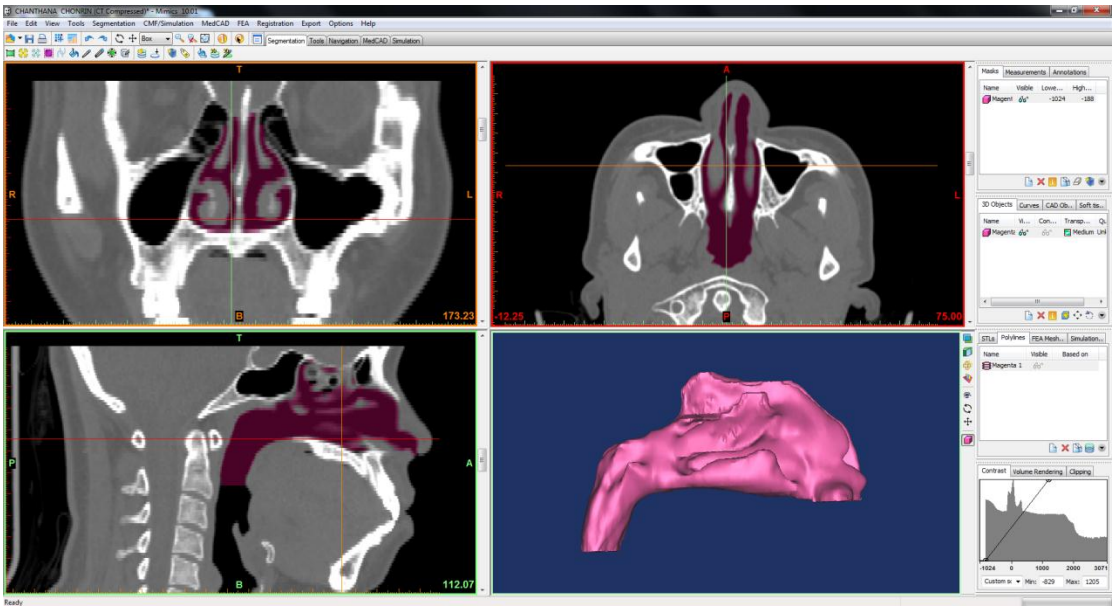

(c) Manual segmentation was performed to remove other air areas which do not need for the modeling, i.e. PNS, upper airway, and surrounding air. In this study, an inlet boundary was the nostrils and an outlet boundary was the end of nasopharynx.

Fig. 4.3 The segmentation processes using MIMIC software.

4.2.2 Three-Dimensional Model Reconstruction

The images containing only nasal cavity area of the previous step are used to generate 3D nose models. The surfaces of the 3D nose models are smoothed by the Laplacian method and exported in the stereolithography (STL) format for mesh generation (Fig. 4.4).

4.2.3 Mesh Generation

The 3D STL models are processed by the Pro-STAR Automated Meshing program (CD-Adapco, UK, version 3.24) to generate the trimmed-meshes with three boundary layers of prism cells. The mesh density study was performed and indicated that a mesh resolution of 1.6 million elements was fine sufficient to provide mesh-independent numerical results and to balance between the calculation accuracy and computational time. (Fig. 4.5).

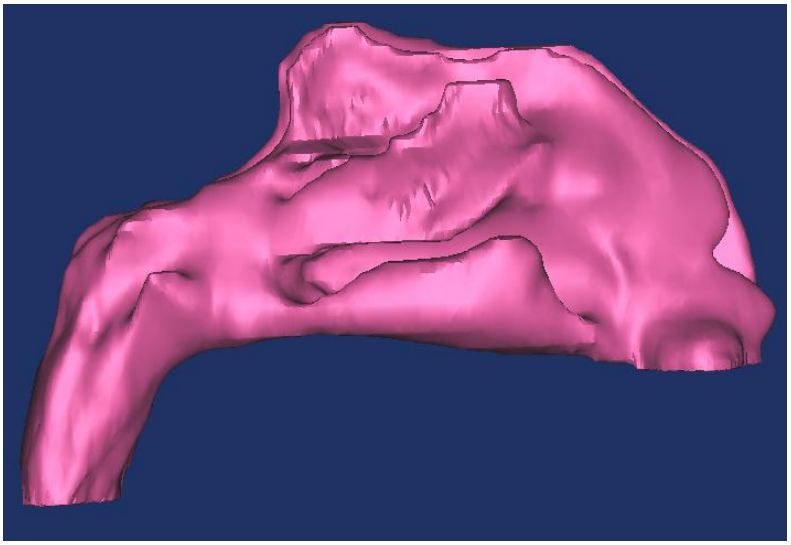

(a) Lateral view

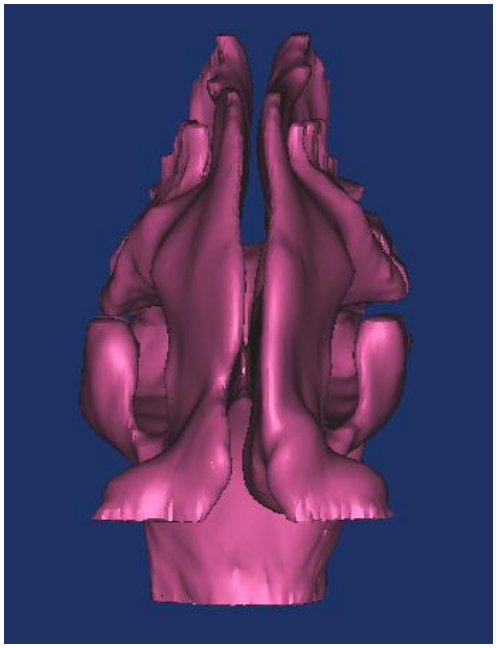

(b) Anterior view

Fig. 4.4 The 3D reconstructed and surface smoothed nose model.

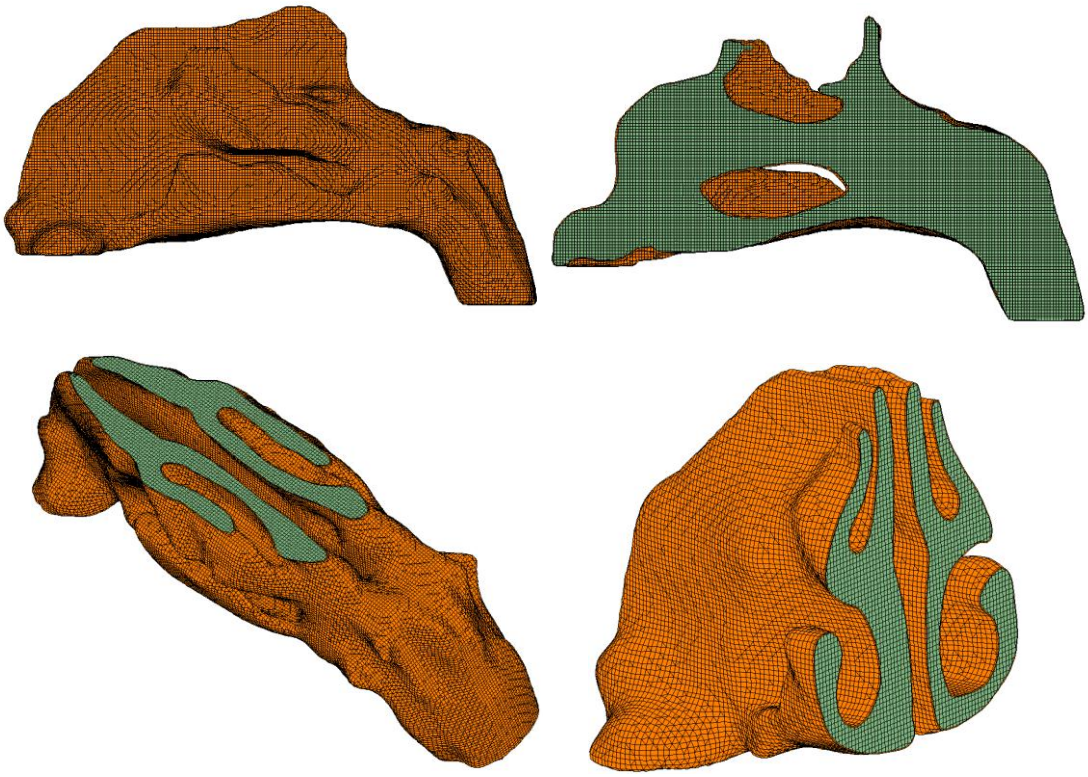

Fig. 4.5 The trimmed-meshes with three-boundary layers of the prism cells generated by Pro-STAR Automated Meshing software (CD-Adapco, UK, version 3.24).

4.2.4 Defining Boundary Regions

In this step, the nostrils and nasopharynx are defined as the airflow inlet and outlet, as shown in Fig. 4.6.

4.2.5 Defining Boundary and Simulation Conditions

The steady-state inspiratory airflow (i.e. time-dependent variable are held constant and all derivatives with respect to time were zero) is computed using the STAR-CD software version 3.24 (CD-Adapco, UK) [99], which uses the finite volume method to numerically solve the governing equations. A published experimental work [80] and several CFD studies [23, 83, 87, 100, 101] assumed that the nasal flow was laminar at rest. However, there exists no experimental report about the airflow patterns inside DNS patients' nasal cavity at rest. In this study, the calculated Reynolds numbers are in a range of 800-1000 in all nose models. Therefore, laminar

flow is conducted in both healthy and DNS noses. Several published DNS studies [26, 28, 31, 98] assumed laminar airflow in their CFD simulation. Although it is reasonable and necessary to implement a turbulent flow model for simulations with a large flow rate, such as 500 mL/s, as in [25], the airflow rate at rest is the sole focus of this study.

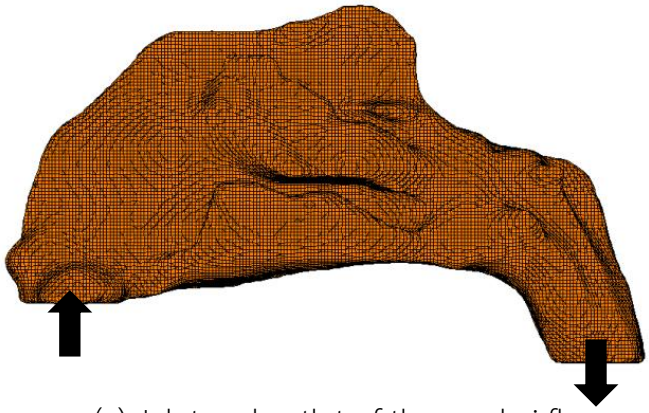

(a) Inlet and outlet of the nasal airflow

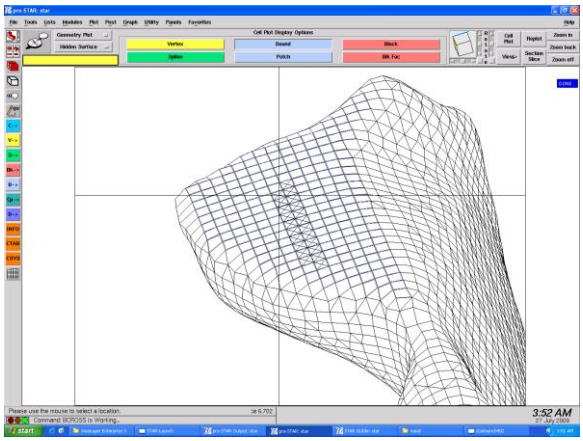

(b) Picked cell faces were manually selected by user to define boundaries.

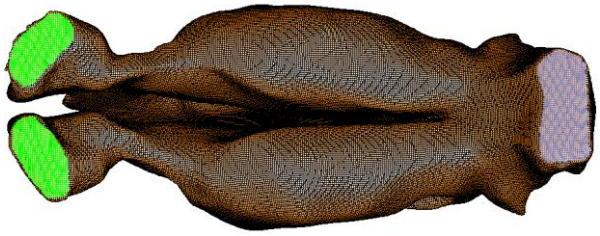

(c) Green areas depict the picked inlet boundaries (nostrils). Purple area depicts an outlet boundary (nasopharynx).

Fig. 4.6 Defining boundary regions in Pro-STAR software (CD-Adapco, UK, version 3.24).

This research assumes that air is incompressible and Newtonian with constant fluid properties. A velocity (u_i, m/s) and a pressure (p, Pa) of nasal airflow require solving the mass and momentum conservation equations (the Navier-Stokes equations) in a Cartesian tensor notation as follows [102]:

$$\frac{\partial \rho}{\partial t} + \frac{\partial (\rho u_j)}{\partial x_j} = S_m \tag{4.1}$$

$$\frac{\partial \rho u_i}{\partial t} + \frac{\partial (\rho u_j u_i - \tau_{ij})}{\partial x_j} = -\frac{\partial p}{\partial x_i} + S_i \tag{4.2}$$

where t is time, x_i is the Cartesian coordinate (i=*1, 2, 3*), u_i is the absolute fluid velocity component in direction x_i, $\boldsymbol{\rho}$ is the fluid density, p is the piezometric pressure, $\boldsymbol{T}_{ij}$ is the stress tensor components, s_m is the mass source, s_i is the momentum source components. The Semi-Implicit Method for Pressure-Linked Equation algorithm [103] is used to manage the pressure-velocity coupling; and discretization of the governing equations is conducted using the second-order Upwind scheme. Convergence of the numerical solutions is confirmed by small residuals of mass and momentum ($<10^{-3}$).

The inlet pressure at nostrils is set to the atmospheric pressure, and the outlet mass flow rate at nasopharynx is assumed fixed. The total volumetric flow (Q) through nasal cavity is 250 cm^3/s, which corresponds to breathing at rest [104]. The wall of nasal cavity is assumed to be rigid and in a non-slip condition (i.e. zero velocity). The average computational time per model is 3 hours on a 64-bit Sun Fire V40z server (two processors, 8 GB RAM) (Fig. 4.7).

4.2.6 Post-Processing and Data Plotting

At this stage, color contours of the calculated velocity magnitudes and pressure magnitudes were plotted (Fig. 4.8). Figure 4.9 shows locations of six coronal cross-sections (planes A to F) used to investigate velocity magnitude distribution of this and other studies [20, 23, 83, 105]. In addition, the nasal airflow patterns are determined by the measurements of velocity magnitude and pressure drop as a function of the distance from nostrils.

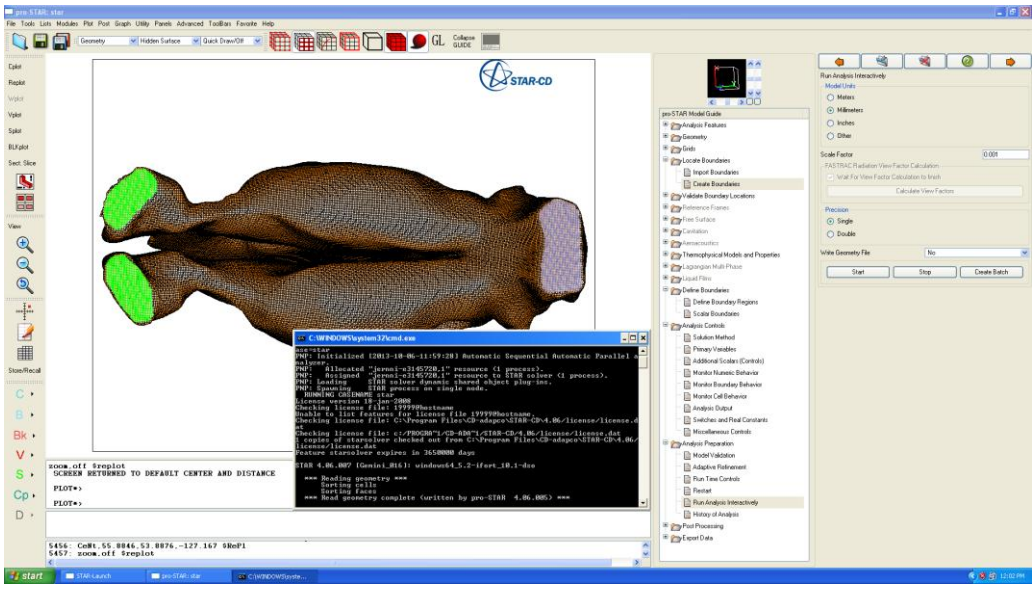

Fig. 4.7 Define boundary conditions, initial conditions, and solve problems in STAR-CD software (CD-Adapco, UK, version 3.24).

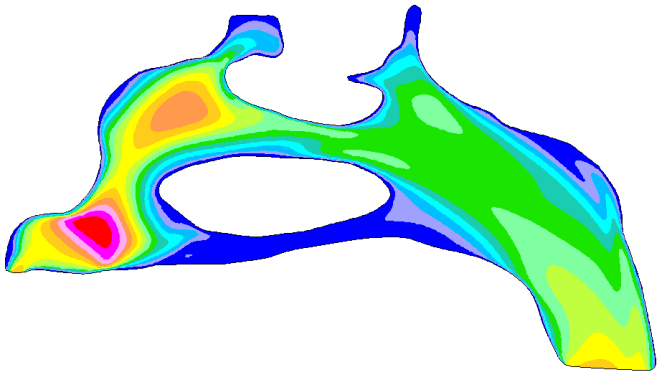

(a) Velocity magnitude contours

(b) Pressure contour

Fig. 4.8 CFD simulation results were plotted in post-processing process.

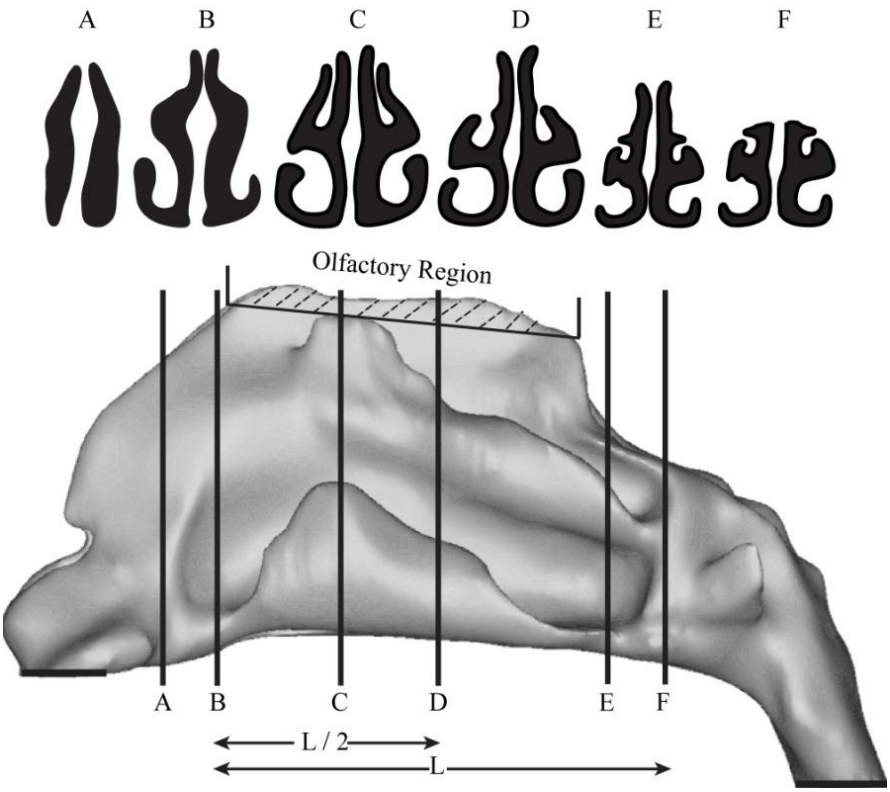

Fig. 4.9 The six coronal cross-sections. Plane A represents the nasal valve region and the narrowest cross-section. Plane B shows the main nasal passage front, which is the head of inferior turbinate. Plane C represents the head of middle turbinate while Plane D is the middle of nasal passage. Plane E is the front of superior turbinate and Plane F is the end of main nasal cavity before the merging of the left and right airways. L and L/2 are the lengths from Planes B to F and Planes B to D.

Nasal resistance (R_N), in Pa·s/cm^3, is calculated by:

$$R_N = \frac{\Delta P}{Q} \tag{4.3}$$

where ΔP is the maximum pressure drop (Pa) between nostrils and the non-dynamic posterior end of nasal septum [33, 98] and Q is an inspiratory flow rate of 250 cm^3/s.

4.3 Establishing the healthy baseline

The healthy baseline benchmark was created using the CT images of five healthy subjects. The five subjects must have a similar mucosal thickness and straight nasal septum nose. Furthermore, they have no history of sinusitis, lung diseases and nasal surgery. Their average age was 32.8±15.4 years. The CT images, produced by an Aquilion ONE^{TM} CT scanner (Toshiba Medical Systems Corporation), were provided by the Advanced Diagnostic Imaging Center (AIMC) of Thailand's Ramathibodi Hospital in Bangkok (Fig. 4.10). The image resolution is 512x512 pixels and the shift between a cross-sectional image and the subsequent image was 1 mm.

Nasal cross-sectional area was measured in the coronal CT image and plotted as a function of distance from nostrils. The 6-step CFD simulation (Fig. 4.2) was performed to determine the airflow conditions of the healthy noses (i.e. velocity magnitude, pressure drop, and R_N). The results of nasal cross-sectional area, velocity magnitude, pressure drop, and R_N were established as the healthy baseline benchmark of the research.

Fig. 4.10 CT images of the healthy noses were selected from the AIMC's PACS server.

4.4 Assessing the possibility of using the CFD-CT aided surgery approach

To evaluate whether the proposed CFD-CT approach had the potential to be a pre-surgical aiding tool that would enable surgeons to perform personalized virtual surgery (VS), a 22-year-old male patient (DNS patient #1) from the Otolaryngology Unit, HRH Princess Maha Chakri Sirindhorn Medical Center (MSMC), Faculty of Medicine, Srinakharinwirot University, Ongkarak, Nakornnayok, Thailand, who had suffered from leftward septal deviation and underwent conventional septoplasty and inferior turbinate reduction without using the CFD-CT aided surgery approach, was recruited in this preliminary study. The patient has given their consent, which has been approved by Thailand's Faculty of Medicine of Srinakharinwiroj University.

In the pre- and post-surgery, the NOSE scoring and rhinomanometry techniques were applied to the patient to determine the NOSE score and nasal resistance to flow. The rhinomanometer is of RhinoStream® SRE 2000 Interacoustics AS, Assens, Denmark and was used to measure nasal resistance (R'_N) at a 75 Pa pressure point.

Before and after surgery, a nasal airway of DNS patient #1 was scanned with a Siemens Somatom Volume Access CT scanner (Siemens AG, Erlargen, Germany). The CT image resolution was 512x512 pixels and the shift between one cross-sectional image and the subsequent image was 1 mm. Nasal geometric data of septal deviation angle and cross-sectional area were calculated. To calculate the angle of septal deviation, a line was drawn from the crista galli to the pre-maxilla (Line 1) and a second line was drawn from the crista galli to the most prominent point (Line 2); then the angle between the first and second lines was measured (Fig. 4.11) [56]. Maximum deviation angle was used for grading the degree of DNS as mild (<9°), moderate (9°-15°), and severe (15° and up) [106]. In addition, nasal cross-sectional area was measured in the coronal CT image and plotted as a function of distance from nostrils.

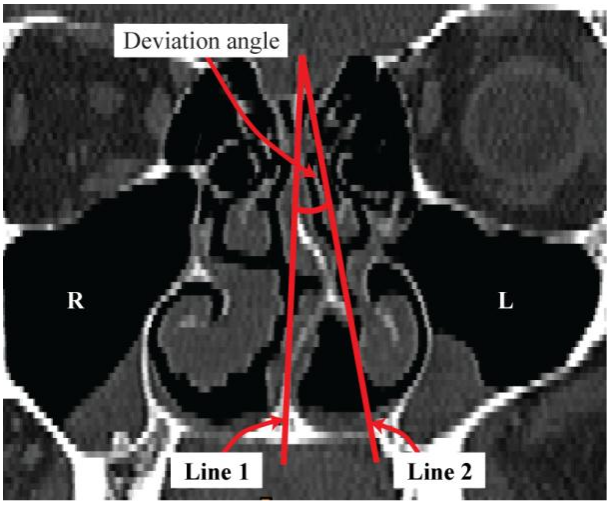

Fig. 4.11 Coronal paranasal sinus CT image demonstrating technique for measurement of the septal deviation angle. R and L are the right and left side of the nose.

Nasal airflow patterns (i.e. velocity magnitude, pressure drop, and R_N) were determined using the six-step CFD method (Fig. 4.2). Figure 4.12 (a) illustrates a segmented CT image of one of the five healthy noses, which is compared among those of the pre-operative DNS nose (Fig. 4.12 (b)) and post-operative DNS nose (Fig. 4.12 (c)). Dashed lines represent shapes of the septal cartilages.

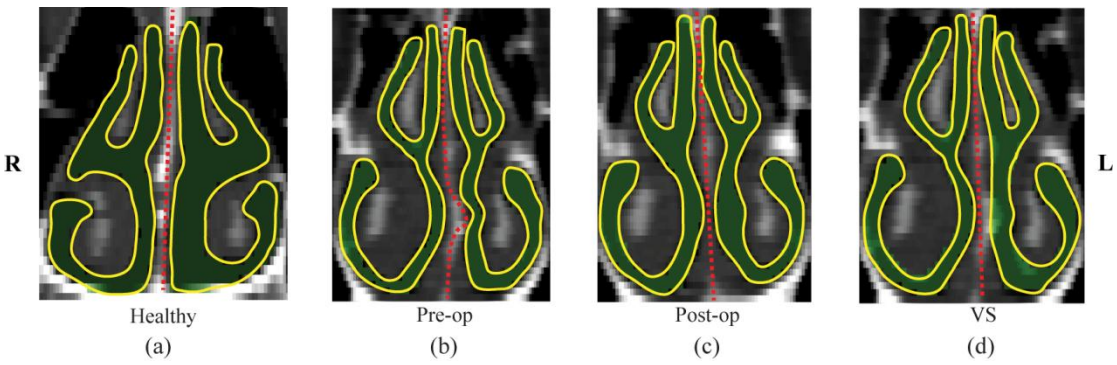

Fig. 4.12 The coronal cross-sectional CT images present the segmented nasal airway of the healthy nose (a) and DNS patient #1's pre-operative nose (b), post-operative nose underwent septoplasty and turbinate reduction (c), and virtual-surgery (VS) model based on septoplasty alone. Dashed lines represent shapes of the septal cartilages. R and L are the right and left side of noses.

4.4.1 The NOSE scores and rhinomanometric data of DNS patient #1

The pre-operative NOSE score was 40, implying that the DNS patient suffered from a moderate nasal obstruction [107]. The pre-operative R'_N was 0.2939 Pa·s/cm^3, which is 55% higher than the Asian adults' mean, at a 75 Pa pressure point, of 0.1900 Pa.s/cm^3 [108].

After conventional surgery by septoplasty and turbinate reduction (without using pre-surgical planning tool), the NOSE score was decreased to 2, equivalent to a 95% reduction, which means very mild problem with nasal obstruction detected after surgery [107]. However, the post-operative R'_N decreased to 0.2636 Pa.s/cm^3, equivalent to a reduction of 10%. Although, the post-operative NOSE score implied that the surgical treatment was satisfying to the patient, the 10% reduction of nasal resistance to flow after treatment was not acceptable to the surgeon.

4.4.2 The nasal geometric data of DNS patient #1

The maximum leftward septal deviation angle was 14.1°, which was observed at 4.75 cm from nostrils of the pre-operative DNS nose, while the nasal septum was straight and divided the nasal cavity into generally symmetrically left and right sides of the healthy baseline's noses (Fig. 4.12 (a)). According to the maximum deviation angle of 14.1°, the patient was classified as moderate DNS [106]. The pre-operative minimal cross-sectional area (MCA_{pre}) was 0.98 cm^2 observed at the right nasal valve region (i.e. 2.80 cm from nostrils) (Fig. 4.13 (a)).

After surgery, no deviated septum remained in the DNS patient #1's nose due to the septoplasty (Fig. 4.12 (c)); and the nasal cross-sectional area became wider than the pre-operative's cross-sectional area on both sides of nasal airway (Fig. 4.13). However, the post-operative cross-sectional area on the right side of the nose (Fig. 4.13 (a)) was much larger than the right cross-sectional area of the healthy baseline (solid line with error bars each indicating 1 standard deviation (SD)). The post-operative minimal cross-sectional area (MCA_{post}) on the right side was 1.78 cm^2, which is higher than the MCA_{pre}, equivalent to 82% (Fig. 4.13 (a)).

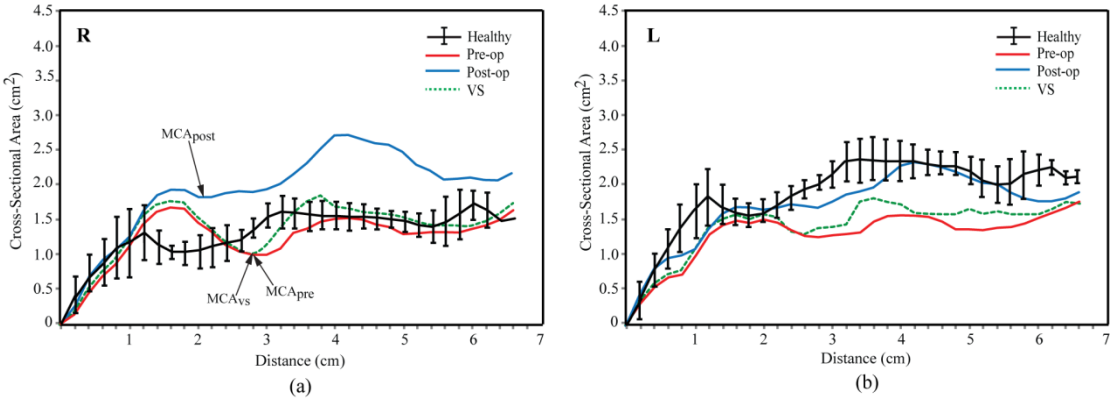

Fig. 4.13 Cross-sectional area of DNS patient #1 in comparison with the healthy baseline with 1 SD represented by an error bar. R (a) and L (b) are the right and left side of noses.

4.4.3 The nasal airflow patterns of DNS patient #1

Before surgery, the incoming air was not well balanced between the two sides of the DNS nose (Fig. 4.14 (a)), while the airflow distributions in all six coronal cross-sections of both sides of healthy noses were almost identical (Fig. 4.15). High velocity magnitudes ran along planes A, B, C, and D (i.e. from the nasal valve to half of the main nasal passage) of the DNS nose (Fig. 4.14 (a)), while an incoming air accelerated due to the narrowing of the nasal valve region and gradually decelerated in the main nasal cavity of the healthy baseline's noses (Fig. 4.15). The high velocity magnitudes were observed along the left (convex) side of DNS patient #1's nose, which was the constricted side due to DNS (Fig. 4.14 (a)). The maximum velocity magnitude of the pre-operative nasal cavity ($Vmax_{pre}$) was 2.61 m/s, which was observed in the main nasal passage at 3.6 cm from nostrils, while the maximum velocity magnitude of the healthy nose ($Vmax_{H}$) was 2.73±0.19 m/s, which was observed at the nasal valve region (1.60-2.20 cm from nostrils) (Fig. 4.16 (a)).

In addition, the DNS induces an increase in pressure drops on the entire nasal cavity; and was in a range of 6.05-7.20 Pa, while the increase in pressure drop was observed in the nasal valve region of the healthy noses and stabilized at 4.45-5.05 Pa (Fig. 4.16 (b)). The maximum pressure drop (ΔP) of the pre-operative nasal cavity (ΔP_{pre}) was 7.20 Pa, which was observed in the main nasal passage where

the $Vmax_{pre}$ existed, while the ΔP_H was 5.96±1.17 Pa (Fig. 4.16 (b)) observed in the nasal valve region. The pre-operative R_N was 0.0288 Pa.s/cm^3, which is 21% higher than the mean of healthy baseline's R_N (i.e. 0.0238±0.0047 Pa.s/cm^3).

After surgery, more balanced nasal airflow distribution between the two sides was presented in Fig. 4.14 (b). However, the post-operative velocity magnitudes were greatly less than the healthy baseline's in almost all nose planes; and no acceleration of airflow in the nasal valve region was detected when compared with those of the healthy baseline (Fig. 4.16 (a)). Moreover, over-reduction of pressure drops was observed after treatment (Fig. 4.16 (b)). The maximum pressure drop of the post-operative DNS patient (ΔP_{post}) was reduced to 3.17 Pa, which is noticeably less than the ΔP_H (Fig. 4.16 (b)). The range of post-operative pressure drops in the main nasal passage was 2.60-3.10 Pa, while the range in the healthy baseline was 4.45-5.05 Pa (Fig. 4.16 (b)). The post-operative R_N was 0.0127 Pa.s/cm^3, which is a 56% reduction from the pre-operation and 7% less than the mean of healthy baseline' R_N.

We hypothesized that the post-operative velocity magnitude and pressure drop of the DNS patient could not be restored to the normal level of the healthy baseline as a result of the excessive tissue removal during the inferior turbinate reduction procedure. Virtual surgery (VS) using the CFD-CT method might be a useful tool to address where it was unclear whether septoplasty with turbinate reduction or septoplasty alone was the best option for surgical treatment this DNS patient. Thus, engineer supervised by the same surgeon drew up a surgical plan relying on the pre-operative CT data (Fig. 4.12 (b)) for formulating septoplasty without inferior turbinate reduction using the Mimics software (Fig. 4.12 (d)). The 6-step CFD simulation based on the post-virtual-airway regions (Fig. 4.12 (d)) was repeated to predict the post-virtual-operative outcomes in terms of the nasal geometric data (i.e. septal deviation angle and cross-sectional area) and the nasal airflow patterns (i.e. velocity magnitude, pressure drop, and R_N).

In the VS model, deviated septal cartilage was corrected and no deviation angle was observed. The minimal cross-sectional area of the VS model (MCA_{vs}) was not changed from the MCA_{pre} and observed at the nasal valve region (Fig. 4.13 (a)).

Beyond the nasal valve region, the nasal cross-sectional area was slightly wider than the pre-operative's cross-sectional area due to septoplasty without a turbinate reduction (Fig. 4.13 (a)). The incoming air was well balanced between the two sides (Fig. 4.14 (c)). High velocity magnitude of the incoming air ran along planes A and B, then it gradually decreased in the main nasal passage. This airflow pattern well closed to the healthy nose's (Fig. 4.15). Velocity magnitudes of the VS model were almost fully restored to the healthy baseline level (Fig. 4.16 (a)). The maximum velocity magnitude of the VS model ($Vmax_{vs}$) was 2.60 m/s, which was observed at the nasal valve region (Fig. 4.16 (a)). In addition, the pressure drops along the main nasal passage were in a range of 5.05-5.60 Pa, which closes to the range of the healthy baseline (4.45-5.05 Pa) (Fig. 4.16 (b)). The maximum pressure drop of the VS model (ΔP_{vs}) decreased from the ΔP_{pre} (i.e. 7.20 Pa) to 5.46 Pa, equivalent to 24% reduction (Fig. 4.16 (b)). The R_N of the VS model was reduced to 0.0218 Pa.s/cm^3, which is a 24% reduction from the pre-operative's R_N (i.e. 0.0288 Pa) and 8% less than the mean of healthy baseline's R_N (i.e. 0.0238±0.0047 Pa.s/cm^3).

The preliminary results presented that the VS using the CFD-CT technique was possible to be used as a pre-surgical planning tool, which might help surgeons to increase a treatment success. It was a motivation, which induced us to propose the three-process CFD-CT aided surgery approach (subsection 4.1). Implementation of the proposed approach in treating a DNS patient was the main goal of this research.

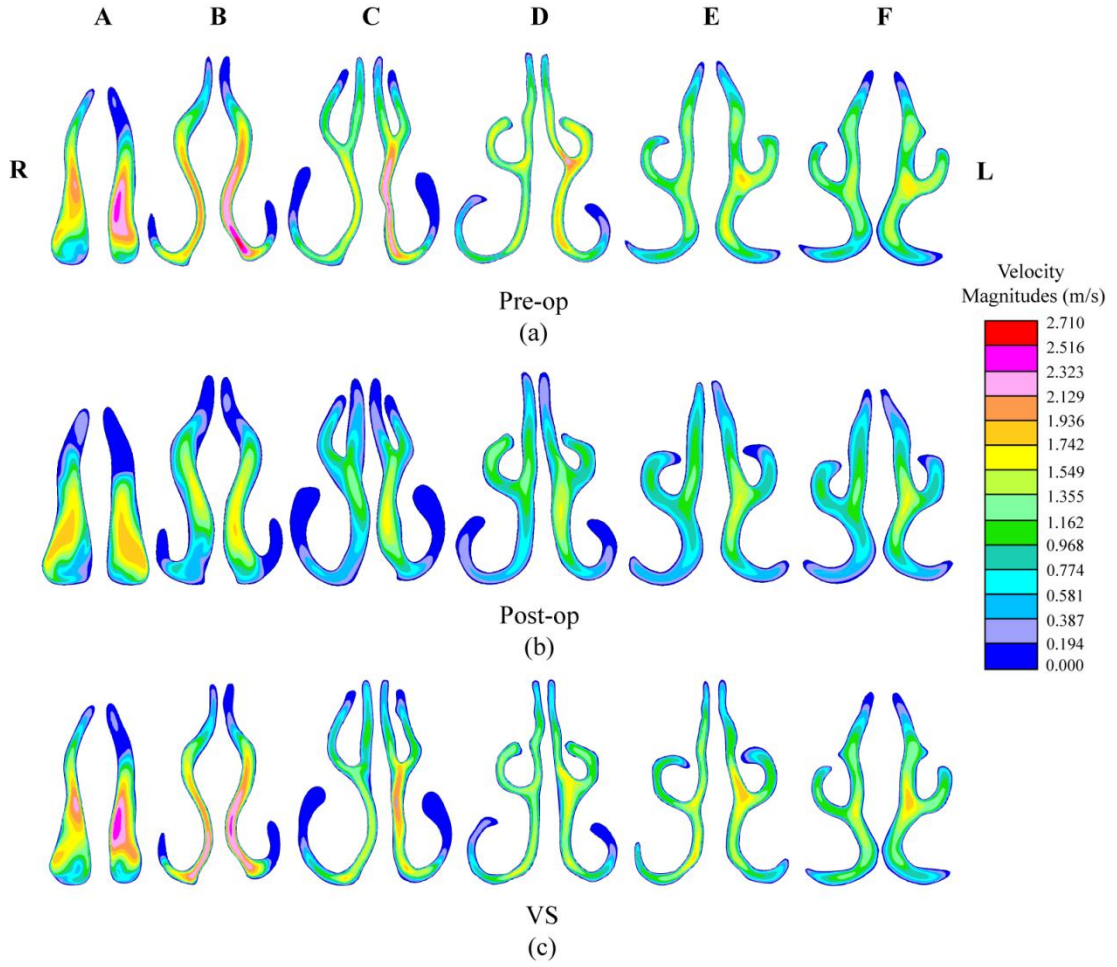

Fig. 4.14 The velocity magnitude distributions in the six coronal cross-sections (planes A to F) of DNS patient #1 in the pre-operative process (a), post-operative process (b), and virtual surgery modeling (c). R and L are the right and left sides of the noses.

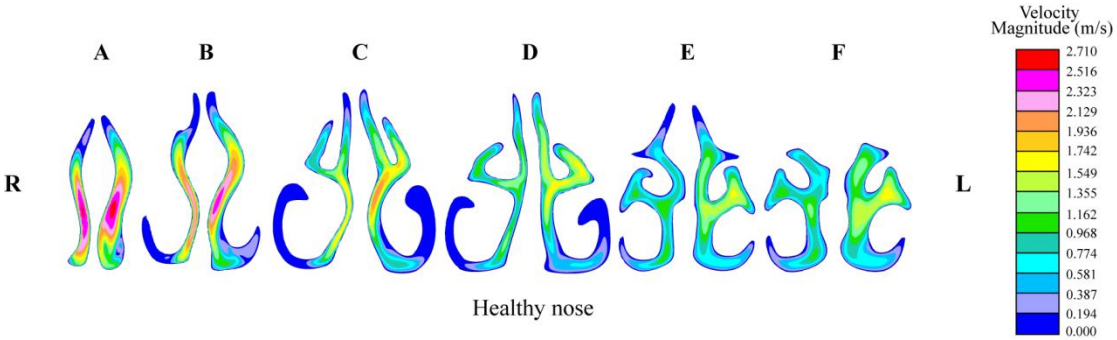

Fig. 4.15 The velocity magnitude distributions in the six coronal cross-sections (planes A to F) of one of the five healthy noses. R and L are the right and left sides of the noses.

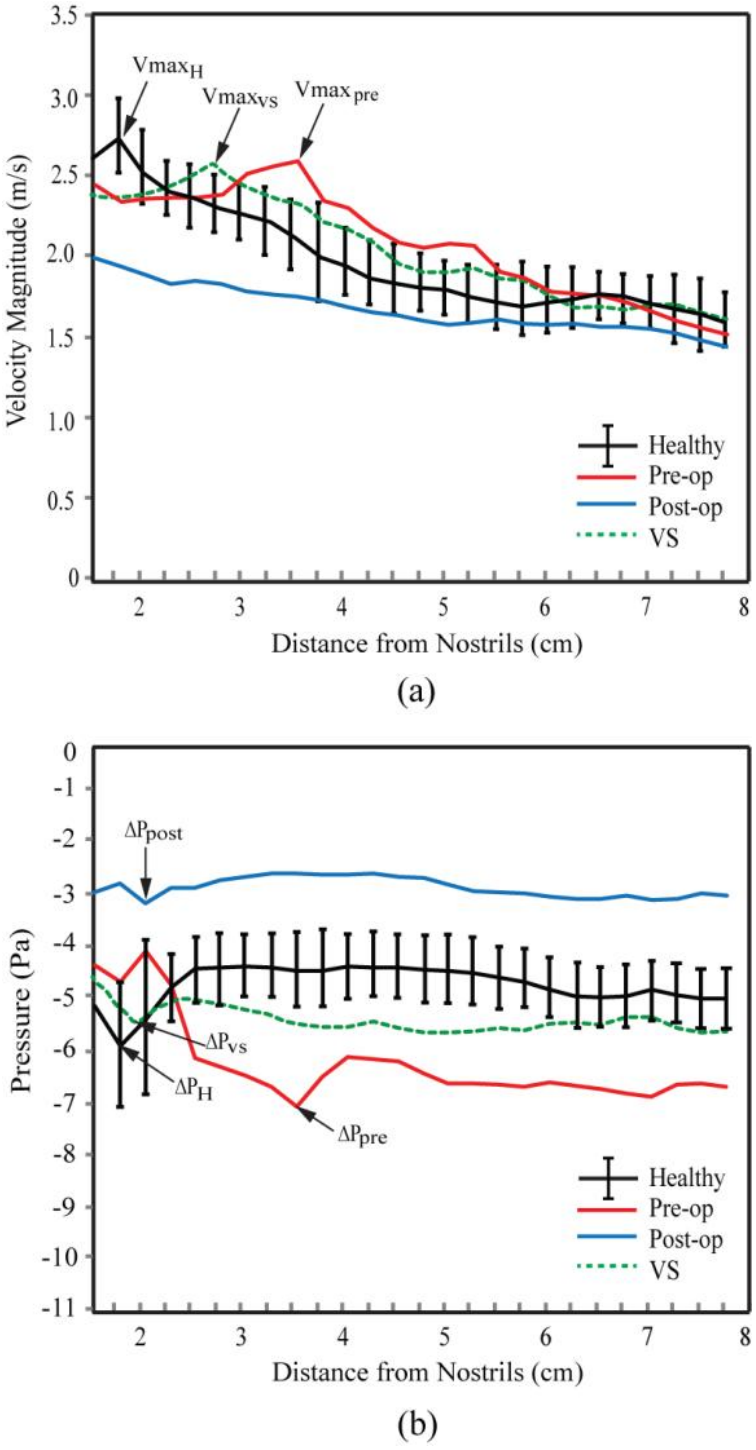

Fig. 4.16 Velocity magnitudes (a) and pressure drops (b) of DNS patient #1 in comparison with the healthy baseline with 1 SD represented by an error bar. Vmax and ΔP indicate maximum velocity magnitudes and maximum pressure drops.

Chapter 5
Implementation the CFD-CT Aided Surgery Approach and Post-Operative Results

5.1 Implementation of the CFD-CT aided surgery approach

5.1.1 Recruitment of DNS patient #2

This research recruited a 30-year-old male adult (DNS patient #2), who suffered from breathing difficulty and nosebleed but had no history of nasal surgery, from the same Otolaryngology Unit, HRH Princess Maha Chakri Sirindhorn Medical Center (MSMC), Faculty of Medicine, Srinakharinwirot University, Ongkarak, Nakornnayok, Thailand. The patient has given their consent, which has been approved by Thailand's Faculty of Medicine of Srinakharinwiroj University. In the pre-surgery, the NOSE scoring and rhinomanometry techniques were applied to the DNS patient to determine NOSE scores and nasal resistance (R'_N). The pre-operative NOSE score was 75, implying that the DNS patient suffered from a severe nasal obstruction [107]. The pre-operative R'_N was 0.3026 Pa.s/cm^3, which is 59% higher than the Asian adults' mean, at a 75 Pa pressure point, of 0.190 Pa.s/cm^3 [108].

5.1.2 The pre-operative process in DNS patient #2

The DNS patient's nose was scanned with a Siemens Somatom Volume Access CT scanner (Siemens AG, Erlargen, Germany). The image resolution is 512x512 pixels and the shift between a cross-sectional image and the subsequent image was 1 mm. Figure 5.1 (a) shows the segmented CT images of the DNS patient's nose prior to surgery, which was input of the CFD simulation. The 6-step CFD simulation (Fig. 4.2) was performed to investigate the pre-operative airflow conditions in terms of the nasal geometric data (i.e. septal deviation angle and cross-sectional area) and the nasal airflow patterns (i.e. velocity magnitude, pressure drop, and R_N).

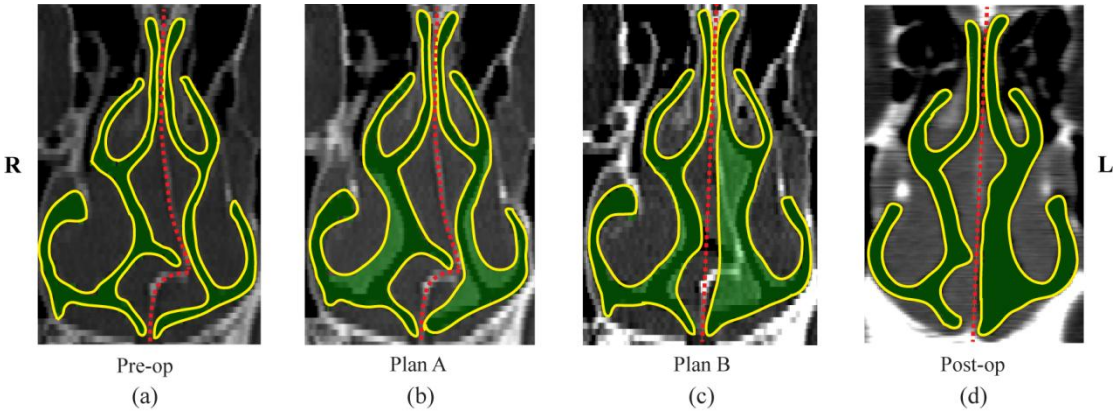

Fig. 5.1 The coronal cross-sectional CT images of DNS patient #2 present the segmented nasal airways of the pre-operative nose (a), pre-surgical planning A (b), pre-surgical planning B (c), and post-operative nose (d). Dashed lines represent shapes of the septal cartilages. R and L are the right and left sides of noses.

This process attempts to determine the impacts of DNS on both nasal geometry and nasal airflow patterns of the pre-operative patient's nose by comparing the pre-operative data against those of the healthy baseline benchmark. Pre-operative deviation angle was measured using coronal CT cross-sections. The maximum leftward septal deviation angle was 24.2° observed at 4.5 cm from nostrils, where the most septal collapse was found. According to the maximum deviation angle of 24.2°, the patient was classified as severe DNS [106]. Figure 5.2 presents the nasal cross-sectional area of the DNS patient's nose compared against the healthy baseline's. The cross-sectional area on the right side (Fig. 5.2 (a)) was generally greater than those of the healthy baseline, while the cross-sectional area on the constricted left side was drastically less than the healthy baseline's due to the septum collapse (Fig. 5.2 (b)). The minimal cross-sectional area of the pre-operative nasal cavity (MCA_{pre}) was 0.83 cm^2 observed at the left nasal valve region (2.6 cm from nostrils) due to the nasal valve collapse in this patient (Fig. 5.2 (b)).

Figure 5.3 (a) illustrates an airflow distribution throughout the DNS patient's nose before surgery. Unlike the healthy nose (Fig. 4.15), the incoming air was not well balanced between sides (Fig. 5.3 (a)). High velocity magnitudes were observed along the right (concave) side of the nose, while nearly complete collapse of the left

(convex) side of the nasal cavity allowed only a small amount of air to pass through the main nasal passage (Fig. 5.3 (a)). Velocity magnitudes were generally greater than those of the healthy baseline's noses (Fig. 5.4 (a)). The maximum velocity magnitude of the pre-operative DNS patient's nose ($Vmax_{pre}$) was 3.13 m/s observed at the nasal valve, which is 15% higher than the $Vmax_{H}$, of 2.73±0.19 m/s (Fig. 5.4 (a)).

Moreover, a severe DNS induces an abrupt pressure drop in the DNS nasal cavity. The maximum pressure drop of the pre-operative DNS nasal cavity (ΔP_{pre}) was 7.95 Pa observed at the nasal valve, which is 33% higher than the ΔP_{H}, of 5.96±1.17 Pa (Fig. 5.4 (b)). The pressure drops along the main nasal passage were in a range of 6.95-7.95 Pa, which is greater than the healthy baseline's (4.45±5.05 Pa). The pre-operative R_N was 0.0318 Pa.s/cm^3, which is 34% higher than the mean of healthy baseline's R_N (i.e. 0.0238±0.0047 Pa.s/cm^3).

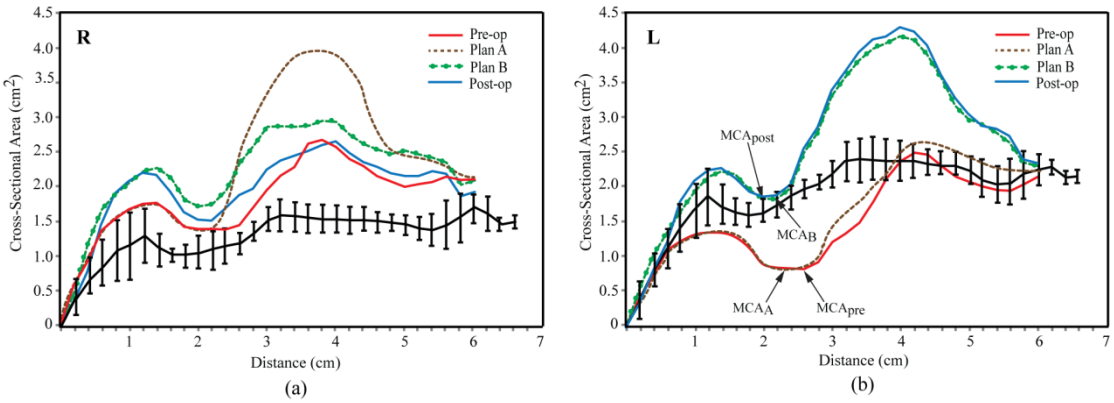

Fig. 5.2 Cross-sectional area of DNS patient #2 in comparison with the healthy baseline with 1 SD represented by an error bar. Dashed lines present nasal cross-sectional areas of the pre-surgical planning A and B. R (a) and L (b) are the right and left sides of the noses.

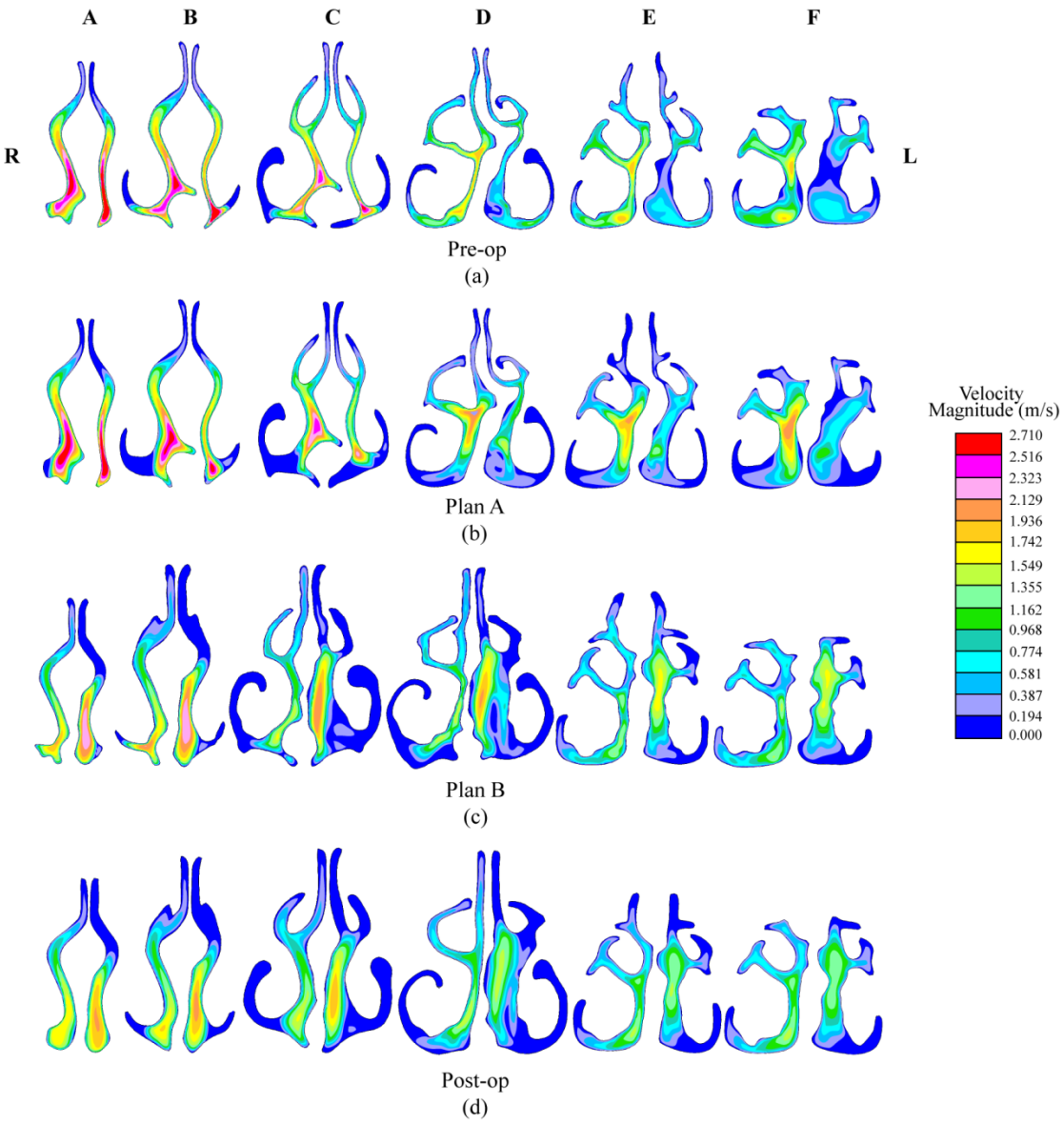

Fig. 5.3 The velocity magnitude distributions in the six coronal cross-sections (planes A to F) of DNS patient #2 in the pre-operative process (a), pre-surgical planning A (b), pre-surgical planning B (c), and post-operative process (d). R and L are the right and left sides of the noses.

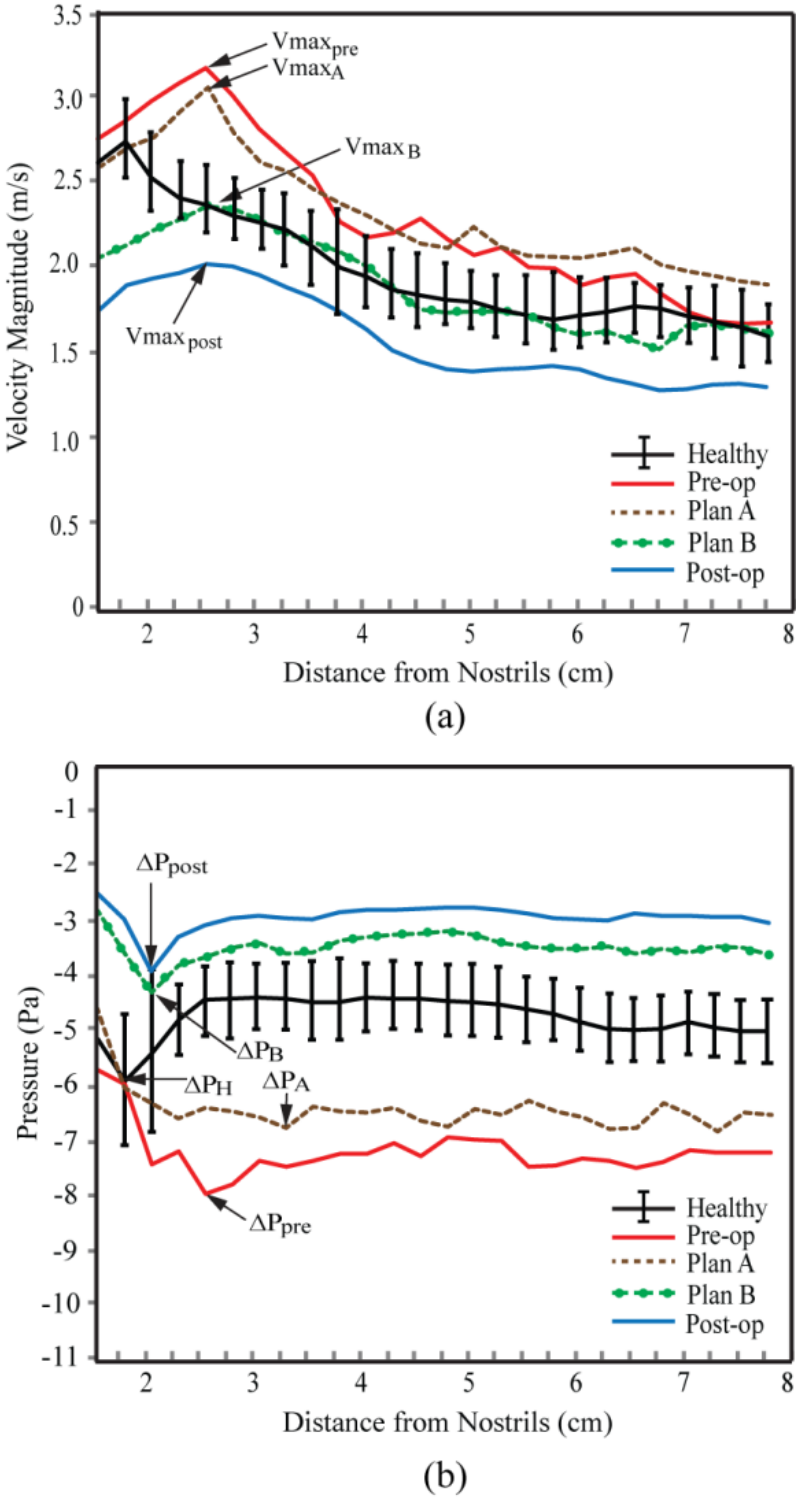

Fig. 5.4 Velocity magnitudes (a) and pressure drops (b) of DNS patient #2 in comparison with the healthy baseline with 1 SD represented by an error bar. R and L are the right and left sides of the noses. Vmax and ΔP indicate maximum velocity magnitudes and maximum pressure drops.

5.1.3 The pre-surgical planning process in DNS patient #2

Prior to surgery of the DNS patient, the pre-operative model was altered to generate two virtual surgery models, i.e. turbinate reduction alone (Plan A) and septoplasty and partially turbinate reduction (Plan B). An engineer supervised by the same surgeon drew up a pre-surgical plans (Figs 5.1 (b and c)) relying on the CT data from the pre-operative process (Fig. 5.1 (a)) using the Mimics software. The 6-step CFD simulation based on post-virtual-airway regions (Figs 5.1 (b and c)) was repeated to predict the post-virtual-operative outcomes in terms of the nasal geometric data (i.e. septal deviation angle and cross-sectional area) and the nasal airflow patterns (i.e. velocity magnitude, pressure drop, and R_N). The post-virtual-operative outcomes of both pre-surgical plans (A and B) were compared among the pre-operative conditions and the healthy baseline benchmark for selection the best course of operation.

A) Plan A

The DNS surgery based on Plan A aimed to restore the nasal airflow pattern by widening the nasal airway alone. Straightening of the septum to reduce septal deviation angle was ignored (i.e. no septoplasty). The nasal airway widening would be achieved by a resection of one-third of inferior turbinates on both sides. In the post-virtual-operative outcomes, the minimal cross-sectional area of the nose in Plan A (MCA_A) was not changed from the MCA_{pre}. However, the right nasal cross-sectional area was much wider than the pre-operative's and healthy baseline's cross-sectional areas, while the left nasal cross-sectional area was slightly wider than the pre-operative's (Fig. 5.2).

Although resection of one-third of inferior turbinates on both sides of the nose led to widening of the nasal cross-sectional area, particularly on the right side (Fig. 5.2 (a)), the nasal airflow distribution was not noticeably improved (Fig. 5.3 (b)), when compared with the pre-operative airflow distribution (Fig. 5.3 (a)). The maximum velocity magnitude of the nose in Plan A ($Vmax_A$) was 3.03 m/s, which is slightly less than in the pre-operative stage of the patient ($Vmax_{pre}$= 3.13 m/s), a reduction of 3% (Fig. 5.4 (a)). We observed an unremarkable reduction of velocity

magnitudes, when compared with those in the pre-operative stage (Fig. 5.4 (a)).

In addition, the maximum pressure drop of the nose in Plan A (ΔP_A) was 6.77 Pa, which is lower than in the pre-operative stage of the patient (ΔP_{pre}= 7.95 Pa), a reduction of 15% (Fig. 5.4 (b)). The pressure drops in the main nasal passage were in a range of 6.15-6.77 Pa, while those of the healthy baseline were at 4.45-5.05 Pa. Predicted post-virtual operative R_N was 0.0271 Pa.s/cm^3, a reduction of 15% from the pre-operative R_N. However, the R_N of 0.0271 Pa.s/cm^3 is greater than the mean of healthy baseline's R_N (i.e. 0.0238±0.0047 Pa.s/cm^3), equivalent to a 14% increase.

B) Plan B

The DNS surgical correction based on Plan B aimed to restore the nasal septum and nasal airflow pattern by straightening the deviated septum and widening the nasal airway. The nasal airway widening would be achieved by a resection of one-fifth of middle and inferior turbinates. According to the surgeon, although the entire cross-sectional area modified in Plan B was noticeably larger than the healthy baseline's cross-sectional area (Fig. 5.2), the surgical procedure was still necessary to correct the septum deviation. The minimal cross-sectional area on the constricted left side was enlarged to 1.83 cm^2 (MCA_B), which is 55% higher than the MCA_{pre} (i.e. 0.83 cm^2); and 16% greater than the mean of healthy baseline's MCA on the same side of nose (i.e. 1.54±1.07 cm^2) (Fig. 5.2 (b)).

As seen in Fig. 5.3 (c), the pre-surgical planning produced airflow distribution that was more balanced between the two sides and broadly similar to the healthy baseline's distribution (Fig. 4.15). However, at the pre-operative stage, a very small quantity of air could enter this patient's left-side nose as a result of a severe DNS (Fig. 5.3 (a)). In Fig. 5.4 (a), maximum velocity magnitude at the stage of pre-surgical planning B ($Vmax_B$) was 2.34 m/s, which is a 25% reduction from $Vmax_{pre}$. Velocity magnitudes were in good agreement with the healthy baseline's (Fig. 5.4 (a)).

In addition, Fig. 5.4 (b) shows no abrupt pressure drop that was observed in the post-virtual-surgery outcomes. The maximum pressure drop observed at the nasal valve region was 4.32 Pa (ΔP_B), which is a 46% reduction from the ΔP_{pre}). The pressure drops in the main nasal passage stabilized at 3.20-4.32 Pa,

which were slightly less than the range of healthy baseline's (i.e. 4.45-5.05 Pa). Predicted post-virtual operative R_N was 0.0173 Pa.s/cm^3, a reduction of 46% from the pre-operation due to no abrupt pressure drops. However, the R_N of 0.0173 Pa.s/cm^3 was 16% less than the mean of healthy baseline's R_N.

5.1.4 The post-operative process in DNS patient #2

From the post-virtual-operative outcomes of Plan A and Plan B, it is evident that the surgical components of Plan B (septoplasty and one-fifth turbinate reduction) could restore the nasal airflow patterns closer to the healthy level than those of the Plan A (one-third turbinate reduction alone). Thus, Plan B was a more suitable course of surgical operation to address a successful outcome of DNS patient #2. Therefore, the surgeon concluded that Plan B would be used as a personalized surgical plan for this DNS patient.

The surgeon performed septoplasty and turbinate reduction to correct deformities of the nose based on the pre-surgical Plan B in DNS patient #2. After the DNS operation, the patient received similar intranasal post-operative care and no sign of complication was detected. In the post-operative outcome assessment, the NOSE scoring, rhinomanometry, CT scan (Fig. 5.1 (d)), and the 6-step CFD simulation were repeated on the same DNS patient. The follow-up study was carried out six months afterward. To minimize potential effects of nasal cycling on the CFD results, the DNS patient's CT data, which mucosal thickness was generally symmetrical in both pre- and post-surgical scans, was used in this study.

The surgical success was assessed by the post-operative outcomes with respect to the geometric data (i.e. septal deviation angle and cross-sectional area), the nasal airflow patterns (i.e. velocity magnitude, pressure drop, and R_N), the patient-reported symptom (i.e. NOSE score), and the rhinomanometry data (i.e. R'_N).

5.2 Post-operative results of DNS patient #2

The post-operative outcomes of the DNS patient #2 (i.e. NOSE scoring, R'_N, deviation angle, MCA, V_{max}, ΔP, and R_N) compared against those of the pre-operative conditions, pre-surgical plan B, and the healthy baseline benchmark presented in Table 5.1 and discussed below.

5.2.1 The post-operative NOSE scores and rhinomanometric data of DNS patient #2

The post-operative patient reported symptom (i.e. NOSE score) drastically decreased to 4 (from 75), equivalent to a 95% reduction, which means very mild problem with nasal obstruction detected after surgery [107]. In addition, the post-operative R'_N measured by rhinomanometer decreased to 0.194 Pa.s/cm^3 (from 0.3026 Pa.s/cm^3), equivalent to a reductions of 36%. The post-operative NOSE score and R'_N data implied that the surgical treatment was clinically acceptable to the surgeon and patient (Table 5.1).

Table 5.1 NOSE score, R'_N, maximum septal deviation angle, Vmax, ΔP, and R_N. Percentage differences between pre- and post-surgical treatment were calculated by: %Difference= [$Value_{post}$-$Value_{pre}$)/ $Value_{pre}$] x100 %

Studies	Evaluation	Pre-op	Planning	Post-op	Healthy baseline	%Difference
NOSE scoring	NOSE score	75	N/A	4	N/A	-95%
Rhinomanometry	R'_N (Pa·s/m^3)	0.3026	N/A	0.1941	N/A	-36%
CT	Max. deviation angle	24.2°	0°	< 4.38°	0°	-82%
	MCA (cm^2)	L=0.83	L=1.83	L=1.81	L=1.54±0.17 R=1.14±0.18	120%
CFD	Vmax (m/s)	3.13	2.34	2.03	2.73±0.19	-35%
	ΔP (Pa)	7.95	4.32	3.83	5.96±1.17	-52%
	R_N (Pa·s/m^3)	0.0318	0.0173	0.0153	0.0238±0.0047	-52%

5.2.2 The post-operative nasal geometric data of DNS patient #2

Surgeon designed septoplasty to restore the DNS (dashed line in Fig. 5.1 (a)) to the midline (dashed line in Fig. 5.1 (d)). Septal deviation angles were reduced in all coronal cross-sections of the nose. Maximum reduction of septal deviation angle (100%) was observed at the areas beyond the nasal valve region, while minimal reduction was in a range of 40%-58% found in the posterior portion of the nasal septum end. The overall deviation angles were less than 4.38° in all planes of the post-operative nose (Table 5.2).

Table 5.2 Percentage differences of septal deviation angles (degree) between pre- and post-surgical treatment.

Distance from nostrils (cm)	Deviation angle		%Difference	Distance from nostrils (cm)	Deviation angle		%Difference
	Pre-op	Post-op			Pre-op	Post-op	
2.1	4.31°	1.43°	67%	4.1	20.9°	1.52°	93%
2.2	5.22°	1.39°	73%	4.2	22.5°	1.48°	93%
2.3	5.84°	1.33°	77%	4.3	23.8°	1.55°	94%
2.4	6.94°	1.34°	81%	4.4	23.6°	1.70°	93%
2.5	6.78°	0°	100%	4.5	24.2°	1.90°	92%
2.6	6.91°	0°	100%	4.6	24.1°	2.17°	91%
2.7	6.48°	0°	100%	4.7	22.7°	2.29°	90%
2.8	7.08°	0°	100%	4.8	13.7°	1.88°	86%
2.9	7.58°	0°	100%	4.9	14.2°	2.08°	85%
3.0	7.78°	0°	100%	5.0	13.7°	2.46°	82%
3.1	8.50°	1.33°	84%	5.1	12.7°	1.83°	86%
3.2	9.01°	1.13°	87%	5.2	11.5°	2.52°	78%
3.3	9.67°	1.32°	86%	5.3	12.0°	1.86°	85%
3.4	10.0°	1.40°	86%	5.4	11.1°	2.18°	80%
3.5	11.4°	1.84°	84%	5.5	10.4°	1.49°	86%
3.6	11.9°	2.45°	79%	5.6	7.63°	4.44°	42%
3.7	12.7°	1.11°	91%	5.7	7.29°	4.38°	40%
3.8	14.6°	1.10°	92%	5.8	7.67°	4.09°	47%
3.9	16.0°	1.06°	93%	5.9	7.32°	4.27°	42%
4.0	17.7°	1.69°	90%	6.0	7.81°	3.80°	51%

After the surgery using the CFD-CT aided surgery approach, severe DNS was corrected. Small variability of post-operative cross-sectional areas from the pre-surgical planning was observed (Fig. 5.2). The minimal cross-sectional area of the post-operative nose (MCA_{post}) was 1.81 cm^2, while MCA_B was 1.83 cm^2. The MCA_{post} of 1.81 cm^2 is 120% higher than the MCA_{pre} (i.e. 0.83 cm^2) and 15% higher than the mean of healthy baseline's MCA (i.e. 1.54±0.17 cm^2) on the same side (Table 5.1).

5.2.3 The post-operative nasal airflow patterns of DNS patient #2

The airflow distribution was well balanced between sides and passed throughout the middle portion of both sides of the nose (Fig. 5.3 (d)), which was the same pattern as observed in the healthy nose (Fig. 4.15). In Fig. 5.4 (a), the post-operative maximum velocity magnitude ($Vmax_{post}$) was 2.03 m/s, which decreased from $Vmax_{pre}$, equivalent to a 35% reduction (Table 5.1). Although the overall velocity magnitudes after surgery was less than those of the healthy baseline, the pattern of post-operative velocity magnitudes reduction in the nasal cavity was generally similar to the healthy baseline's, i.e. the acceleration of air velocity magnitudes observed near the nasal valve region was found and the velocity magnitude gradually decreased beyond the nasal valve region (Fig. 5.4 (a)).

In addition, no abrupt pressure drop was found in the post-operative DNS patient's nose (Fig. 5.4 (b)). As shown in Fig. 5.4 (b), the maximum pressure drop in the nasal valve region (ΔP_{post}) was 3.83 Pa, which decreased from ΔP_{pre} (i.e. 7.95 Pa), equivalent to a 52% reduction, and is 36% less than ΔP_H (Table 5.1). The pressure drops stabilized at 2.80-3.18 Pa in the main nasal passage, while those of the healthy baseline were in a range of 4.45-5.05 Pa (Fig. 5.4 (b)). Post-operative R_N was 0.0153 Pa.s/cm^3, a decrease of 52% from the pre-operative's R_N (i.e. 0.0318 Pa.s/cm^3)), which is attributable to no post-operative abrupt pressure drops; and was 36% less than the mean of healthy baseline's R_N (i.e. 0.0238±0.0047 Pa.s/cm^3).

5.2.4 Assessment of the implementation of the CFD-CT aided surgery approach in DNS patient #2

As a result (Fig. 5.3 (d), Fig. 5.4, Tables 5.1 and 5.2), the surgery with the implementation of the CFD-CT approach could effectively and generally restore airflow patterns to the healthy baseline's with some variability from the predicted pre-surgical planning's outcomes.

Chapter 6
Discussion

This study used NOSE scores for evaluating the patient reported symptom of the pre- and post-operative DNS patients' noses. According to [33], they found that the CFD variables, e.g. airflow, wall shear stress, nasal resistance, or heat flux, stronger correlated with the NOSE survey than for those measured by other patient-self assessment, e.g. VAS scale.

In DNS patient #1, who underwent conventional surgery without adoption of the CFD-CT approach, the post-operative nasal cross-sectional area was excessively wider than the pre-operative nose, a phenomenon which led to variations of nasal airflow patterns. Virtual surgery reveals that only septoplasty (inducing a slightly enlargement of nasal airway compared with the pre-operative airway) could restore nasal airflow patterns to the healthy baseline benchmark. Although DNS patient #1's surgical outcome was relatively satisfying to the patient, assessing from the reduction of the NOSE score, the oversized bilateral cross-sectional area could induce water loss in nasal mucosa, giving rise to a worse crust formation and infection [97]. Consistent with [26, 29, 109], in case of moderate DNS, i.e. DNS patient #1, a surgical correction in the nasal anterior section was sufficient. According to [30], an over-widening airway does not always induce a normal airflow pattern; on the other hand, it might deteriorate R_N, heat transfer, olfactory perception. Also, the over-widening airway could increase the wall shear stress of the patient's nose. The conventional surgical method without CFD-CT pre-surgical planning could induce an excessive excision of airway, thus a water loss in nasal mucosa and a large airflow velocity reduction.

In DNS patient #2 who underwent surgery using the proposed CFD-CT aided surgery approach, the pre-operative sudden pressure drops were observed beyond the septum deviation areas. The sudden drops in pressure induced high pre-operative R_N and thus breathing difficulty. No high velocity magnitudes were

observed in the constricted convex (left) side beyond plane C since very small amounts of air could enter as a result of the septum collapse (Fig. 5.3 (a)). Rather, the high velocity magnitudes were found in the concave (right) side (Fig. 5.3 (a)). This observation confirms the notion that the region of constriction within a coronal cross-section would not increase the speed of flow through it provided that the flow deflected to a more open region. In addition, it is consistent with Liu et al [27], who reported that although the maximum velocity magnitude was normally found in the convex side of DNS (as observing in DNS patient #1), a larger velocity magnitude was sometimes observed in the concave (right) side of a DNS nose like that found in DNS patient #2. These discrepancies were due to the anatomical differences among individual subjects. Thus, evaluating patient-specific aerodynamic effects due to DNS using the CFD-CT approach is an essential technique, which can help surgeons to diagnose and treat a DNS effectively.

In the pre-surgical planning step, the approach enables the surgeon to localize DNS, specify the amount of nasal tissues to remove as well as predict the surgical outcomes. A prediction of most likely post-operative outcomes, e.g. post-virtual-airway regions, nasal cross-sectional area, and nasal airflow patterns could be made. The findings show that the CFD-CT approach can be applied to and is suitable for the pre-surgical planning of DNS noses. At this stage, the best course of nasal operation for DNS patient #2 (Plan B: septoplasty and one-fifth turbinate reduction) was identified using the CFD-CT approach. According to [30], who demonstrated the effects of individual components of three functional nasal airway surgery approaches, i.e. (1) excision of the head of the inferior turbinate, (2) resection of the lower fifth of the inferior turbinate, and (3) resection of almost the entire inferior turbinate, they found that the pressure decreased smoothly along the nasal cavities of the model (2), while the nasal resistance was deteriorated in both models (1) and (3). We agrees with [30] that excessive airway expansion due to nose surgery doses not always relieve the patient.

After the surgery with the CFD-CT aided surgery approach, the severe DNS of patient was corrected. The septal deviation angle of the post-operative nose was

reduced to less than 4.38° (82% reduction), which is implied that the nasal septum was almost restored to the normal shape. In addition, the constricted left side was wider due to the septoplasty and turbinate reduction performed in the surgical processes. The post-operative Vmax, ΔP, and R_N were decreased by 35%, 52%, and 52%, respectively, when compared with the pre-operative's (Table 5.1). Nonetheless, there were some small discrepancies between the post-virtual-operative outcomes and the post-actual-operative outcomes as a result of the random effects of post-treatment healing. Although the post-operative nasal airway of the DNS patient was noticeably larger than the healthy baseline's, the post-operative results were clinically acceptable to the surgeon as indicated by the 36% reductions in R'_N (nasal resistance measured by rhinomanometer); and satisfying to the DNS patient, as indicated by a 95% reduction in the clinical symptom score (NOSE score).

In the healthy baseline, half-nasal cross-sectional areas measured by the CT-based method correlated well with those of the other study [26]. For CFD modeling results, air evenly distributes throughout the middle meatus of the left and right sides of the nose, a fact which was also reported in Chen et al. [25], Croce et al. [88] and Wen et al. [24]. Furthermore, according to [83, 84], the smell sensory region receives the least amount of air. To validate the CFD modeling, velocity magnitudes of the healthy baseline of this research work were compared with those of the healthy noses of the existing research studies [20, 23, 83, 105] in the same coronal cross-sections (Table 6.1). A fitted linear regression was used to identify the relationship between velocity magnitudes and distances from nostrils among all healthy subjects. It was reported that velocity magnitudes decreased as a function of distance from nostrils in all studies. R^2 ranged from 0.85 to 0.98, except for that of the Keyhani (R^2=0.36) [83]. Although the velocity magnitudes of our healthy baseline were less than those of the previous studies, patterns of velocity magnitudes along the nasal cavities in our healthy baseline correlated well with those of the other studies. These discrepancies were probably due to the anatomical differences among individual subjects [88]. Differences of boundary and initial conditions assumed in the CFD simulations were possible causes of the variations.

Table 6.1 Velocity magnitudes of inspired airflow obtained from the healthy noses compare with the same results from existing literature [20, 23, 83, 105]. The values in parentheses represent the ranges of velocity magnitudes in each plane of our study.

Studies	Geometries	Q (L/min)	Velocity magnitudes (m/s)						Linear Eq.	R^2
			A	B	C	D	E	F		
Keyhani	Half-nasal	7.5	2.93	3.82	3.58	2.71	2.70	2.34	-0.23x+3.76	0.35
Jeong	Both sides	12	2.70	N/A	2.17	1.70	N/A	1.61	-0.27x+2.84	0.93
Subramaniam	Both sides	15	4.23	N/A	3.89	3.34	N/A	2.73	-0.44x+4.69	0.97
Ishikawa	Both sides	15	3.40	3.15	2.30	2.10	N/A	1.80	-0.43x+3.83	0.95
Present study	Both sides	15	2.32 (1.7-2.6)	2.21 (1.8-2.4)	1.96 (1.3-2.3)	1.79 (1.3-2.1)	1.67 (1.0-2.0)	1.78 (1.3-2.1)	-0.13x+2.40	0.85

R_N is calculated from the maximum pressure drop (ΔP) from nostrils to nasal septum end at a fixed flow rate (Q) of 250 cm^3/s (i.e. the CFD method). On the other hand, R'_N is determined by the rhinomanometry technique by measuring nasal resistance at a 75 Pa pressure point. In this study, R_N of the CFD modeling was less than R'_N due to the different definitions of nasal resistance between the two techniques as mentioned above; and could not be compared each other [26]. However, we fundamentally focused the amount of nasal resistance reduction as a result of the surgical treatment using CFD-CT approach.

This research contains the following limitations: first, the dynamic nature of nasal mucosa (nasal cycling) was ignored as the nasal wall was assumed fixed. Second, the effect of DNS on inspiratory flow was the sole focus of the research study. In fact, expiratory flow should have been taken into consideration in the pre-surgical planning, especially in patients with middle and posterior deviations. Expiratory airflow will be studied in our future work. Third, although DNS patients could mount-breathe to increase total airflow volume, this research disregards this fact. Fourth, the unsteady-state (time-dependent airflow) was not assumed in this study due to computational constraint. However, steady-state airflow was sufficient since we aimed to investigate effects of geometric changes on the nasal airflow patterns due to treatment using the CFD-CT aided surgery approach. In addition steady-state airflow was assumed in many other existing DNS studies [26, 28, 98].

Finally, the healthy baseline was established from five healthy subjects, so future research should recruit more healthy subjects.

Chapter 7
Conclusion and Suggestion

This study presents the CFD-CT approach for deviated nasal septum (DNS) surgical operation using the computational fluid dynamic (CFD) technique in combination with the computed tomography (CT) imaging technique, which is called the CFD-CT aided surgery approach. The CFD-CT aided surgery approach consists of three main processes of pre-operative process, pre-surgical planning process, and post-operative process. Thai healthy baseline benchmark was created as the basis for comparison of the approach (n=5).

This study is the first that proposes a comprehensive surgery-assisted approach that help the surgeon in formulating and selecting the best course of patient-specific DNS surgery with predictable post-operative outcomes. Furthermore, it is possible to apply the CFD-CT approach to surgery of other nose disorders, such as atrophic rhinitis, turbinate hypertrophy, nasal polyps, and septal perforation.

Future Works and Suggestions

1. Future research should recruit more healthy subjects for establishing the Thai healthy baseline benchmark.

2. The CFD-CT aided surgery approach should be applied to surgically correct other nasal deformities.

3. Unsteady-state airflow should be studied to simulate more realistic nasal airflow. However, increased performance workstation must be employed for this purpose.

4. Effects of DNS on an expiratory nasal airflow should be investigated particularly in patients with posterior septal deviation.

Appendix A

Nasal Obstruction and Septoplasty Effectiveness (NOSE) Scale

Nasal Obstruction and Septoplasty Effectiveness Scale

To the Patient: Please help us to better understand the impact of nasal obstruction on your quality of life by completing following survey. Thank you!

NAME (required) :_____**Date:**_____**(mm/dd/yy)**

Over the past *ONE* month, how much of a problem were the following conditions for you?

Please circle the most correct response

	***Not** a Problem*	*Very Mild Problem*	*Moderate problem*	*Fairly Bad Problem*	*Severe problem*
1. Nasal congestion or stuffiness	0	1	2	3	4
2. Nasal blockage or obstruction	0	1	2	3	4
3. Trouble breathing through my nose	0	1	2	3	4
4. Trouble sleeping	0	1	2	3	4
5. Unable to get enough air through my nose during exercise or exertion	0	1	2	3	4

Appendix B

Rhinomanometric Data of the DNS Patients

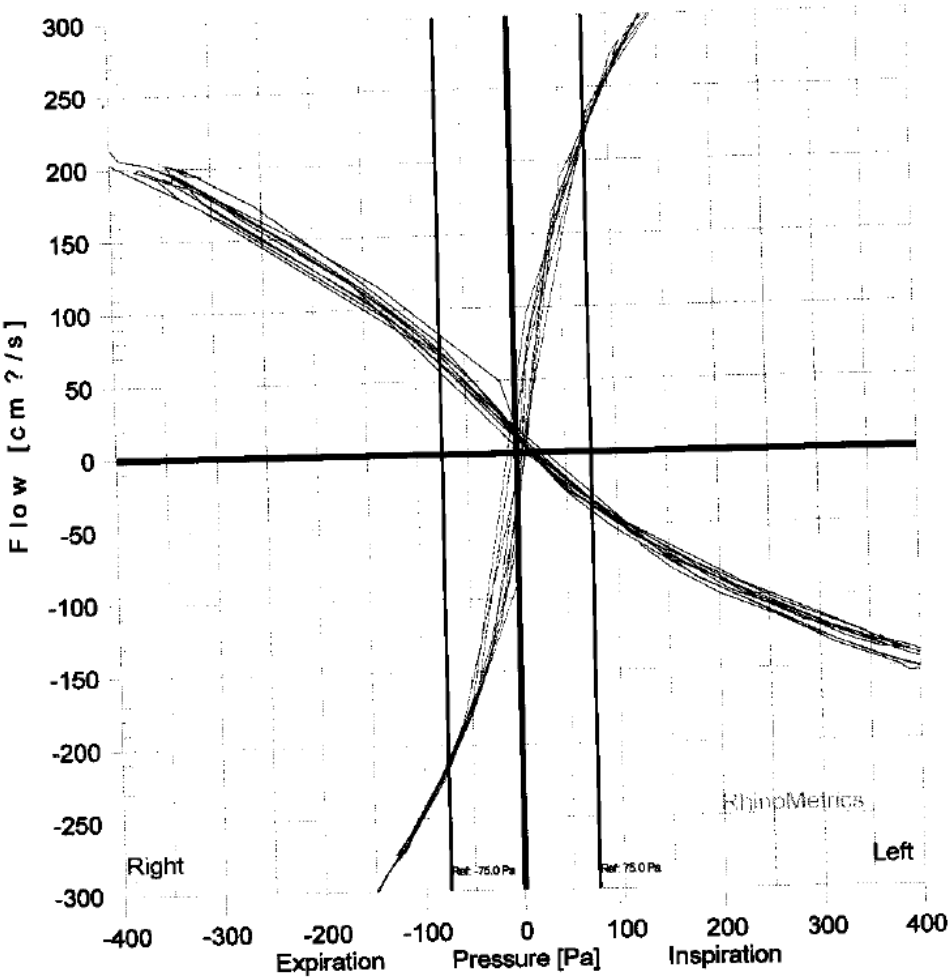

Side	Expiration		Inspiration	
	R'_N at 75 Pa ($Pa \cdot s/cm^3$)	Flow (cm^3/s)	R'_N at 75 Pa ($Pa \cdot s/cm^3$)	Flow (cm^3/s)
L (Obstructed)	1.12	67.22	2.17	34.63
R	0.35	213.12	0.34	219.31

The pre-operative nasal air flow (cm^3/s) and nasal resistance ($Pa \cdot s/cm^3$) of DNS patient #1

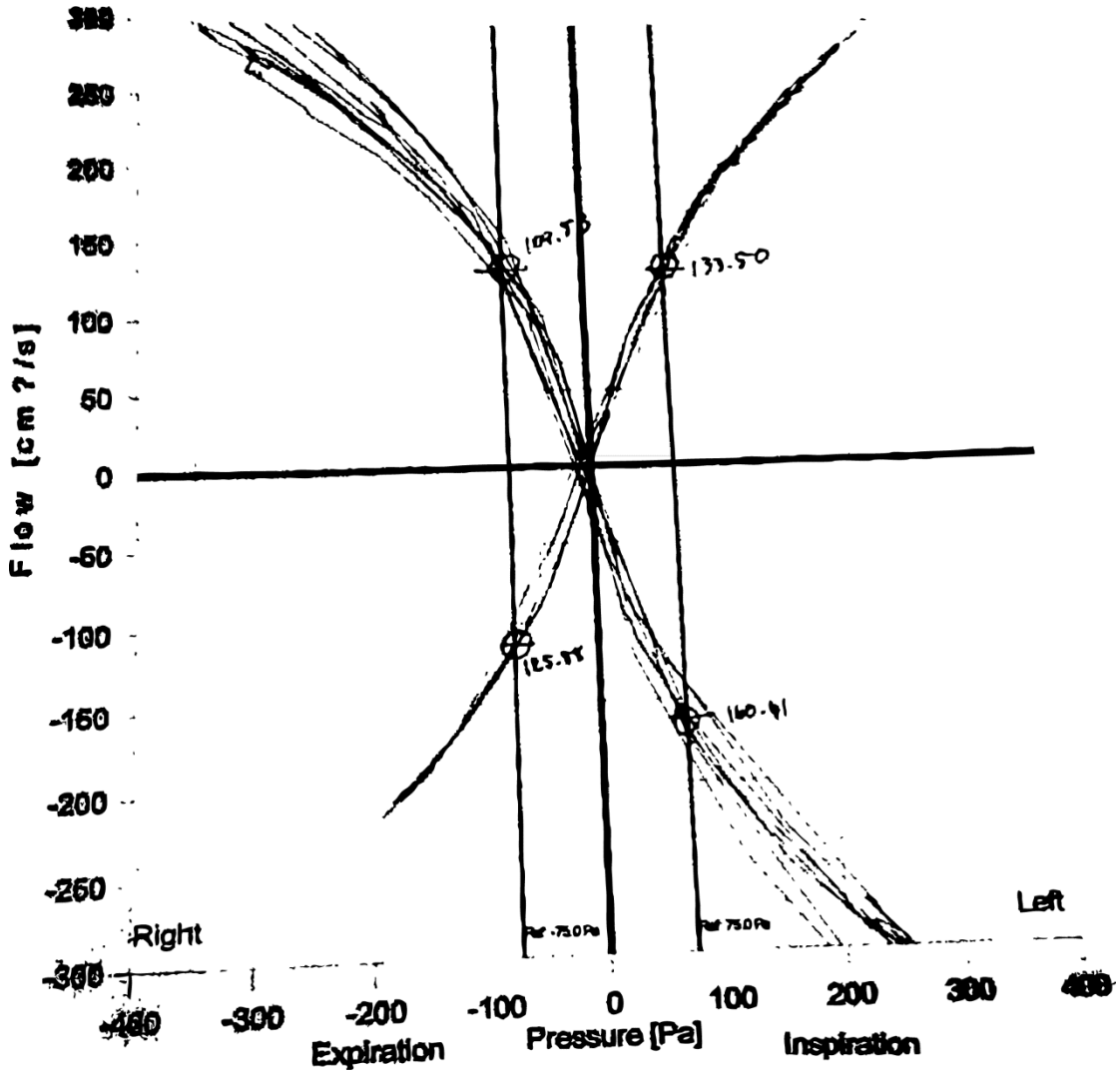

Side	Expiration		Inspiration	
	R'_N at 75 Pa ($Pa \cdot s/cm^3$)	Flow (cm^3/s)	R'_N at 75 Pa ($Pa \cdot s/cm^3$)	Flow (cm^3/s)
L (Obstructed)	0.56	133.50	0.47	160.41
R	0.68	109.53	0.60	125.88

The post-operative nasal air flow (cm^3/s) and nasal resistance ($Pa \cdot s/cm^3$) of DNS patient #1

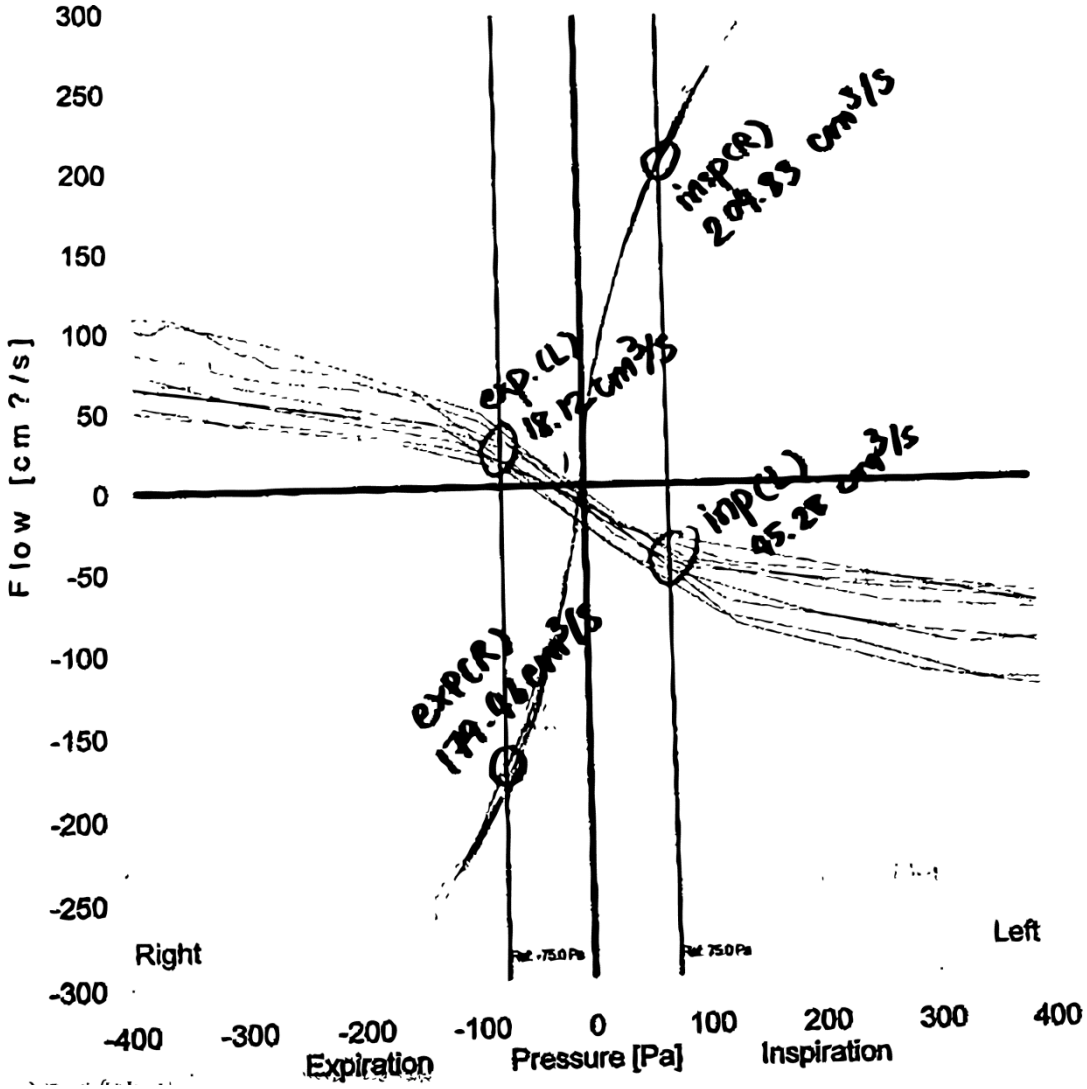

Side	Expiration		Inspiration	
	R'_N at 75 Pa ($Pa \cdot s/cm^3$)	Flow (cm^3/s)	R'_N at 75 Pa ($Pa \cdot s/cm^3$)	Flow (cm^3/s)
L (Obstructed)	4.14	18.12	1.66	45.28
R	0.42	179.46	0.37	204.83

The pre-operative nasal air flow (cm^3/s) and nasal resistance ($Pa \cdot s/cm^3$) of DNS patient #2

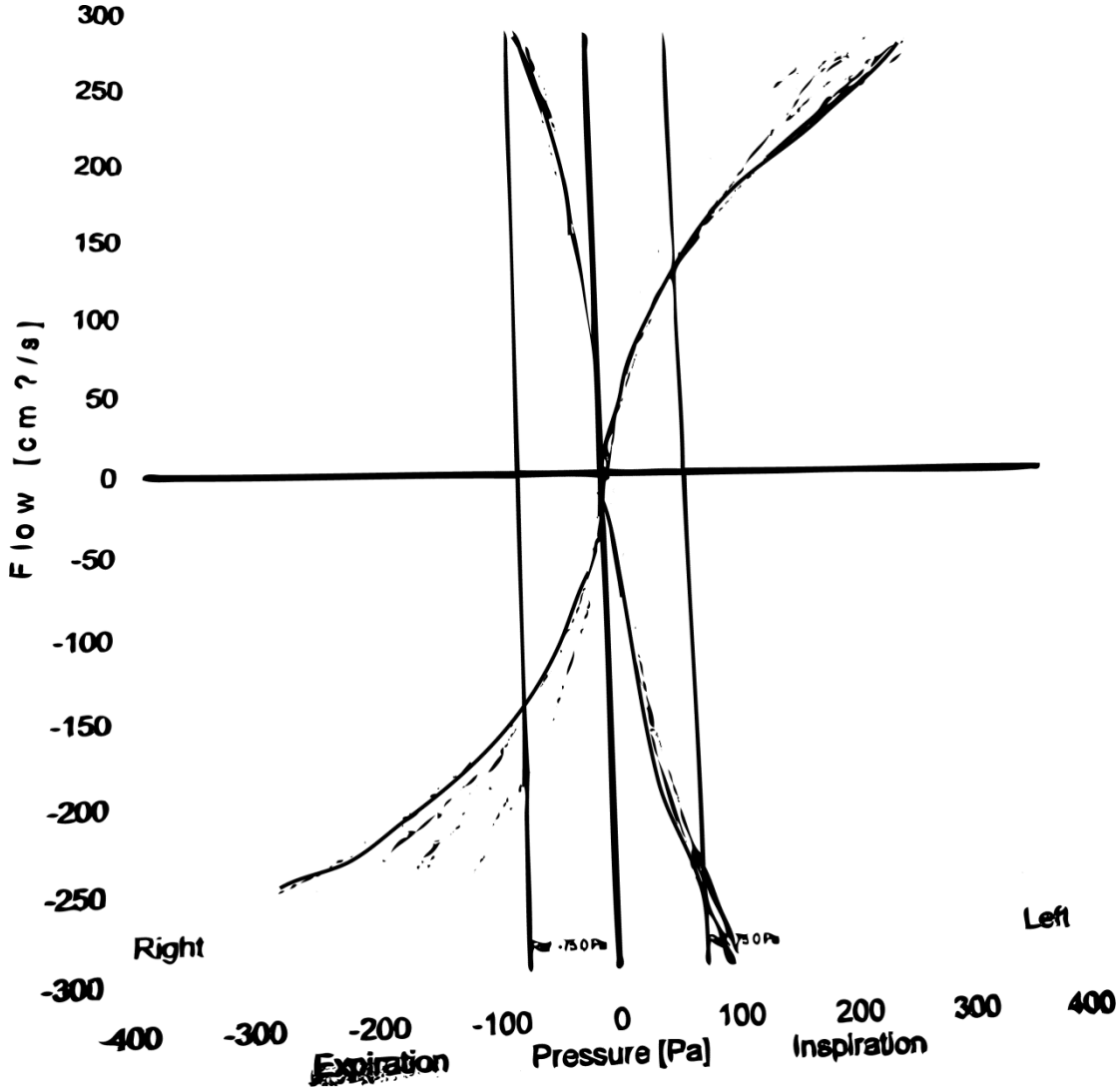

Side	Expiration		Inspiration	
	R'_N at 75 Pa ($Pa \cdot s/cm^3$)	Flow (cm^3/s)	R'_N at 75 Pa ($Pa \cdot s/cm^3$)	Flow (cm^3/s)
L (Obstructed)	0.24	315.41	0.30	250.69
R	0.45	165.92	0.55	136.75

The post-operative nasal air flow (cm^3/s) and nasal resistance ($Pa \cdot s/cm^3$) of DNS patient #2

References

[1] Rhee JS, Poetker DM, Smith TL, Bustillo A, Burzynski M, and Davis RE, "Nasal valve surgery improves disease-specific quality of life," *Laryngoscope,* vol. 115, pp. 437-440, 2005.

[2] Mladina R, Cujic E, Subaric M, and Vukovic K, "Nasal septal deformities in ear, nose, and throat patients: an international study," *Am J of Otolaryngol,* vol. 29, pp. 75-82, 2008.

[3] Oliveira AKP, Elias Jr E, Santos LV, Bettega SG, and Mocellin M, "Prevalence of deviated nasal septum in Curitiba, Brazil," *Int Arch Otorinolaryngol,* vol. 9, pp. 288-292, 2005.

[4] Gray LP, "Deviated nasal septum, incidence and aetiology," *Ann Otol Rhinol Laryngol Suppl,* vol. 87, pp. 3-20, 1978.

[5] Gray LP, "Septal manipulation in the neonate: method and results," *Int J Pediatr Otorhinolaryngol,* vol. 8, pp. 195-209, 1985.

[6] Hartikainen SA, Sorri M, Valnio MJ, and Ojala K, "Aetiology and detection of congenital nasal deformities," *Int J Pediatr Otorhinolaryngol,* vol. 6, pp. 83-88, 1983.

[7] Podoshin L, Gertner R, Fradis M, and Berger A, "Incidence and treatment of deviation of nasal septum in newborns," *Ear Nose Throat J,* vol. 70, pp. 458-487, 1991.

[8] Subaric M and Mladina R, "Nasal septum deformities in children and adolescent: a cross sectional study of children from Zagrep, Crotia," *Int J of Pediatr Otorhinolaryngol,* vol. 63, pp. 41-48, 2002.

[9] Yildirim I and Okur E, "The prevalence of nasal septal deviation in children from Kahramanmaras, Turkey," *Int J Pediatr Otorhinolaryngol,* vol. 67, pp. 1203-1206, 2003.

[10] Min YG, Jung HW, and Kim CS, "Prevalence study of nasal septal deformities in Korea: results of a nation-wide survey," *Rhinology,* vol. 33, pp. 61-65, 1995.

[11] Wolfensberger M and Hummel T, "Anti-inflammatory and surgical therapy of

olfactory disorders related to sino-nasal disease," *Chem Senses,* vol. 27, pp. 617-622, September 1, 2002 2002.

[12] Stewart MG, Smith TL, Weaver EM, Witsell DL, Yueh B, Hannley MT, and Johnson JT, "Outcome after nasal septoplasty: results from the Nasal Obstruction Septoplasty Effectiveness (NOSE) study," *Otolaryngol Head Neck Surg,* vol. 130, pp. 283-290, 2004.

[13] Gulati SP, Sachdeva OP, Wadhera R, Sodhi N, and Garg A, "Role of rhinomanometry to assess nasal airflow and resistance in patients undergoing septoplasty," *Indian J Otolaryngol Head Neck Surg,* vol. 60, pp. 133-136, 2008.

[14] Chandra RK, Patadia MO, and Raviv J, "Diagnosis of nasal airway obstruction," *Otolaryngol Clin North Am,* vol. 42, pp. 207-225, 2009.

[15] Hilberg O, Jackson AC, Swift DL, and Pedersen OF, "Acoustic rhinometry: Evaluation of the nasal cavity geometry by acoustic reflection," *J Appl Physiol,* vol. 66, pp. 295-303, 1989.

[16] Terheyden H, Maune S, Mertens J, and Hilberg O, "Acoustic rhinometry: Validation by threedimensionallyreconstructed computer tomographic scans," *J Appl Physiol. ,* vol. 89, pp. 1013-1021, 2000.

[17] Cakmak O, Celik H, Ergin T, and Sennaroglu L, "Accuracy of acoustic rhinometry measurements," *Laryngoscope,* vol. 111, pp. 587-594, 2001.

[18] Egeli E, Demirci L, Yazycy B, and Harputluoglu U, "Evaluation of the inferior turbinate in patients with deviated nasal septum by using computed tomography," *Laryngoscope,* vol. 114, pp. 113-117, 2004.

[19] Valencia MP and Castillo M, "Congenital and acquired lesions of the nasal septum: a practical guide for differential diagnosis," *Radiographics,* vol. 28, pp. 205-224, 2008.

[20] Ishikawa S, Nakayama T, Watanabe M, and Matsuzawa T, "Visualization of flow resistance in physiological nasal respiration: analysis of velocity and vorticities using numerical simulation," *Arch Otolaryngol Head Neck Surg,* vol. 132, pp. 1203-1209, 2006.

[21] Lee JH, Na Y, Kim SK, and Chung SK, "Unsteady flow characteristics through a

human nasal airway," *Respir Physiol Neurobiol,* vol. 172, pp. 136-146, 2010.

[22] Segal RA, Kepler GM, and Kimbell JS, "Effects of differences in nasal anatomy on airflow distribution: a comparison of four individuals at rest," *Ann of Biomed Eng,* vol. 36, pp. 1870-1882, 2008.

[23] Subramaniam RP, Richardson RB, Morgan KT, Kimbell JS, and Guilmette RA, "Computational fluid dynamics simulations of inspiratory airflow in the human nose and nasopharynx," *Inhalation Toxicology,* vol. 10, pp. 91-120, 1998.

[24] Wen J, Inthavong K, Tu J, and Wang S, "Numerical simulations for detailed airflow dynamics in a human nasal cavity," *Respir Physiol Neurobiol,* vol. 161, pp. 125-135, 2008.

[25] Chen XB, Lee HP, Chong VF, and Wang DY, "Assessment of septal deviation effects on nasal air flow: a computational fluid dynamics model," *Laryngoscope,* vol. 119, pp. 1730-1736, 2009.

[26] Garcia GJM, Rhee JS, Senior BA, and Kimbell JS, "Septal deviation and nasal resistance: an investigation using virtual surgery and computational fluid dynamics," *Am J Rhinol Allergy,* vol. 24, pp. 46-53, 2010.

[27] Lui T, Han D, Wang J, Tan J, Zang H, Wang T, Li Y, and Cui S, "Effects of septal deviation on the airflow characteristics: Using computational fluid dynamics models," *Acta Oto-Laryngologica,* vol. 132, pp. 290-298, 2012.

[28] Moghadas H, Abouali O, Faramarzi A, and Ahmadi G, "Numerical investigation of septal deviation effect on deposition of nano/microparticles in human nasal passage," *Respir Physiol Neurobiol,* vol. 177, pp. 9-18, 2011.

[29] Ozlugedik S, Nakiboglu G, Sert C, Elhan A, Tonuk E, Akyar S, and Tekdemir I, "Numerical study of the aerodynamic effects of septoplasty and partial lateral turbinectomy," *Laryngoscope* vol. 118, pp. 330-334, 2008.

[30] Na Y, Chung KS, Chung SK, and Kim SK, "Effects of single-sided inferior turbinectomy on nasal function and airflow characteristics," *Resp Physiol & Neurobiol,* vol. 180, pp. 289-297, 2012.

[31] Rhee JS, Cannon DE, Frank DO, and Kimbel JS, "Role of virtual surgery in pre-operative planning: Assessing the individual components of functional

nasal airway surgery," *Arch Facial Plast Surg,* vol. 14, pp. 354-359, 2012.

[32] Wexler D, Segal R, and Kimbell J, "Aerodynamic effects of inferior turbinate reduction: computation fluid dynamics simulation," *Arch Otolaryngol Head Neck Surg,* vol. 131, pp. 1102-1107, 2005.

[33] Kimbell JS, Frank DO, Laud P, Garcia GJM, and Rhee JS, "Changes in nasal airflow and heat transfer correlate with symptom improvement after surgery for nasal obstruction," *J of Biomechanics,* vol. 46, pp. 2634-2643, 2013.

[34] Rhee JS, Pawar SS, Garcia GJM, and Kimbell JS, "Towards personalized nasal surgery using computational fluid dynamics," *Arch Facial Plast Surg,* vol. 13, pp. 305-310, 2011.

[35] Jiyuan Tu, Guan Heng Yeoh, and C. Liu, "Computational fluid dynamics: a practical approach," 1st ed Burlington, MA: Elsevier Inc, 2008, pp. 1-2.

[36] Versteeg HK and Malalasekera W, *An Introduction to Computational Fluid Dynamics: The Finite Volume Method*, 1st ed. New York: John Wiley & Sons Inc., 1995.

[37] W. Becker, H. H. Naumann, and C. R. Pfaltz, *Ear, Nose and Throat Diseases. A Pocket Reference*. New York: Thieme Medical Publishers Inc., 1989.

[38] Proctor DF, "The nose," in *The Upper Airway*. vol. 12, Proctor DF and Anderson I, Eds. New York: Elsevier Biomedical Press, 1982, pp. 23-43.

[39] Malm L, "Measuremnet of nasal patency," *Allergy,* vol. 52 (suppl 40), pp. 19-23, 1997.

[40] Silvana Brescovici and Renato Roitbmann, "Modified glatzel mirror test reproducibility in the evaluation of nasal patency," *Rev Bras Otorrinolaringol,* vol. 74, pp. 215-222, 2008.

[41] Hansen BJ, Christiansen NB, and Osterhammel PAA, "Morphometric evaluations of nosecasts compared to acoustic rhinometry.," *Jpn J Rhinol* vol. 30, p. 124, 1991.

[42] Peter M. Som and Hugh D. Curtin, *Head and Neck Imaging* vol. 1. St. Louis, Missouri 63043: Elsevier Mosby, 2011.

[43] Besson WH, "Septal Surgery," in *Aesthetic Plastic Surgery--Rhinoplasty*, D. RK,

Ed. Boston, Little, Brown, 1993.

[44] Brain D, "The nasal septum," in *Scott-Brrown's otolaryngology: Rhinology*, 5th ed. vol. 4, Mackay IS and Bull TR, Eds. London: Butterworth & Co. Ltd, 1987, pp. 154-179.

[45] Berger G, Hamel I, and Berger R, "Histopathology of the inferior turbinate with compensatory hypertrophy in patients with deviated nasal septum," *Laryngoscope,* vol. 110, pp. 2100-2105, 2000.

[46] Singh A, Patel N, Kenyon G, and et al., "Is there objective evidence that septal surgery improves nasal airflow?," *J Laryngol Otol,* vol. 120, pp. 916-920, 2006.

[47] Courtiss EH and Goldwyn IEM, "The effects of nasal surgery on airflow," *Plast Reconstr Surg,* vol. 72, pp. 9-21, 1983.

[48] Ho WK, Yuen AP, Tang KC, Wei WI, and Lam PK, "Time course in the relief of nasal blockage after septal and turbinate surgery: A prospective study," *Arch Otolaryngo Head Neck Surg,* vol. 130, pp. 324-328, 2004.

[49] Pirila T and Tikanto, "Unilateral and bilateral effects of nasal septum surgery demonstrated with acoustic rhinometry, rhinomanometry, and subjective assessment," *Am J Rhinol,* vol. 15, pp. 127-133, 2001.

[50] Carney AS, Bateman ND, and Jones NS, "Reliable and reproducible anterior active rhinomanometry for the assessment of unilateral nasal resistance," *Clin Otolaryngol Allied Sci,* vol. 25, pp. 499-503, 2000.

[51] Roithmann R, Cole P, Chapnik J, and et al., "Acoustic rhinometry, rhinomanometry, and the sensation of nasal patency: A correlative study," *J Otolaryngol,* vol. 23, pp. 454-458, 1994.

[52] Tomkinson A and Eccles R, "The identification of the potential limitations of acoustic rhinometry using computer-generated, three-dimensional reconstructions of simple models," *Am J Rhinol,* vol. 10, pp. 77-82, 1996.

[53] Bahar K, Kayhan O, Deniz U, Hamadi A, and Bedri O, "Is there any relationship between nasal septal deviation and concha bullosa," *Eur J Gen Med,* vol. 7, pp. 359-364, 2010.

[54] Alireza M, Aslan A, Maryam E, Manouchehr S, and Shadi G, "An epidemiologic

study of factors associated with nasal septum deviation by computed tomography scan: a cross-sectional study," *BMC Ear, Nose and Throat Disorders* pp. 12-15, 2012.

[55] Parul G, "Septoplasty & turbinate surgery," in *http://care.american-rhinologic.org/septoplasty_turbinates*, 2011.

[56] Ertap A, Sinem K, Ali B, Semsettin O, Haldun S, and Ali SD, "Evaluation of the turbinate hypertrophy by computed tomography by computed tomography in patients with deviated nasal septum," *Otolaryngol-Head and Neck Surg,* vol. 136, pp. 380-384, 2007.

[57] Theissing J, Werner JA, and Rettinger G, *ENT-Head and Neck Surgery: Essential Procedures*. New York: Thieme, 2011.

[58] Hans Behrbohm, Oliver Kaschke, Tadeus Nawka, and Andrew Swift, "Ear, Nose, and Throat Diseases with Head and Neck Surgery," 3rd ed New York: Thieme New York, 2009.

[59] Passali D, Lauriello M, Anselmi M, and Bellussi L, "Treatment of hypertrophy of the inferior turbinate: long-term results in 382 patients randomly assigned to therapy," *Ann Otol Rhinol Laryngol,* vol. 108, pp. 569-575, 1999.

[60] Mabry RL, "Surgery of the inferior turbinates: how much and when?," *Otolaryngol Head Neck Surg,* vol. 92, pp. 571-576, 1984.

[61] Friedman M, Tanyeri H, and Lim J, "A safe, alternate technique for inferior turbinate reduction," *Laryngoscope,* vol. 109, pp. 1834-1837, 1999.

[62] Fanous N, "Anterior turbinectomy," *Arch Otolaryngo Head Neck Surg,* vol. 112, pp. 850-852, 1986.

[63] Rakover Y and Rosen G, "A comparison of partial inferior turbinectomy and cryosurgery for hypertrophic inferior turbinates," *J Laryngol Otol,* vol. 110, pp. 732-735, 1996.

[64] Yanez C, "New technique for turbinate reduction in chronic hypertrophic rhinitis: intraturbinate stroma removal using the miroderider," *Operat Tech Otolaryngol Head Neck Surg,* vol. 9, pp. 135-137, 1998.

[65] Ophir D, "Inferior turbinectomy," *Operat Tech Otolaryngol Head Neck Surg,*

vol. 2, pp. 189-193, 1991.

[66] Talmon Y, Samet A, and Gilbey P, "Total inferior turbinectomy: operative results and technique," *Ann Otol Rhinol Laryngol,* vol. 109, pp. 1117-1119, 2000.

[67] Roblin DG and Eccles R, "What, if any, is the value of septal surgery?," *Clin Otolaryngol Allied Sci,* vol. 27, pp. 77-80, 2002.

[68] Konstantinidis I, Triaridis S, Triaridis A, Karagiannidis K, and Kontzoglou G, "Long term results following nasal septal surgery. Focus on patients' satisfaction," *Auris Nasus Larynx,* vol. 32, pp. 369-374, 2005.

[69] Dinis PB and Haider H, "Septoplasty: Long-term evaluation of results," *Am J Otolaryngol,* vol. 23, pp. 85-90, 2002.

[70] Jessen M, Ivarsson A, and Malm L, "Nasal airway resistance and symptoms after functional septoplasty: Comparison of findings at 9 months and 9 years," *Clin Otolaryngol Allied Sci,* vol. 14, pp. 231-234, 1989.

[71] Mertz JS, McCaffrey TV, and Kern EB, "Objective evaluation of anterior septal surgical reconstruction," *Otolaryngol Head Neck Surg,* vol. 92, pp. 308-311, 1984.

[72] Broms P, Jonson B, and Malm L, "Rhinomanometry. IV. A pre- and postoperative evaluation in functional septoplasty," *Acta Otolaryngol,* vol. 94, pp. 523-529, 1982.

[73] Sipila J and Suonpaa J, "A prospective study using rhinometry and patient clinical satisfaction to determine if objective measurements of nasal airway resistance can improve the quality of septoplasty," *Eur Arch Otorhinolaryngol,* vol. 254, pp. 387-390, 1997.

[74] Simola M and Malmberg H, "Sensation of nasal airflow compared with nasal airway resistance in patients with rhinitis," *Clin Otolaryngol Allied Sci,* vol. 22, pp. 260-262, 1997.

[75] Grymer LF, Hilberg O, Elbround O, and Pedersen OF, "Acoustic rhinometry: Evaluation of the nasal cavity with septal deviations, before and after septoplasty," *Laryngoscope,* vol. 99, pp. 1180-1187, 1989.

[76] Jessen M, Kopman A, and Malm L, "Selection with and without rhinomanometry of patients for septoplasty," *Am J Rhinol,* vol. 3, pp. 201-203, 1989.

[77] Kim CS, Moon BK, Jung DH, and Min YG, "Correlation between nasal obstruction symptoms and objective parameters of acoustic rhinometry and rhinomanometry," *Auris Nasus Larynx,* vol. 25, pp. 45-48, 1998.

[78] Yaniv E, Hadar T, Shevero J, and Raveh E, "Objective and subjective nasal airflow," *Am J Otolaryngol,* vol. 18, pp. 29-32, 1997.

[79] Reber M, Rahm F, and Monnier II, "The role of acoustic rhinometry in the pre- and postoperative evaluation of surgeyr for nasal obstruction," *Rhinology,* vol. 36, pp. 184-187, 1998.

[80] Hahn I, Scherer PW, and Mozell MM, "Velocity profiles measured for airflow through a large-scale model of the human nasal cavity," *J Appl Physiol,* vol. 75, pp. 2273-2287, 1993.

[81] Kelly JT, Prasad AK, and Wexler AS, "Detailed flow patterns in the nasal cavity," *J Appl Physiol,* vol. 89, pp. 323-337, 2000.

[82] Churchill SE, Shackelford LL, Georgi JN, and Black MT, "Morphological variation and airflow dynamics in the human nose," *Am J Hum Biol,* vol. 16, pp. 625-638, 2004.

[83] Keyhani K, Scherer PW, and Mozell MM, "Numerical simulation of airflow in the human nasal cavity," *J Biomech Eng,* vol. 117, pp. 429-441, 1995.

[84] Elad D, Liebenthal R, Wenig B, and Einav S, "Analysis of air flow patterns in the human nose," *Med Biol Eng Comput,* vol. 31, pp. 585-592, 1993.

[85] Zhao K, Schere PW, Hajiloo SA, and Dalton P, "Effect of anatomy on human nasal air flow and odorant transport patterns: implications for olfaction," *Chem Senses,* vol. 29, pp. 365-379, 2004.

[86] Pless D, Keck T, Wiesmiller K, Rettinger G, Aschoff AJ, Fleiter TR, and Lindermann J, "Numerical simulation of air temperature and airflow patterns in the human nose during expiration," *Clin Otolaryngol* vol. 29, pp. 642-647, 2004.

[87] Naftali S, Rosenfeld M, Wolf M, and Elad D, "The air-conditioning capacity of the human nose," *Ann Biomed Eng,* vol. 33, pp. 545-553, 2005.

[88] Croce C, Fodil R, Durand M, Sbibl-Apiou G, Caillibotte G, Papon JF, Blondeau JR, Coste A, Isabey D, and Louis B, "In vitro experiments and numerical simulations of airflow in realistic nasal airway geometry," *Ann of Biomed Eng* vol. 34, pp. 997-1007, 2006.

[89] Kimbell JS, Garcia GJM, Frank DO, Cannon DE, Pawar SS, and Rhee JS, "Computed nasal resistance compared with patient-reported symptoms in surgically treated nasal airway passages: A preliminary report," *Am J Rhinol Allergy,* vol. 26, pp. e94-e98, 2012.

[90] Leong SC, Chen XB, Lee HP, and Wang DY, "A review of the implications of computational fluid dynamic studies on nasal airflow and physiology," *Rhinology,* vol. 48, pp. 139-145, 2010.

[91] Yu S, Liu Y, Sun X, and Li S, "Influence of nasal structure on the distribution of airflow in nasal cavity," *Rhinology,* vol. 46, pp. 137-143, 2008.

[92] Manoukian PD, Wyatt JR, Leopold DA, and Bass EB, "Recent trends in utilization of procedures in otolaryngology-head and neck surgery," *Laryngoscope,* vol. 107, pp. 472-477, 1997.

[93] Kim SK, Na Y, Kim JI, and Chung SK, "Patient specific CFD models of nasal airflow: Overview of methods and challenges," *J of Biomechanics,* vol. 46, pp. 299-306, 2013.

[94] Lindemann J, Leiacker R, Stehmer V, Rettinger G, and Keck T, "Intranasal temperature and humidity profile in patients with nasal septal perforation before and after surgical closure," *Clin Otolaryngol Allied Sci,* vol. 26, pp. 433-437, 2001.

[95] Lindemann J, Brambs HJ, Keck T, Wiesmiller KM, Rettinger G, and Pless D, "Numerical simulation of intranasal airflow after radical sinus surgery," *Am J Otolaryngol,* vol. 26, pp. 175-180, 2005/6// 2005.

[96] Xiong G, Zhan J, Zuo K, Li J, Rong L, and Xu G, "Numerical flow simulation in the post-endoscopic sinus surgery nasal cavity," *Med Biol Eng Comput,* vol.

46, pp. 1161-1167, 2008.

[97] Garcia GJM, Bailie N, Martins DA, and Kimbell JS, "Atrophic rhinitis: a CFD study of air conditioning in the nasal cavity," *J Appl Physiol,* vol. 103, pp. 1082-1092, 2007.

[98] Kim SK, Heo GE, Seo A, Na Y, and Chung SK, "Correlation between nasal airflow characteristics and clinical relevance of nasal septal deviation to nasal airway obstruction," *Respiratory Physiology & Neurobiology,* vol. 192, pp. 95-101, 2014.

[99] *STAR-CD 3.22 users' guide*: Computational Fluid Dynamics Ltd., 2004.

[100] Naftali S, Schroter RC, Shiner RJ, and Elad D, "Transport phenomena in the human nasal cavity: a computational model," *Ann Biomed Eng,* vol. 26, pp. 831-839, 1998.

[101] Schreck S, Sullivan KJ, Ho CM, and Chang HK, "Correlations between flow resistance and geometry in a model of the human nose," *J Appl Physiol,* vol. 75, pp. 1767-1775, 1993

[102] Warsi ZVA, "Conservation form of the Navier-Stokes equations in general nonsteady coordinates," *AIIA Journal,* vol. 19, pp. 240-242, 1981.

[103] Patankar SV and Spalding DB, "A calculation procedure for heat, mass and momentum transfernin three-dimensional parabolic flows," *Int J Heat Mass Transfer,* vol. 15, pp. 1778-1806, 1972.

[104] "Human respiratory tract model for radiological protection," in *Annals of the International Commission on Radiological Protection (ICRP Publication 66)*. vol. 24 Oxford: Pergamon, 1994.

[105] Jeong SJ, Kim WS, and Sung SJ, "Numerical investigation on the flow characteristics and aerodynamic force of the upper airway of patient with obstructive sleep apnea using computational fluid dynamics," *Med Eng Phys* vol. 29, pp. 637-651, 2007.

[106] Elahi MM, Frenkiel S, and Fageeh N, "Paraseptal structural changes and chronic sinus disease in relation to the deviated septum," *J Otolaryngol,* vol. 26, pp. 236-240, 1997.

[107] Stewart MG, Witsell DL, Smith TL, Weaver EM, Yueh B, and Hannley MT, "Development and validation of the Nasal Obstruction Systom Evaluation (NOSE scale)," *Otolaryngol Head and Neck Surg,* vol. 130, pp. 157-163, 2004.

[108] Suzina AH, Hamzah M, and Samsudin AR, "Active anterior rhinomanometry analysis in normal adult Malays," *The Journal of Laryngology & Otology* vol. 117, pp. 605-608, 2003.

[109] Korantzis A, Cardamakis E, Chelidonis E, and Papamihalis T, "Nasal septum deformity in the newborn infant during labour," *Eur J Obstet Gynecol Reprod Biol,* vol. 44, pp. 41-46, 1992.

Biography

Personal Information

Name	KHAISANG HEMTIWAKORN
Nationality	Thai
Date of birth	September 1, 1983
Place of birth	Bangkok, Thailand

Education

Bachelor degree

Field	Radiological Technology
Duration	2001-2004
Department	Radiological Technology
University	Mahidol University, Thailand

Master degree

Field	Radiological Technology
Duration	2005-2007
Department	Radiological Technology
University	Mahidol University, Thailand

Research and Working Experiences

2010-2011	Research assistant at University of Minnesota, MN, USA
2011-2013	Research assistant at Advance Diagnostic Imaging Center (AIMC), Ramathibodi Hospital, Mahidol University, Bangkok, Thailand
2014	Teacher assistant at Department of Radiological technology, Faculty of Medical Technology, Mahidol University, Bangkok, Thailand

Research Interests

Computational Fluid Dynamics, Advanced Medical Imaging, Upper Airway Obstruction

List of International Papers

1- K. Hemtiwakorn, N. Phoocharoen, S. Tungjitkusolmun, C. Pintavirooj. **"Nasal Airflow Simulation in Human using a Computational Fluid Dynamics (CFD)"**, in *Proceeding of 2nd Biomedical Engineering International Conference (BMEiCON 2009)*, Thailand, August 13-14, 2009, pp. 335-338.

2- K. Hemtiwakorn, N. Phoocharoen, S. Tungjitkusolmun, V. Mahasittiwat, C. Pintavirooj. **"Combined Medical Imaging with CFD Analysis for Application of Diagnostic and Treatment Planning: The Case Study of Human Nasal Airflow Simulation based on CT Imaging"** in *Proceeding of Asia Simulation Conference (JSST 2009)*, Ritsumeikan University, Shiga, Japan, October 7-9, 2009.

3- K. Hemtiwakorn, N. Phoocharoen, V. Mahasittiwat, S. Tungjitkusolmun, M. Sangworasil, and C. Pintavirooj. **"Combined Medical Imaging and Computational Fluid Dynamic (CFD) Analysis of Nasal Airflow Simulation"** in *Proceeding of The 4th International Symposium on Biomedical Engineering (ISBME 2009)*, Thailand, December 14-18, 2009.

4- K. Hemtiwakorn, N. Phoocharoen, V. Mahasittiwat, and C. Pintavirooj. **"Treatment Planning Technique Applying the Combined CT Imaging and Computational Fluid Dynamics (CFD) Analysis"** in *the Paper of International Journal of Applied Biomedical Engineering,* Vol 2(2), 2009, pp. 43-49.

5- V. Mahasittiwat, K. Hemtiwakorn, and C. Pintavirooj, **"Use of computational fluid dynamics nasal airflow measurement to design septoplasty: a pilot study,"** in *J Med Assoc Thai (จดหมายเหตุแพทยสภาแห่งประเทศไทย)*, Vol. 96, 2013, pp. S12-7.

6- K. Hemtiwakorn, V. Mahasittiwat, S. Tungjitkusolmun, K. Hamamoto, and C. Pintavirooj, **“Patient Specific Aided Surgery Approach of Deviated Nasal Septum using Computational Fluid Dynamics,”** in *The Paper of IEEJ Transactions on Electrical and Electronic Engineering*, Vol. 10(3), 2015.

The Institute of Electrical Engineers of Japan
Homat Horizon Bldg. 8F. 6-2, Go-bancho Chiyoda-ku, Tokyo 102-0076, Japan

Dear Ms. Khaisang Hemtiwakorn,

Notification of Publication

It is our pleasure to accept for your submitted paper.
Following paper you submitted has been accepted and will be published on IEEJ Transactions on Electrical and Electronic Engineering.

..... Receipt Number (IEEJ ID) : c13009182
..... Title of Manuscript : Patient Specific Aided Surgery Approach of Deviated Nasal Septum using Computational Fluid Dynamics
..... Author(s) : Ms. HEMTIWAKORN KHAISANG
..... Vol./No : Vol. 10 No.3, May 2015 issue

Sincerely Yours,

The Chairperson of the Editorial Affairs,IEEJ

Tel: +81-3-3221-7302 Fax: +81-3-3221-3704

IEEJ TRANSACTIONS ON ELECTRICAL AND ELECTRONIC ENGINEERING
IEEJ Trans 2014; **00**: 1–13
Published online in Wiley Online Library (wileyonlinelibrary.com). DOI:10.1002/tee

Paper

Patient Specific Aided Surgery Approach of Deviated Nasal Septum using Computational Fluid Dynamics

Khaisang Hemtiwakorn[*,**], Non-member. Visan Mahasitthiwat[***], Non-member. Supan Tungjitkusolmun[*], Non-member. Kazuhiko Hamamoto[****], Member. Chuchart Pintavirooj[*a], Member.

In treating a patient with deviated nasal septum (DNS), a surgeon draws up a surgical plan based on the patient's rhinomanometry outcomes and self-assessment of nose conditions, e.g. the nasal obstruction septoplasty effectiveness (NOSE) score. However, the procedure fails to localize the DNS and determine the nose's aerodynamic effects. This research proposes a DNS aided surgery approach using the computational fluid dynamics (CFD) and the computed tomography (CT) techniques consisting of three main processes: pre-operative, pre-surgical planning, and post-operative processes. The healthy baseline refers to a benchmark consisting of five subjects without DNS and nasal airway obstructions. To assess the possibility of using the CFD-CT aided surgery approach as a pre-surgical planning tool in the DNS operation, comparative tests were carried out with DNS patient #1, who received a conventional nasal surgery without the proposed pre-surgical planning. Although DNS patient #1's surgical outcome was relatively satisfying to the patient, evaluating from the reduction of the NOSE score, the conventional surgical method could induce an excessive excision of nasal airway, resulting in a water loss in nasal mucosa and a large airflow velocity reduction. In addition, the post-operative nasal resistance measured by rhinomanometer was not acceptable to the surgeon. Virtual surgery using the CFD-CT approach performed after surgery could suggest suitable patient-specific components of nasal operation with predictable results. Subsequently, implementation of the proposed CFD-CT approach in aid of the DNS surgery was performed in DNS patient #2. The benefits of the CFD-CT aided surgery approach is determined based on the pre- and post-operative's outcomes (i.e. nasal geometric data and nasal airflow patterns), NOSE scores, and rhinomanometric data of DNS patient #2, which were compared against those of the healthy baseline benchmark. The CFD-CT approach could assist the surgeon to localize the DNS and determine the defective nasal tissues to remove. The post-actual-operative outcomes were clinically acceptable to the surgeon and DNS patient #2. It is evident that the CFD-CT aided surgery approach is suitable for and applicable to surgery of DNS patients with small variability from the pre-surgical planning stage. © 2014 Institute of Electrical Engineers of Japan. Published by John Wiley & Sons, Inc.

Keywords: nasal septum deviation, nasal airway obstruction, septoplasty, turbinate hypertrophy reduction, virtual surgery, pre-surgical planning

Received . . .

1. Introduction

A nasal airway obstruction is common in ear-nose-throat patients with sino-nasal diseases and contributes to the patients' poor quality of life [1]. The nasal anatomy and nomenclature [2] are illustrated in Fig. 1. Figure 1(a) is a CT image of a normal nose in which a septal cartilage divides the nasal cavity into two sides. Figure 1(b) shows a deformation of septal cartilage from the midline to the left side of the nose, i.e. deviated nasal septum (DNS), which induces the nasal airway obstruction. DNS impairs smell sensory [3] and induces sinusitis, epistaxis, snoring, upper airway infection, and various middle ear infections [4].

Surgeons have many approaches at their disposal to diagnose DNS patients. According to [5], an assessment using the nasal obstruction septoplasty effectiveness (NOSE) scoring technique could fail to reveal irregular airflow patterns and to localize septal deformity in the nasal passage. The NOSE scoring technique is a clinical symptoms scoring system that evaluates the degrees of: (i) nasal congestion, (ii) nasal blockage, (iii) breathing difficulty,

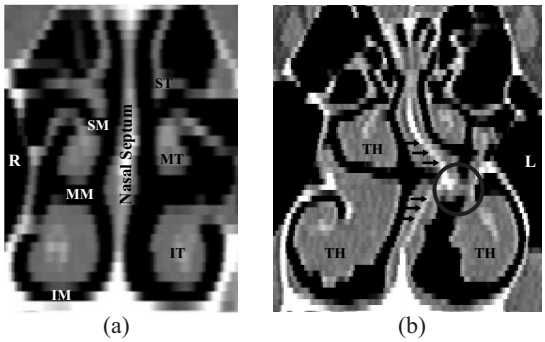

(a) (b)

Fig. 1. The anatomy of a healthy nasal cavity and of a leftward DNS (see arrows) are presented in (a) and (b), where IT denotes the inferior turbinate, MT the middle turbinate, ST the superior turbinate, IM the inferior meatus, MM the middle meatus, and SM the superior meatus. In the case of DNS nose, compensatory turbinate hypertrophies (TH) are typically found. Nasal airway obstruction (circle), as a result of DNS, is observed in the left side of the nose. R and L indicate right and left sides.

[a]Correspondence to: Chuchart Pintavirooj
E-mail: kpchucha@kmitl.ac.th, chuchartpintavirooj@gmail.com

[*]Department of Electronics Engineering, Faculty of Engineering, King Mongkut's Institute of Technology Ladkrabang (KMITL), Bangkok, Thailand.
[**]Department of Radiological Technology, Faculty of Medical Technology, Mahidol University, Bangkok, Thailand.
[***]Department of Otolaryngology, Faculty of Medicine, Srinakarinwirot University, Nakornnayok, Thailand.
[****]Department of Information Media Technology, School of Information and Telecommunication Eng., Tokai University, Tokyo, Japan.

(iv) sleep disorder, and (v) insufficient air through the nose during exertion.

Rhinomanometry is a technique for examining the volume flow in a nose [6] at a given pressure difference required to transport air in the atmosphere to the pharyngeal cavity [7]. The rhinomanometry technique determines the nasal resistance (i.e. the pressure-flow relationship) in each side of the nose. Compared to a non-DNS patient, a DNS patient's nasal resistance in the obstructed side is higher while the air flow rate is lower. Nevertheless, the rhinomanometry technique fails to reveal the precise location of DNS [8].

The CT and magnetic resonance imaging (MRI) technologies were adopted to diagnose anatomical deformities in the nasal cavity [9, 10]. The technologies produce high resolution images of nasal airway and thereby enable localization of DNS. However, similar to the rhinomanometry technique, the CT and MRI fail to show the airflow characteristics, e.g. velocity and pressure. To overcome this limitation, the CFD technique should be employed together with either CT or MRI.

In [11-15], the CFD-CT technique was used to generate images of the anatomy and physiology of nasal cavity of normal noses. [16-18] studied the effects that DNS had on the nasal airflow patterns prior to surgery using the CFD-CT technique. [19, 20] examined the post-operative nasal airflow patterns using the same technique. [21-23] studied the post-operative outcomes of applying CFD-CT to various surgical procedures. Previous studies by [24, 25] used the CFD-CT technique as a pre-surgical tool in surgery of nasal cavity. However, no study on the use of CFD-CT as a pre-surgical tool in DNS patients exists.

In the current study, we propose the integrated CFD-CT aided surgery approach as a patient-specific surgical planning tool in DNS noses. The approach is designed for a non-invasive procedure where surgeons map out DNS surgical plans on reconstructed airways relying on the data from the pre-operative DNS noses to achieve optimal post-virtual-operative outcomes, i.e. nasal geometric data (i.e. septal deviation angle and cross-sectional area) and nasal airflow patterns (i.e. velocity magnitude, pressure drop and, nasal resistance (R_N)). Post-actual-operative outcomes are compared with the pre-operative conditions (both nasal geometric data and nasal airflow patterns) to determine the success of the DNS surgery and to assess the efficacy of the CFD-CT aided surgery approach. In addition, the healthy baseline consists of five subjects without DNS and nasal airway obstructions and is used as a benchmark against which the comparisons are made.

2. Materials and methods

2.1. Design of the CFD-CT aided surgery approach

The proposed CFD-CT aided surgery approach was created for a patient-specific surgical planning tool. Figure 2 present the design process of the CFD-CT approach consisting of three main parts: pre-operative process, pre-surgical planning process, and post-operative process. First, the pre-operative process aims to investigate the effects of septal deviation on nasal airflow. Second, the pre-surgical planning process purposes to demonstrate the effect of individual components of nasal airway surgery designed by a surgeon; and to predict the post-virtual-surgical outcomes. The best course of surgical operation will be selected to perform in an actual nasal surgical procedure. Finally, the post-operative process aims at investigating the aerodynamic changes induced by the nasal operation, then actual-post-operative outcomes were assessed. Each process individually determined both nasal geometric data (i.e. septal deviation angle and cross-sectional area) and nasal airflow patterns (i.e. velocity magnitude, pressure drop, and R_N) using the CFD simulation method.

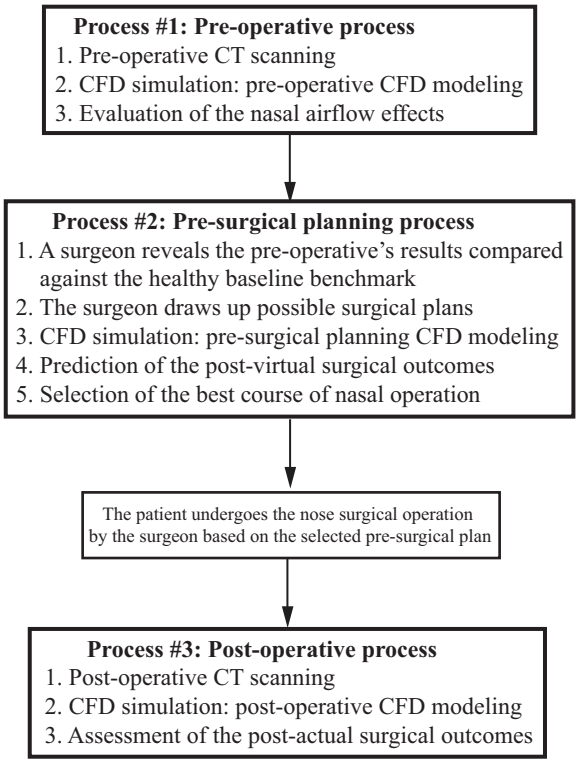

Fig. 2. The three-process CFD-CT aided surgery approach.

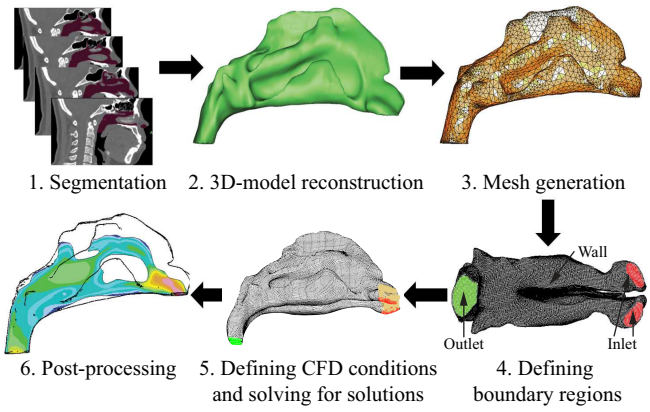

Fig. 3. The six-step CFD method

2.2. CFD simulation method A six-step CFD simulation method (Fig. 3) is described as follows:

2.2.1. Segmentation Two-dimensional CT images containing nasal cavity, oral cavity, paranasal sinuses and skull bones are imported to the Mimics medical imaging program (Mimics, Materialise version 13.1, Ann Arbor, MI). The area of skull bones on the images is filtered out by setting the lower and upper thresholds at -1024 and -210 Hounsfield unit to retain the air regions of nasal cavity, oral cavity and paranasal sinuses. Then, the areas of paranasal sinuses and oral cavity are manually removed with the Mimics software's manual editing tools to retain only the nasal cavity for the next step.

2.2.2. 3D model reconstruction The images containing only nasal cavity area of the previous step are used to generate 3D nose models. The surfaces of the 3D nose models are smoothed by the Laplacian method and exported in the stereolithography (STL) format for mesh generation.

2.2.3. Mesh generation The 3D STL models are processed by the Pro-STAR Automated Meshing program (CD-Adapco, UK, version 3.24) to generate the trimmed-meshes with three boundary layers of prism cells. The mesh density study was performed and indicated that a mesh resolution of 1.6 million elements was fine sufficient to provide mesh-independent numerical results and to balance between the calculation accuracy and computational time.

2.2.4. Defining boundary regions In this step, the nostrils and nasopharynx are defined as the airflow inlet and outlet, as shown in Fig. 3.

2.2.5. Defining CFD conditions and solving for solutions The steady-state inspiratory airflow (i.e. time-dependent variable are held constant and all derivatives with respect to time were zero) is computed using the STAR-CD software version 3.2 (CD-Adapco, UK) [26], which uses the finite volume method to numerically solve the governing equations. A published experimental work [27] and several CFD studies [14, 28-31] assumed that the nasal flow was laminar at rest. However, there exists no experimental report about the airflow patterns inside DNS patients' nasal cavity at rest. In this study, the calculated Reynolds numbers are in a range of $800 - 1000$ in all nose models. Therefore, laminar flow is conducted in both healthy and DNS noses. Several published DNS studies [17, 19, 22, 32] assumed laminar airflow in their CFD simulation. Although it is reasonable and necessary to implement a turbulent flow model for simulations with a large flow rate, such as 500 mL/s, as in [16], the airflow rate at rest is the sole focus of this study.

This research assumes that air is incompressible and of Newtonian with constant fluid properties. A velocity (u_i, m/s) and a pressure (p, Pa) of nasal airflow require solving the mass and momentum conservation equations (the Navier-Stokes equations) in a Cartesian tensor notation as follows [33]:

$$\frac{\partial \rho}{\partial t} + \frac{\partial}{\partial x_j}(\rho\, u_j) = s_m \tag{1}$$

$$\frac{\partial \rho\, u_i}{\partial t} + \frac{\partial}{\partial x_j}(\rho\, u_j\, u_i - \tau_{ij}) = -\frac{\partial p}{\partial x_i} + s_i \tag{2}$$

where t is time, x_i is the Cartesian coordinate ($i = 1, 2, 3$), u_i is the absolute fluid velocity component in direction x_i, ρ the fluid density (1.205 kg/m^3), p the piezometric pressure, τ_{ij} stress tensor components, s_m is the mass source, s_i is the momentum source components. The Semi-Implicit Method for Pressure-Linked Equation algorithm [34] is used to manage the pressure-velocity coupling; and discretization of the governing equations is conducted using the second-order Upwind scheme. Convergence of the numerical solutions is confirmed by small residuals of mass and momentum ($< 10^{-3}$).

The inlet pressure at nostrils is set to the atmospheric pressure, and the outlet mass flow rate at nasopharynx is assumed fixed. The total volumetric flow (Q) through nasal cavity is 250 cm^3/s, which corresponds to breathing at rest [35]. The wall of nasal cavity is assumed to be rigid and in a non-slip condition (i.e. zero velocity). The average computational time per model is 3 hours on a 64-bit Sun Fire V40z server (two processors, 8 GB RAM).

2.2.6. Post-processing In the post-processing step, the nasal airflow patterns are determined by the measurements of velocity magnitude and pressure drop as a function of the distance from nostrils. Figure 4 shows locations of six coronal cross-sections (planes A to F) used to investigate velocity magnitude distribution of this and other studies [11, 14, 28, 36]. Nasal resistance (R_N), in Pa·s/cm^3, is calculated by:

$$R_N = \frac{\Delta P}{Q} \tag{3}$$

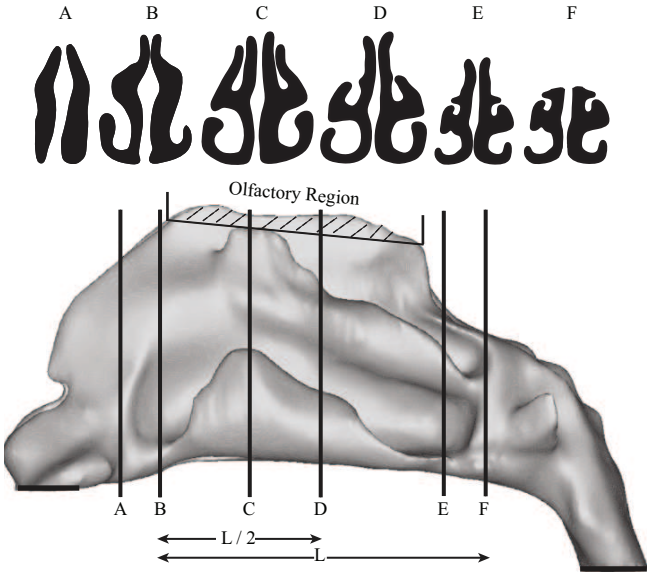

Fig. 4. The six coronal cross-sections. Plane A represents the nasal valve region and the narrowest cross-section. Plane B shows the main nasal passage front, which is the head of inferior turbinate. Plane C represents the head of middle turbinate while Plane D is the middle of nasal passage. Plane E is the front of superior turbinate and Plane F is the end of main nasal cavity before the merging of the left and right airways. L and L/2 are the lengths from Planes B to F and Planes B to D.

where ΔP is the maximum pressure drop (Pa) between nostrils and the posterior end of nasal septum [24, 32] and Q is an inspiratory flow rate of 250 cm^3/s.

2.3. Establishing the healthy baseline The healthy baseline benchmark was created using the CT images of five healthy subjects. The five subjects must have a similar mucosal thickness and straight nasal septum nose. Furthermore, they have no history of sinusitis, lung diseases and nasal surgery. Their average age was 32.8 ± 15.4 years. The CT images, produced by an Aquilion ONE^{TM} CT scanner (Toshiba Medical Systems Corporation), were provided by the Advanced Diagnostic Imaging Center (AIMC) of Thailand's Ramathibodi Hospital in Bangkok. The image resolution is 512x512 pixels and the shift between a cross-sectional image and the subsequent image was 1 mm.

Nasal cross-sectional area was measured in the coronal CT image and plotted as a function of distance from nostrils. The 6-step CFD simulation (Fig. 3) was performed to determine the airflow conditions of the healthy noses (i.e. velocity magnitude, pressure drop, and R_N). The results of nasal cross-sectional area, velocity magnitude, pressure drop, and R_N were established as the healthy baseline benchmark of the research.

2.4. Assessing the possibility of using the CFD-CT aided surgery approach To evaluate whether the proposed CFD-CT approach had the potential to be a pre-surgical aiding tool that would enable surgeons to perform personalized virtual surgery (VS), a 22 year old male patient (DNS patient #1) from the Otolaryngology Unit, HRH Princess Maha Chakri Sirindhorn Medical Center (MSMC), Faculty of Medicine, Srinakharinwirot University, Ongkarak, Nakornnayok, Thailand, who had suffered from leftward septal deviation and underwent conventional septoplasty and inferior turbinate reduction without using the CFD-CT aided surgery approach, was recruited in this preliminary study. The patient has given their consent, which has been approved by

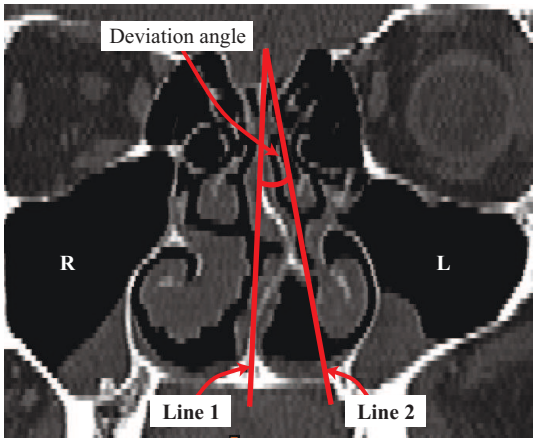

Fig. 5. Coronal paranasal sinus CT image demonstrating technique for measurement of the septal deviation angle. R and L are the right and left side of the nose

Thailand's Faculty of Medicine of Srinakharinwiroj University. In the pre- and post-surgery, the NOSE scoring and rhinomanometry techniques were applied to the patient to determine the NOSE score and nasal resistance to flow. The rhinomanometer is of RhinoStream® SRE 2000 Interacoustics AS, Assens, Denmark and was used to measure nasal resistance (R'_N) at a 75 Pa pressure point.

Before and after surgery, a nasal airway of DNS patient $\#1$ was scanned with a Siemens Somatom Volume Access CT scanner (Siemens AG, Erlargen, Germany). The CT image resolution was 512x512 pixels and the shift between one cross-sectional image and the subsequent image was 1 mm. Nasal geometric data of septal deviation angle and cross-sectional area were calculated. To calculate the angle of septal deviation, a line was drawn from the crista galli to the pre-maxilla (Line 1) and a second line was drawn from the crista galli to the most prominent point (Line 2); then the angle between the first and second lines was measured (Fig. 5) [37]. Maximum deviation angle was used for grading the degree of DNS as mild ($<9^\circ$), moderate ($9^\circ - 15^\circ$), and severe (15° and up) [38]. In addition, nasal cross-sectional area was measured in the coronal CT image and plotted as a function of distance from nostrils. Nasal airflow patterns (i.e. velocity magnitude, pressure drop, and R_N) was determined using the six-step CFD method (Fig. 3). Figure 6(a) illustrates a segmented CT image of one of the five healthy noses, which is compared among those of the pre-operative DNS nose (Fig. 6(b)) and post-operative DNS nose (Fig. 6(c)). Dashed lines represent shapes of the septal cartilages.

2.4.1. The NOSE scores and rhinomanometric data of DNS patient $\#1$ The pre-operative NOSE score was 40, implying that the DNS patient suffered from a moderate nasal obstruction [39]. The pre-operative R'_N was 0.2939 Pa$\cdot s/$cm^3, which is 55% higher than the Asian adults' mean, at a 75 Pa pressure point, of 0.1900 Pa$\cdot s/$cm^3 [40].

After conventional surgery by septoplasty and turbinate reduction (without using pre-surgical planning tool), the NOSE score was decreased to 2, equivalent to a 95% reduction, which means very mild problem with nasal obstruction detected after surgery [39]. However, the post-operative R'_N decreased to 0.2636 Pa$\cdot s/$cm^3, equivalent to a reduction of 10%. Although, the post-operative NOSE score implied that the surgical treatment was satisfying to the patient, the 10% reduction of nasal resistance to flow after treatment was not acceptable to the surgeon.

2.4.2. The nasal geometric data of DNS patient $\#1$ The maximum leftward septal deviation angle was 14.1°, which was observed at 4.75 cm from nostrils of the pre-operative DNS nose, while the nasal septum was straight and divided the nasal cavity into generally symmetrically left and right sides of the healthy baseline's noses (Fig. 6(a)). According to the maximum deviation angle of 14.1°, the patient was classified as moderate DNS [38]. The pre-operative minimal cross-sectional area (MCA_{pre}) was 0.98 cm^2 observed at the right nasal valve region (i.e. 2.80 cm from nostrils) (Fig. 7(a)).

After surgery, no deviated septum remained in the DNS patient $\#1$'s nose due to the septoplasty (Fig. 6(c)); and the nasal cross-sectional area became wider than the pre-operative's cross-sectional area on both sides of nasal airway (Fig.7). However, the post-operative cross-sectional area on the right side of the nose (Fig. 7(a)) was much larger than the right cross-sectional area of the healthy baseline (solid line with error bars each indicating 1 standard deviation (SD)). The post-operative minimal cross-sectional area (MCA_{post}) on the right side was 1.78 cm^2, which is higher than the MCA_{pre}, equivalent to a 82% (Fig. 7(a)).

2.4.3. The nasal airflow patterns of DNS patient $\#1$ Before surgery, the incoming air was not well balanced between the two sides of the DNS nose (Fig. 8(a)), while the airflow distributions in all six coronal cross-sections of both sides of healthy noses were almost identical (Fig. 9). High velocity magnitudes ran along planes A, B, C, and D (i.e. from the nasal valve to half of the main nasal passage) of the DNS nose (Fig. 8(a)), while an incoming air accelerated due to the narrowing of the nasal valve region and gradually decelerated in the main nasal cavity of the healthy baseline's noses (Fig. 9). The high velocity magnitudes were observed along the left (convex) side of DNS patient $\#1$'s nose, which was the constricted side due to DNS (Fig. 8(a)). The maximum velocity magnitude of the pre-operative nasal cavity ($Vmax_{pre}$) was 2.61 m/s, which was observed in the main nasal passage at 3.6 cm from nostrils, while the maximum velocity magnitude of the healthy nose ($Vmax_H$) was 2.73 ± 0.19 m/s, which was observed at the nasal valve region ($1.60 - 2.20$ cm from nostrils) (Fig. 10(a)). In addition, the DNS induces an increase in pressure drops on the entire nasal cavity; and was in a range of $6.05 - 7.20$ Pa, while the increase in pressure drop was observed in the nasal valve region of the healthy noses and stabilized at $4.45 - 5.05$ Pa (Fig. 10(b)). The maximum pressure drop (ΔP) of the pre-operative nasal cavity (ΔP_{pre}) was 7.20 Pa, which was observed in the main nasal passage where the $Vmax_{pre}$ existed, while the ΔP_H was 5.96 ± 1.17 Pa (Fig. 10(b)) observed in the nasal valve region. The pre-operative R_N was 0.0288 Pa$\cdot s/$cm^3, which is 21% higher than the mean of healthy baseline's R_N (i.e. 0.0238 ± 0.0047 Pa$\cdot s/$cm^3).

After surgery, more balanced nasal airflow distribution between the two sides was presented in Fig. 8(b). However, the post-operative velocity magnitudes were greatly less than the healthy baseline's in almost all nose planes; and no acceleration of airflow in the nasal valve region was detected when compared with those of the healthy baseline (Fig. 10(a)). Moreover, over-reduction of pressure drops was observed after treatment (Fig. 10(b)). The maximum pressure drop of the post-operative DNS patient (ΔP_{post}) was reduced to 3.17 Pa, which is noticeably less than the ΔP_H (Fig. 10(b)). The range of post-operative pressure drops in the main nasal passage was $2.60 - 3.10$ Pa, while the range in the healthy baseline was $4.45 - 5.05$ Pa (Fig. 10(b)). The post-operative R_N was 0.0127 Pa$\cdot s/$cm^3, which is a 56% reduction from the pre-operation and 7% less than the mean of healthy baseline' R_N.

We hypothesized that the post-operative velocity magnitude and pressure drop of the DNS patient could not be restored to the normal level of the healthy baseline as a result of the excessive tissue removal during the inferior turbinate reduction procedure. Virtual surgery (VS) using the CFD-CT method might be a useful tool to address where it was unclear whether septoplasty with turbinate

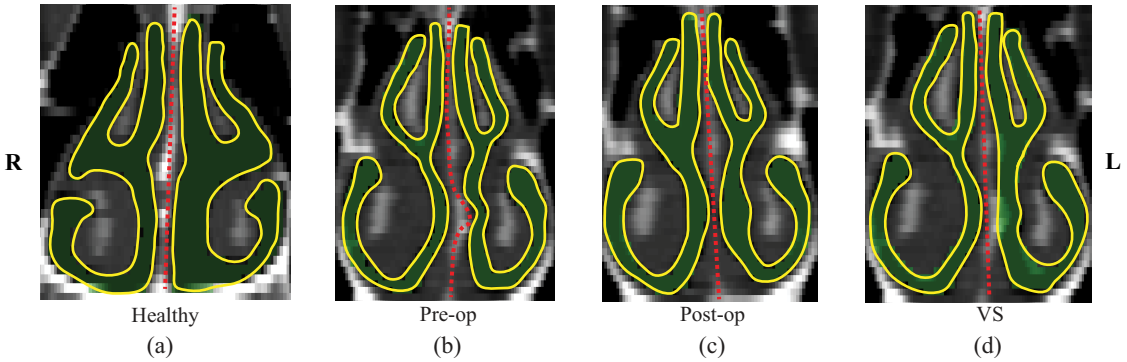

Fig. 6. The coronal cross-sectional CT images present the segmented nasal airway of the healthy nose (a) and DNS patient #1's pre-operative nose (b), post-operative nose underwent septoplasty and turbinate reduction (c), and virtual-surgery (VS) model based on septoplasty alone. Dashed lines represent shapes of the septal cartilages. R and L are the right and left side of noses

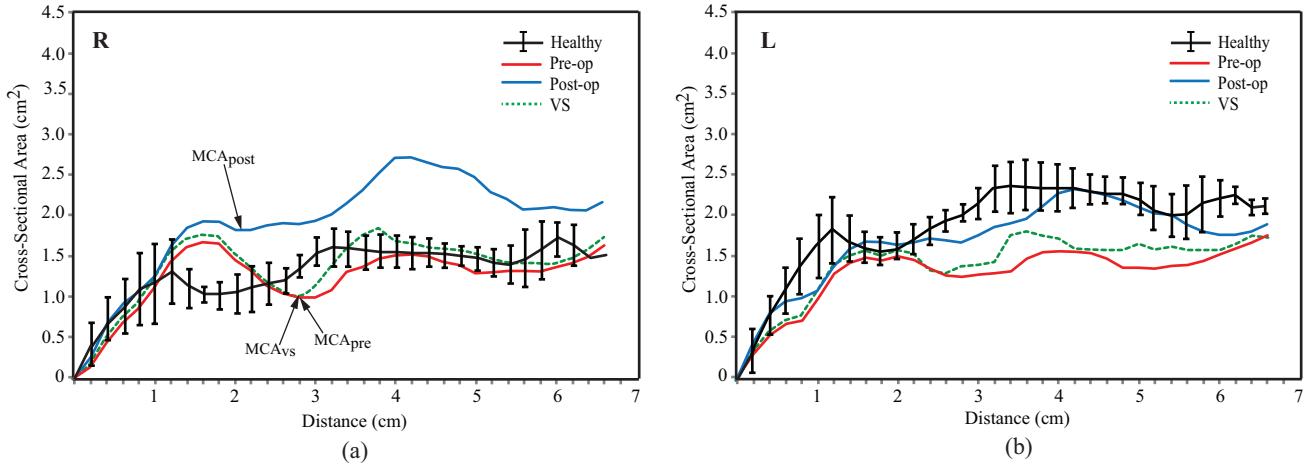

Fig. 7. Cross-sectional area of DNS patient #1 in comparison with the healthy baseline with 1 SD represented by an error bar. R (a) and L (b) are the right and left side of noses.

reduction or septoplasty alone was the best option for surgical treatment this DNS patient. Thus, engineer supervised by the same surgeon drew up a surgical plan relying on the pre-operative CT data (Fig. 6(b)) for formulating septoplasty without inferior turbinate reduction using the Mimics software (Fig. 6(d)). The 6-step CFD simulation based on the post-virtual-airway regions (Fig. 6(d)) was repeated to predict the post-virtual-operative outcomes in terms of the nasal geometric data (i.e. septal deviation angle and cross-sectional area) and the nasal airflow patterns (i.e. velocity magnitude, pressure drop, and R_N).

In the VS model, deviated septal cartilage was corrected and no deviation angle was observed. The minimal cross-sectional area of the VS model (MCA_{vs}) was not changed from the MCA_{pre} and observed at the nasal valve region (Fig. 7(a)). Beyond the nasal valve region, the nasal cross-sectional area was slightly wider than the pre-operative's cross-sectional area due to septoplasty without a turbinate reduction (Fig. 7(a)). The incoming air was well balanced between the two sides (Fig. 8(c)). High velocity magnitude of the incoming air ran along planes A and B, then it gradually decreased in the main nasal passage. This airflow pattern well closed to the healthy nose's (Fig. 9). Velocity magnitudes of the VS model were almost fully restored to the healthy baseline level (Fig. 10(a)). The maximum velocity magnitude of the VS model ($Vmax_{vs}$) was 2.60 m/s, which was observed at the nasal valve region (Fig. 10(a)). In addition, the pressure drops along the main nasal passage were in a range of $5.05 - 5.60$ Pa, which closes to the range of the healthy baseline ($4.45 - 5.05$ Pa) (Fig. 10(b)). The maximum pressure drop of the VS model (ΔP_{vs}) decreased from the ΔP_{pre} (i.e. 7.20 Pa) to 5.46 Pa, equivalent to 24% reduction (Fig. 10(b)). The R_N of the VS model was reduced to 0.0218 Pa·s/cm^3, which is a 24% reduction from the pre-operative's R_N (i.e. 0.0288 Pa) and 8% less than the mean of healthy baseline's R_N (i.e. 0.0238 ± 0.0047 Pa·s/cm^3).

The preliminary results presented that the VS using the CFD-CT technique was possible to be used as a pre-surgical planning tool, which might help surgeons to increase a treatment success. It was a motivation, which induced us to propose the three-process CFD-CT aided surgery approach (subsection 2.1). Implementation of the proposed approach in treating a DNS patient was the main goal of this research.

2.5. Implementing the CFD-CT aided surgery approach

2.5.1. Recruitment of DNS patient #2 This research recruited a 30 years old male adult (DNS patient #2), who suffered from breathing difficulty and nosebleed but had no history of nasal surgery, from the same Otolaryngology Unit, HRH Princess Maha Chakri Sirindhorn Medical Center (MSMC), Faculty of Medicine, Srinakharinwirot University, Ongkarak, Nakornnayok, Thailand. The patient has given their consent, which has been approved by Thailand's Faculty of Medicine of Srinakharinwiroj University. In the pre-surgery, the NOSE scoring and rhinomanometry techniques were applied to the DNS patient to determine NOSE scores and nasal resistance (R'_N). The pre-operative NOSE score was

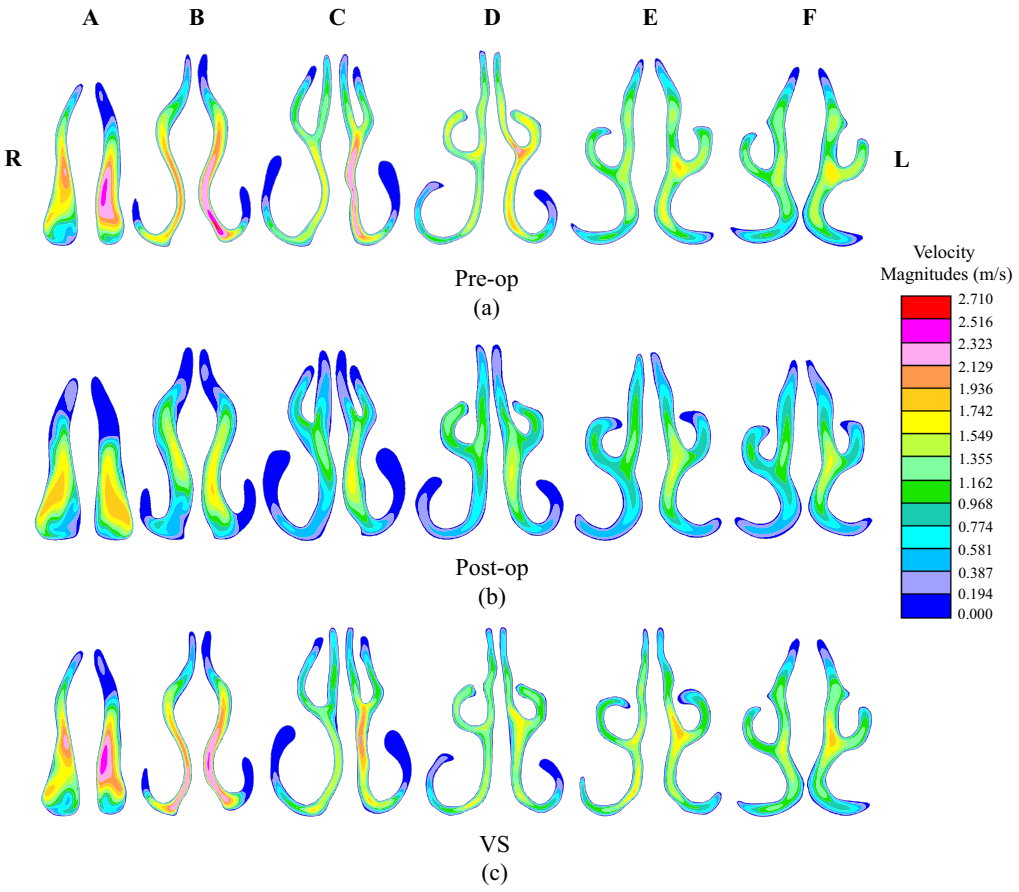

Fig. 8. The velocity magnitude distributions in the six coronal cross-sections (planes A to F) of DNS patient #1 in the pre-operative process (a), post-operative process (b), and virtual surgery modeling (c). R and L are the right and left sides of the noses.

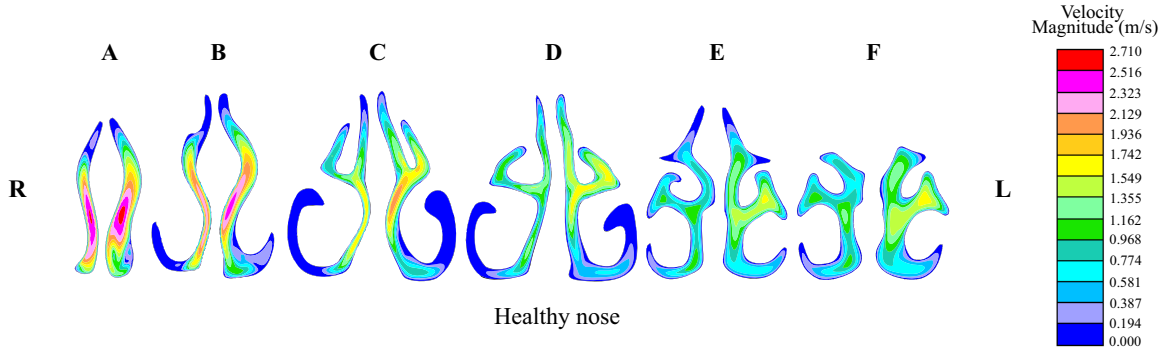

Fig. 9. The velocity magnitude distributions in the six coronal cross-sections (planes A to F) of one of the five healthy noses. R and L are the right and left sides of the noses.

75, implying that the DNS patient suffered from a severe nasal obstruction [39]. The pre-operative R'_N was 0.3026 Pa·s/cm^3, which is 59% higher than the Asian adults' mean, at a 75 Pa pressure point, of 0.190 Pa·s/cm^3 [40].

2.5.2. The pre-operative process in DNS patient #2

The DNS patient's nose was scanned with a Siemens Somatom Volume Access CT scanner (Siemens AG, Erlargen, Germany). The image resolution is 512x512 pixels and the shift between a cross-sectional image and the subsequent image was 1 mm. Figure 11(a) shows the segmented CT images of the DNS patient's nose prior to surgery, which was input of the CFD simulation. The 6-step CFD simulation (Fig. 3) was performed to investigate the pre-operative airflow conditions in terms of the nasal geometric data (i.e. septal deviation angle and cross-sectional area) and the nasal airflow patterns (i.e. velocity magnitude, pressure drop, and R_N).

This process attempts to determine the impacts of DNS on both nasal geometry and nasal airflow patterns of the pre-operative patient's nose by comparing the pre-operative data against those of the healthy baseline benchmark. Pre-operative deviation angle was measured using coronal CT cross-sections. The maximum leftward septal deviation angle was 24.2° observed at 4.5 cm from nostrils, where the most septal collapse was found. According to the maximum deviation angle of 24.2°, the patient was classified as severe DNS [38]. Figure 12 presents the nasal cross-sectional area of the DNS patient's nose compared against the healthy baseline's. The cross-sectional area on the right side (Fig. 12(a)) was generally greater than those of the healthy baseline, while the cross-sectional

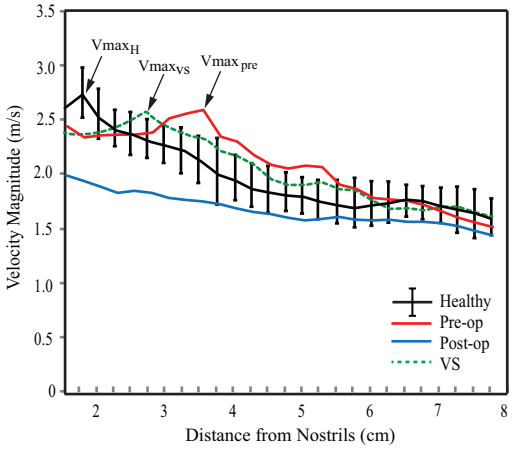

(a)

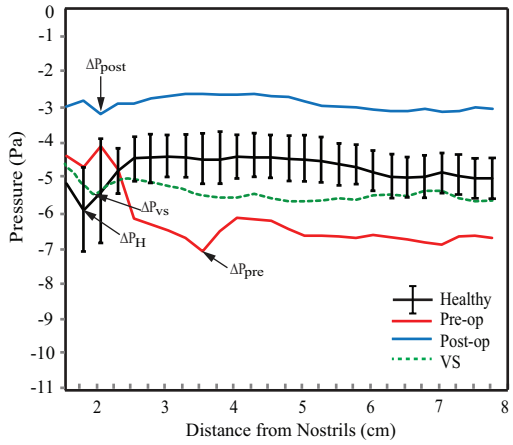

(b)

Fig. 10. Velocity magnitudes (a) and pressure drops (b) of DNS patient #1 in comparison with the healthy baseline with 1 SD represented by an error bar. $Vmax$ and ΔP indicate maximum velocity magnitudes and maximum pressure drops.

area on the constricted left side was drastically less than the healthy baseline's due to the septum collapse (Fig. 12(b)). The minimal cross-sectional area of the pre-operative nasal cavity (MCA_{pre}) was 0.83 cm^2 observed at the left nasal valve region (2.6 cm from nostrils) due to the nasal valve collapse in this patient (Fig. 12(b)).

Figure 13(a) illustrates an airflow distribution throughout the DNS patient's nose before surgery. Unlike the healthy nose (Fig. 9), the incoming air was not well balanced between sides (Fig. 13(a)). High velocity magnitudes were observed along the right (concave) side of the nose, while nearly complete collapse of the left (convex) side of the nasal cavity allowed only a small amount of air to pass through the main nasal passage (Fig. 13(a)). Velocity magnitudes were generally greater than those of the healthy baseline's noses (Fig. 14(a)). The maximum velocity magnitude of the pre-operative DNS patient's nose ($Vmax_{pre}$) was 3.13 m/s observed at the nasal valve, which is 15% higher than the $Vmax_H$, of 2.73 ± 0.19 m/s (Fig. 14(a)). Moreover, a severe DNS induces an abrupt pressure drop in the DNS nasal cavity. The maximum pressure drop of the pre-operative DNS nasal cavity (ΔP_{pre}) was 7.95 Pa observed at the nasal valve, which is 33% higher than the ΔP_H, of 5.96 ± 1.17 Pa (Fig. 14(b)). The pressure drops along the main nasal passage were in a range of $6.95 - 7.95$ Pa, which is greater than the healthy baseline's (4.45 ± 5.05 Pa). The pre-operative R_N was 0.0318 Pa·s/cm^3, which is 34% higher than the mean of healthy baseline's R_N (i.e. 0.0238 ± 0.0047 Pa·s/cm^3).

2.5.3. The pre-surgical planning process in DNS patient #2 Prior to surgery of the DNS patient, the pre-operative model was altered to generate two virtual surgery models, i.e. turbinate reduction alone (Plan A) and septoplasty and partially turbinate reduction (Plan B). An engineer supervised by the same surgeon drew up a pre-surgical plans relying on the CT data from the pre-operative process (Fig. 11(a)) using the Mimics software (Figs 11(b and c)). The 6-step CFD simulation based on post-virtual-airway regions was repeated to predict the post-virtual-operative outcomes in terms of the nasal geometric data (i.e. septal deviation angle and cross-sectional area) and the nasal airflow patterns (i.e. velocity magnitude, pressure drop, and R_N). The post-virtual-operative outcomes of both pre-surgical plans (A and B) were compared among the pre-operative conditions and the healthy baseline benchmark for selection the best course of operation.

i) Plan A

The DNS surgery based on Plan A aimed to restore the nasal airflow pattern by widening the nasal airway alone. Straightening of the septum to reduce septal deviation angle was ignored (i.e. no septoplasty). The nasal airway widening would be achieved by a resection of one-third of inferior turbinates on both sides. In the post-virtual-operative outcomes, the minimal cross-sectional area of the nose in Plan A (MCA_A) was not changed from the MCA_{pre}. However, the right nasal cross-sectional area was much wider than the pre-operative's and healthy baseline's cross-sectional areas, while the left nasal cross-sectional area was slightly wider than the pre-operative's (Fig. 12).

Although resection of one-third of inferior turbinates on both sides of the nose led to widening of the nasal cross-sectional area, particularly on the right side (Fig. 12(a)), the nasal airflow distribution was not noticeably improved (Fig. 13 (b)), when compared with the pre-operative airflow distribution (Fig. 13(a)). The maximum velocity magnitude of the nose in Plan A ($Vmax_A$) was 3.03 m/s, which is slightly less than in the pre-operative stage of the patient ($Vmax_{pre}$=3.13 m/s), a reduction of 3% (Fig. 14(a)). We observed an unremarkable reduction of velocity magnitudes, when compared with those in the pre-operative stage (Fig. 14(a)). In addition, the maximum pressure drop of the nose in Plan A (ΔP_A) was 6.77 Pa, which is lower than in the pre-operative stage of the patient (ΔP_{pre}=7.95 Pa), a reduction of 15% (Fig. 14(b)). The pressure drops in the main nasal passage were in a range of $6.15 - 6.77$ Pa, while those of the healthy baseline were at $4.45 - 5.05$ Pa. Predicted post-virtual operative R_N was 0.0271 Pa·s/cm^3, a reduction of 15% from the pre-operative R_N. However, the R_N of 0.0271 Pa·s/cm^3 is greater than the mean of healthy baseline's R_N (i.e. 0.0238 ± 0.0047 Pa·s/cm^3), equivalent to a 14% increase.

ii) Plan B

The DNS surgical correction based on Plan B aimed to restore the nasal septum and nasal airflow pattern by straightening the deviated septum and widening the nasal airway. The nasal airway widening would be achieved by a resection of one-fifth of middle and inferior turbinates. According to the surgeon, although the entire cross-sectional area modified in Plan B was noticeably larger than the healthy baseline's cross-sectional area (Fig. 12), the surgical procedure was still necessary to correct the septum deviation. The minimal cross-sectional area on the constricted left side was enlarged to 1.83 cm^2 (MCA_B), which is 55% higher than the MCA_{pre} (i.e. 0.83 cm^2); and 16% greater than the mean of healthy baseline's MCA on the same side of nose (i.e. 1.54 ± 1.07 cm^2) (Fig. 12(b)).

As seen in Fig. 13(c), the pre-surgical planning produced airflow distribution that was more balanced between the two sides and broadly similar to the healthy baseline's distribution (Fig. 9). However, at the pre-operative stage, a very small quantity of air could enter this patient's left-side nose as a result of a severe DNS

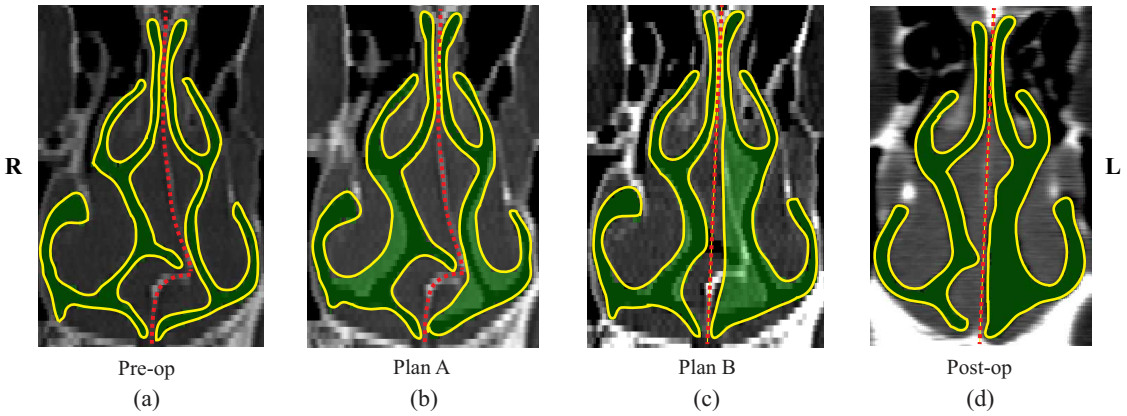

Fig. 11. The coronal cross-sectional CT images of DNS patient #2 present the segmented nasal airways of the pre-operative nose (a), pre-surgical planning A (b), pre-surgical planning B (c), and post-operative nose (d). Dashed lines represent shapes of the septal cartilages. R and L are the right and left sides of noses.

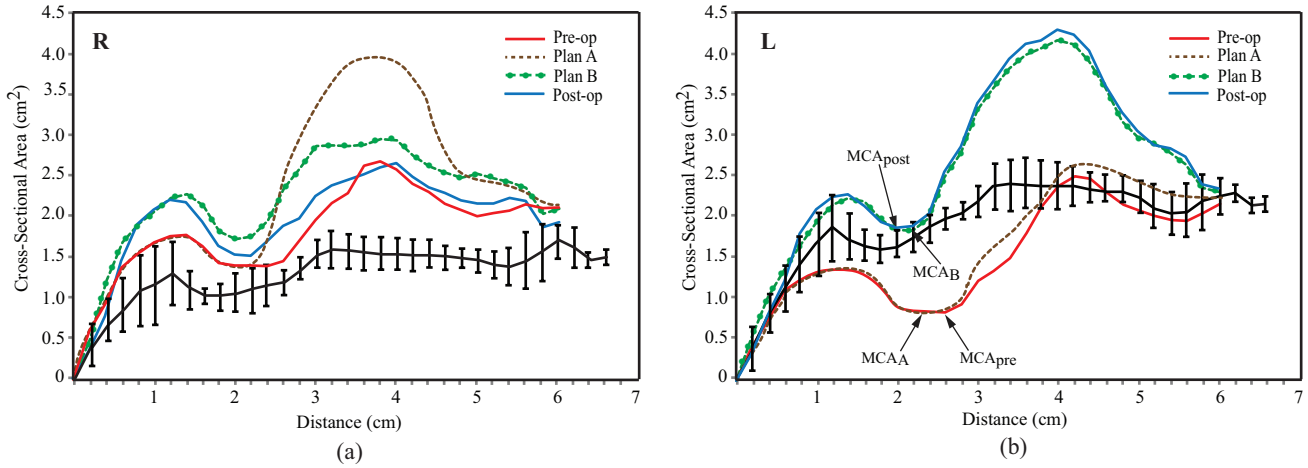

Fig. 12. Cross-sectional area of DNS patient #2 in comparison with the healthy baseline with 1 SD represented by an error bar. Dashed lines present nasal cross-sectional areas of the pre-surgical planning A and B. R (a) and L (b) are the right and left sides of the noses.

(Fig. 13(a)). In Fig. 14(a), maximum velocity magnitude at the stage of pre-surgical planning B ($Vmax_B$) was 2.34 m/s, which is a 25% reduction from $Vmax_{pre}$. Velocity magnitudes were in good agreement with the healthy baseline's (Fig. 14(a)). In addition, Fig. 14(b) shows no abrupt pressure drop that was observed in the post-virtual-surgery outcomes. The maximum pressure drop observed at the nasal valve region was 4.32 Pa (ΔP_B), which is a 46% reduction from the ΔP_{pre}). The pressure drops in the main nasal passage stabilized at $3.20 - 4.32$ Pa, which were slightly less than the range of healthy baseline's (i.e. $4.45 - 5.05$ Pa). Predicted post-virtual operative R_N was 0.0173 Pa·s/cm^3, a reduction of 46% from the pre-operation due to no abrupt pressure drops. However, the R_N of 0.0173 Pa·s/cm^3 was 16% less than the mean of healthy baseline's R_N.

From the post-virtual-operative outcomes of Plan A and Plan B, it is evident that the surgical components of Plan B (septoplasty and one-fifth turbinate reduction) could restore the nasal airflow patterns closer to the healthy level than those of the Plan A (one-third turbinate reduction alone). Thus, Plan B was a more suitable course of surgical operation to address a successful outcome of DNS patient #2. Therefore, the surgeon concluded that Plan B would be used as a personalized surgical plan for this DNS patient.

2.5.4. The post-operative process in DNS patient #2 The surgeon performed septoplasty and turbinate reduction to correct deformities of the nose based on the pre-surgical Plan B in DNS patient #2. After the DNS operation, the patient received similar intranasal post-operative care and no sign of complication was detected. In the post-operative outcome assessment, the NOSE scoring, rhinomanometry, CT scan (Fig. 11(d)), and the 6-step CFD simulation were repeated on the same DNS patient. The follow-up study was carried out six months afterward. To minimize potential effects of nasal cycling on the CFD results, the DNS patient's CT data, which mucosal thickness was generally symmetrical in both pre- and post-surgical scans, was used in this study. The surgical success was assessed by the post-operative outcomes with respect to the geometric data (i.e. septal deviation angle and cross-sectional area), the nasal airflow patterns (i.e. velocity magnitude, pressure drop, and R_N), the patient-reported symptom (i.e. NOSE score), and the rhinomanometry data (i.e. R'_N).

3. Results

The post-operative outcomes of the DNS patient #2 (i.e. NOSE scoring, R'_N, deviation angle, MCA, V_{max}, ΔP, and R_N) compared against those of the pre-operative conditions, pre-surgical plan B, and the healthy baseline benchmark presented in Table 1 and discussed below.

3.1. The post-operative NOSE scores and rhinomanometric data of DNS patient #2 The post-operative patient

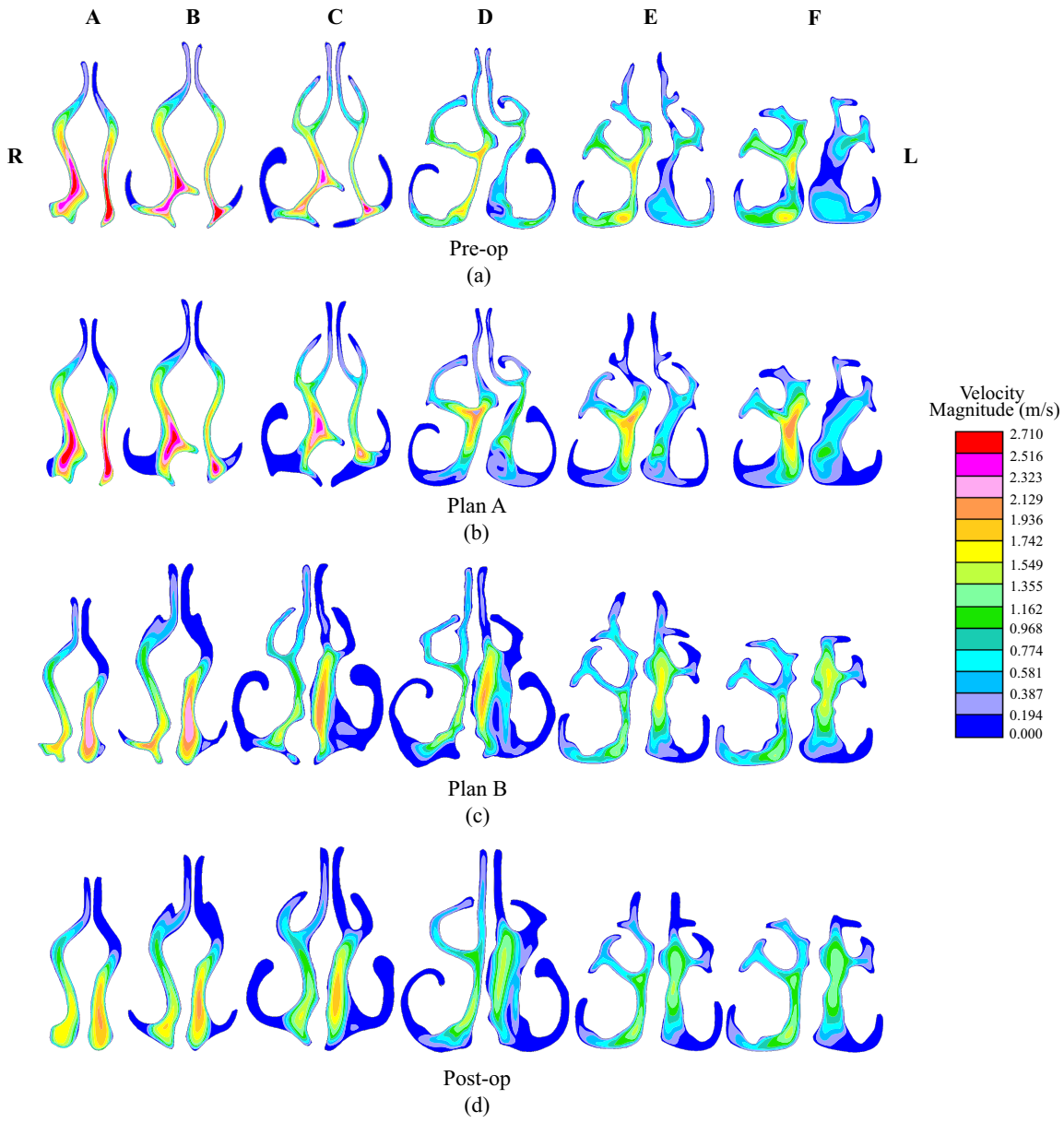

Fig. 13. The velocity magnitude distributions in the six coronal cross-sections (planes A to F) of DNS patient $\#2$ in the pre-operative process (a), pre-surgical planning A (b), pre-surgical planning B (c), and post-operative process (d). R and L are the right and left sides of the noses.

reported symptom (i.e. NOSE score) drastically decreased to 4 (from 75), equivalent to a 95% reduction, which means very mild problem with nasal obstruction detected after surgery [39]. In addition, the post-operative R'_N measured by rhinomanometer decreased to 0.194 Pa$\cdot s/\text{cm}^3$ (from 0.3026 Pa$\cdot s/\text{cm}^3$), equivalent to a reductions of 36%. The post-operative NOSE score and R'_N data implied that the surgical treatment was clinically acceptable to the surgeon and patient (Table 1).

3.2. The post-operative nasal geometric data of DNS patient $\#2$ Surgeon designed septoplasty to restore the DNS (dashed line in Fig. 11(a)) to the midline (dashed line in Fig. 11(d)). Septal deviation angles were reduced in all coronal cross-sections of the nose. Maximum reduction of septal deviation angle (100%) was observed at the areas beyond the nasal valve region, while minimal reduction was in a range of $40\%-58\%$ found in the posterior portion of the nasal septum end. All deviation angles were less than 4.38° in all planes of the post-operative nose (Table 2).

After the surgery using the CFD-CT aided surgery approach, severe DNS was corrected. Small variability of post-operative cross-sectional areas from the pre-surgical planning was observed (Fig. 12). The minimal cross-sectional area of the post-operative nose (MCA_{post}) was 1.81 cm^2, while MCA_B was 1.83 cm^2. The MCA_{post} of 1.81 cm^2 is 120% higher than the MCA_{pre} (i.e. 0.83 cm^2) and 15% higher than the mean of healthy baseline's MCA (i.e. 1.54 ± 0.17 cm^2) on the same side (Table 1).

3.3. The post-operative nasal airflow patterns of DNS patient $\#2$ The airflow distribution was well balanced between sides and passed throughout the middle portion of both sides of the nose (Fig. 13(d)), which was the same pattern as observed in the healthy nose (Fig. 9). In Fig. 14(a), the post-operative maximum velocity magnitude ($Vmax_{post}$) was 2.03 m/s, which decreased from $Vmax_{pre}$, equivalent to a 35% reduction (Table 1). Although the overall velocity magnitudes after surgery

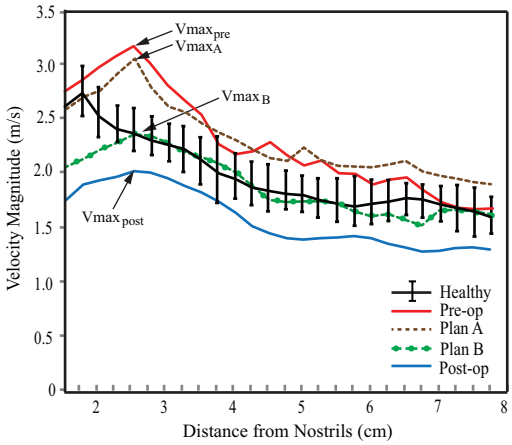

(a)

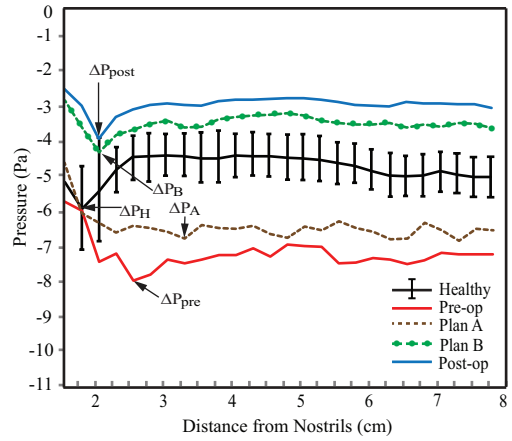

(b)

Fig. 14. Velocity magnitudes (a) and pressure drops (b) of DNS patient #2 in comparison with the healthy baseline with 1 SD represented by an error bar. R and L are the right and left sides of the noses. $Vmax$ and ΔP indicate maximum velocity magnitudes and maximum pressure drops.

was less than those of the healthy baseline, the pattern of post-operative velocity magnitudes reduction in the nasal cavity was generally similar to the healthy baseline's, i.e. the acceleration of air velocity magnitudes observed near the nasal valve region was found and the velocity magnitude gradually decreased beyond the nasal valve region (Fig. 14(a)). In addition, no abrupt pressure drop was found in the post-operative DNS patient's nose (Fig. 14(b)). As shown in Fig. 14(b), the maximum pressure drop in the nasal valve region (ΔP_{post}) was 3.83 Pa, which decreased from ΔP_{pre} (i.e. 7.95 Pa), equivalent to a 52% reduction, and is 36% less than ΔP_H (Table 1). The pressure drops stabilized at $2.80 - 3.18$ Pa in the main nasal passage, while those of the healthy baseline were in a range of $4.45 - 5.05$ Pa (Fig. 14(b)). Post-operative R_N was 0.0153 Pa$\cdot s/\text{cm}^3$, a decrease of 52% from the pre-operative's R_N (i.e. 0.0318 Pa$\cdot s/\text{cm}^3$)), which is attributable to no post-operative abrupt pressure drops; and was 36% less than the mean of healthy baseline's R_N (i.e. 0.0238 ± 0.0047 Pa$\cdot s/\text{cm}^3$).

As a result (Fig. 13(d), Fig. 14, Tables 1 and 2), the surgery with the implementation of the CFD-CT approach could effectively and generally restore airflow patterns to the healthy baseline's with some variability from the predicted pre-surgical planning's outcomes.

4. Discussion

In DNS patient #1, who underwent conventional surgery without adoption of the CFD-CT approach, the post-operative nasal cross-sectional area was excessively wider than the pre-operative nose, a phenomenon which led to variations of nasal airflow patterns. Virtual surgery reveals that only septoplasty (inducing a slightly enlargement of nasal airway compared with the pre-operative airway) could restore nasal airflow patterns to the healthy baseline benchmark. Although DNS patient #1's surgical outcome was relatively satisfying to the patient, assessing from the reduction of the NOSE score, the oversized bilateral cross-sectional area could induce water loss in nasal mucosa, giving rise to a worse crust formation and infection [43]. Consistent with [17, 20, 44], in case of moderate DNS, i.e. DNS patient #1, a surgical correction in the nasal anterior section was sufficient. According to [21], an over-widening airway does not always induce a normal airflow pattern; on the other hand, it might deteriorate R_N, heat transfer, olfactory perception. Also, the over-widening airway could increase the wall shear stress of the patient's nose. The conventional surgical method without CFD-CT presurgical planning could induce an excessive excision of airway, thus a water loss in nasal mucosa and a large airflow velocity reduction.

In DNS patient #2, who underwent surgery using the proposed CFD-CT aided surgery approach, the pre-operative sudden pressure drops were observed beyond the septum deviation areas. The sudden drops in pressure induced high pre-operative R_N and thus breathing difficulty. No high velocity magnitudes were observed in the constricted convex (left) side beyond plane C since very small amounts of air could enter as a result of the septum collapse (Fig. 13(a)). Rather, the high velocity magnitudes were found in the concave (right) side (Fig. 13(a)). This observation confirms the notion that the region of constriction within a coronal cross-section would not increase the speed of flow through it provided that the flow deflected to a more open region. In addition, it is consistent with Liu et al [18], who reported that although the maximum velocity magnitude was normally found in the convex side of DNS (as observing in DNS patient #1), a larger velocity magnitude was sometimes observed in the concave (right) side of a DNS nose like that found in DNS patient #2. These discrepancies were due to the anatomical differences among individual subjects. Thus, evaluating patient-specific aerodynamic effects due to DNS using the CFD-CT approach is an essential technique, which can help surgeons to diagnose and treat a DNS effectively.

In the pre-surgical planning step, the best course of nasal operation for DNS patient #2 was identified using the CFD-CT approach. At this stage, the approach enables the surgeon to localize DNS, specify the amount of nasal tissues to remove as well as predict the surgical outcomes. A prediction of most likely post-operative outcomes, e.g. post-virtual-airway regions, nasal cross-sectional area, and nasal airflow patterns could be made. The findings show that the CFD-CT approach can be applied to and is suitable for the pre-surgical planning of DNS noses.

After the surgery with the CFD-CT aided surgery approach, the severe DNS of patient was corrected. The septal deviation angle of the post-operative nose was reduced to less than 4.38° (82% reduction), which is implied that the nasal septum was almost restored to the normal shape. In addition, the constricted left side was wider due to the septoplasty and turbinate reduction performed in the surgical processes. The post-operative $Vmax$, ΔP, and R_N were decreased by 35%, 52%, and 52%, respectively, when compared with the pre-operative's (Table 1). Nonetheless, there were some small discrepancies between the post-virtual-operative outcomes and the post-actual-operative outcomes as a result of the random effects of post-treatment healing. Although the post-operative nasal airway of the DNS patient was noticeably larger

Table I. NOSE score, R'_N, maximum septal deviation angle, $Vmax$, ΔP, and R_N. Percentage differences between pre- and post-surgical treatment were calculated by: %Difference= [$Value_{post}$-$Value_{pre}$)/ $Value_{pre}$] x100 %

Studies	Evaluation	Pre-op	Planning	Post-op	Healthy baseline	%Difference
NOSE scoring	NOSE score	75	N/A	4	N/A	-95%
Rhinomanometry	R'_N (Pa·s/m^3)	0.3026	N/A	0.1941	N/A	-36%
CT	Max. deviation angle	24.2°	0°	< 4.38°	0°	-82%
	MCA (cm^2)	L=0.83	L=1.83	L=1.81	L=1.54±0.17 R=1.14±0.18	120%
CFD	Vmax (m/s)	3.13	2.34	2.03	2.73±0.19	-35%
	ΔP (Pa)	7.95	4.32	3.83	5.96±1.17	-52%
	R_N (Pa·s/m^3)	0.0318	0.0173	0.0153	0.0238±0.0047	-52%

Table II. Percentage differences of septal deviation angles (degree) between pre- and post-surgical treatment.

Distance from nostrils (cm)	Deviation angle		%Difference	Distance from nostrils (cm)	Deviation angle		%Difference
	Pre-op	Post-op			Pre-op	Post-op	
2.1	4.31°	1.43°	67%	4.1	20.9°	1.52°	93%
2.2	5.22°	1.39°	73%	4.2	22.5°	1.48°	93%
2.3	5.84°	1.33°	77%	4.3	23.8°	1.55°	94%
2.4	6.94°	1.34°	81%	4.4	23.6°	1.70°	93%
2.5	6.78°	0°	100%	4.5	24.2°	1.90°	92%
2.6	6.91°	0°	100%	4.6	24.1°	2.17°	91%
2.7	6.48°	0°	100%	4.7	22.7°	2.29°	90%
2.8	7.08°	0°	100%	4.8	13.7°	1.88°	86%
2.9	7.58°	0°	100%	4.9	14.2°	2.08°	85%
3.0	7.78°	0°	100%	5.0	13.7°	2.46°	82%
3.1	8.50°	1.33°	84%	5.1	12.7°	1.83°	86%
3.2	9.01°	1.13°	87%	5.2	11.5°	2.52°	78%
3.3	9.67°	1.32°	86%	5.3	12.0°	1.86°	85%
3.4	10.0°	1.40°	86%	5.4	11.1°	2.18°	80%
3.5	11.4°	1.84°	84%	5.5	10.4°	1.49°	86%
3.6	11.9°	2.45°	79%	5.6	7.63°	4.44°	42%
3.7	12.7°	1.11°	91%	5.7	7.29°	4.38°	40%
3.8	14.6°	1.10°	92%	5.8	7.67°	4.09°	47%
3.9	16.0°	1.06°	93%	5.9	7.32°	4.27°	42%
4.0	17.7°	1.69°	90%	6.0	7.81°	3.80°	51%

Table III. Velocity magnitudes of inspired airflow obtained from the healthy noses compare with the same results from existing literature [11, 14, 28, 36]. The values in parentheses represent the ranges of velocity magnitudes in each plane of our study.

Studies	Geometries	Q (L/min)	Velocity magnitudes (m/s)						Linear Eq.	R^2
			A	B	C	D	E	F		
Keyhani	Half-nasal	7.5	2.93	3.82	3.58	2.71	2.70	2.34	-0.23x+3.76	0.35
Jeong	Both sides	12	2.70	N/A	2.17	1.70	N/A	1.61	-0.27x+2.84	0.93
Subramaniam	Both sides	15	4.23	N/A	3.89	3.34	N/A	2.73	-0.44x+4.69	0.97
Ishikawa	Both sides	15	3.40	3.15	2.30	2.10	N/A	1.80	-0.43x+3.83	0.95
Present study	Both sides	15	2.32 (1.7-2.6)	2.21 (1.8-2.4)	1.96 (1.3-2.3)	1.79 (1.3-2.1)	1.67 (1.0-2.0)	1.78 (1.3-2.1)	-0.13x+2.40	0.85

than the healthy baseline's, the post-operative results were clinically acceptable to the surgeon as indicated by the 36% reductions in R'_N (nasal resistance measured by rhinomanometer); and satisfying to the DNS patient, as indicated by a 95% reduction in the clinical symptom score (NOSE score).

In the healthy baseline, half-nasal cross-sectional areas measured by the CT-based method correlated well with those of the other study [17]. For CFD modeling results, air evenly distributes throughout the middle meatus of the left and right sides of the nose, a fact which was also reported in Chen et al. [16], Croce et al. [41] and Wen et al. [15]. Furthermore, according to [28, 42], the smell sensory region receives the least amount of air. To validate the CFD modeling, velocity magnitudes of the healthy baseline of this research work were compared with those of the healthy noses of the

existing research studies [11, 14, 28, 36] in the same coronal cross-sections (Table 3). A fitted linear regression was used to identify the relationship between velocity magnitudes and distances from nostrils among all healthy subjects. It was reported that velocity magnitudes decreased as a function of distance from nostrils in all studies. R^2 ranged from 0.85 to 0.98, except for that of the Keyhani (R^2=0.36) [28]. Although the velocity magnitudes of our healthy baseline were less than those of the previous studies, patterns of velocity magnitudes along the nasal cavities in our healthy baseline correlated well with those of the other studies. These discrepancies were probably due to the anatomical differences among individual subjects [41]. Differences of boundary and initial conditions assumed in the CFD simulations were possible causes of the variations.

R_N is calculated from the maximum pressure drop (ΔP) from nostrils to nasal septum end at a fixed flow rate (Q) of 250 cm^3/s (i.e. the CFD method). On the other hand, R'_N is determined by the rhinomanometry technique by measuring nasal resistance at a 75 Pa pressure point. In this study, R_N of the CFD modeling was less than R'_N due to the different definitions of nasal resistance between the two techniques as mentioned above; and could not be compared each other [17]. However, we fundamentally focused the amount of nasal resistance reduction as a result of the surgical treatment using CFD-CT approach.

This research contains the following limitations: first, the dynamic nature of nasal mucosa (nasal cycling) was ignored as the nasal wall was assumed fixed. Second, the effect of DNS on inspiratory flow was the sole focus of the research study. In fact, expiratory flow should have been taken into consideration in the pre-surgical planning, especially in patients with middle and posterior deviations. Expiratory airflow will be studied in our future work. Third, although DNS patients could mount-breathe to increase total airflow volume, this research disregards this fact. Fourth, the unsteady-state (time-dependent airflow) was not assumed in this study due to computational constraint. However, steady-state airflow was sufficient since we aimed to investigate effects of geometric changes on the nasal airflow patterns due to treatment using the CFD-CT aided surgery approach. In addition steady-state airflow was assumed in many other existing DNS studies [17, 19, 32]. Finally, the healthy baseline was established from five healthy subjects, so future research should recruit more healthy subjects.

5. Conclusion

This research presents the CFD-CT aided surgery approach, which is the use of the CFD and CT scanning techniques, as a pre-surgical aiding tool in DNS surgery. The approach consists of three parts: the pre-operative process, pre-surgical planning process and post-operative process. This study is the first that proposes a comprehensive surgery-assisted approach that help the surgeon in formulating and selecting the best course of patient-specific DNS surgery with predictable post-operative outcomes. Furthermore, it is possible to apply the CFD-CT approach to surgery of other nose disorders.

6. Acknowledgments

Thank you Prof. Emad S. Ebbini of the Department of Electrical and Computer Engineering, University of Minnesota, MN, USA, for the Mimic software program; and to the Computer Service Center, King Mongkut's Institute of Technology Ladkrabang, Thailand, for the STAR-CD software program. This research was the jointed project supported by King Mongkut's Institute of Technology Ladkrabang (KMITL Research Fund: S. Tungjitkusolmun) and Faculty of Medicine, Srinakarinwirot University, Thailand.

References

(1) J. S. Rhee, D. M. Poetker, T. L. Smith, A. Bustillo, M. Burzynski, and R. E. Davis, "Nasal valve surgery improves disease-specific quality of life," Laryngoscope, vol. 115, no. 3, pp. 437-440, 2005.

(2) D. F. Proctor, "The nose: the upper airway," vol. 12, Proctor DF and Anderson I, Eds. New York: Elsevier Biomedical Press; 1982, pp. 23-43.

(3) M. Wolfensberger and T. Hummel, "Anti-inflammatory and surgical therapy of olfactory disorders related to sino-nasal disease," Chem. Senses, vol. 27, no. 7, pp. 617-622, 2002.

(4) I. Yildirim and E. Okur, "The prevalence of nasal septal deviation in children from Kahramanmaras,Turkey," Int. J. Pediatr. Otorhinolaryngol., vol. 67, no. 11, pp. 1203-1206, 2003.

(5) M. G. Stewart, T. L. Smith, E. M. Weaver, D. L. Witsell, B. Yueh, M. T. Hannley, J. T. Johnson, "Outcome after nasal septoplasty: Results from the Nasal Obstruction Septoplasty Effectiveness (NOSE) study," Otolaryngol. Head Neck Surg., vol. 130, pp. 283-290, 2004.

(6) S. P. Gulati, O. P. Sachdeva, R. Wadhera, N. Sodhi, and A. Garg, "Role of rhinomanometry to assess nasal airflow and resistance in patients undergoing septoplasty," Indian J. Otolaryngol. Head Neck Surg., vol. 60, no. 2, pp. 133-136, 2008.

(7) J. Theissing, J.A. Werner, and G. Rettinger, "ENT-Head and Neck Surgery: Essential Procedures," NY: Thieme New York; 2011.

(8) R. K. Chandra, M. O. Patadia, and J. Raviv, "Diagnosis of nasal airway obstruction," Otolaryngol. Clin. North. Am., vol. 42, no. 2, pp. 207-225, 2009.

(9) E. Egeli, L. Demirci, B. Yazycy, and U. Harputluoglu, "Evaluation of the inferior turbinate in patients with deviated nasal septum by using computed tomography," Laryngoscope, vol. 114, no. 1, 113-117, 2004.

(10) M. P. Valencia and M. Castillo, "Congenital and acquired lesions of the nasal septum: a practical guide for differential diagnosis," Radiographics, vol.128, no. 1, pp. 205-224, 2008.

(11) S. Ishikawa, T. Nakayama, M. Watanabe, and T. Matsuzawa, "Visualization of flow resistance in physiological nasal respiration: analysis of velocity and vorticities using numerical simulation," Arch. Otolaryngol. Head Neck Surg., vol. 132, no. 11, pp. 1203-1209, 2006.

(12) J. H. Lee, Y. Na, S. K. Kim, and S. K. Chung. "Unsteady flow characteristics through a human nasal airway," Respir. Physiol. Neurobiol., vol. 172, no. 3, pp. 136-146, 2010.

(13) R. A. Segal, G. M. Kepler, and J. S. Kimbell, "Effects of differences in nasal anatomy on airflow distribution: a comparison of four individuals at rest," Ann. of Biomed. Eng., vol. 36, no. 11, pp. 1870-1882, 2008.

(14) R. P. Subramaniam, R. B. Richardson, K. T. Morgan, J. S. Kimbell, and R. A. Guilmette, "Computational fluid dynamics simulations of inspiratory airflow in the human nose and nasopharynx," Inhal. Toxicol., vol. 10, no. 2, pp. 91-120, 1998.

(15) J. Wen, K. Inthavong, J. Tu, and S. Wang, "Numerical simulations for detailed airflow dynamics in a human nasal cavity," Respir. Physiol. Neurobiol., vol. 161, no. 2, pp. 125-135, 2008.

(16) X. B. Chen, H. P. Lee, V. F. Chong, and D. Y. "Assessment of septal deviation effects on nasal air flow: a computational fluid dynamics model," Laryngoscope, vol. 119, no. 9, pp. 1730-1736, 2009.

(17) G. J. M. Garcia, J. S. Rhee, B. A. Senior, and J. S. Kimbell, "Septal deviation and nasal resistance: an investigation using virtual surgery and computational fluid dynamics," Am. J. Rhinol. Allergy., vol. 24, no. 1, pp. 46-53, 2010.

(18) T. Lui, D. Han, J. Wang, J. Tan, H. Zang, T. Wang, Y. Li, and S. Cui, "Effects of septal deviation on the airflow characteristics: Using computational fluid dynamics models," Acta. Oto-Laryngol., vol. 132, pp. 290-298, 2012.

(19) H. Moghadas, O. Abouali, A. Faramarzi, and G. Ahmadi, "Numerical investigation of septal deviation effect on deposition of nano/microparticles in human nasal passage," Respir. Physiol. Neurobiol., vol. 177, no. 1, pp. 9-18, 2011.

(20) S. Ozlugedik, G. Nakiboglu, C. Sert, A. Elhan, E. Tonuk, S. Akyar, and I. Tekdemir, "Numerical study of the aerodynamic effects of septoplasty and partial lateral turbinectomy," Laryngoscope, vol. 118, no. 2, pp. 330-334, 2008.

(21) Y. Na, K. S. Chung, S. K. Chung, and S. K. Kim, "Effects of single-sided inferior turbinectomy on nasal function and airflow characteristics," Respir. Physiol. Neurobiol., vol. 180, pp. 289-297,

2012.

(22) J. S. Rhee, D. E. Cannon, D. O. Frank, and J. S. Kimbel, "Role of virtual surgery in pre-operative planning: Assessing the individual components of functional nasal airway surgery," Arch. Facial Plast. Surg., vol. 14, no. 5, pp. 354-359, 2012.

(23) D. Wexler, R. Segal, and J. Kimbell, "Aerodynamic effects of inferior turbinate reduction: computational fluid dynamics simulation," Arch. Otolaryngol. Head Neck Surg., vol. 131, no. 12, pp. 1102-1107, 2005.

(24) J. S. Kimbell, D.O. Frank, P. Laud, G.J.M. Garcia, and J.S. Rhee, "Changes in nasal airflow and heat transfer correlate with symptom improvement after surgery for nasal obstruction," J. of Biomech., vol. 46, pp. 2634-2643, 2013.

(25) J. S. Rhee, S. S. Pawar, G. J. M. Garcia, and J. S. Kimbell, "Towards personalized nasal surgery using computational fluid dynamics," Arch. Facial Plast. Surg., vol. 13, no.5, pp. 305-310, 2011.

(26) "STAR-CD 3.22 users' guide". Computational Fluid Dynamics Ltd., 2004.

(27) I. Hahn, P. W. Scherer, and M. M. Mozell, "Velocity profiles measured for airflow through a large-scale model of the human nasal cavity," J. Appl. Physiol., vol. 75, no. 5, pp. 2273-2287, 1993.

(28) K. Keyhani, P. W. Scherer, and M. M. Mozell, "Numerical simulation of airflow in the human nasal cavity," J. Biomech. Eng., vol. 117, no. 4, pp. 429-441, 1995.

(29) S. Naftali, M. Rosenfeld, M. Wolf, and D. Elad, "The air-conditioning capacity of the human nose," Ann. Biomed. Eng., vol. 33, no. 4, pp. 545-553, 2005.

(30) S. Naftali, R. C. Schroter, R. J. Shiner, and D. Elad, "Transport phenomena in the human nasal cavity: a computational model," Ann. Biomed. Eng., vol. 26, no. 5, pp. 831-839, 1998.

(31) S. Schreck, K. J. Sullivan, C. M. Ho, and H. K. Chang, "Correlations between flow resistance and geometry in a model of the human nose," J. Appl. Physiol., vol. 75, no. 4, pp. 1767-1775, 1993.

(32) S. K. Kim, G.E. Heo, A. Seo, Y. Na, and S.K. Chung, "Correlation between nasal airflow characteristics and clinical relevance of nasal septal deviation to nasal airway obstruction," Resp. Physiol. Neurobiol., vol. 192, pp. 95-101, 2014.

(33) Z. V. A. Warsi. "Conservation form of the Navier-Stokes equations in general nonsteady coordinates," AIIA Journal, vol. 19, no. 2, pp. 240-242, 1981.

(34) S. V. Patankar and D. B. Spalding, "A calculation procedure for heat, mass and momentum transfer in three-dimensional parabolic flows," Int. J. Heat. Mass. Transfer., vol. 15, no. 10, pp. 1778-1806, October 1972.

(35) "Human respiratory tract model for radiological protection" in Annals of the International Commission on Radiological Protection (ICRP Publication 66), vol. 24, Oxford: Pergamon, 1994.

(36) S. J. Jeong, W. S. Kim, and S. J. Sung, "Numerical investigation on the flow characteristics and aerodynamic force of the upper airway of patient with obstructive sleep apnea using computational fluid dynamics," Med. Eng. Phys., vol. 29, no. 6, pp. 637-651, 2007.

(37) A. Ertap, K. Sinem, B. Ali, O. Semsettin, S. Haldun, and S.D. Ali, "Evaluation of the turbinate hypertrophy by computed tomography by computed tomography in patients with deviated nasal septum," Otolaryngol. Head Neck Surg., vol. 136, pp. 380-384, 2007.

(38) M. M. Elahi, S. Frenkiel, and N. Fageeh, "Paraseptal structural changes and chronic sinus disease in relation to the deviated septum," J. of Otolaryngol., vol. 26, pp. 236-240, 1997.

(39) M. G. Stewart, D. L. Witsell, T. L. Smith, E. M. Weaver, B. Yueh, and M. T. Hannley, "Development and validation of the Nasal Obstruction Systom Evaluation (NOSE) Scale," Otolaryngol Head and Neck Surg., vol. 130 (2), pp. 157-163, 2004.

(40) A. H. Suzina, M. Hamzah, and A.R. Samsudin, "Active anterior rhinomanometry analysis in normal adult Malays," The J. of Laryngol. Otol. vol. 117, pp. 605-608, 2003.

(41) C. Croce, R. Fodil, M. Durand, G. Sbibl-Apiou, G. Caillibotte, J. F. Papon, J. R. Blondeau, A. Coste, D. Isabey, and B. Louis, "In vitro experiments and numerical simulations of airflow in realistic nasal airway geometry," Ann. of Biomed. Eng., vol. 34, no. 6, pp. 997-1007, 2006.

(42) D. Elad, R. Liebenthal, B. Wenig, and S. Einav, "Analysis of air flow patterns in the human nose," Med. Biol. Eng. Comput., vol.31, no. 6, pp. 585-592, 1993.

(43) G. J. M. Garcia, N. Bailie, D. A. Martins, and J. S. Kimbell, "Atrophic rhinitis: a CFD study of air conditioning in the nasal cavity," J. Appl. Physiol., vol. 103, pp. 1082-1092, 2007.

(44) A. Korantzis, E. Cardamakis, E. Chelidonis, and T. Papamihalis, "Nasal septum deformity in the newborn infant during labour," Eur. J. Obstet. Gynecol. Reprod. Biol., vol. 44, pp. 41-46, 1992.

Khaisang Hemtiwakorn (Non-member) received the B.Sc. and M.Sc. (Radiological Technology) from Mahidol University, Bangkok, Thailand in 2004 and 2007 respectively. She currently pursues her Ph.D in Electricals Engineering from Faculty of Engineering, King Mongkut's Institute of Technology Ladkrabang (KMITL), Thailand. Her research works focus on a computational fluid dynamics (CFD) modeling in a human upper airway and its applications for the advanced diagnostic and pre-surgical tools of deviated nasal septum (DNS) and obstructive sleep apnea syndrome (OSAS).

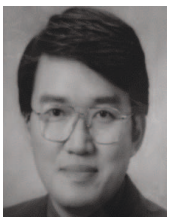

Visan Mahasittiwat (Non-member) received the M.D. from Prince of Songkla Univesity (PSU) in 1987. He is currently Assistant Professor in Otolaryngology, Department of Ophthalmology and Otolaryngology, Faculty of Medicine, Srinakarinwirot University (SWU), Thailand. His research interests include earring aids, eye tracking, and using computational fluid dynamics (CFD) for improving the surgical outcomes of DNS patients.

Supan Tungjitkusolmun (Non-member) recieved the B.S.E.E.degree from the University of Pennsylvania, Philadephia, in 1995, and the M.S.E.E. and Ph.D. degrees from the University of Wisconsin, Madison, in 1996, and 2000. He is currently Assistant Professor of KMITL, Thailand. His research interests include finite-element modeling, radio-frequency cardiac ablation, microwave ablation, signal processing, and image processing.

Kazuhiko Hamamoto (Member) received the B.Eng., M.Eng., and D.Eng from Tokyo University of Agriculture and Technology. He works as a Professor in Department of Information Media Technology, School of Information and Telecommunication Engineering, Tokai University, Japan. His expertise lies in information architecture, medical information, human interface design and virtual reality.

Chuchart Pintavirooj (Member) received the B. Sc. (Radiological Technology) and M.Sc. (Biomedical Instrumentation) from Mahidol University, Bangkok, Thailand in 1985 and 1989 respectively. In 1995, he received another master degree in Biomedical Engineering from Worcester Polytechnic Institute, MA., USA. In 2000, he earned a Ph. D. in Biomedical Engineering from Drexel University, Philadelphia. His current research is in Biomedical Image/Signal Processing with emphasis on image reconstruction, image classification and image restoration.